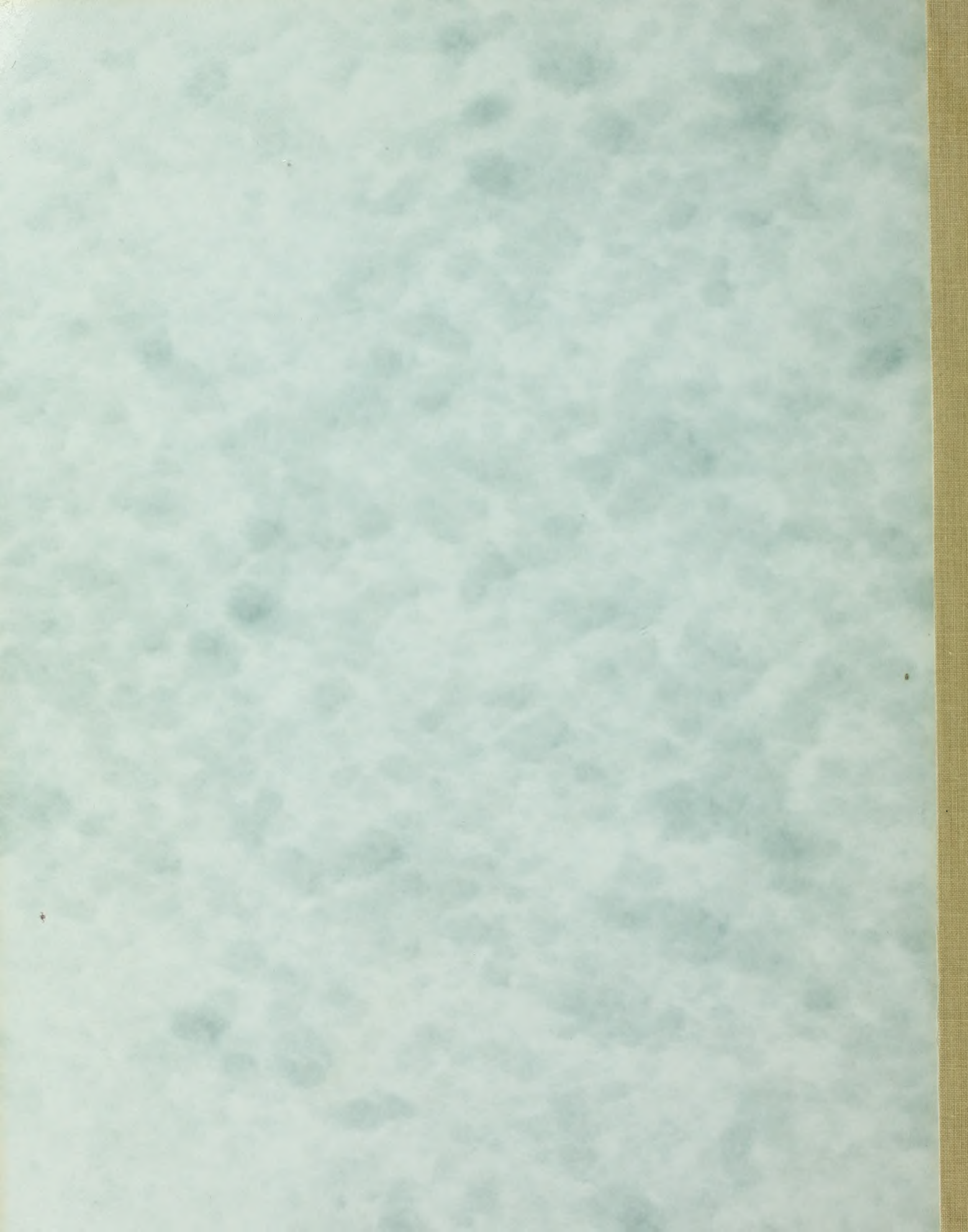


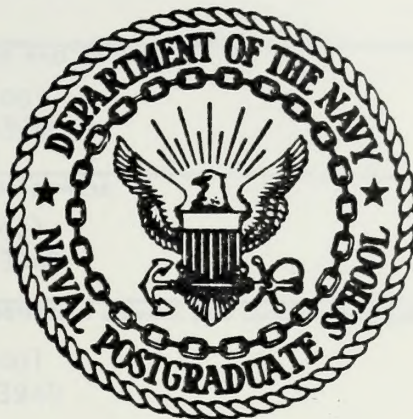
HYDROELASTIC OSCILLATIONS OF SMOOTH
AND ROUGH CYLINDER IN HARMONIC
FLOW

Farhad Rajabi



NAVAL POSTGRADUATE SCHOOL

Monterey, California



THESIS

HYDROELASTIC OSCILLATIONS OF SMOOTH AND ROUGH
CYLINDERS IN HARMONIC FLOW

by

Farhad Rajabi

December 1979

Thesis Advisor:

T. Sarpkaya

Approved for public release; distribution unlimited.

T191046

REPORT DOCUMENTATION PAGE

READ INSTRUCTIONS
BEFORE COMPLETING FORM

1. REPORT NUMBER		2. GOVT ACCESSION NO.	3. RECIPIENT'S CATALOG NUMBER
4. TITLE (and Subtitle) Hydroelastic Oscillations of Smooth and Rough Cylinders in Harmonic Flow			5. TYPE OF REPORT & PERIOD COVERED Ph. D. Thesis; December 1979
			6. PERFORMING ORG. REPORT NUMBER
7. AUTHOR(s) Farhad Rajabi, LCDR Iranian Navy			8. CONTRACT OR GRANT NUMBER(s)
9. PERFORMING ORGANIZATION NAME AND ADDRESS Naval Postgraduate School Monterey, California 93940			10. PROGRAM ELEMENT, PROJECT, TASK AREA & WORK UNIT NUMBERS
11. CONTROLLING OFFICE NAME AND ADDRESS Naval Postgraduate School Monterey, California 93940			12. REPORT DATE December 1979
			13. NUMBER OF PAGES 295
14. MONITORING AGENCY NAME & ADDRESS (if different from Controlling Office) Naval Postgraduate School Monterey, California 93940			15. SECURITY CLASS. (of this report) Unclassified
			16a. DECLASSIFICATION/DOWNGRADING SCHEDULE

16. DISTRIBUTION STATEMENT (of this Report)

Approved for public release; distribution unlimited.

17. DISTRIBUTION STATEMENT (of the abstract entered in Block 20, if different from Report)

18. SUPPLEMENTARY NOTES

19. KEY WORDS (Continue on reverse side if necessary and identify by block number)

Hydroelasticity	Harmonic Flow
Transverse Oscillations	Oscillations in Harmonic Flow
Circular Cylinder	

20. ABSTRACT (Continue on reverse side if necessary and identify by block number)

A comprehensive experimental and analytical investigation has been undertaken to determine the hydroelastic response of elastically-mounted smooth and rough cylinders in harmonically-oscillating flow.

The forces acting on the cylinder and the cylinder response have been measured together with the characteristics of the flow and analyzed through the use of the Fourier analysis, spectral analysis, Duhamel's integral, and the wake-oscillator model. In addition, the in-line force has been analyzed

through the use of Morison's equation.

The results have shown that hydroelastic oscillations occur in a narrow range of the reduced velocity and give rise to significant amplification of the exciting force.

The use of the Fourier and spectral analysis together with the governing equations of motion was shown to predict the hydroelastic response of the cylinders in the synchronous region.

The investigation shed considerable light on the interaction between the harmonic fluid motion and the hydroelastic response of cylinders and provided definitive information for the prediction of the force and response characteristics of the type of oscillations considered herein.

Approved for public release; distribution unlimited.

Hydroelastic Oscillations of Smooth and Rough
Cylinders in Harmonic Flow

by

Farhad Rajabi

LCDR, Iranian Navy

B.S., Italian Naval Academy, 1969

B.S., Naval Postgraduate School, 1978

Submitted in partial fulfillment of the
requirements for the degree of

DOCTOR OF PHILOSOPHY

from the

NAVAL POSTGRADUATE SCHOOL

December 1979

ABSTRACT

A comprehensive experimental and analytical investigation has been undertaken to determine the hydroelastic response of elastically-mounted smooth and rough cylinders in harmonically-oscillating flow.

The forces acting on the cylinder and the cylinder response have been measured together with the characteristics of the flow and analyzed through the use of the Fourier analysis, spectral analysis, Duhamel's integral, and the wake-oscillator model. In addition the in-line force has been analyzed through the use of Morison's equation.

The results have shown that hydroelastic oscillations occur in a narrow range of the reduced velocity and give rise to significant amplification of the exciting force.

The use of the Fourier and spectral analysis together with the governing equations of motion was shown to predict the hydroelastic response of the cylinders in the synchronous region.

The investigation shed considerable light on the interaction between the harmonic fluid motion and the hydroelastic response of cylinders and provided definitive information for the prediction of the force and response characteristics of the type of oscillations considered herein.

TABLE OF CONTENTS

I.	GENERAL SURVEY	23
	A. INTRODUCTION	23
	B. VORTEX SHEDDING FROM A STATIONARY BLUFF BODY	24
	C. LOCK-IN OR SYNCHRONIZATION IN STEADY FLOW	37
	D. LOCK-IN OR SYNCHRONIZATION IN OSCILLATING FLOW	46
II.	EXPERIMENTAL EQUIPMENT AND PROCEDURES	49
	A. U-SHAPED OSCILLATING FLOW TUNNEL	49
	1. Original Design	49
	2. First Design Improvement	53
	3. Second Design Improvement	60
	B. CIRCULAR CYLINDER MODELS	64
	C. FORCE MEASUREMENTS	68
	D. CYLINDER DISPLACEMENT MEASUREMENTS	71
	E. ACCELERATION, ELEVATION, OR VELOCITY MEASUREMENTS	74
	F. MEASUREMENT OF OTHER BASIC PARAMETERS	76
	G. INSTRUMENTATION AND ELECTRONIC CIRCUITRY	78
	H. PROCEDURES	80
III.	METHOD OF DATA ANALYSIS	86
	A. INTRODUCTION	86
	B. ANALYSIS OF THE PEAK AMPLITUDES	86
	C. DIGITIZATION OF THE DATA	87
	D. EVALUATION OF THE ROOT MEAN SQUARES	88
	E. SPECTRAL ANALYSIS	89

F.	IN-LINE FORCE	95
G.	DUHAMEL'S INTEGRAL	98
IV.	RESULTS	102
A.	INTRODUCTION	102
B.	REPRESENTATIVE RELATIVE DISPLACEMENTS AND LIFT COEFFICIENTS	102
C.	FOURIER ANALYSIS OF THE SYNCHRONIZATION REGION	120
D.	SPECTRAL ANALYSIS	147
E.	DUHAMEL'S INTEGRAL	152
F.	DRAW COEFFICIENTS FOR TRANSVERSELY-OSCILLATING CYLINDERS	159
V.	ANALYSIS AND DISCUSSION OF RESULTS	164
A.	INTRODUCTION	164
B.	EQUATION OF MOTION AND COMPARISON OF RESULTS	164
C.	APPLICATION OF THE WAKE-OSCILLATOR MODEL	175
VI.	CONCLUSIONS	183
APPENDIX A:	PEAK RELATIVE AMPLITUDES AS A FUNCTION OF K , U_r , f_f/f_{nw} , and f_c/f_{nw}	185
APPENDIX B:	ROOT-MEAN-SQUARE VALUES OF THE RELATIVE AMPLITUDES AS A FUNCTION OF K , U_r , f_f/f_{nw} , and f_c/f_{nw}	202
APPENDIX C:	PEAK LIFT COEFFICIENTS AS A FUNCTION OF K , U_r , f_f/f_{nw} , AND f_f/f_c	219
APPENDIX D:	ROOT-MEAN-SQUARE VALUES OF THE LIFT COEFFICIENT AS A FUNCTION OF K , U_r , f_f/f_{nw} , AND f_f/f_c	236
APPENDIX E:	SPECTRAL ANALYSIS FOR A 3 in. SMOOTH CYLINDER FOR VARIOUS VALUES OF K	253
APPENDIX F:	SPECTRAL ANALYSIS FOR A 4 in. ROUGH CYLINDER FOR VARIOUS VALUES OF K	270

REFERENCES 286

INITIAL DISTRIBUTION LIST 295

LIST OF FIGURES

1a.	Initiation of vortex shedding [10]	26
1b.	Alternate shedding of vortices and its relation to the lift force [10]	27
2.	Strouhal number versus Reynolds number	29
3.	Response characteristics of a freely oscillating cylinder, from Feng [54], (see also [2])	39
4.	Schematic drawing of the initial version of the U-shaped water tunnel	51
5.	Photograph of butterfly valve system	52
6.	Preliminary sketch of the support and housings	54
7.	Side cutaway view of a load cell and bearing housing, (dimensions in cm)	55
8.	Side view of a cylinder-support mount and housing, (dimensions in cm)	57
9.	Top view of a cylinder-support mount and housing, (dimensions in cm)	58
10.	Support housing, (dimensions in cm)	59
11.	Sketch of the air supply system	61
12.	Sketch of the air valve	63
13a.	Completed tunnel with air supply system	65
13b.	Back view of the tunnel with the side windows	66
14.	Schematic of the final version of the tunnel	67
15.	A cutaway sketch of a cylinder with accelerometer	69
16.	Scanning Electron Microscope photograph of sand-roughened surface	70
17.	Force transducer	72
18.	Free-body diagram of the test cylinder	73

19a.	Sample displacement trace of a cylinder	75
19b.	Sample force trace	75
19c.	Sample acceleration trace of the tunnel	75
19d.	Displacement trace of a "plucked" cylinder	77
20.	LVDT (Linear-variable-displacement-transducer) electronic circuit	79
21.	Force and accelerometer electronic circuit	81
22.	Differential pressure transducer and circuitry	82
23.	Flow chart of the computer program for the evaluation of the spectral density	96
24.	A sample of the in-line force trace	99
25.	A sample of the transverse force trace	100
26.	X_M/D versus K for 3 in. smooth cylinder, $\zeta = 0.052$	104
27.	X_M/D versus U_r for 3 in. smooth cylinder, $\zeta = 0.052$	105
28.	X_M/D versus f_f/f_{nw} for 3 in. smooth cylinder, $\zeta = 0.052$. .	106
29.	X_M/D versus f_c/f_{nw} for 3 in. smooth cylinder, $\zeta = 0.052$. .	107
30.	X_M/D versus K for 3 in. rough cylinder, $\zeta = 0.067$	186
31.	X_M/D versus U_r for 3 in. rough cylinder, $\zeta = 0.067$	187
32.	X_M/D versus f_f/f_{nw} for 3 in. rough cylinder, $\zeta = 0.067$. .	188
33.	X_M/D versus f_c/f_{nw} for 3 in. rough cylinder, $\zeta = 0.067$. .	189
34.	X_M/D versus K for 4 in. smooth cylinder, $\zeta = 0.046$	190
35.	X_M/D versus U_r for 4 in. smooth cylinder, $\zeta = 0.046$	191
36.	X_M/D versus f_f/f_{nw} for 4 in. smooth cylinder, $\zeta = 0.046$. .	192
37.	X_M/D versus f_c/f_{nw} for 4 in. smooth cylinder, $\zeta = 0.046$. .	193
38.	X_M/D versus K for 4 in. rough cylinder, $\zeta = 0.060$	194
39.	X_M/D versus U_r for 4 in. rough cylinder, $\zeta = 0.060$	195
40.	X_M/D versus f_f/f_{nw} for 4 in. rough cylinder, $\zeta = 0.060$. .	196

41.	X_M/D versus f_c/f_{nw} for 4 in. rough cylinder, $\zeta = 0.060$. . .	197
42.	X_M/D versus K for 5 in. smooth cylinder, $\zeta = 0.055$	198
43.	X_M/D versus U_r for 5 in. smooth cylinder, $\zeta = 0.055$	199
44.	X_M/D versus f_f/f_{nw} for 5 in. smooth cylinder, $\zeta = 0.055$. .	200
45.	X_M/D versus f_c/f_{nw} for 5 in. smooth cylinder, $\zeta = 0.055$. .	201
46.	$(X/D)_{rms}$ versus K for 3 in. smooth cylinder, $\zeta = 0.052$. . .	108
47.	$(X/D)_{rms}$ versus U_r for 3 in. smooth cylinder, $\zeta = 0.052$. .	109
48.	$(X/D)_{rms}$ versus f_f/f_{nw} for 3 in. smooth cylinder, $\zeta = 0.052$	110
49.	$(X/D)_{rms}$ versus f_c/f_{nw} for 3 in. smooth cylinder, $\zeta = 0.052$	111
50.	$(X/D)_{rms}$ versus K for 3 in. rough cylinder, $\zeta = 0.067$	203
51.	$(X/D)_{rms}$ versus U_r for 3 in. rough cylinder, $\zeta = 0.067$. . .	204
52.	$(X/D)_{rms}$ versus f_f/f_{nw} for 3 in. rough cylinder, $\zeta = 0.067$	205
53.	$(X/D)_{rms}$ versus f_c/f_{nw} for 3 in. rough cylinder, $\zeta = 0.067$	206
54.	$(X/D)_{rms}$ versus K for 4 in. smooth cylinder, $\zeta = 0.046$. . .	207
55.	$(X/D)_{rms}$ versus U_r for 4 in. smooth cylinder, $\zeta = 0.046$. .	208
56.	$(X/D)_{rms}$ versus f_f/f_{nw} for 4 in. smooth cylinder, $\zeta = 0.046$	209
57.	$(X/D)_{rms}$ versus f_c/f_{nw} for 4 in. smooth cylinder, $\zeta = 0.046$	210
58.	$(X/D)_{rms}$ versus K for 4 in. rough cylinder, $\zeta = 0.060$. . .	211
59.	$(X/D)_{rms}$ versus U_r for 4 in. rough cylinder, $\zeta = 0.060$. . .	212
60.	$(X/D)_{rms}$ versus f_f/f_{nw} for 4 in. rough cylinder, $\zeta = 0.060$	213
61.	$(X/D)_{rms}$ versus f_c/f_{nw} for 4 in. rough cylinder, $\zeta = 0.060$	214
62.	$(X/D)_{rms}$ versus K for 5 in. smooth cylinder, $\zeta = 0.055$. . .	215
63.	$(X/D)_{rms}$ versus U_r for 5 in. smooth cylinder, $\zeta = 0.055$. .	216
64.	$(X/D)_{rms}$ versus f_f/f_{nw} for 5 in. smooth cylinder, $\zeta = 0.055$	217
65.	$(X/D)_{rms}$ versus f_c/f_{nw} for 5 in. smooth cylinder, $\zeta = 0.055$	218

66.	C_{LM} versus K for 3 in. smooth cylinder, $\zeta = 0.052$	112
67.	C_{LM} versus U_r for 3 in. smooth cylinder, $\zeta = 0.052$	113
68.	C_{LM} versus f_f/f_{nw} for 3 in. smooth cylinder, $\zeta = 0.052$	114
69.	C_{LM} versus f_f/f_c for 3 in. smooth cylinder, $\zeta = 0.052$	115
70.	C_{LM} versus K for 3 in. rough cylinder, $\zeta = 0.067$	220
71.	C_{LM} versus U_r for 3 in. rough cylinder, $\zeta = 0.067$	221
72.	C_{LM} versus f_f/f_{nw} for 3 in. rough cylinder, $\zeta = 0.067$	222
73.	C_{LM} versus f_f/f_c for 3 in. rough cylinder, $\zeta = 0.067$	223
74.	C_{LM} versus K for 4 in. smooth cylinder, $\zeta = 0.046$	224
75.	C_{LM} versus U_r for 4 in. smooth cylinder, $\zeta = 0.046$	225
76.	C_{LM} versus f_f/f_{nw} for 4 in. smooth cylinder, $\zeta = 0.046$	226
77.	C_{LM} versus f_f/f_c for 4 in. smooth cylinder, $\zeta = 0.046$	227
78.	C_{LM} versus K for 4 in. rough cylinder, $\zeta = 0.060$	228
79.	C_{LM} versus U_r for 4 in. rough cylinder, $\zeta = 0.060$	229
80.	C_{LM} versus f_f/f_{nw} for 4 in. rough cylinder, $\zeta = 0.060$	230
81.	C_{LM} versus f_f/f_c for 4 in. rough cylinder, $\zeta = 0.060$	231
82.	C_{LM} versus K for 5 in. smooth cylinder, $\zeta = 0.055$	232
83.	C_{LM} versus U_r for 5 in. smooth cylinder, $\zeta = 0.055$	233
84.	C_{LM} versus f_f/f_{nw} for 5 in. smooth cylinder, $\zeta = 0.055$	234
85.	C_{LM} versus f_f/f_c for 5 in. smooth cylinder, $\zeta = 0.055$	235
86.	$(C_L)_{rms}$ versus K for 3 in. smooth cylinder, $\zeta = 0.052$	116
87.	$(C_L)_{rms}$ versus U_r for 3 in. smooth cylinder, $\zeta = 0.052$	117
88.	$(C_L)_{rms}$ versus f_f/f_{nw} for 3 in. smooth cylinder, $\zeta = 0.052$. . .	118
89.	$(C_L)_{rms}$ versus f_f/f_c for 3 in. smooth cylinder, $\zeta = 0.052$. .	119
90.	$(C_L)_{rms}$ versus K for 3 in. rough cylinder, $\zeta = 0.067$	237

91.	$(C_L)_{rms}$ versus U_r for 3 in. rough cylinder, $\zeta = 0.067$	238
92.	$(C_L)_{rms}$ versus f_f/f_{nw} for 3 in. rough cylinder, $\zeta = 0.067$. .	239
93.	$(C_L)_{rms}$ versus f_f/f_c for 3 in. rough cylinder, $\zeta = 0.067$. .	240
94.	$(C_L)_{rms}$ versus K for 4 in. smooth cylinder, $\zeta = 0.046$	241
95.	$(C_L)_{rms}$ versus U_r for 4 in. smooth cylinder, $\zeta = 0.046$. . .	242
96.	$(C_L)_{rms}$ versus f_f/f_{nw} for 4 in. smooth cylinder, $\zeta = 0.046$	243
97.	$(C_L)_{rms}$ versus f_f/f_c for 4 in. smooth cylinder, $\zeta = 0.046$. .	244
98.	$(C_L)_{rms}$ versus K for 4 in. rough cylinder, $\zeta = 0.060$	245
99.	$(C_L)_{rms}$ versus U_r for 4 in. rough cylinder, $\zeta = 0.060$	246
100.	$(C_L)_{rms}$ versus f_f/f_{nw} for 4 in. rough cylinder, $\zeta = 0.060$. .	247
101.	$(C_L)_{rms}$ versus f_f/f_c for 4 in. rough cylinder, $\zeta = 0.060$. .	248
102.	$(C_L)_{rms}$ versus K for 5 in. smooth cylinder, $\zeta = 0.055$	249
103.	$(C_L)_{rms}$ versus U_r for 5 in. smooth cylinder, $\zeta = 0.055$. . .	250
104.	$(C_L)_{rms}$ versus f_f/f_{nw} for 5 in. smooth cylinder, $\zeta = 0.055$	251
105.	$(C_L)_{rms}$ versus f_f/f_c for 5 in. smooth cylinder, $\zeta = 0.055$. .	252
106.	Normalized displacement and Fourier coefficients for 3 in. smooth cylinder, $\zeta = 0.052$	122
107.	Normalized displacement and Fourier coefficients for 3 in. rough cylinder, $\zeta = 0.067$	123
108.	Normalized displacement and Fourier coefficients for 4 in. smooth cylinder, $\zeta = 0.046$	124
109.	Normalized displacement and Fourier coefficients for 4 in. rough cylinder, $\zeta = 0.030$	125
110.	Normalized displacement and Fourier coefficients for 4 in. smooth cylinder, $\zeta = 0.060$	126
111.	Normalized displacement and Fourier coefficients for 5 in. smooth cylinder, $\zeta = 0.067$	127
112.	Normalized displacement and Fourier coefficients for 5 in. smooth cylinder, $\zeta = 0.055$	128

113.	Normalized displacement and Fourier coefficients for 5 in. smooth cylinder, $\zeta = 0.054$, (with lead blocks)	129
114.	Normalized lift force and Fourier coefficients for 3 in. smooth cylinder, $\zeta = 0.052$	130
115.	Normalized lift force and Fourier coefficients for 3 in. rough cylinder, $\zeta = 0.067$	131
116.	Normalized lift force and Fourier coefficients for 4 in. smooth cylinder, $\zeta = 0.046$	132
117.	Normalized lift force and Fourier coefficients for 4 in. rough cylinder, $\zeta = 0.060$	133
118.	Normalized lift force and Fourier coefficients for 4 in. rough cylinder, $\zeta = 0.030$	134
119.	Normalized lift force and Fourier coefficients for 5 in. smooth cylinder, $\zeta = 0.061$, (with lead blocks)	135
120.	Normalized lift force and Fourier coefficients for 5 in. smooth cylinder, $\zeta = 0.055$, (with lead blocks)	136
121.	Normalized lift force and Fourier coefficients for 5 in. smooth cylinder, $\zeta = 0.054$, (with lead blocks)	137
122a.	Predominant harmonic representation of the displacement trace for a 4 in. rough cylinder, $\zeta = 0.030$	139
122b.	Two-term Fourier series representation of the displacement trace for a 4 in. rough cylinder, $\zeta = 0.030$	140
122c.	Three-term Fourier series representation of the displacement trace for a 4 in. rough cylinder, $\zeta = 0.030$	141
123a.	Predominant harmonic representation of the force trace for a 4 in. rough cylinder, $\zeta = 0.030$	142
123b.	Two-term Fourier series representation of the force trace for a 4 in. rough cylinder, $\zeta = 0.030$	143
123c.	Three-term Fourier series representation of the force trace for a 4 in. rough cylinder, $\zeta = 0.030$	144
123d.	Four-term Fourier series representation of the force trace for a 4 in. rough cylinder, $\zeta = 0.030$	145
123e.	Five-term Fourier series representation of the force trace for a 4 in. rough cylinder, $\zeta = 0.030$	146

124.	Spectral analysis for a 3 in. smooth cylinder at resonance, $\zeta = 0.052$, $K = 51$	148
125.	Spectral analysis for a 4 in rough cylinder at resonance, $\zeta = 0.030$, $K = 49$	149
126.	Spectral analysis for a 3 in. smooth cylinder, $\zeta = 0.052$, $K = 80$	150
127.	Spectral analysis for a 4 in. rough cylinder, $\zeta = 0.030$, $K = 80$	151
128.	Spectral analysis for a 3 in. smooth cylinder, $\zeta = 0.052$, $K = 36$	254
129.	Spectral analysis for a 3 in. smooth cylinder, $\zeta = 0.052$, $K = 39$	255
130.	Spectral analysis for a 3 in. smooth cylinder, $\zeta = 0.052$, $K = 43$	256
131.	Spectral analysis for a 3 in. smooth cylinder, $\zeta = 0.052$, $K = 46$	257
132.	Spectral analysis for a 3 in. smooth cylinder, $\zeta = 0.052$, $K = 48$	258
133.	Spectral analysis for a 3 in. smooth cylinder, $\zeta = 0.052$, $K = 56$	259
134.	Spectral analysis for a 3 in. smooth cylinder, $\zeta = 0.052$, $K = 57$	260
135.	Spectral analysis for a 3 in. smooth cylinder, $\zeta = 0.052$, $K = 60$	261
136.	Spectral analysis for a 3 in. smooth cylinder, $\zeta = 0.052$, $K = 64$	262
137.	Spectral analysis for a 3 in. smooth cylinder, $\zeta = 0.052$, $K = 69$	263
138.	Spectral analysis for a 3 in. smooth cylinder, $\zeta = 0.052$, $K = 88$	264
139.	Spectral analysis for a 3 in. smooth cylinder, $\zeta = 0.052$, $K = 99$	265
140.	Spectral analysis for a 3 in. smooth cylinder, $\zeta = 0.052$, $K = 112$	266

141.	Spectral analysis for a 3 in. smooth cylinder, $\zeta = 0.052$, K = 123	267
142.	Spectral analysis for a 3 in. smooth cylinder, $\zeta = 0.052$, K = 134	268
143.	Spectral analysis for a 3 in. smooth cylinder, $\zeta = 0.052$, K = 141	269
144.	Spectral analysis for a 4 in. rough cylinder, $\zeta = 0.030$, K = 29	271
145.	Spectral analysis for a 4 in. rough cylinder, $\zeta = 0.030$, K = 32	272
146.	Spectral analysis for a 4 in. rough cylinder, $\zeta = 0.030$, K = 35	273
147.	Spectral analysis for a 4 in. rough cylinder, $\zeta = 0.030$, K = 36	274
148.	Spectral analysis for a 4 in. rough cylinder, $\zeta = 0.030$, K = 38	275
149.	Spectral analysis for a 4 in. rough cylinder, $\zeta = 0.030$, K = 40	276
150.	Spectral analysis for a 4 in. rough cylinder, $\zeta = 0.030$, K = 43	277
151.	Spectral analysis for a 4 in. rough cylinder, $\zeta = 0.030$, K = 45	278
152.	Spectral analysis for a 4 in. rough cylinder, $\zeta = 0.030$, K = 46	279
153.	Spectral analysis for a 4 in. rough cylinder, $\zeta = 0.030$, K = 51	280
154.	Spectral analysis for a 4 in. rough cylinder, $\zeta = 0.030$, K = 55	281
155.	Spectral analysis for a 4 in. rough cylinder, $\zeta = 0.030$, K = 57	282
156.	Spectral analysis for a 4 in. rough cylinder, $\zeta = 0.030$, K = 64	283
157.	Spectral analysis for a 4 in. rough cylinder, $\zeta = 0.030$, K = 70	284

158.	Spectral analysis for a 4 in. rough cylinder, $\zeta = 0.030$, K = 84	285
159.	Comparison of measured and calculated displacement by Duhamel's integral for a 3 in. smooth cylinder, $\zeta = 0.052$	154
160.	Comparison of measured and calculated displacement by Duhamel's integral for a 4 in. smooth cylinder, $\zeta = 0.046$	155
161.	Comparison of measured and calculated displacement by Duhamel's integral for a 4 in. rough cylinder, $\zeta = 0.030$	156
162.	Comparison of measured and calculated displacement by Duhamel's integral for a 4 in. rough cylinder, $\zeta = 0.060$	157
163.	Comparison of measured and calculated displacement by Duhamel's integral for a 5 in. smooth cylinder, $\zeta = 0.054$	158
164.	C_d versus K for a 3 in. smooth cylinder, $\zeta = 0.052$	161
165.	C_d versus K for a 3 in. rough cylinder, $\zeta = 0.067$	162
166.	C_d versus K for a 5 in. smooth cylinder, $\zeta = 0.055$	163
167.	Measured and predicted response for a 3 in. smooth cylinder, $\zeta = 0.052$	168
168.	Measured and predicted response for a 4 in. rough cylinder, $\zeta = 0.030$	169
169.	\bar{X}/D versus response parameter R_p	171
170.	Comparison of cylinder oscillation in harmonic and steady flow	174
171.	Response characteristics in steady flow as predicted by Hartlen and Currie model [87]	179
172a.	\bar{C}_l and \bar{X}_r versus U_r in harmonic flow as predicted by Hartlen and Currie model	180
172b.	f_c/f_n versus U_r in harmonic flow as predicted by Hartlen and Currie model	181

LIST OF SYMBOLS

A	Cylinder displacement in steady flow
A_m	Maximum amplitude of flow oscillation
a_0	Mass parameter
a_n	Fourier coefficient
B	Interaction parameter
b_n	Fourier coefficient
C_d	Drag coefficient
C_L	Lift coefficient
C_{LM}	Peak lift coefficient
\bar{C}_{Ln}	Amplitude of the lift coefficient
C_L^0	Peak lift coefficient for stationary cylinder
C_{Lpi}	Amplitude of predominant harmonics of the lift coefficient
$(C_L)_{rms}$	Root-mean-square value of the lift coefficient
C_m	Inertia coefficient
C_{pb}	Base pressure coefficient
C_{xy}	Co-spectrum
D	Cylinder diameter
F	Force
F_d	Drag force
F_i	Inertia force
F_L	Lift force
F_{LM}	Maximum lift force
F_m	Measured force
$F_x(f)$	Forward Fourier transform of x
f	Frequency

f_c	Cylinder oscillation frequency
f_f	Lift force frequency
f_n	Natural frequency
f_{na}	Natural frequency in air
f_{nw}	Natural frequency in water
f_{Ny}	Nyquist frequency
f_v	Vortex shedding frequency
f_w	Flow oscillation frequency, $1/T$
f_o	Frequency of vortex shedding for a stationary cylinder
G_x	One-sided spectral density
\hat{G}_x	Estimate of the one-sided spectral density
G_{xy}	One-sided cross spectrum
\hat{G}_{xy}	Estimate of the one-sided cross spectrum
g	Gravitational acceleration
H	Water height above the pressure tap in the tunnel
h'	Wake width
h_v	Transverse vortex spacing
i	$\sqrt{-1}$
K	Keulegan-Carpenter number, $K = U_m T/D$
K_r	$M\zeta/\rho D^2$
K_s	System spring constant
K_w	$(1 - c_{pb})^{1/2}$
k	Number of sample functions
k_c	Height of the sand roughness
L	Cylinder length
ℓ_f	Length of the vortex formation region
ℓ_w	Wake width at a distance of the wake establishment region

M	Mass
M_a	Added mass
N	An integer
P	Pressure
Q_{xy}	Quad-spectrum
Re	Reynolds number, $Re = UD/\nu$
R_p	Response parameter, $R_p = M\zeta/[\rho LD^2(C_L^0)_{rms}]$
R_x	Autocorrelation function
R_{xy}	Cross-correlation function
rms	Root-mean-square
S	Strouhal number, $S = f_v D/V$
S_0	Strouhal number for a stationary cylinder, $S_0 = f_0 D/V$
S_x	Power spectrum
T	Period of flow oscillations
T_c	Period of the cylinder oscillations
T_f	Period of the lift force oscillations
T_v	Vortex shedding period, $1/f_v$
t	time
t_v	Variable time
U	Ambient flow velocity
U_m	Maximum velocity in a cycle of flow oscillation
U_r	Reduced velocity, $U_r = U_m/f_{nw} D$
u_s	Velocity of the vortex street
V	Velocity of the steady ambient flow
V_r	Reduced velocity in steady flow
x	A time-dependent variable

$X(n)$	Finite Fourier transform of x
$X(t)$	Transverse displacement of the cylinder
X_M	Peak cylinder displacement
\dot{X}	Cylinder velocity
\ddot{X}	Cylinder acceleration
X_0	Initial cylinder displacement
\dot{X}_0	Initial cylinder velocity
\bar{X}_n	Amplitude of the cylinder displacement
y	A time-dependent variable
$Y(n)$	Finite Fourier transform of y
α	van der Pol parameter
α_{xy}	Phase between sample functions
Γ	Vortex strength
γ	van der Pol parameter
Δ_r	Another response parameter
Δt	Digitization interval
ϕ	Phase angle
λ	Number of degrees of freedom
ν	Kinematic viscosity of fluid
Ω	Normalized frequency, f/f_n
Ω_c	Normalized cylinder oscillation frequency, f_c/f_n
Ω_o	Normalized vortex shedding frequency, f_o/f_n
ω	Circular frequency, $2\pi f$
ω_c	Circular cylinder-oscillation frequency, $2\pi f_c$
ω_f	Circular lift force frequency, $2\pi f_f$
ω_n	Circular natural frequency, $2\pi f_n$

ω_{na}	Circular natural frequency in air, $2\pi f_{na}$
ω_{nw}	Circular natural frequency in water $2\pi f_{nw}$
ω_v	Circular vortex-shedding frequency, $2\pi f_v$
ω_0	Circular vortex shedding frequency for a stationay cylinder
ρ	Density of fluid
ρ_r	Relative density, ρ_s/ρ
σ_x^2	Variance of x
θ	Angle, $2\pi t/T$
θ_s	Separation angle
τ	Dimensionless time, $\tau = \omega_n t$
ζ	Damping ratio
ζ_a	Damping ratio in air
ζ_w	Damping ratio in water

ACKNOWLEDGEMENTS

The author wishes to express his sincere appreciation to Professor T. Sarpkaya for his inspiration and for his invaluable help, advice, and guidance throughout the course of the investigation. The author will always remember his warm friendship and honest dedication to research.

Special thanks are due Mr. Jack McKay for his outstanding help with the construction of the test facilities.

Lastly, the author wishes to thank his family for their patience and understanding during his tenure at the Naval Postgraduate School.

I. GENERAL SURVEY

A. INTRODUCTION

Experience has shown that elastic structures near linear-resonance conditions can develop flow-induced oscillations by extracting energy from the flow about them. The oscillations of the structure modify the flow and give rise to nonlinear interaction. This is in addition to any non-linearity which can arise from the restoring force (variable support stiffness) and/or from response-dependent structural damping. The understanding of these nonlinear interactions is of paramount importance.

Four general classes cover a wide range of the fluid-structure interaction phenomenon: vortex-induced oscillation, flutter, galloping and buffeting. This survey will deal with only the first of these phenomena.

The problems associated with vortex-induced oscillations and their important consequences have proved to be exceedingly difficult both theoretically and experimentally. The difficulty is partly due to our incomplete knowledge of the flow field about a stationary body but it is also due to fundamental problems associated with the coupling of the oscillations and the flow field. It would indeed be gratifying to note that our understanding of the separated flow about a bluff body, particularly in the region enclosing the body and its near wake, is complete through laboratory and numerical experiments. This is, regrettably, not yet the case, but there have been nevertheless significant advances since the time attention has shifted from idealized vortex streets to the details of separation, three-dimensional flow, and the role played by the

afterbody on the formation, growth, and motion of vortices. Many of the key developments of the past decade have been incorporated into the experimental investigation of flow-induced oscillations and into the evolution of conceptually plausible idealized models.

In the material to follow emphasis is placed on the understanding of the transverse oscillations of cylinders. No attempt has been made to be encyclopedic in coverage as there are recent texts and survey articles, for example, Blevins [1], Parkinson [2], King [3], and McCroskey [4], which cover the field in some detail.

B. VORTEX SHEDDING FROM A STATIONARY BLUFF BODY

There are substantial gaps in the understanding of the fundamental mechanisms at work in the forcing of the body by the forces acting on its afterbody and in the prediction of the lock-in range in which resonant oscillations occur. To a degree, the difficulties in obtaining a solution or in devising a model stem from an inadequate knowledge of the precise mechanism of flow separation and its consequences in steady flow past a stationary body (see, e.g., Morkovin [5], Marris [6], Mair and Maull [7], and Berger and Wille [8] for comprehensive reviews and references).

Observations as well as numerical experiments have shown that the wake of a bluff body is comprised of an alternating vortex street. This phenomenon is intrinsic to the flow itself and is a consequence of the interaction between the shear layers, base pressure, diffusion and dissipation of vorticity, and far wake, i.e., a consequence of the particular vorticity distribution throughout the field.

As the vortices grow symmetrically, say, in an impulsively-started flow about a cylinder, the shear layer joining the separation point to one of

the vortices begins to develop instabilities (presumably Tollmien-Schlichting instabilities [9]) and is drawn across the wake in response to the base pressure reduced by the action of the vortex growing across the wake (see Fig. 1) [10]. This nearly corresponds to a time when the sheet drawn in has least circulation or is most permeable. The stretching, diffusion, and dissipation of vorticity break up the deforming turbulent sheet and thereby the further supply of circulation to the vortex whose rate of growth has already been reduced to its minimum. This corresponds to the shedding of the first vortex. The vortex across the wake still continues to grow (but at a decreasing rate) and entrains part of the oppositely-signed vorticity left in the wake by the cut sheet and the irrotational fluid drawn from outside through the opening created by the shedding of the first vortex. The shedding process for the second vortex does not commence until the circulation in its feeding sheet decreases to its minimum, making the sheet most susceptible to rapid diffusion. Simultaneously, the sheet deforms, diffuses, and is drawn across the wake by the action of the base pressure and the vortex growing on the other side of the wake. Then the shedding cycle repeats itself.¹ The above mechanism, exhibited by numerical experiments [10] is quite similar, but not identical, to that suggested by Gerrard [11].

The separation point at the side of the cut sheet just passes through its minimum angle. The sheet at the opposite side of the wake bears nearly the maximum circulation, relative to any other time, and its separation-point

¹For a circular cylinder there is a 60 degree phase difference between the lift maximum and the sheet cutting time, i.e., a vortex is shed when the lift force decreases to 50 percent of the absolute value of its maximum.

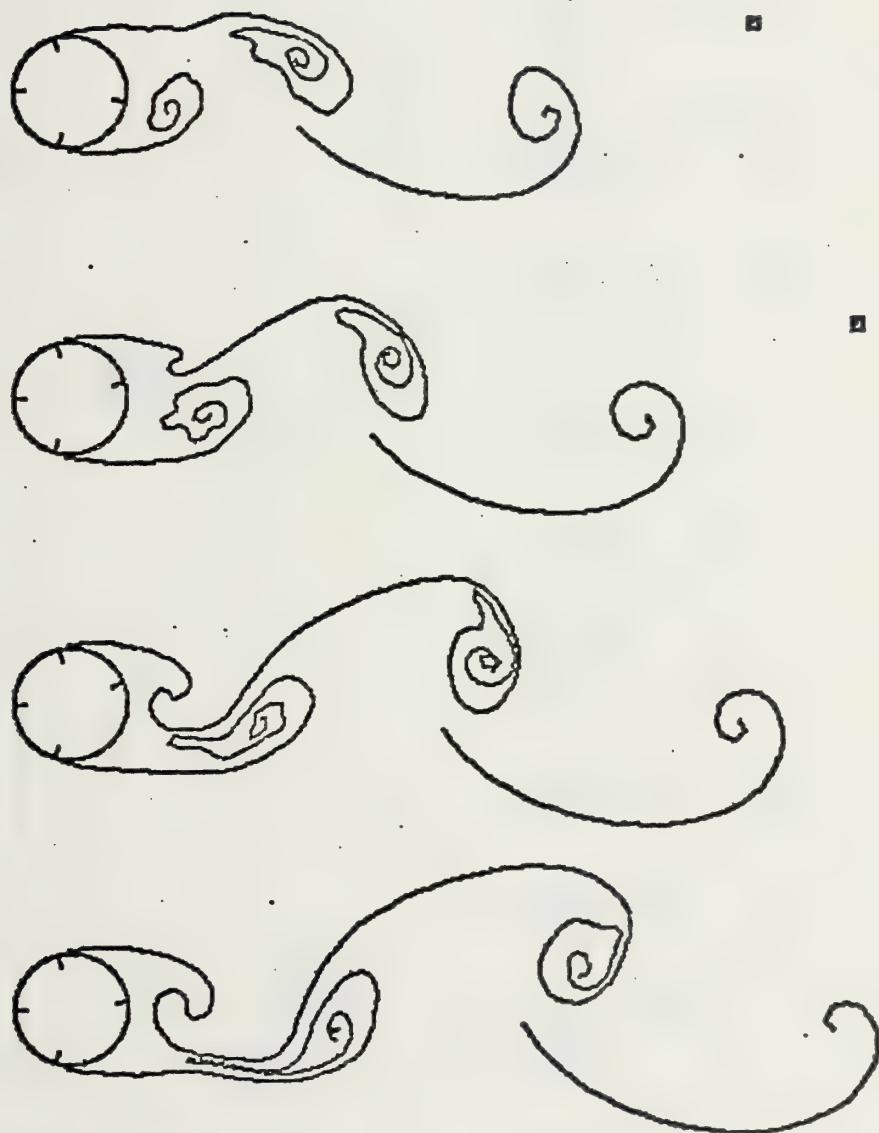


Fig. 1a. Initiation of vortex shedding [10]

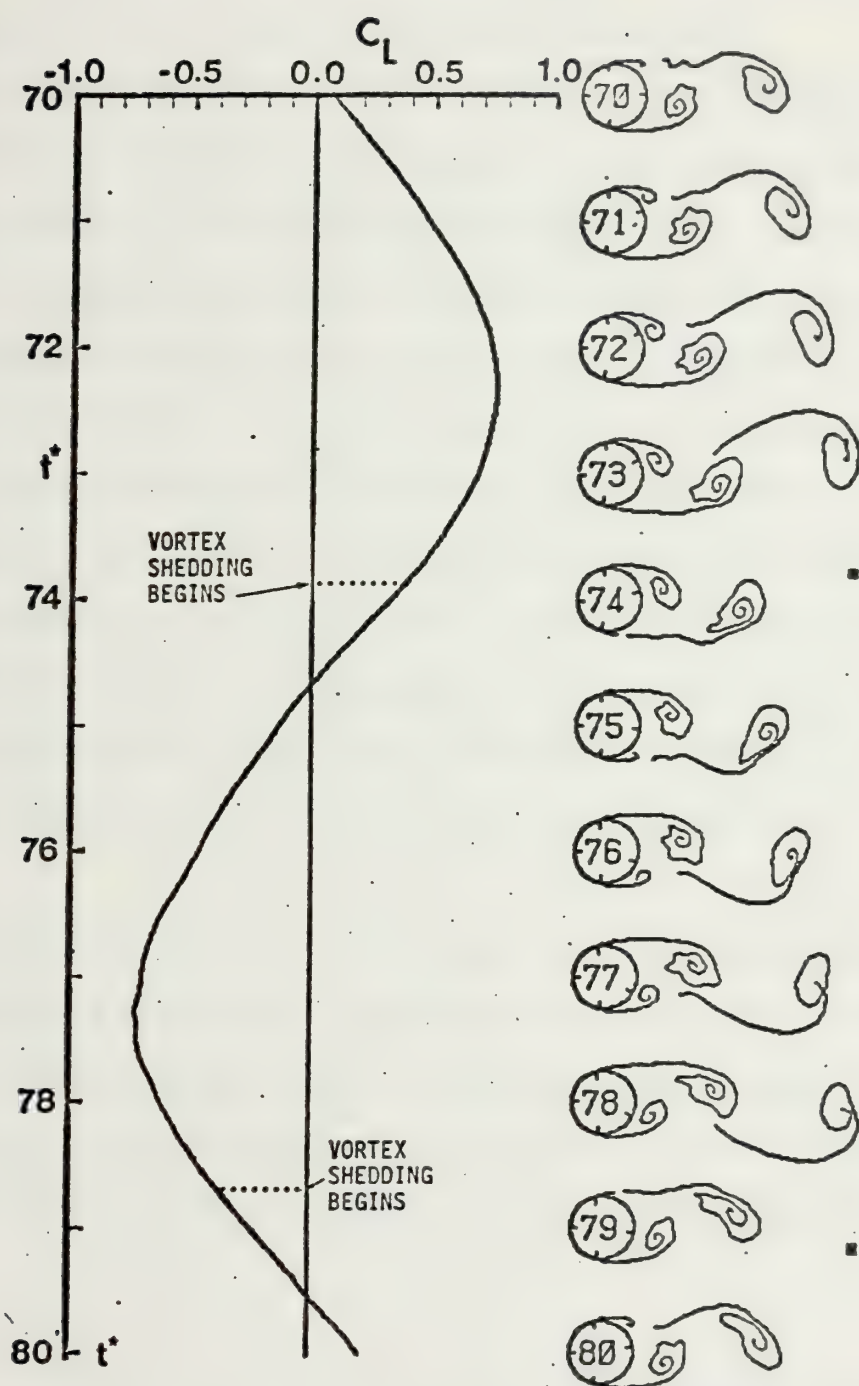


Fig. 1b Alternate shedding of vortices and its relation to the lift force [10]

angle just passes through a maximum. The motion of the stagnation point is such that it is 180 degrees out of phase with the separation points, i.e., the separation point is below the x-axis (flow from left to right) when a vortex is shed from the bottom of the cylinder.

The shedding of the vortices gives rise to an oscillating side thrust, upon a cylinder of suitable afterbody, in a direction away from the last detached vortex. The relationship between the vortex-shedding frequency, cylinder diameter, and the velocity of the ambient flow has been discovered by Strouhal [12] almost exactly 100 years ago in connection with his work on a special method of creation of sound. His data showed that the product fD/V is nearly constant for a wide range of values of D and V . This postulated constant is often called the Strouhal number and Strouhal's own data suggested a value of about 0.185. The characterization of the vortex shedding process by a simple frequency is a practical simplification. As first noted by Lord Rayleigh [13], the Strouhal number is a function of the Reynolds number for a given body² and f should be written as $f = S_0(\text{Re})V/D$, (see Fig. 2).

At relatively low subcritical Reynolds numbers, the energy containing frequencies are confined to a narrow band, and the Strouhal number is about 0.20 for smooth cylinders [8]. For Reynolds numbers larger than about 20,000, only an average Strouhal number may be defined. In the range $0.5 \times 10^6 < \text{Re} < 2.5 \times 10^6$ no periodicity is observed in either the unsteady

² $S_0 = 0.21(1 - 20/\text{Re})$ for $40 < \text{Re} < 1,000$ (Goldstein [14]);
 $S_0 = 0.212(1 - 12.7/\text{Re})$ in the range $400 < \text{Re} < 100,000$ according to a correlation obtained by Roshko [15]. In the range $400 < \text{Re} < 1,200$ the results of Roshko's correlation are slightly below the best-fit line to the existing data [8].

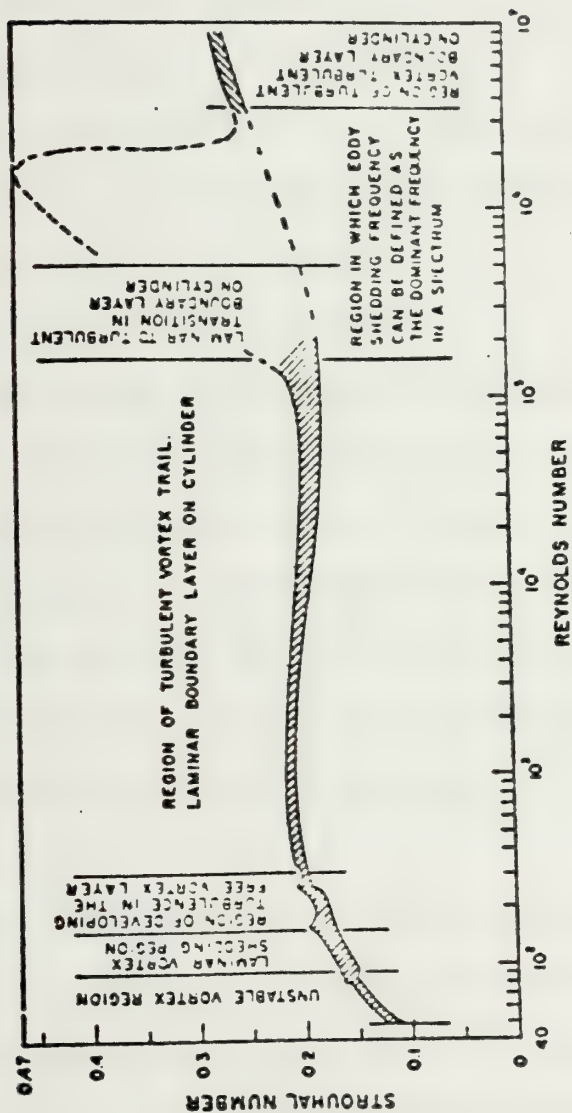


Fig. 2 Strouhal number versus Reynolds number

lift or the unsteady pressures. In the range $2.5 \times 10^6 < Re < 6.5 \times 10^6$ a small peak is observed at $S_0 = 0.2$ in the unsteady lift and in unsteady pressures only at the front part of the cylinder. No peak is found behind the separation point. For $Re > 6.5 \times 10^6$, a definite peak is found in both the unsteady lift and the unsteady pressures at $S_0 = 0.3$. The said periodicity occurs both at the front and rear part of the cylinder [16]. The foregoing categorization is somewhat arbitrary. Jones et al., [17] classified the unsteady lift force in three regimes: wide-band random for $1.1 \times 10^6 < Re < 3.5 \times 10^6$; narrow-band random for $3.5 \times 10^6 < Re < 6 \times 10^6$; and quasi-periodic for $6 \times 10^6 < Re < 18.7 \times 10^6$.

The spectral content of the exciting forces is particularly important for bodies which may undergo in-line and/or transverse oscillations since the vortex shedding frequency locks on to the frequency of the transverse oscillations of the cylinder when there is a transverse force and when the vortex shedding frequency is in the neighborhood of the natural frequency of the cylinder. When the flow about a freely oscillating cylinder is in the critical regime, the sharp rise in the Strouhal number does not occur and remains at a value nearly equal to that found at subcritical Reynolds numbers [18].

Various attempts have been made to devise a universal Strouhal number which would remain constant for differently shaped two-dimensional and axisymmetric bodies (see Table-I). In Table-I h' represents the wake width as determined from Roshko's notched hodograph theory [19]; ℓ_v , the longitudinal spacing of the vortices as determined by Kronauer's minimum drag criteria as reported by Bearman [20]; ℓ_w , the wake width at a distance of the wake establishment region; and $K_w = (1 - C_{pb})^{\frac{1}{2}}$ where C_{pb} is the base pressure coefficient.

Table I Universal Strouhal numbers

S_0	value	Body shape	Source
$f_0 h' / VK_W$	0.163	two-dimensional	Roshko [19]
$f_0 \ell_V / V$	0.181	two-dimensional	Bearman [20]
$f_0 \ell_W / VK_W$	0.190	axisymmetric	Calvert [21]
$f_0 \ell_W / VK_W$	0.163	two-dimensional	Simmons [22]

The foregoing definitions suffer from the obvious drawback that they require the solution of the wake formation problem first, or the measurement of one or more flow characteristics.

Theoretical or semi-empirical predictions of the wake characteristics have been attempted by various researchers. Birkhoff [23] demonstrated that the longitudinal spacing ℓ_V is trivially invariant since the longitudinal velocity of vortices is uniformly bounded. He has shown further that in an inviscid fluid the lateral spacing also remains constant at a value equal to the initial spacing of the shear layers. These led Birkhoff to the conclusion that h_V / ℓ_V is determined by its initial value and not by von Karman's stability criteria of $h_V / \ell_V = 0.281$. The use of a wake oscillator model ("the wake swings from side to side, somewhat like the tail of a swimming fish" [23]) and some experimentally-determined values led Birkhoff to $S_0 = 0.2$. One must keep in mind that vorticity in real vortices is not concentrated in points, the vortices are non-circular and distort and rotate as they move downstream [24], vorticity diffuses and is swept across the wake [25], and dissipates by turbulence [8]. Vortices are subjected to strain fields imposed by nearby vortices. The resulting patterns are ever changing vortex shapes encompassing elliptic and

pearlike geometries. The complexity of the interaction between strained distorting vortices is further exacerbated by the addition of turbulence to the wake, as this is likely to produce a more diffusive vorticity distribution and thus an additional shear field [24]. Thus, the near constancy of wake characteristics in the range of Reynolds numbers where a vortex street might be observed is primarily due to the slow variation of ℓ_v , h_v , and S_0 with respect to the strength and deformation of vortices. Nevertheless, theoretical idealizations of the wake give some clues about the asymptotic behavior of the wake. In particular, one obtains from $f_0 \ell_v = V - u_s$, where $V - u_s$ is the velocity relative to the body, and from the use of von Karman's stability criteria that

$$S_0 = \frac{1}{\ell_v/D} - \frac{\Gamma/VD}{2\sqrt{2}(\ell_v/D)^2} \quad (1)$$

where Γ represents the strength of a vortex. Assuming that ℓ_v/D remains nearly constant ($\ell_v/D \simeq 5$), one concludes that the smaller the strength of the vortices, the larger is the Strouhal number (smaller drag and narrower wake) and vice versa. The vortices which are subjected to smaller dissipation linger a little while longer in the near wake relative to those which are dissipated more, i.e., strong vortices get stronger. However, the dependence of S_0 on Γ/VD is rather weak. This explains in part the reason for the success of the discrete vortex models in predicting the Strouhal number fairly accurately [26,27] in spite of the fact that the calculated vortex strengths are about 35 percent larger than those estimated experimentally. However weak, the dependence of S_0 on Γ/VD becomes a primary factor in the locking-on of the vortex shedding to the natural frequency of the body. The vortices which are stronger continue

to be fed by their shear layers a longer time period, thus further reducing the Strouhal number. In this process the mobility of the separation points is important but not necessary.

Sacksteder [28] pursued a theoretical approach to determine the Strouhal number at large Reynolds numbers by perturbing the d'Alembert flow and obtained $S_0 = 0.2028$. His analysis does not consider the wake formation and thus it is not expected that flows around objects that induce large wakes could be treated with a simple perturbation of the unseparated flow.

The constancy of the Strouhal number over a broad range of Reynolds numbers does not imply that the base pressure remains constant and that a simple two-dimensional vortex emanates from a separation line. In reality, there is not only a phase shift between various sections of the vortex, separated by a correlation length,³ but also variations in both the intensity and the frequency of vortex segments.

The variation of the base pressure with Reynolds number, in the range where the Strouhal number remains practically constant, may be related to the variation of the mean vorticity flux or to the variation of the correlation length with the Reynolds number, turbulence, length-to-diameter ratio, and surface roughness [29-33]. Table-2, as compiled by King [3], gives an approximate idea about the typical values of the correlation length. The net effect of the spanwise variations of the vortex tube is that the transverse force (lift) coefficient obtained from a pressure integration is not necessarily identical with that obtained from the direct measurements of the lift force. Partial spanwise correlation leads to

³The equivalent length over which the velocity fluctuations in the wake may be described as perfectly correlated.

Table 2 Correlation lengths

<u>Reynolds No. range</u>	<u>Correlation length</u>	<u>Source</u>
$40 < Re < 150$	$15D - 20D$	[34]
$150 < Re < 10^5$	$2D - 3D$	[34]
$10^4 < Re < 4.5 \times 10^4$	$3D - 6D$	[32]
$Re > 10^5$	$0.05D$	[34]
$Re = 2 \times 10^5$	$1.56D$	[29]

variations in both the frequency and the amplitude of the lift force, the variation of the latter being more pronounced than that of the former.

The lack of correlation exists not only spanwise but also chordwise [35-38] and the chordwise correlation is related to the spanwise correlation. Comparison between various results suggests that with increasing Reynolds number over the range 10^4 to 10^5 , the chordwise correlation for square and circular cross-section cylinders is maintained or improved. This leads to an increase in fluctuating lift coefficient. The reasons for these variations are not quite clear. The end effects [29, 39-41], wall boundary layers, freestream turbulence [42-44], and non-uniformity of the flow are mentioned often as possible reasons. The complexity of the three-dimensional nature of the flow about a cylinder is clearly demonstrated with measurements by Tournier and Py [45].

It would not be correct to assume that the mobility of the separation points is primarily responsible for the imperfect coherence. Even bodies such as 90-degree wedges, square cylinders, with fixed separation lines, do not exhibit perfect correlation. However, the variation of the base-pressure coefficient for bodies with mobile separation lines is greater

than that for bodies with fixed separation lines [46]. In fact, for flow over symmetrical wedges the base pressure appears to be insensitive to the nose angle [46].

As noted earlier, the strength of the vortices plays an important role, particularly in the near wake. Laboratory and numerical experiments have shown that [7, 19, 47-50] the net circulation of a rolled-up vortex of the street is 40 to 60 percent smaller than that generated in the boundary layer during a shedding cycle. Prandtl determined that the initial vorticity decreases to about half where the first vortex centers appear. Vorticity is ultimately dissipated by viscosity to which it owes its generation. Nevertheless, one may think of loss of circulation through cancellation of oppositely-signed vorticity. Primarily, there are three mechanisms whereby oppositely-signed vorticity are brought close together: vorticity generated on the forebody is carried by the shear layers near that generated on the afterbody; vorticity of the deformed and cut sheet is carried across the near wake by the entrainment of the irrotational fluid; and, finally, vorticity is swept across the entire wake [25]. The percentages quoted in the literature [8] for the total loss of vorticity often imply that the vortices, once having acquired a certain circulation, retain that circulation throughout the rest of their motion. The fact that circulation decreases continuously with time or distance is demonstrated clearly by the experiments of Schmidt and Tilmann [50] and Bloor and Gerrard [48]. The amount of vorticity generated in the boundary layers and the amount dissipated are of prime importance not only for the flow about stationary bluff bodies but also for those undergoing resonant oscillations. In fact, the entire bluff body problem may be reduced to the determination of the vorticity distribution throughout the flow field.

This is not yet possible for Re larger than about 100. The determination of the vortex strengths is difficult and sensitive to the theoretical and experimental means employed.

It is evident from the foregoing and from a more detailed perusal of the references cited that the description of the near wake of a bluff body is in a primitive state. Much of what is known about the consequences of separation has come from laboratory experiments. It has not yet been possible to develop a numerical model with which experiments may be conducted to explain the observed or inferred relationships between various parameters and to guide and complement the laboratory experiments. The principal difficulties are as follows: (i) Separation points. They represent a mobile boundary between two regions of vastly different scales. This in turn leads to complex physical nonuniformities in relatively narrow regions which cannot be handled within the framework of the boundary-layer theory [51]. Finite difference and Marker and Cell (MAC) techniques require in such regions very small computational times. The discretization of the continuous process of vorticity generation by line vortices in the vicinity of a mobile or fixed singular point (discrete vortex model) strongly affects the existing non-uniformities and promotes earlier separation. Attempts to preserve the prevailing flow conditions, say by limiting the influence of the nascent vortices, while satisfying a relatively simple separation criterion lead to hydrodynamical inconsistencies and non-disposable parameters. (ii) Reynolds number. Finite difference schemes for bluff-body flows are limited to relatively small Reynolds numbers whether the scale of flow is assumed to be governed by a constant viscosity or by a constant eddy viscosity. The large recirculation region of the flow is often comprised of turbulent vortices even when the boundary

layer is laminar. The transition to turbulence moves upstream in the shear layers as the Reynolds number is increased from about 10^3 to 5×10^4 . At $Re = 5 \times 10^4$, it reaches the shoulder of the cylinder [52].

It does not move appreciably further upstream before the critical Reynolds number is reached. Thus, the distribution, turbulent diffusion, and decay of vorticity and the interaction between the wake and the boundary layers cannot be subjected to numerical simulation without recourse to some heuristic turbulence models and inspired foresight.

The representation of the wake by clouds of point vortices or discretized spiralling sheets (see, e.g., [10, 26, 49, 53]) is not immune to scaling problems. In fact, not a particular Reynolds number but only a particular flow regime may be specified, depending on the separation criteria used. (iii) Three-dimensionality. As noted earlier, even a uniform flow about a stationary cylinder exhibits chordwise and spanwise variations. These three-dimensional effects may play a major role in the stretching of vortex filaments and in the redistribution of vorticity in all directions. The numerical models are not in a position to account for such complex effects. One may hope to assess the effects of three dimensionality by means of two-dimensional numerical experiments.

It is against this background that the nonlinear fluid-structure interaction projects an order of magnitude more complex problems. The picture emerging from the numerous experiments and mathematical models is that there are phenomena to be explained, parameters to be quantified, and conjectures to be justified.

C. LOCK-IN OR SYNCHRONIZATION IN STEADY FLOW

Numerous experiments have shown that when the vortex-shedding frequency brackets the natural frequency of an elastic or elastically-mounted rigid

cylinder with a suitable afterbody (capable of giving rise to a transverse force), the cylinder takes control of the shedding in apparent violation of the Strouhal relationship. Then the frequencies of vortex shedding and the body oscillation collapse into a single frequency close to the natural frequency of the body (see Fig. 3). This phenomenon is known by various names: lock-in, locking-on, synchronization, hydro-elastic or fluidelastic oscillations, wake capture, self-controlled or self-excited oscillations, etc.⁴

The facts which have emerged from two decades of work on vortex-induced oscillations may be summarized as follows:

1. When a body is close to its linear resonance conditions it can undergo sustained oscillations at a frequency close to its natural frequency [55]. That a cylinder should be excited at its natural frequency when the frequency of the exciting force is equal to its natural frequency is not surprising. But that the phenomenon encompasses a range of ± 25 to 30 percent of the natural vortex-shedding frequency and that the vibration and vortex shedding frequencies lock together and control the shedding process are surprising.

⁴A vortex-excited oscillation is actually a forced one having a self-excited character also to some degree due to lift force amplification through nonlinear interactions. By definition, self-excited oscillation is one where the alternating force that sustains the motion is created or controlled by the motion itself; when the motion stops, the alternating force disappears. For the phenomenon discussed herein the alternating lift force does not disappear when there is no oscillation. In fact, when there is no alternating force (a flat plate normal to the flow) there is no lock-in. Apparently, the often-used definition of 'self-excited oscillation' is a misnomer.

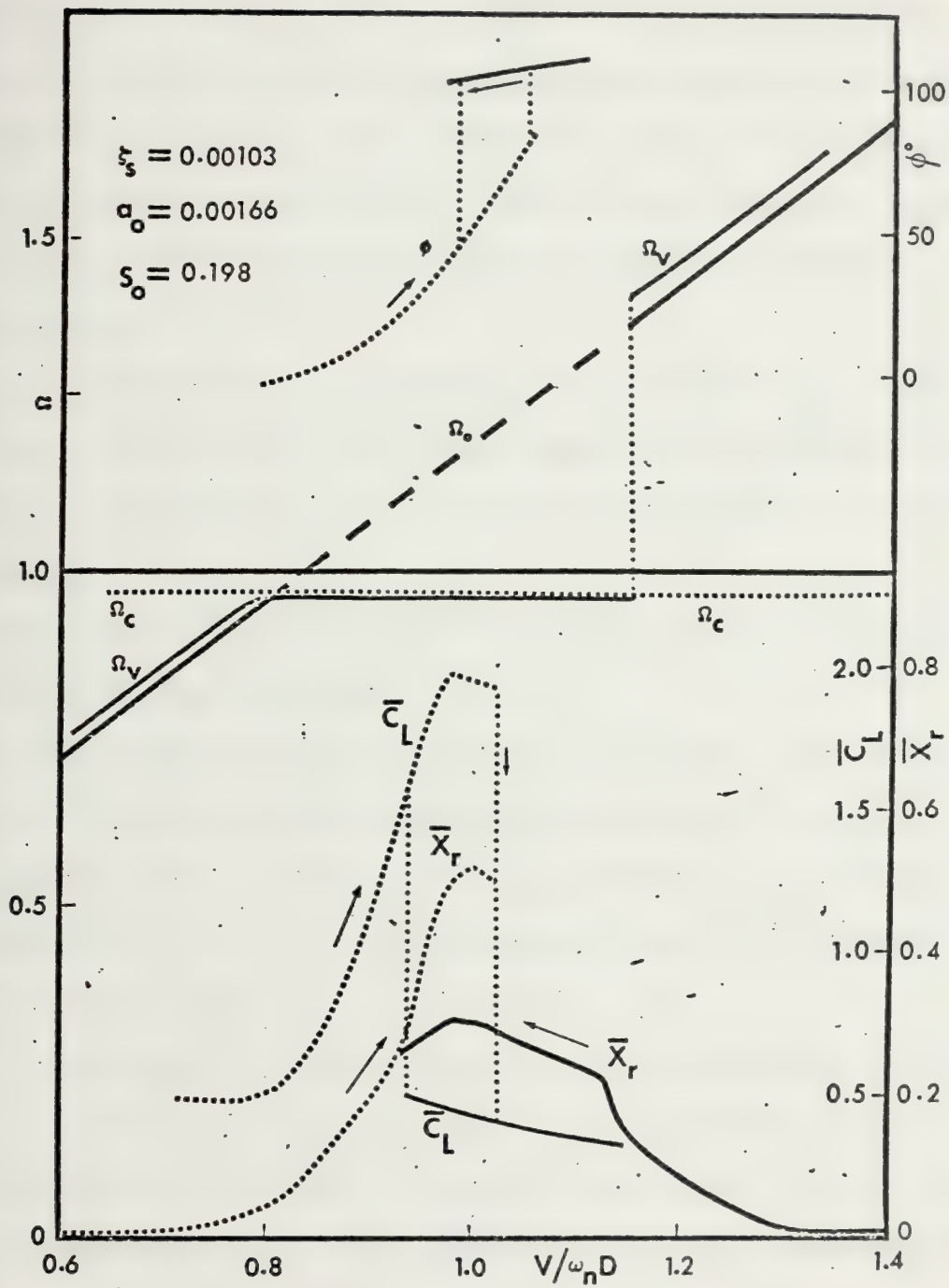


Fig. 3 Response characteristics of a freely-oscillating cylinder, from Feng [54], (see also [2])

2. The interaction between the oscillation of the body and the action of the fluid is nonlinear (e.g., [56-57]).

3. The vortex shedding does not necessarily result in an alternating transverse force. There must be a suitable afterbody, and hence an alternating lift force, and the shedding frequency should coincide with or be near the natural frequency of the body, or one of its harmonics, for sustained oscillations to occur. Thus, the magnitude and occurrence of sustained oscillations strongly depend on the lift coefficient of the stationary body.

4. The parameters $V_r = V/f_n D$ and $K_r = m\zeta/\rho D^2$ [58] or $R_p = m\zeta/\rho L D^2 (C_L^0)_{rms}$ [60] or $\Delta_r = (2\pi\zeta)(\pi S_0)^2/\rho_r$ are of major importance in determining the amplitude of oscillations and the range of synchronization for a given body [59-61].

5. The velocity range over which synchronization occurs increases with oscillation amplitude [62].

6. The excitation range of cross-flow oscillations in air extends over $4.75 < V_r < 8$ and maximum amplitudes occur in the range $5.5 < V_r < 6.5$ [3]. In water, the excitation range of the transverse oscillations can be increased to $4.5 < V_r < 10$ with maximum amplitude falling within the range of $6.5 < V_r < 8$.

7. For a circular cylinder with large L/D , synchronization begins when $f_o \simeq f_n$ and ends at about $f_o/f_n \simeq 1.4$. The maximum amplitude occurs near the middle of this range. At the end of the lock-in range, vortex-shedding frequency jumps to that governed by the Strouhal relationship, but the cylinder continues to oscillate at $f_c \simeq f_n$. This is true at both ends of the lock-in range [54] and shows that the response is not a simple forced vibration at the exciting natural Strouhal frequency.

8. For a cylinder with fixed separation points (e.g., a D-shaped cylinder) synchronization extends over a range of 0.96 to 1.1 of the resonant velocity (f_0/f_n from about 0.85 to 1.1) [24]. According to Feng [54], the said range extends over a range of $5 < V_r < 7$. Gowda [39] found that the lock-in begins already when f_0 is about 80 percent of f_n and ends when $f_0 \simeq f_n$. The maximum amplitude occurs near the end of the synchronization.

9. In synchronization, the slantwise vortex shedding is replaced by parallel vortex shedding [44, 62].

10. The correlation length increases rapidly with amplitude [57, 62-65]. The increase of the correlation length in smooth flow is much larger than in turbulent flow [66]. In smooth flow the correlation length is estimated by numerical extrapolation to increase from about $3.5D$ to $40D$ for $Re = 1.9 \times 10^4$ in the range⁵ $0.05 < A/D < 0.1$. In turbulent flow, it is again estimated to vary from about $2.5D$ to $10D$ in the same A/D range. The rate of increase is steeper than linear but does not show any abrupt change which would indicate a sudden development of the lock-in once a threshold amplitude is achieved.

11. For bodies, with mobile or fixed separation points, undergoing sustained oscillations, the vortex strength is increased [24, 67]. This could be either or both due to increased rate of vorticity flux or due to less destruction of vorticity in the near wake. The growing vortex on a vibrating cylinder seems to roll up more quickly [24].

⁵The generality of these values is not certain since in Novak and Tanaka's [66] experiments the cylinder length (between the end plates) was only 12 diameters.

12. The transverse force needed to excite a cylinder to large amplitude oscillations is far greater than that exerted by vortex shedding, i.e., the transverse force is amplified (e.g., [54], [56], [61]). The increase of the correlation length is responsible only for about 10 percent of the lift increase, i.e., it is not the major factor for the lock-in phenomenon.

13. A hysteresis behavior may exist in the amplitude variation and frequency capture depending on the approach to the resonance range -- whether from a low velocity or from a high velocity [54]. No universal behavior is noted and the reasons are not clear. The jump condition (double amplitude response) may originate in the fluid system, and therefore in the lift force, and not in the cylinder elastic system [2]. The 'combination-oscillation' model [68], (based on the assumption that the lift oscillator has two components, one at the cylinder frequency, representing lock-in, and the other approximately at the frequency of vortex shedding for the stationary cylinder) gives rise to jumps between two stable oscillation amplitudes but only at the ends of the lock-in range and not in the middle of the said range, as found by Feng [54], (see Fig. 3). The jump may be the consequence of a variable structural damping (dependent on the interaction of the ambient velocity and structure support, vibration velocity and/or amplitude, etc.) [69-70] or of a nonlinear spring behavior [71]. It is also entirely possible that the jump condition originates in both the fluid and the cylinder elastic system, including blockage effects [72] and the vibrations of the test apparatus [54].

14. The absolute value of the base pressure and the in-line or drag force increase with the amplitude of oscillation [3, 56, 61, 72, 73]. For

a circular cylinder, C_{pb} increases as much as 60 percent for $A/D = 0.29$ [72].⁶ For a D-shaped cylinder, Davies [24] found an increase of 70 percent relative to the stationary D-cylinder value.

15. The phase difference between the displacement and force signals increases almost linearly at first and then rapidly [54, 56].

16. The mobility of the separation points is important but not necessary for synchronization. The separation point on a circular cylinder moves over an arc whose magnitude depends on the frequency and amplitude of the oscillation. The magnitude of the separation-point travel reaches a peak when the cylinder frequency is about 0.9 of the wake frequency [74, 75].

17. The actual instantaneous value of the wake angle is greater than that between the ambient flow velocity and the relative fluid velocity [74, 75].

18. The overall wake width is practically unaffected in spite of the lateral movement of the body that generates it. Koopman [62] inferred from flow-visualization studies an apparent decrease in lateral vortex spacing in the resonant wake of an oscillating circular cylinder. Davies [24] found about a 20 percent increase for a D-shaped cylinder synchronized in a flow at much high Reynolds numbers ($7 \times 10^3 < Re < 4 \times 10^4$, $A/D = 0.2$). Griffin [67] found that the lateral spacing of the vortices decreases with increasing amplitude and is unaffected by changes in frequency of oscillation.

⁶Fixing separation at $\theta_s = \pm 70$ degrees by a tripping wire on a circular cylinder yielded a nearly constant C_{pb} at -1.39 for $A/D = 0.1$ for all values of f/f_0 from 0.4 to 1.3 [72].^{pb} The reason for this anomalous behavior is not clear. Confirmatory experiments are needed.

19. Longitudinal spacing λ_v does not change with the amplitude of motion in the synchronization region but it varies inversely with the frequency ratio [77]. For a cylinder undergoing forced transverse oscillations with the frequency f_c , λ_v decreases from its value at $f_c = f_n$ as f_c/f_0 increases and vice versa. In other words, the wake contracts for $f_c/f_0 > 1$ and expands for $f_c/f_0 < 1$.

20. The formation length λ_f exhibits a similar variation with f_c/f_0 . However, unlike the longitudinal spacing, the formation length decreases systematically with increasing amplitude of vibration [76]. For a given f_c/f_0 , the vortices in the near wake go through a spacing adjustment from an amplitude-dependent spacing to an amplitude-independent longitudinal spacing.

21. Forced vibrations may differ from the naturally occurring vortex-induced vibrations since the latter depend, to some extent, on the history of the fluid motion. History effects may be particularly important in cases where hysteresis occurs. Driven models overshadow the intricate interaction between the evolution of the motion and the variations of the pressure distribution.

22. Frequency demultiplication or frequency division (existence of the natural vortex-shedding frequency in the state of synchronization in the wake) may occur when the forced cylinder frequency f_c is an integral multiple of the shedding frequency⁷ [56, 57, 72, 77].

⁷For example $x = 2b^{-1/2}\sin t$ is the exact solution of

$$\ddot{x} - 2a\omega(1-bx^2)\dot{x} + \omega^2x = -4ab^{-1/2}\sin(3\omega t)$$

and is a special case of the phenomenon called 'frequency demultiplication' by van der Pol [78].

23. In-line oscillations occur within two adjacent regions [79-86]. The first is in the range of $1.25 < V_r < 2.5$, maximum amplitudes occurring at $V_r \approx 2.1$. The second region extends from $V_r \approx 2.7$ to $V_r \approx 3.8$ with maximum amplitudes at $V_r \approx 3.2$. The first instability region is accompanied by symmetric vortex shedding (as if the flow started impulsively from rest at each cycle) and the second by alternate vortex shedding.

Several mathematical models have been proposed [87-91], (see also [2, 55, 71, and 92] for additional models) in an attempt to simulate and/or explain some of the experimental results summarized above. These models do not include the analysis of the flow field and the fluid-mechanical arguments invoked in their evolution are not altogether convincing. Thus, their worth should be measured not so much by their capacity to obtain functional relations among significant parameters that lead to the basic understanding of the phenomenon but rather by their ability to produce results which are qualitatively similar to those obtained experimentally.

The most noteworthy among the oscillator models is the one proposed by Hartlen and Currie [87] where a van der Pol type soft nonlinear oscillator for the lift force is coupled to the body motion by a linear dependence on cylinder velocity. This model is based partly on a suggestion by Birkhoff and Zarantonello [23], mentioned earlier in connection with the estimation of the Strouhal number, and by Bishop and Hassan [56] in connection with their now classic experiments with oscillating cylinders in uniform flow. The model has its roots in mechanics and electricity rather than in the equations of fluid motion. The details of this model will be described later.

D. LOCK IN OR SYNCHRONIZATION IN OSCILLATING FLOW

There has been relatively little theoretical and experimental work on the complex dynamic response of elastic structures to oscillating flows.

Laird [93] explored, in 1962, the effects of support flexibility by oscillating a vertical cylinder through still water. He found that the forces acting on a flexibly-supported oscillating cylinder can exceed 4.5 times the drag force on the cylinder rigidly-supported while moving at a uniform velocity equal to the maximum velocity during the oscillation and that a cylinder, flexible enough to have transverse oscillations with amplitudes more than half the diameter, while performing large amplitude oscillations in water, tends to oscillate transversely at the eddy-shedding frequency and to vibrate at twice the eddy frequency in the in-line direction. Laird's work pointed out the significance of the vibrations in harmonic flow and the need for a detailed investigation of the phenomenon.

Vaicaitis [94] investigated the response of deep-water piles due to cross-flow forces generated by wind-induced ocean waves. The resulting cross-flow forces were treated as random processes in the time-space domain and are assumed to be dependent on fluid velocities and vortex shedding processes. Out of necessity, Vaicaitis had to make a number of assumptions regarding the structural motion, the added mass coefficient, Strouhal number, etc. Vaicaitis was careful to note that some of his conclusions were based on a particular example and that they might not be true for piles with different dynamic characteristics.

Selna and Cho [95] investigated the in-line resonant response of a tall structure by assuming constant drag and inertia coefficients in calculating the exciting fluid force through Morison's equation [96],

modified to take into account the motion of the structure. Their calculations have shown that a resonant motion is possible and that the dynamic deflection of a flexible structure can considerably exceed its static deflection.

Verly and Every [97] measured wave-induced stress on similar rigid and flexible vertical cylinders in a wave channel at relatively low Keulegan-Carpenter and Reynolds numbers. Even though they were unable to correlate their data with any suitable parameter governing the motion, they concluded that the vibration is caused by the cylinder's response to eddy shedding and that there is no fluid-structure interaction. They found that the vibration occurs if $U_m/f_n D$ (U_m represents the maximum velocity of flow or wave in a cycle; and D , the diameter of the cylinder) is greater than about unity for any natural frequency, wave frequency, and damping. The $U_m/f_n D$ parameter never reached high enough values in Verly and Every's experiments for the cylinder to undergo synchronized oscillations as the present investigation has shown.

McConnell and Wilson [98] conducted experiments similar to those of Laird [93] by sinusoidally driving a circular cylinder in still water. These experiments were conducted at rather small Reynolds numbers with 0.25 in and 0.50 in cylinders. Furthermore, these investigators measured only the amplitude of oscillation and calculated the lift coefficient at resonance from a slightly-modified version of an equation developed by Sarpkaya [60]. They have concluded that $U_m/f_n D$ is one of the most important parameters governing the resonant oscillations.

Sawaragi et al., [99] investigated the in-line and transverse dynamic response of a cantilevered circular cylinder, with a concentrated mass

at its top, in waves of small amplitude. The Reynolds number ranged from 1,500 to 6,200 and the rms value of the Keulegan-Carpenter number ($K = U_m T/D$, calculated over the submerged length of the cylinder through the use of rms value of the maximum of the horizontal velocities) ranged from 2 to about 20. They have approximated the lift coefficient for a rigid cylinder by a Rayleigh distribution and calculated the dynamic response of the test cylinder. The results are of limited value since the interaction between the synchronization and the force amplification was ignored and since no more than three vortices were shed during a half cycle. Furthermore, the rapid variation of the Reynolds number, Keulegan-Carpenter number, vortex-shedding coherence, and lift force with depth, in a range of Keulegan-Carpenter numbers where the phenomenon is least understood, obscured the role played by the governing parameters.

It is clear from the foregoing that there are no well-established analytical methods either to analyze the data or to predict the characteristics of the flow or of the vibration. Thus, it was decided to undertake a comprehensive investigation of the dynamic response of elastically-mounted smooth and rough cylinders in harmonic flow particularly at high Reynolds numbers and Keulegan-Carpenter numbers.

II. EXPERIMENTAL EQUIPMENT AND PROCEDURES

A. U-SHAPED OSCILLATING-FLOW TUNNEL

1. Original Design

Experiments carried out by Sarpkaya and Tuter [100] on small smooth cylinders at low Reynolds numbers, in 1974, showed the necessity of an apparatus capable of producing larger Reynolds numbers. Various designs were considered, ranging in a broad spectrum of complexity and versatility. One of the options was to oscillate the fluid by a suitable piston mechanism. The achievement of desired amplitudes and frequencies needed to obtain high Reynolds and Keulegan-Carpenter numbers required an extremely complex system. Furthermore, the vibrations generated by the piston motion could not have been easily overcome. Thus, this design has been abandoned. Finally, among various options, a U-shaped oscillating-flow tunnel was designed and built [101]. The tunnel in its original design consisted of 11 modules for ease of construction, transportation, and mounting. Each module is made of 3/8 inch aluminum plates and reinforced with 1/2x4x18 inch aluminum flanges welded to the plates. The modules were assembled with the help of an air drying silicon-rubber seal between the flanges of two adjacent modules and 1 inch steel bolts placed 6 inches apart. The inside of each module was precision machined so that the largest misalignment was about 0.04 inches.

The cross-section of the two legs is 6x3 feet whereas that of the test section is 3x3 feet. This selection was dictated by several factors such as:

- (a) available ceiling height;
- (b) pressures to be encountered;

- (c) desire to obtain, at the test section, an amplitude or velocity of oscillation at least twice that of the free surface;
- (d) period of oscillation;
- (e) desired Reynolds numbers and relative amplitudes;
- (f) possible separation of the flow at the corners;
- (g) natural damping of the oscillation; and
- (h) magnitude and the frequency of the forces.

The length of the horizontal test section was chosen larger than twice the actual amplitude (amplitude at the test section or virtual amplitude) to ensure fully developed uniform flow at the test section. Finally, the two corners of the tunnel were carefully streamlined to prevent flow separation (see Fig. 4). This design proved to be more than adequate for the experiments planned at that time.

The auxiliary components of the tunnel consisted of plumbing for the filling and emptying of the tunnel with hot and cold water (50° to 120°F), a heat exchanger, butterfly-valve system, and the air supply system. The tunnel capacity is about 6000 gallons and could be filled by city water or by means of a pump from a reservoir.

The butterfly-valve system (mounted on top of one of the legs of the tunnel) consisted of four plates, each 18 inches wide and 36 inches long. A 1 inch steel shaft was placed at the axis of each valve plate (see Fig. 5). Aluminum housings supported both ends of the shaft with self-aligning ball bearings. A 6 inch gear was attached to one end of each shaft which extended beyond the bearing. All four valve plates were then aligned and driven by a simple rack and piston system. The rack

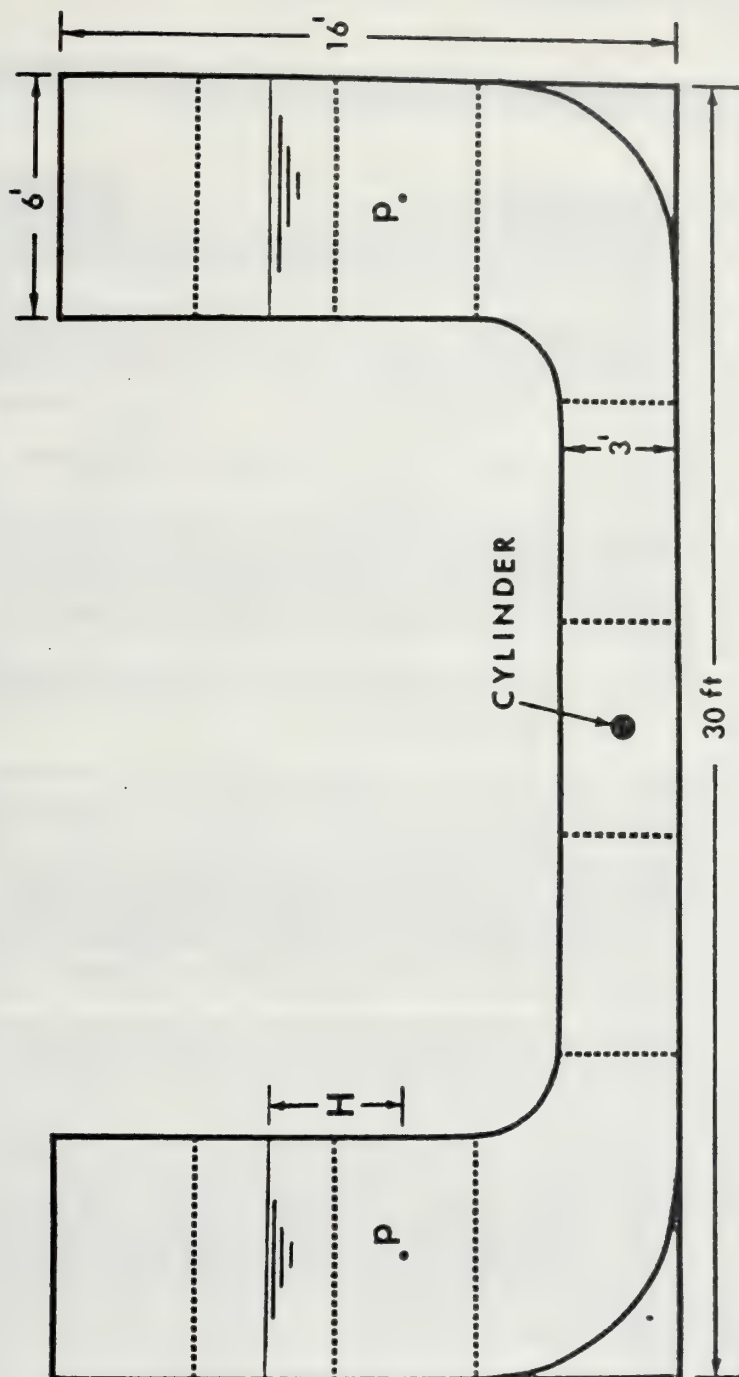


Fig. 4 Schematic drawing of the initial version of the U-shaped water tunnel



Fig. 5 Photograph of butterfly valve system

as actuated by an air-driven piston with the help of a three-way valve connected to the laboratory air supply system.

To set the fluid in harmonic oscillation, butterfly valves at the top of one of the vertical legs were closed allowing the sealed chamber to be charged with high pressure air. This above-ambient pressure caused the water tunnel to rise in the opposite leg, left open to the atmosphere. The three-way control valve enabled one to release the air quickly by sudden opening of the butterfly-valve and put the bulk of fluid into a harmonic oscillation. The damping of the fluid oscillation was in a very acceptable range in the case for the experiments with the fixed cylinders. But, as will be seen later, design improvement was necessary in the case of oscillating cylinders.

2. First Design Improvement

In order to investigate the effect of cylinder oscillations on the transverse forces acting on it, it was necessary to construct an elastic mounting with only one degree of freedom. Several design options were considered. Finally, the requirements for rigidity, strength and torsional stability in the in-line direction quickly led to the use of helical steel springs. In the final design, the cylinder was rigidly fixed to two low-friction linear bearings resting on two matched helical springs. The motion of the bearings was constrained by two rods perpendicular to the direction of flow as shown in Fig. 6.

The force transducers were mounted as shown in Fig. 7 to the aluminum split-bearing housing blocks. Each block was manufactured to accommodate an adjustable ball bearing with a nominal 2.5 in. bore and a length of 5.0 in. The bearings rode on 2.5 in. diameter stainless steel,

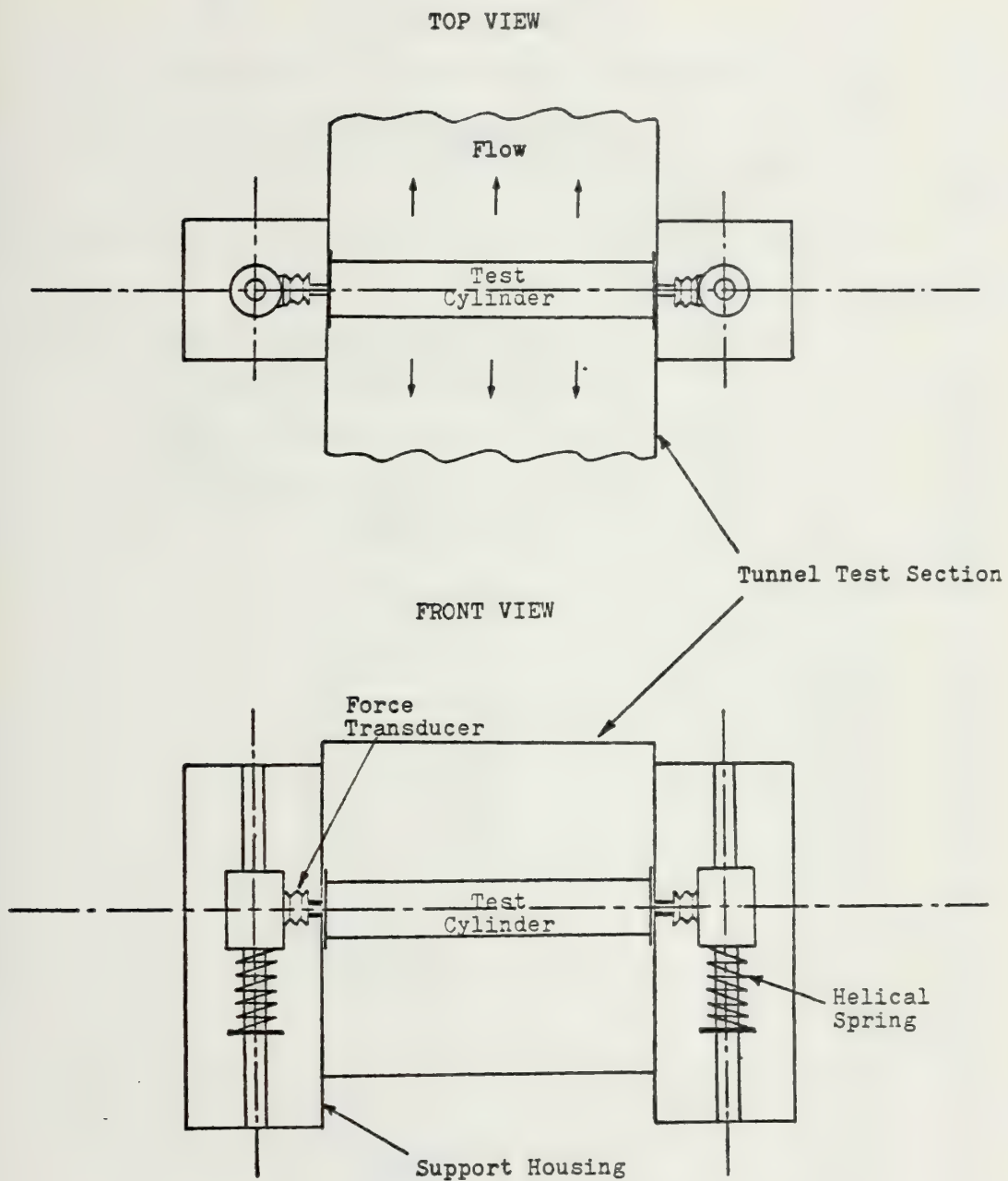


Fig. 6 Preliminary sketch of the support and housings

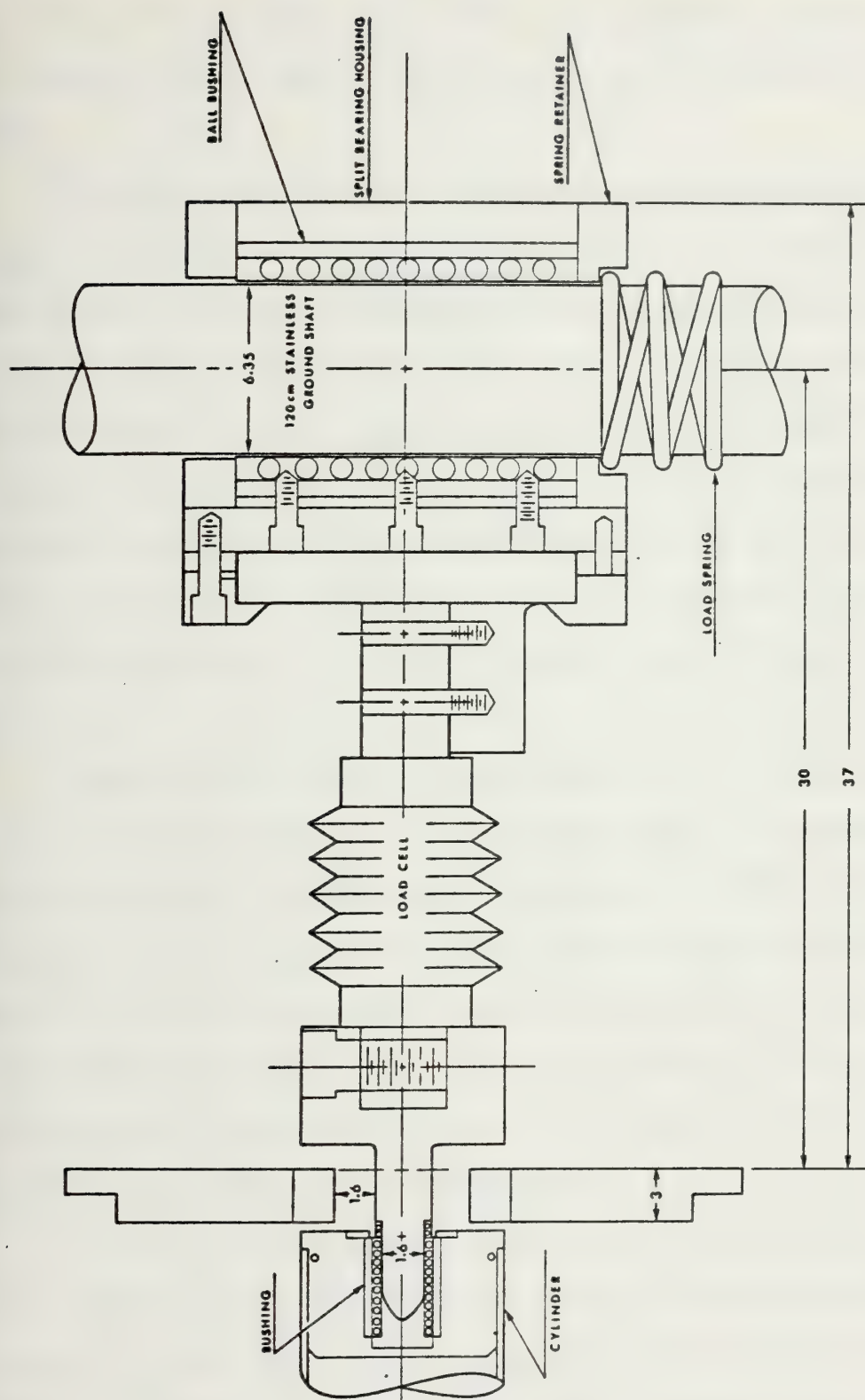


Fig. 7 Side cutaway view of a load cell and bearing housing, (dimensions in cm)

hardened and ground, solid shafts. Adjustments of the bearing diameter eliminated bearing chatter. The springs were centered around the shafts by a retaining ring on the housing blocks and by the yoke support at the bottom.

The yoke supports allowed the blocks and springs to be raised or lowered to center the cylinders vertically in the test section and permitted the use of various cylinders, springs and weights while accommodating the effects of the buoyant force. Each yoke was positioned by another yoke which was positioned with precision by a threaded third brass rod passing through the upper yoke and lifting against the housing top. Alignment of mounts and rods was accomplished by a jig which was placed between the two blocks, leveled, then raised, and lowered to position the two stainless steel rods. Detailed drawings of the system are shown in Figs. 8 and 9.

Figure 10 shows a dimensioned drawing of one of the two support housings. Each was welded of 3/8 in. aluminum plate. The windows were covered by removable Plexiglas plates for access for calibration and maintenance, or, when mounted in place, for the observation of cylinder movement during tunnel operation. Vents and drains were installed at top and bottom of the housing to remove air or water in filling or draining. The housings were flanged and bolted to the U-tunnel wall with O-ring seals for water proofing as may be seen in Fig. 9.

A 6.0 in. circular access hole was cut in the tunnel walls at the test section. Each hole was covered with a plate of identical size. A slot of 1 in. by 6 in. was cut in each cover. The covers allowed the installation of the cylinders; and the slots, the unobstructed linear oscillation of the force-transducer arms attached to the cylinder.

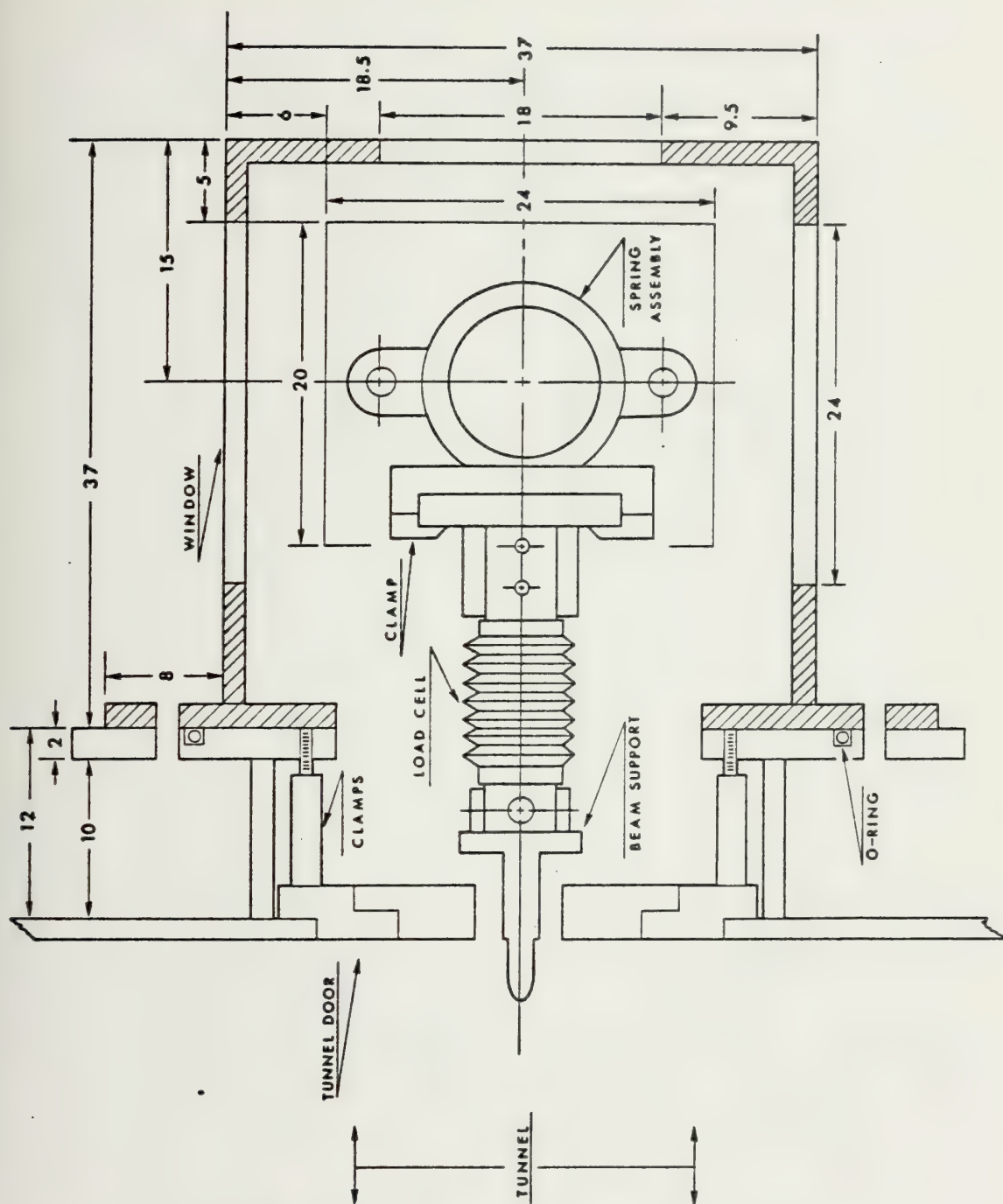


Fig. 9 Top view of a cylinder-support mount and housing, (dimensions in cm)

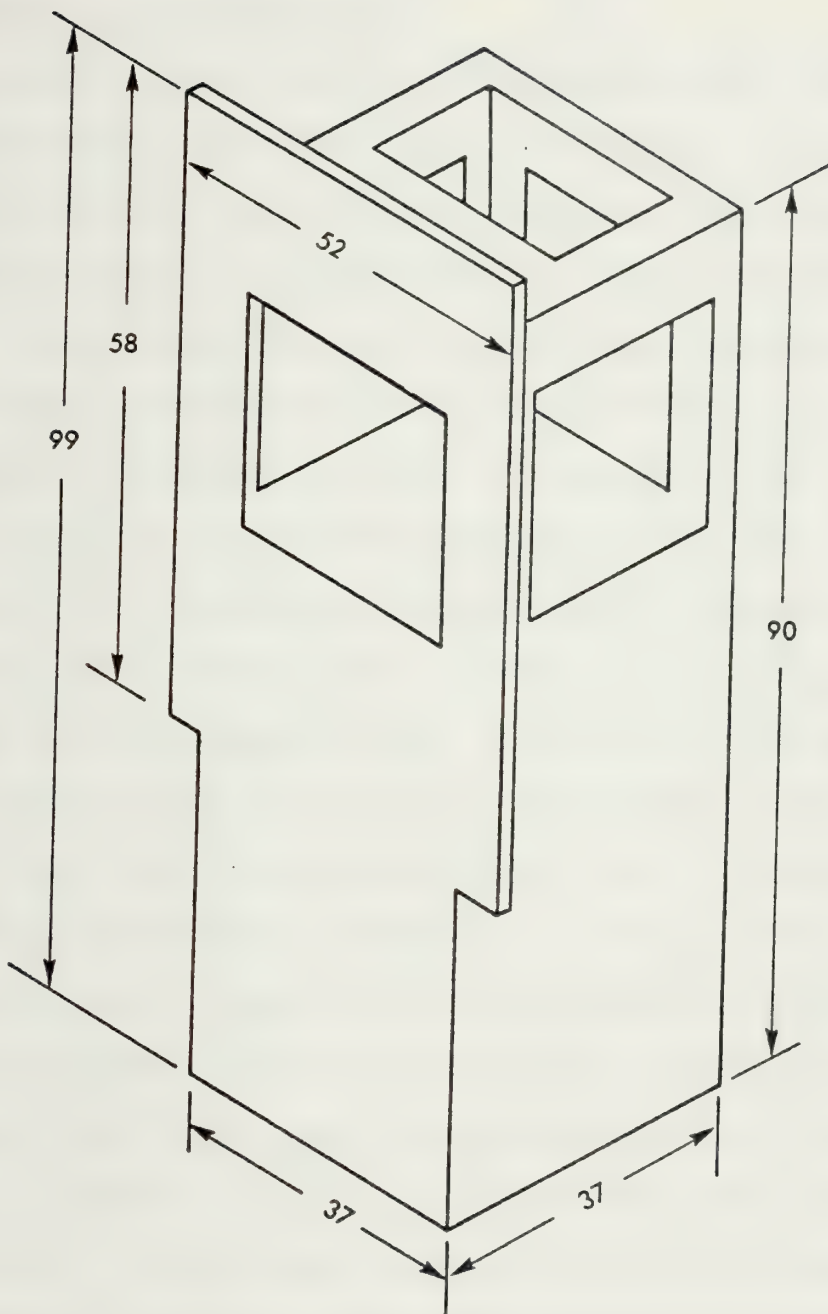


Fig. 10 Support housing, (dimensions in cm)

The usefulness of this design stems from the fact that the support-housing assembly could be rotated 90 degrees, thus enabling one to conduct experiments for cylinder oscillations in the in-line direction.

3. Second Design Improvement

A body oscillating in a fluid will extract energy from it.

Therefore one might expect this energy loss would add up to the natural damping of fluid oscillation in the tunnel giving rise to a faster rate of decay of fluid oscillation amplitudes. This would mean that lock-in phenomenon could not be observed over many cycles of oscillation. Experiments performed by Klinkhamer [102] suggested the necessity of devising a system capable of restoring the energy lost, due to damping, to the fluid. This would enable one to maintain the amplitude of the flow oscillation at a desired level thus allowing the observation of the lock-in over a large number of flow cycles. For this purpose an air-supply system was designed to introduce large quantities of air in one of the legs of the tunnel during prescribed time intervals. The necessary air was supplied by a centrifugal fan driven by a 3HP electric motor. The fan was first connected to a 30x30x33 inch air-control box which regulated the quantity of air supplied to the tunnel. The air-control box consisted of a gate valve at the exhaust of the fan and another gate valve on top of the box. The first gate valve was raised and lowered vertically by a threaded rod attached to a manually operated gear. This allowed a fine adjustment of the air supply. The gate valve on top of the box was activated by moving it horizontally by hand for a coarse adjustment of the air supply.

The air was introduced into the tunnel by a duct through a simple control system (see Fig. 11). The function of the control system was to introduce the air into the tunnel at prescribed time intervals so that

1. Blower.
2. Air-control box.
3. Vertical gate valve.
4. Horizontal gate valve.
5. Air duct.
6. Air valve.
7. Adjustable connecting rod.
8. Sprocket and chaine.
9. Variable speed motor.
10. Flywheel.
11. Butterfly valve.
12. Vertical leg of the tunnel.

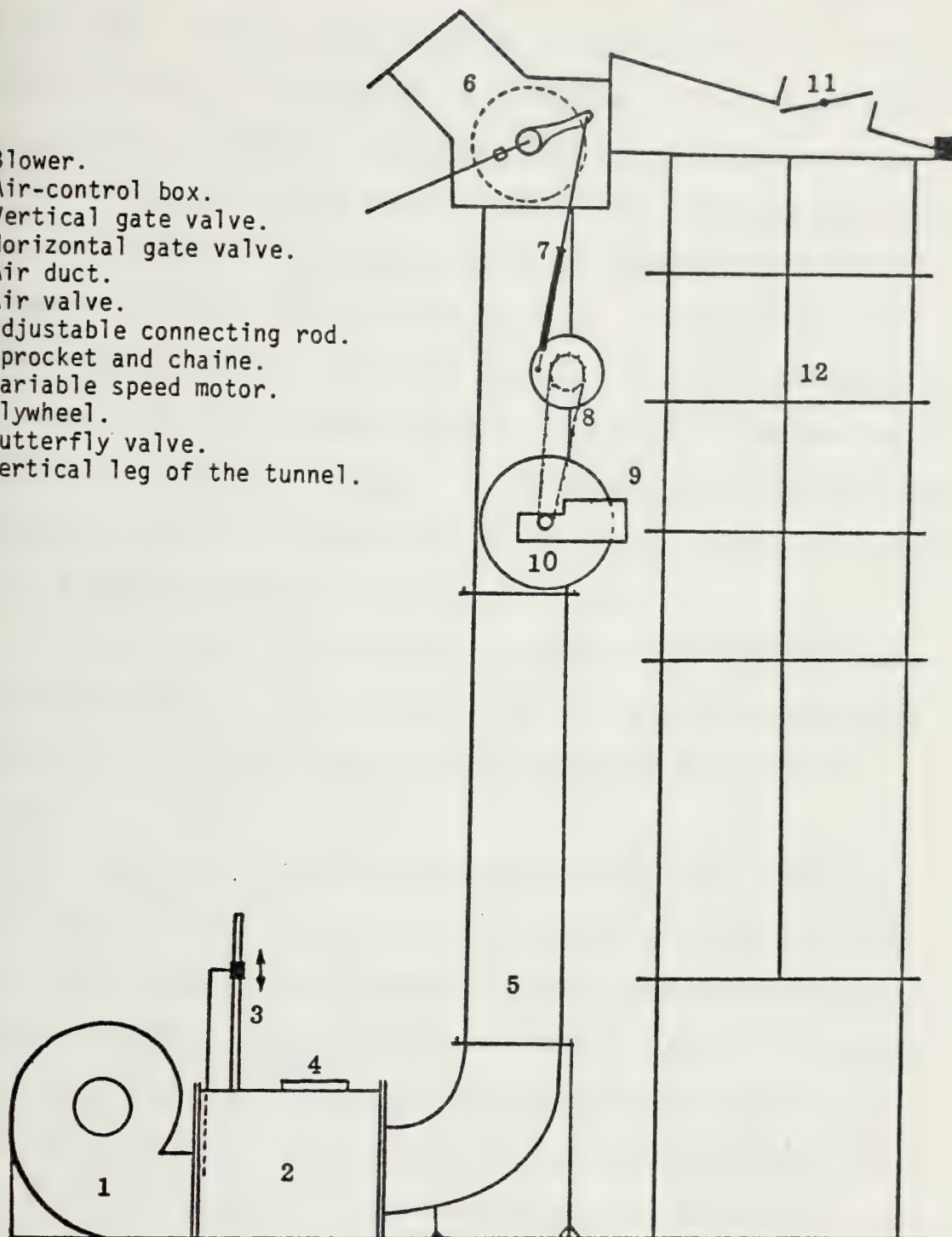


Fig. 11 Sketch of the air supply system

the energy lost due to damping could be restored to the fluid (see Fig. 12). The air control system consisted of a drum of 2 feet in diameter and 3 feet long. Three openings at angles as specified in Fig. 12 were cut into the drum. The door number (1) functioned as inlet to the tunnel and door number (2) worked as exhaust to the ambient. Inside the drum a vane of the same size as the diameter and length of the drum was placed. The vane was rocked about a mean position by an adjustable connecting rod through a sprocket wheel and chain mechanism. The system was driven by a variable speed electric motor and gear. Two flywheels, one attached to the drive shaft of the connecting rod and the other to the motor shaft assured smooth and uniform rotation. An RPM counter switch was installed at the other end of the drive shaft and the signal was electrically transmitted to a digital counter on the instrument panel.

The top of the leg of the tunnel to which air was supplied had to be sealed to prevent air from escaping. This was done by plywood boards in such a way so as to create an air-tight chamber on the top of the tunnel leg.

With this system very high amplitudes of flow oscillation were achieved. This, in turn, necessitated the lengthening of the horizontal section of the tunnel in order to maintain uniform flow about the test cylinders. For this purpose two additional modules (each 2.5 ft long) of the same cross section as the existing test section were added to each side of the test section. On both sides of these new modules two side windows (14x19 in.) were cut. One of the modules also had a door on top of it. The side windows were covered with plexiglass for the observation of the cylinder motion. However the main purpose of these windows was

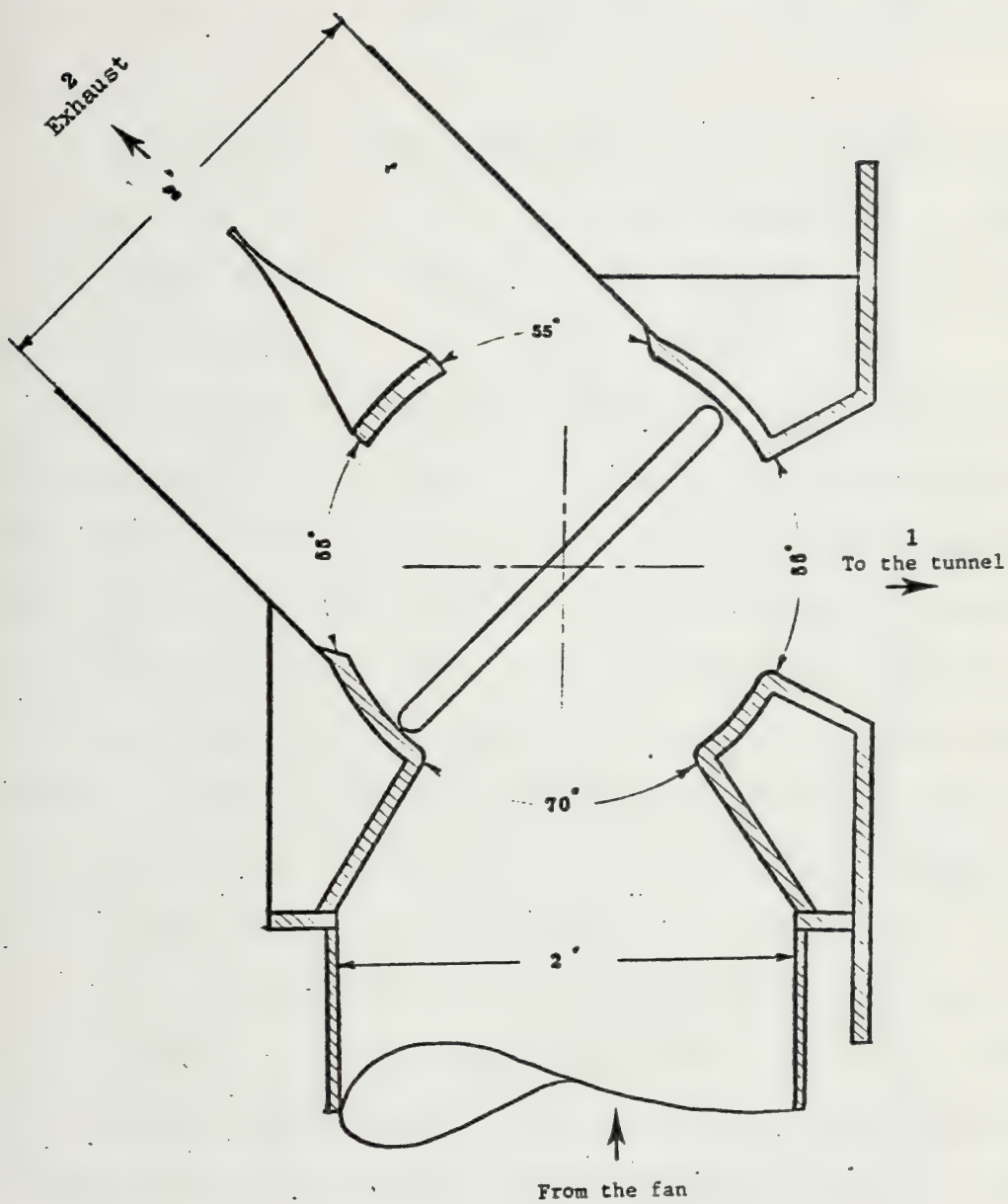


Fig. 12 Sketch of the air valve

to provide an easy and quick access into the tunnel for the mounting of the cylinders and force calibrations. Finally, a new water level sight window was cut into the wall of the vertical leg to facilitate the reading of the water level. The old butterfly-valve system on top of the other leg was not removed since by closing it the flow oscillation could be quickly stopped.

Figures 13a and 13b show photographs of the two sides of the tunnel after its completion. Figure 14 shows a schematic drawing of the tunnel.

The natural period of the tunnel after these modifications turned out to be 5.960 seconds.

To put the fluid in the tunnel into oscillation, the RPM of the variable speed motor driving the air-valve was set at such a value that the period of the rotation of the vane was exactly the same as that of the tunnel. Once the fan was turned on, every time the vane cleared port (1) of the air-valve, air flowed into the tunnel and pushed the water down. The time of opening of the port (1) was exactly synchronized to the time when the water had reached its maximum amplitude and began to fall down. The pressure of the supplied air restored the necessary energy to the water to maintain its amplitude at a certain level. By opening or closing the gate-valves on the air-control box, one could change the quantity of air and consequently the amplitude. This design turned out to be extremely successful because the tunnel could sustain oscillations at a desired amplitude for an indefinite period of time.

B. CIRCULAR CYLINDER MODELS

Circular cylinders with diameters ranging in size from 2.5 in. to 5 in. were used in the experiments. The cylinders were turned on a lathe

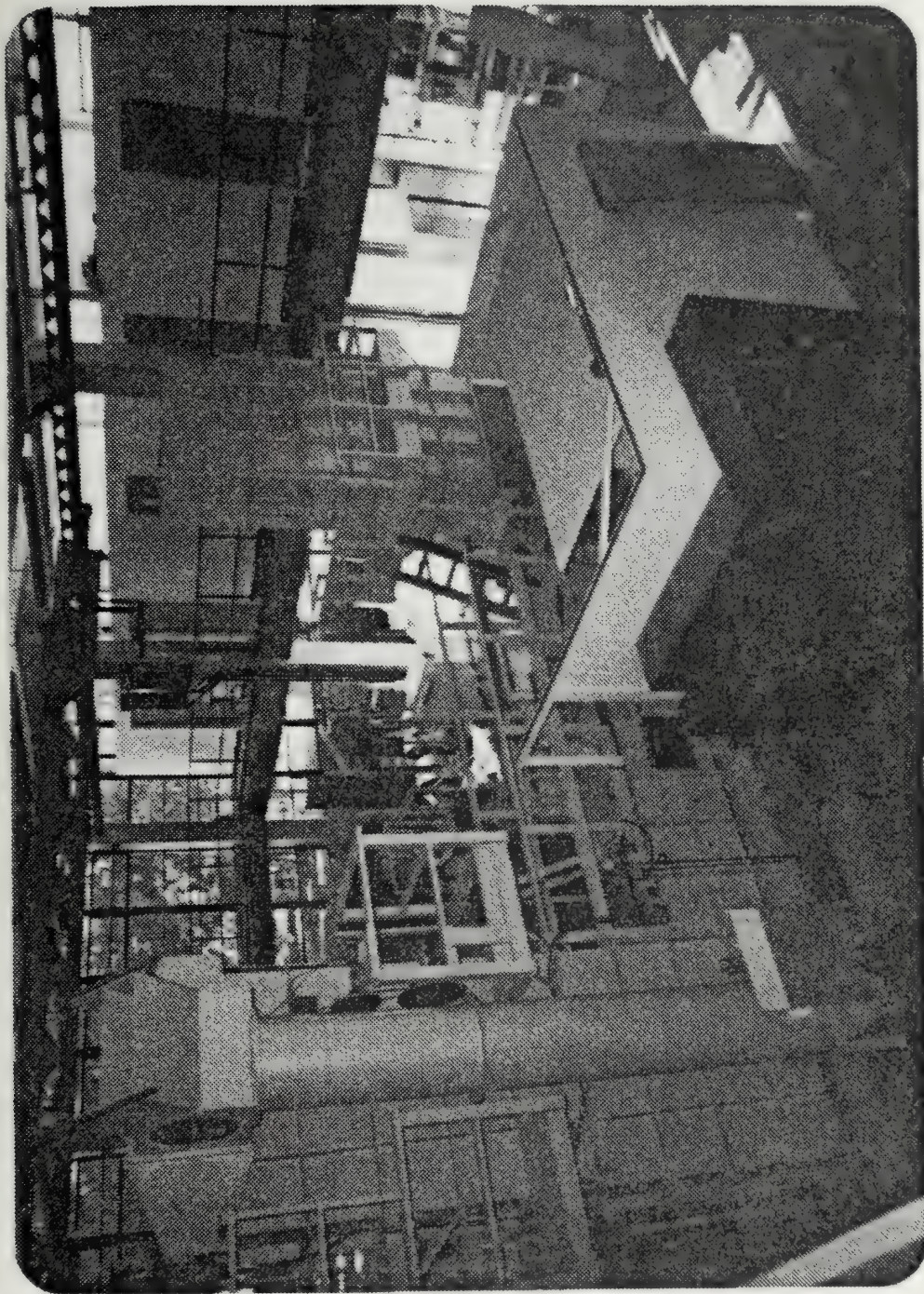


Fig. 13a Completed tunnel with air supply system

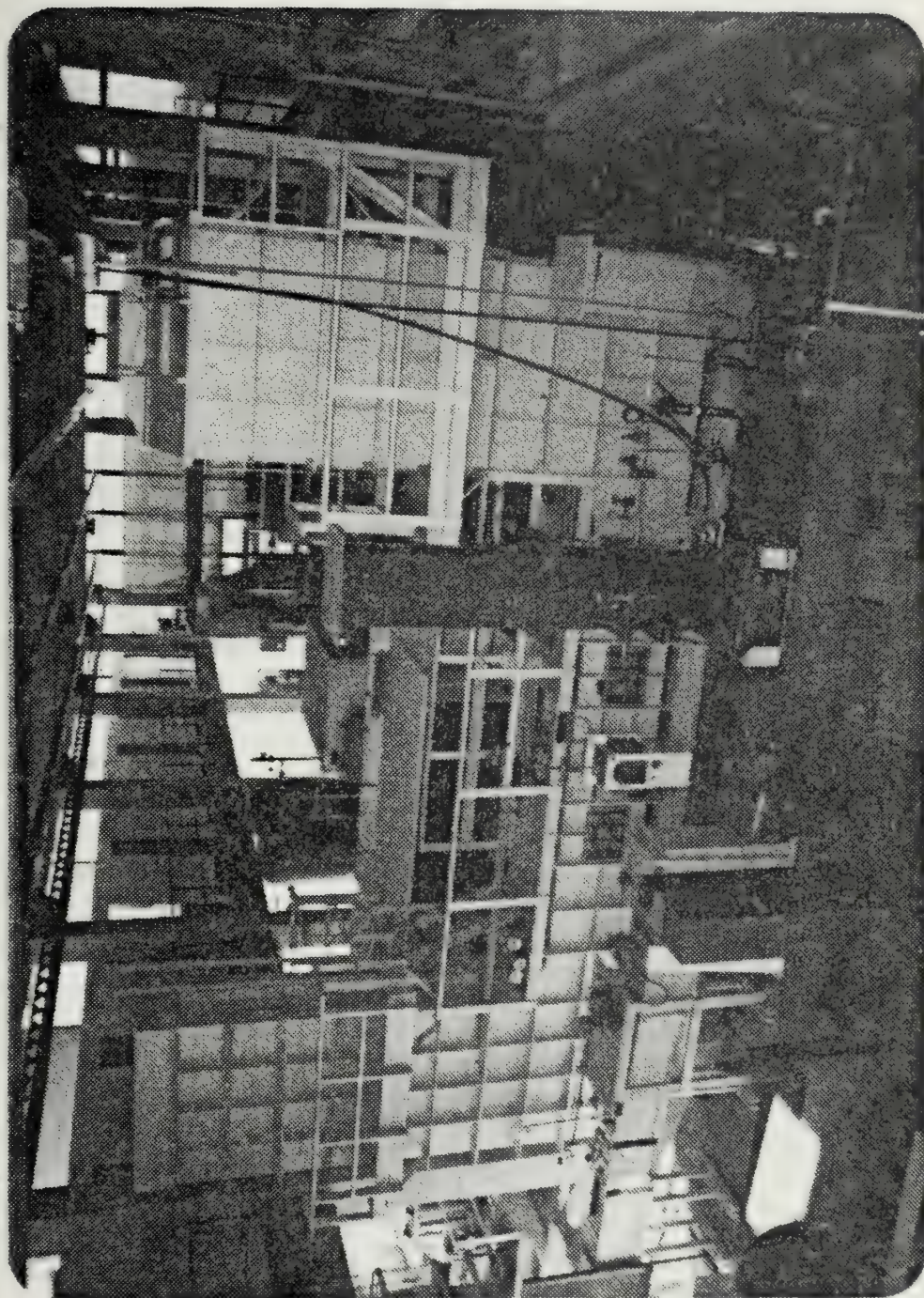


Fig. 13b Back view of the tunnel with the side windows

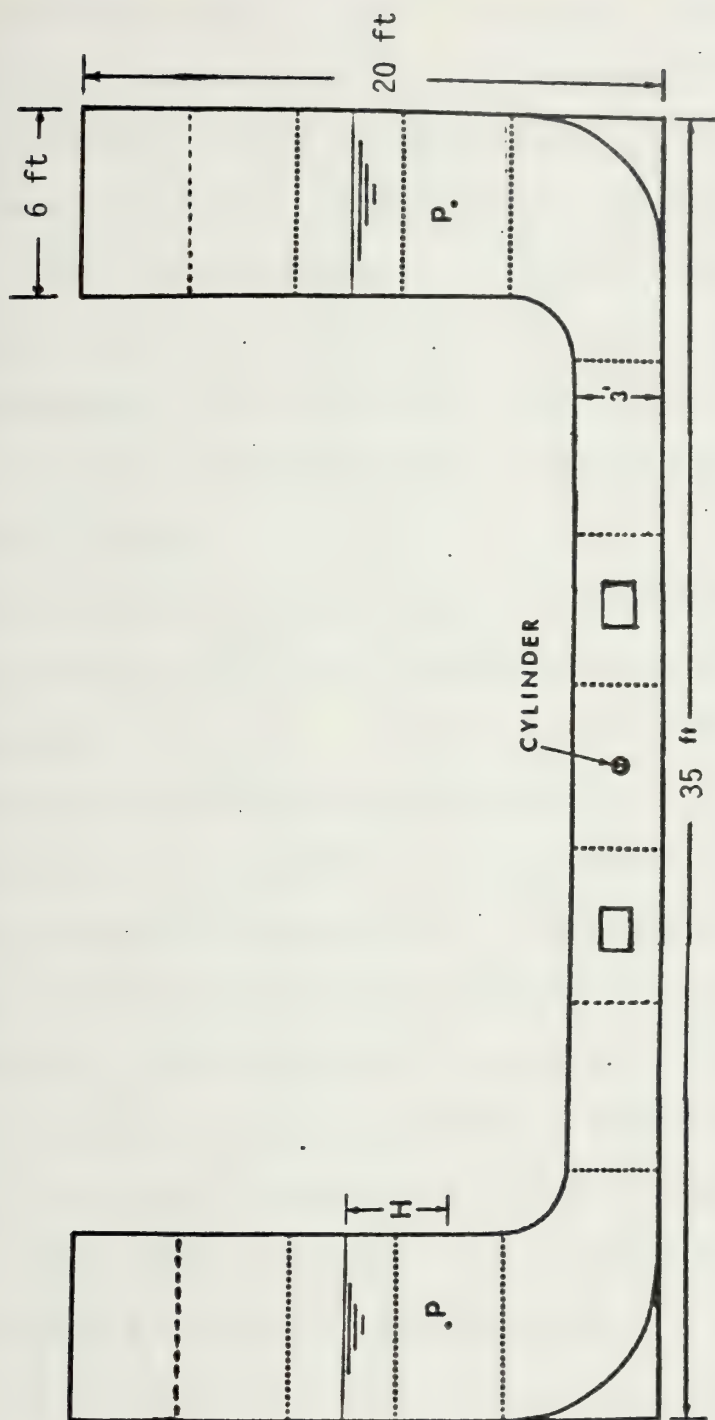


Fig. 14 Schematic of the final version of the tunnel.

from aluminum pipes and polished to a mirror-shine surface. The length of each cylinder was such as to allow a 1/32 in. clearance between the tunnel wall and each end. As part of the total length, smooth circular flanges 6.0 in. in diameter and 1.8 in. thick were attached to the ends of the cylinder to eliminate the end effects.

Cylinders were hollow, and each contained a beam type accelerometer. Figure 15 shows a cutaway drawing of a cylinder with the accelerometer installed in the exact center of the cylinder. The electrical connection to the accelerometer was led through a notch in the male fitting at the end of the cylinder. Sealing of the unit was accomplished by O-rings and threaded fittings.

The same cylinders were also used as rough cylinders by coating them with sand of desired size. The relative roughness used in the present experiments was $k_c = 1/100$. For this purpose clean sand was screened through the use of a combination of appropriate size of sieves to separate the desired size. The cylinder surface was then cleaned with alcohol and carefully coated with an epoxy paint. It was possible to obtain an extremely thin and uniform coating which was free of ridges, waves and local buildup. Next, the selected sand was sprinkled over the cylinder. The excess sand was easily removed after 15 minutes through gentle rubbing by hand. The resulting roughness was uniform as evidenced by the two sample photographs shown in Figure 16. The pictures of the rough surface were taken with a scanning electron microscope. The actual size of the sample sand is shown in the figure.

C. FORCE MEASUREMENTS

Two identical force transducers, one at each end of the cylinder, were used to measure the instantaneous force. The basic transducer was

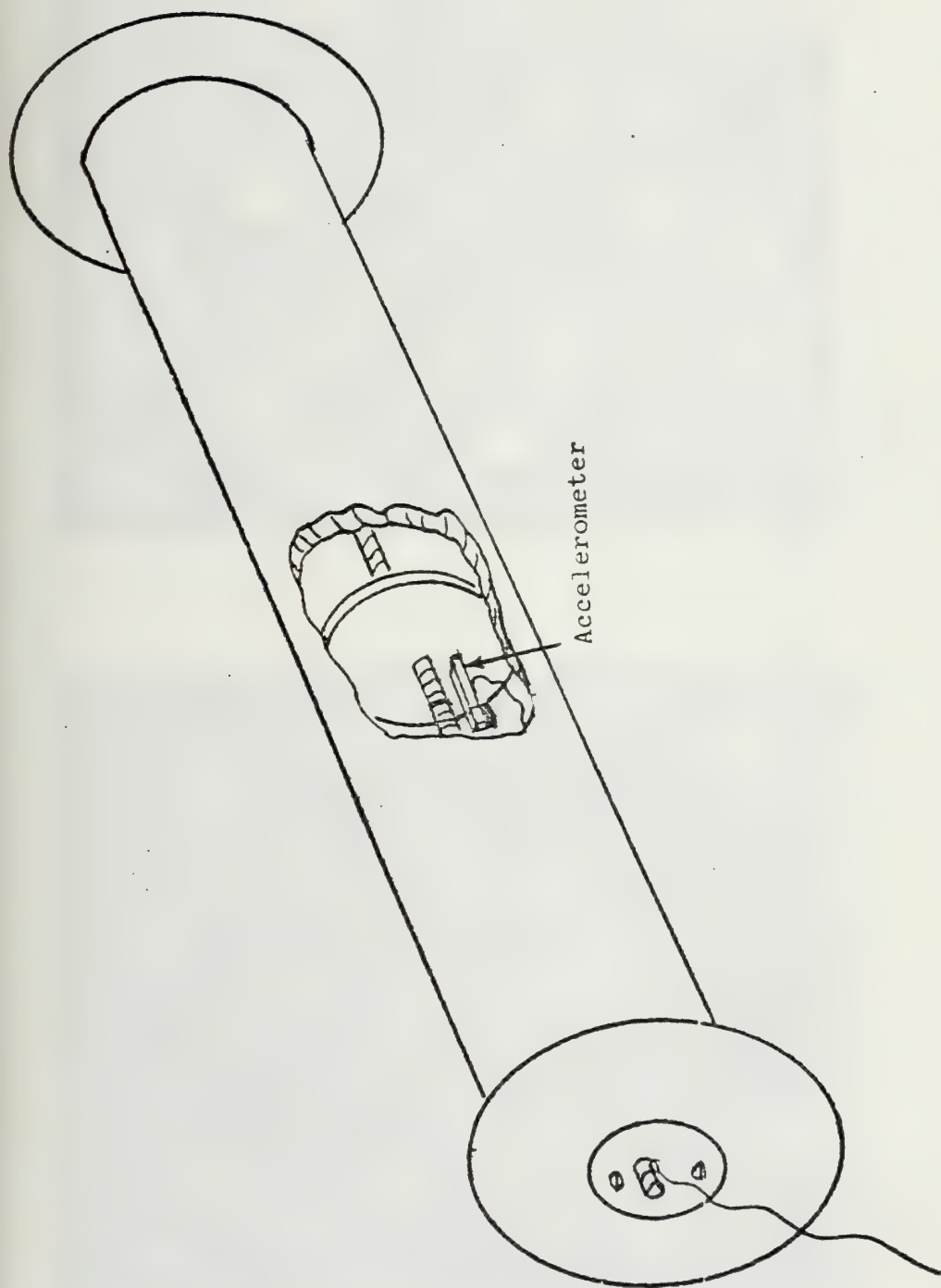
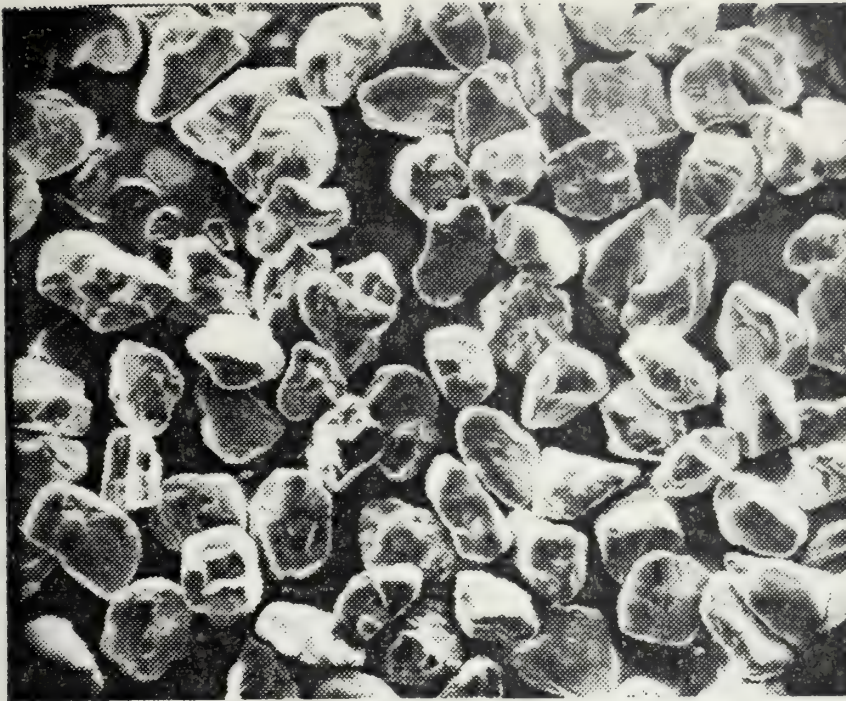
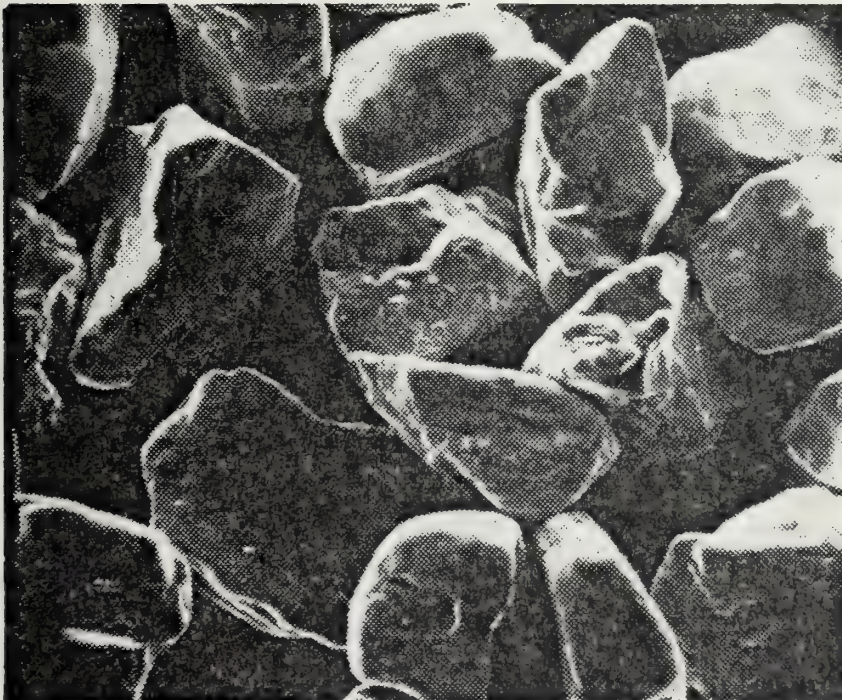


Fig. 15 A cutaway sketch of a cylinder with accelerometer



$k_c = 0.018''$
20-X



$k_c = 0.018''$
50-X

Fig. 16 Scanning Electron Microscope Photographs of sand-roughened surface

manufactured by B.L.H. Electronics, Inc., under the trade name of LBP-1. Two sets of transducers were used in the experiments. Each gage in one of the sets had a capacity of 500 lb and in the other set a capacity of 250 lb. The overload capacity of the gages was 200 percent. The deflection of the gage under 500 lb load was 0.01 inch. A photograph of the basic transducer is shown in Fig. 17. The bellows which protected the strain gages had to be waterproofed in such a manner that they would not adversely affect the operation of the gage when subjected to about 20 feet water pressure at temperatures ranging from 65°F to 160°F. For this purpose the bellows were completely filled with Dow Corning 340-RTV coating without bringing the rubber into contact with air during the filling operation. After filling, the ends of the bellows were sealed air tight with special clamps. The transducers then were mounted, as shown in Fig. 7, to the aluminum split-bearing housing blocks.

It is seen from Fig. 18 that the transverse force acting on the cylinder is given by

$$F_L = F_1 + F_2 - M\ddot{X} \quad (2)$$

in which $M\ddot{X}$ represents the inertial force due to the acceleration of the cylinder. The sensitivity of the accelerometer was adjusted to yield $F_L = 0$ while the cylinder freely oscillated in air. This method allowed the measurement of the net fluid force with an error less than 1.5 percent.

D. CYLINDER DISPLACEMENT MEASUREMENTS

To measure the transverse displacement of the cylinder during its oscillations a linear-variable-displacement transducer (LVDT) was installed

CAP. (LBS)	100	250	500	1000	1250
CAT. NO.	425185	420270	420271	420272	420269

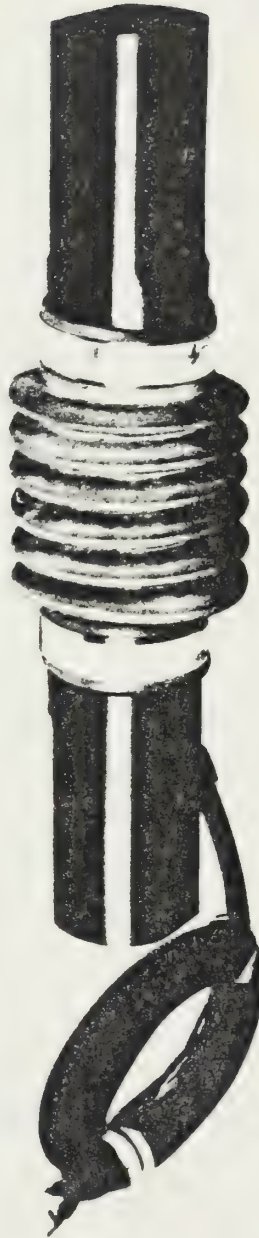
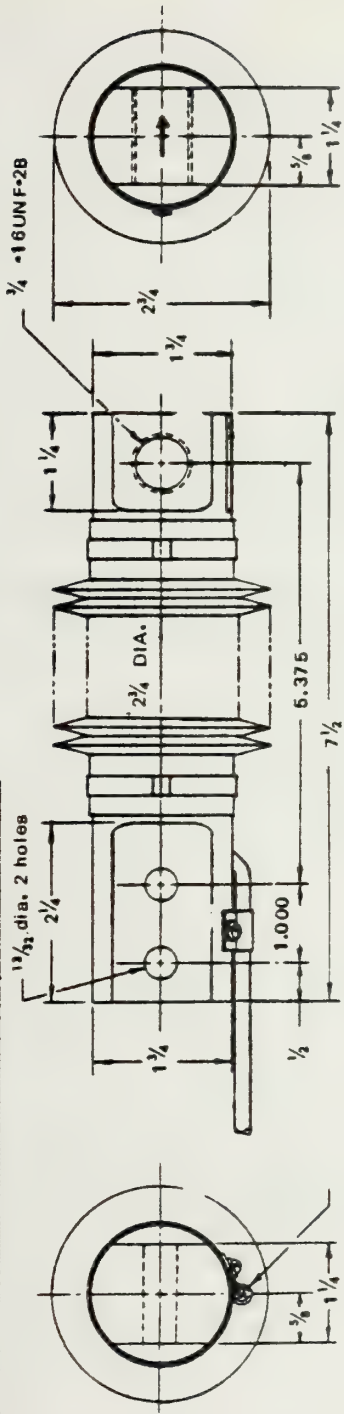
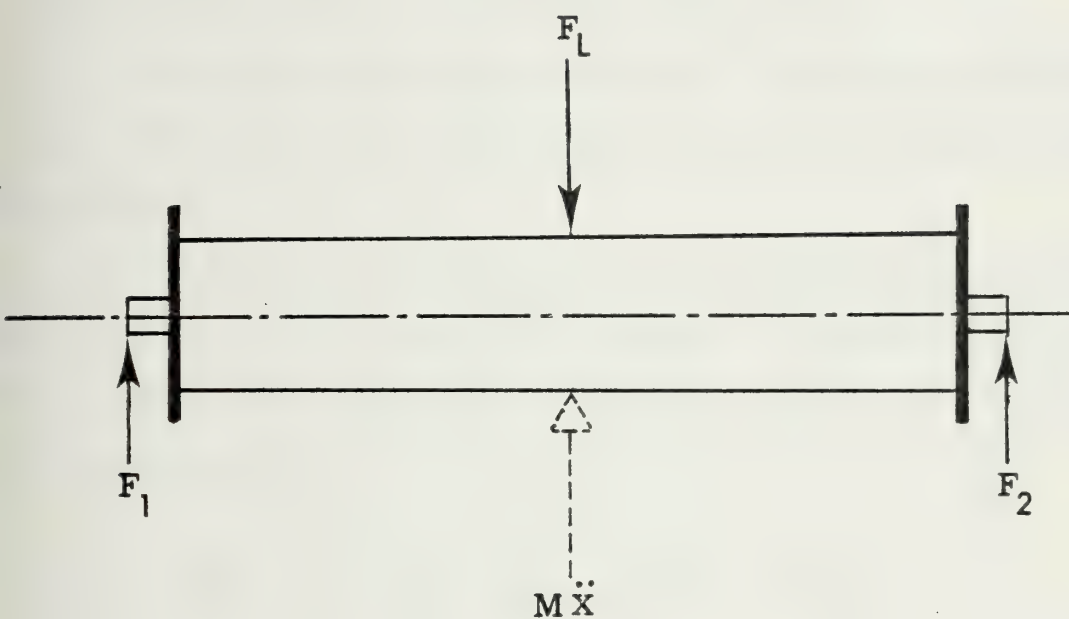


Fig. 17 Force transducer



$$F_L = F_1 + F_2 - M\ddot{x}$$

Fig. 18 Free-body diagram of the test cylinder

between each bearing block and housing. Each LVDT was energized by a six volt DC regulated power supply. The LVDT's provided displacement from the equilibrium position and also helped to verify the simultaneous and in-phase oscillation of both ends of the cylinder (see Figs. 19a through 19c for sample displacement, force, and acceleration traces.

E. ACCELERATION, ELEVATION, OR VELOCITY MEASUREMENTS

It is because of the extreme importance of the accurate measurement of the instantaneous value of these quantities that they are discussed here separately.

It should be noted that the measurement of the amplitude, acceleration, elevation, or the velocity is a matter of interpretation of the signal received from the appropriate transducer in light of one of the following expressions.

$$U_m = \frac{2\pi A}{T}, \quad a_m = \frac{dU}{dt} = \left(\frac{2\pi}{T}\right)^2 A = \frac{2\pi}{T} U_m \quad (3)$$

in which T is the tunnel period and is a constant. In these experiments use was made of a differential pressure transducer with pressure taps located symmetrically on the two legs of the tunnel at an elevation 50 inches below the mean water level, i.e., $H = 38$ in. Applying Bernoulli's equation for unsteady flow between each pressure tap and the instantaneous level of water, it is easy to show that twice the amplitude of the free surface oscillation (virtual amplitude) is given by

$$A_m = 2A_1 = \frac{\Delta P}{1 - \frac{1}{g}\left(\frac{2\pi}{T}\right)^2 H} \quad (4)$$

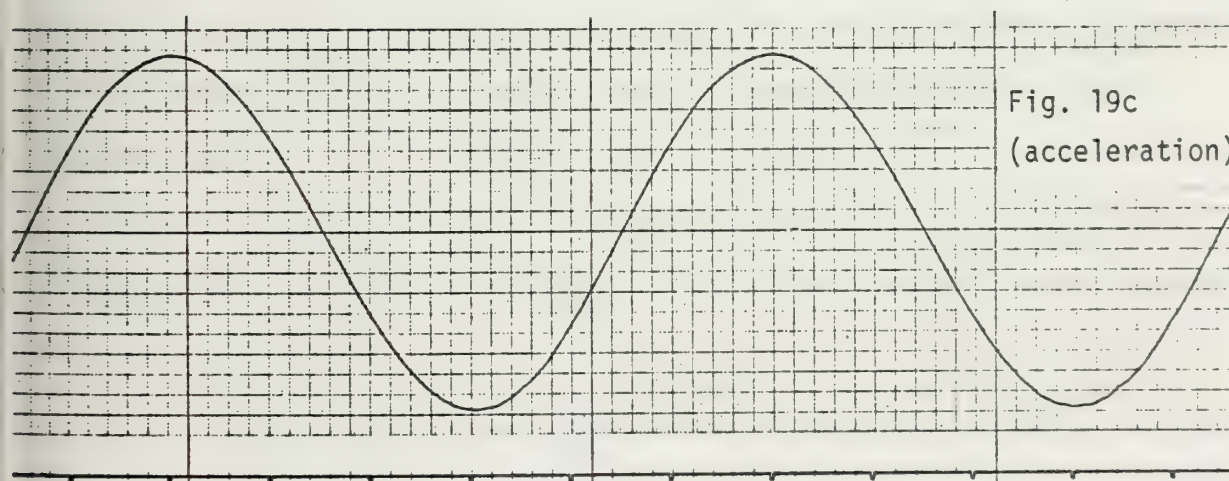
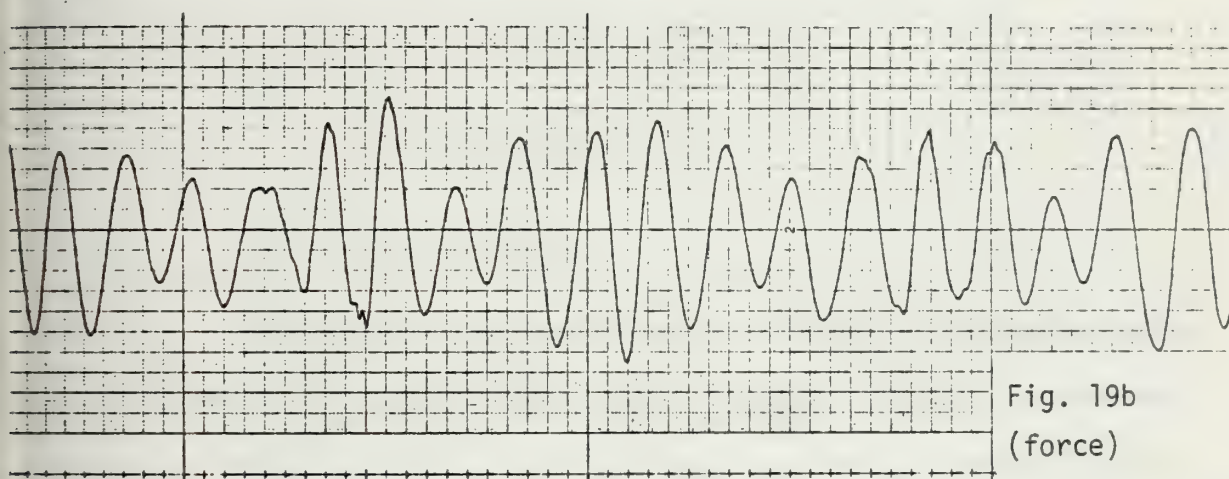
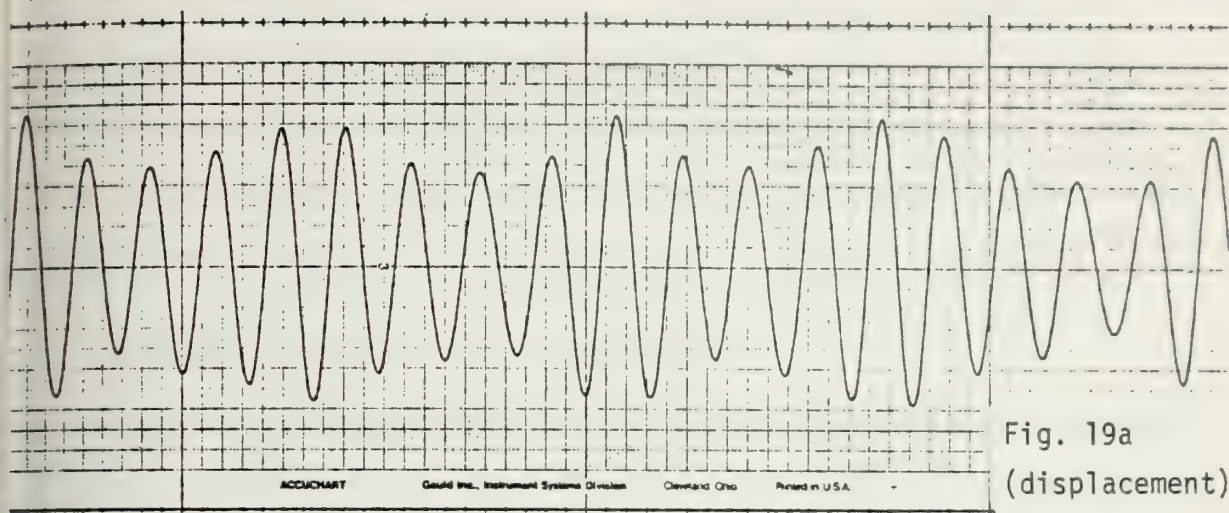


Fig. 19 Sample displacement, force, and acceleration traces

in which g and T are constant and H is kept constant (see Fig. 14). Thus the signal of this transducer yielded the virtual amplitude or maximum velocity in each cycle. It was entirely free from noise or free surface effects. The transducer was calibrated and its linearity checked before each series of experiments.

F. MEASUREMENT OF OTHER BASIC PARAMETERS

The total stiffness of the system, K_s , was determined by suspending a known weight from the center of the cylinder, and the displacement was measured. Then K_s was calculated from the relation

$$K_s = \frac{\text{Force}}{\text{Displacement}} \quad (5)$$

The natural frequency in air, f_{na} , and the natural frequency in water, f_{nw} , were determined by plucking the cylinder and allowing it to oscillate freely in each particular fluid medium. The displacement was recorded on one channel of a three channel recorder. A sample trace is shown in Fig. 19d. Along with the frequencies, the logarithmic decrement and the damping factor, ζ_a , and ζ_w , were determined in air and water, respectively.

Total mass of the system was measured by adding up the mass of the components of the oscillating system. The system mass was also calculated from

$$M = \frac{K_s}{(2\pi f_{na})^2} \quad (6)$$

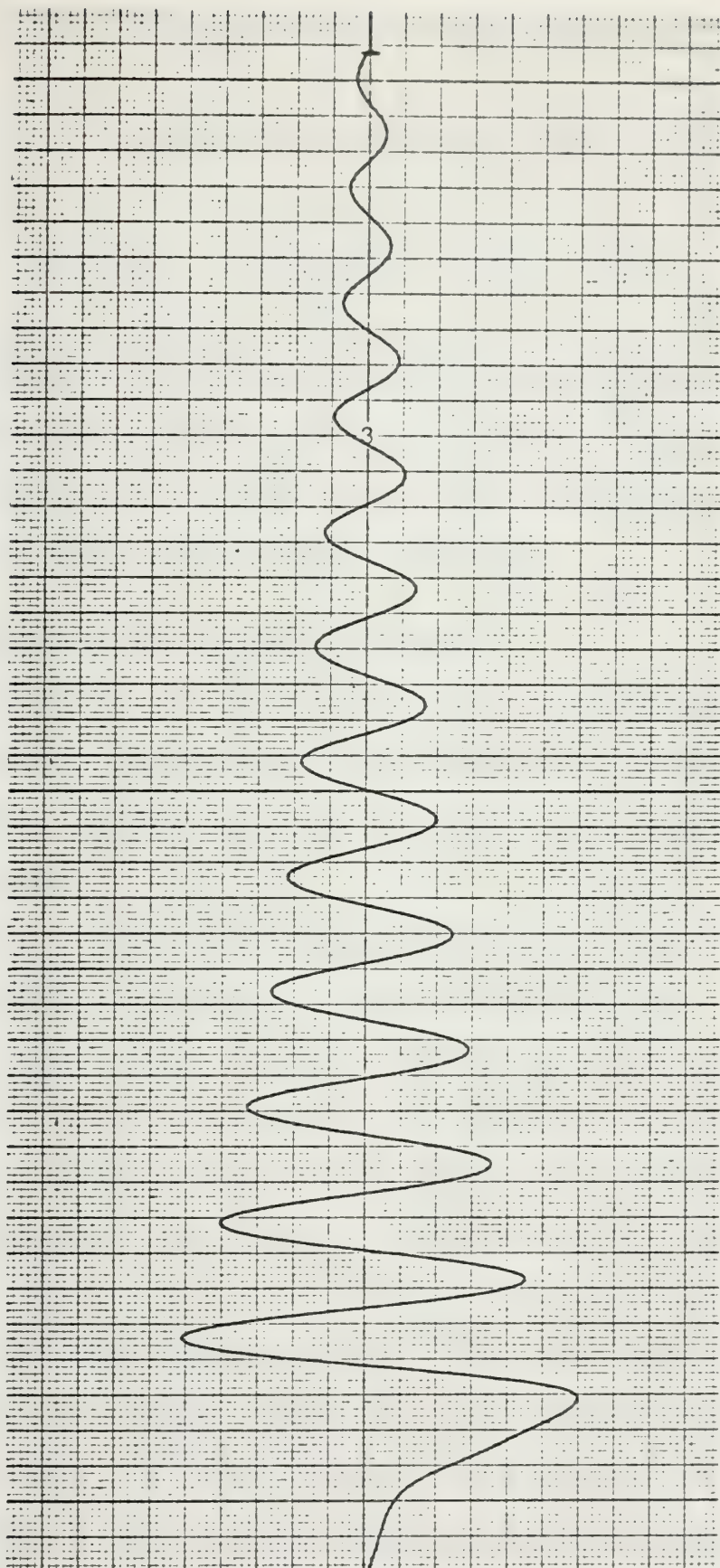


Fig. 19d Displacement trace of a "plucked" cylinder.

to check the correctness of the frequency evaluation. The results were identical.

Added mass M_a of the system was determined from

$$M_a + M = \frac{K_s}{(2\pi f_{nw})^2} = M \left(\frac{f_{nw}}{f_{na}} \right)^2 \quad (7)$$

For the purpose of verification of the measured values, M_a , for the cylinder was computed through the use of the observed values of frequencies and found to be within one tenth of one percent of that given by the potential flow theory and independent experiments.

G. INSTRUMENTATION AND ELECTRONIC CIRCUITRY

The output of each of the two LVDT's, after amplification by a low-gain amplifier, was displayed on an eight-channel recorder as in Fig. 20. One of the two signals was additionally displayed on a three-channel recorder.

The output of the force transducers was separately amplified by a carrier amplifier, filtered by a Krohn-Hite electronic filter and displayed on an eight-channel recorder. Then the two signals were added together by an electronic summing circuit, amplified again by a low level preamplifier and displayed on the eight-channel recorder.

The accelerometer output was similarly amplified by a carrier amplifier and filtered by a low pass filter. This signal was also displayed on the eight-channel recorder. It was then subtracted from the sum of the force signals through the use of a summing-differencing electronic circuit. The resultant signal, representing the fluid force on the cylinder, F_L , was again amplified by a low level preamplifier and

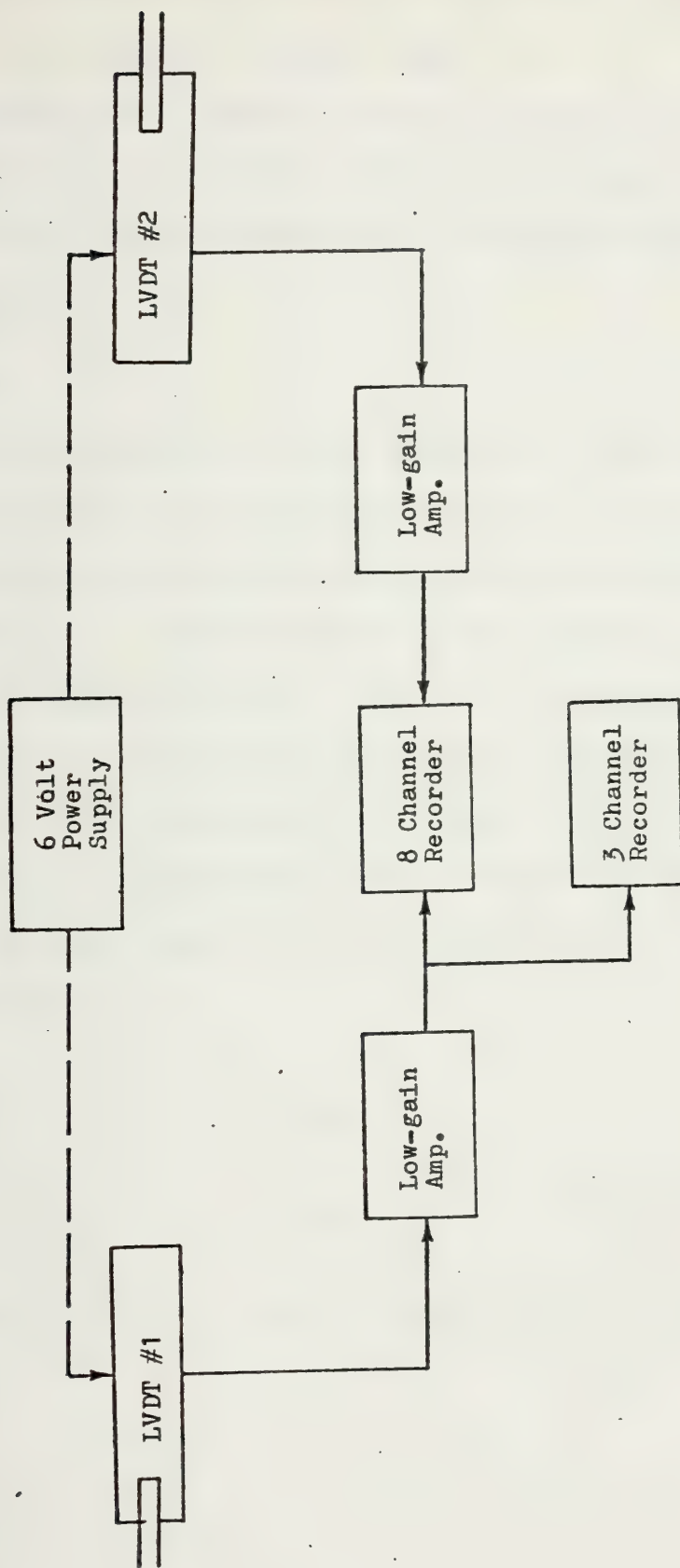


Fig. 20 LVDT (Linear-variable-displacement-transducer) electronic circuit

displayed on both three- and eight-channel recorders. Figure 21 is a block diagram of the circuit described above.

The signal from the differential pressure transducer was of such quality that it did not require any filtering. As shown in Fig. 22, it was amplified by a carrier amplifier and displayed on the two aforementioned recorders.

H. PROCEDURES

Five cylinders were used in these experiments. Additionally two springs, manufactured to the specification desired, were used. The diameter of the springs were sufficiently large to work freely over the 2.5 in. diameter rod. The coil diameter of the springs was 0.255 inches and were made of carbon steel wire. Table 3 is a condensed list of the cylinders used, kind of force measured, surface condition, and spring constant employed in the experiment. The number of (x) in each box indicates the number of experiments performed under that particular conditions. The check mark under the spring-constant box indicates the kind of spring used.

Table 3

Diam. in.	LIFT		DRAG		K_s (Lb/ft)	
	Smooth	Rough	Smooth	Rough	418	392
2.	X				✓	
2.5		X	X		✓	
3.	XXX	X	X	X	✓	
4	XX	XX			✓	✓
5	XXX		XX		✓	

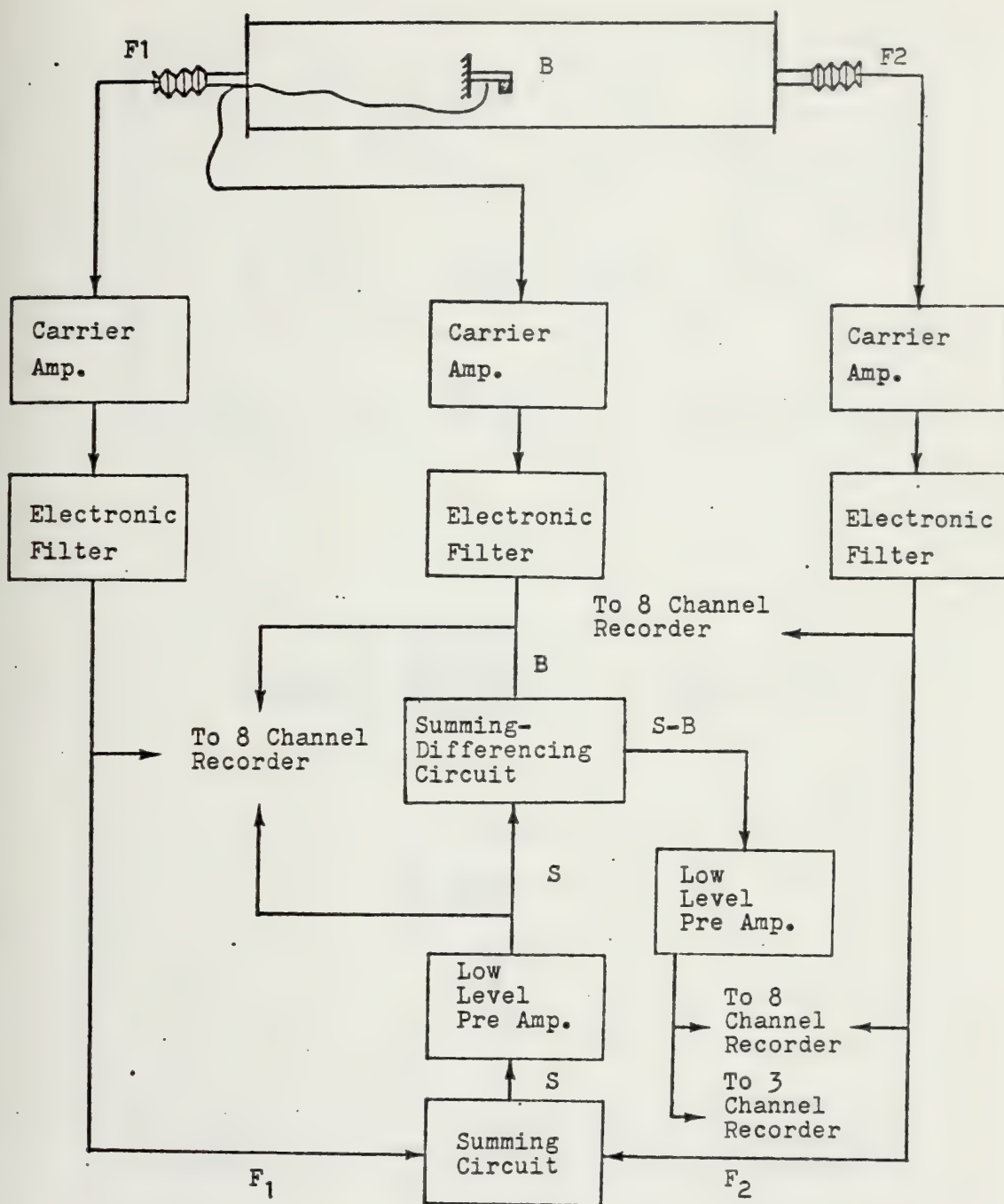


Fig. 21 Force and accelerometer electronic circuit

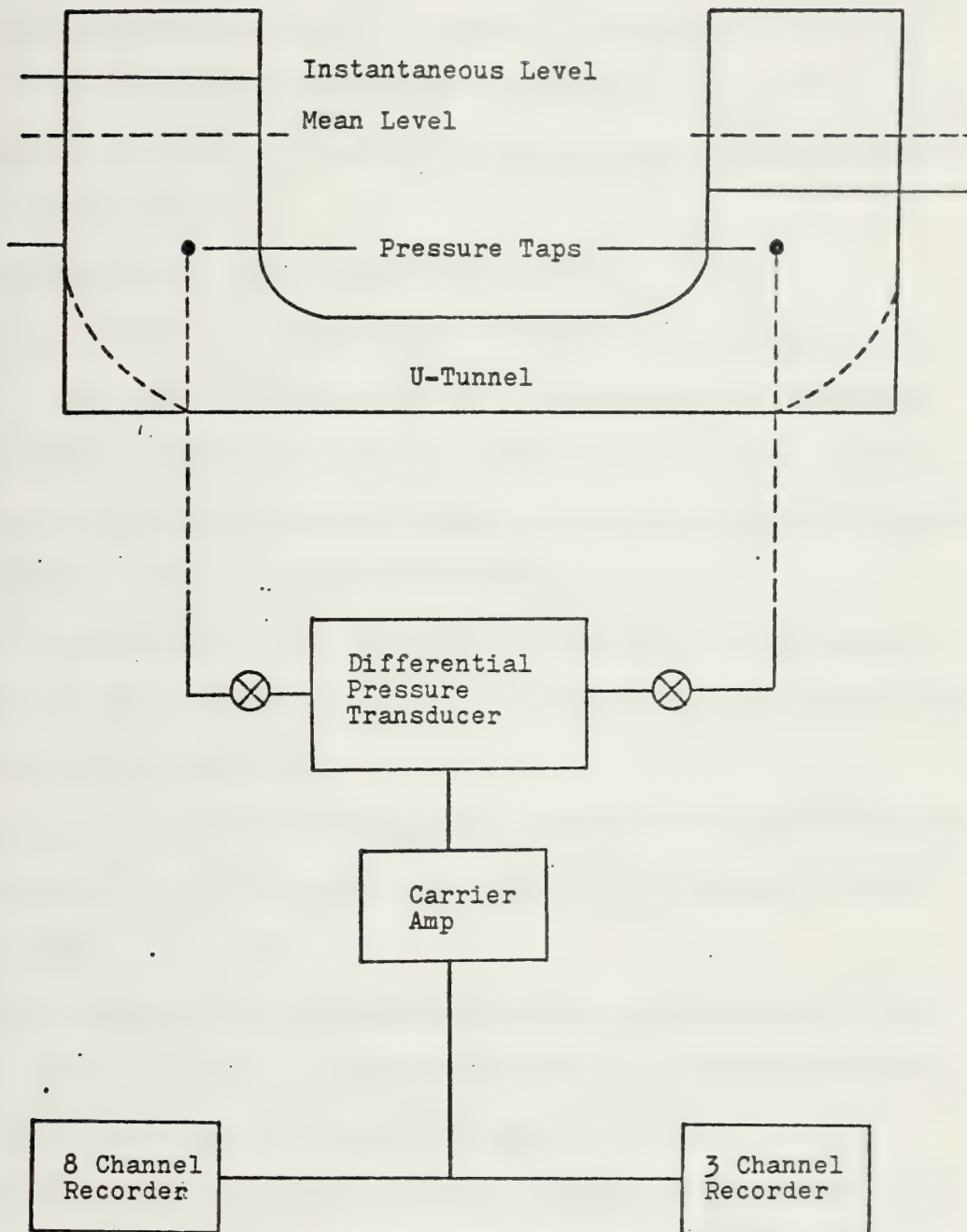


Fig. 22 Differential pressure transducer and circuitry

In some of the experiments it was found advantageous to increase the weight of the oscillating system by mounting rectangular lead blocks to the side of the oscillating bearing blocks away from the cylinder mountings. Beside adding mass and therefore lowering the natural frequency, it was discovered that adding the weight at this location also served to distribute the load better on the bearings, thereby reducing friction and damping.

Procedures for an experiment were as follows:

1. The cylinder was aligned with the tunnel by adjusting the bearings. The sensitivities of the force transducers were matched by hanging a known weight from the exact center of the cylinder. At the same time a calibration factor was determined by measuring the displacement and comparing it with the output of the LVDT.
2. The accelerometer was calibrated by plucking the cylinder and adjusting the amplifier gain until the fluid force in air was nulled to within 1.5 percent deviation.
3. f_{na} and ζ_a were also determined by plucking the cylinder in air from the trace of cylinder oscillation on the three-channel recorder (see Fig. 19d).
4. The weight was then suspended from the cylinder center, this time for the measurement of a calibration factor in lb/mm of the three-channel-recorder output at a particular gain setting.
5. The U-tunnel and cylinder-support housing were again filled to the top of the test section, and all air was vented from the housings.
6. The cylinder was then lowered to the center of the test section by simultaneously lowering both sets of spring yokes, each the same

number of turns, to compensate for the buoyant force on the displaced cylinder.

7. The cylinder was plucked, and f_{nw} and ζ_w were calculated from the free-oscillation traces.

8. The access to the horizontal test section above the cylinder, through which the weights were lowered to the cylinder, was closed. The tunnel was filled with water from a sump tank located near the apparatus or from the city water.

9. The differential-pressure transducer was bled of any entrained air and its calibration verified.

10. Variable speed motor control, driving the air valve, was adjusted to yield a period exactly equal to that of the tunnel.

11. Butterfly-valve on top of the air chamber and the gate-valve on top of the air control box were fully closed. The gate valve at the outlet of the fan was fully opened, and the butterfly-valve on top of the other leg was fully opened before the fan was turned on. With this arrangement the largest amplitude of the tunnel oscillation was obtained.

12. Several tunnel oscillations were allowed to pass in order to achieve a steady state tunnel oscillation.

13. Amplifier gain settings or calibration factors were recorded on the chart paper as they were changed as desired.

14. Several cycles of oscillation were recorded at a chart speed of 2 and 10 mm/sec to ensure that a steady state is reached for that particular amplitude of the tunnel.

15. Several runs were made at a chart speed of 25 mm/sec.

16. The position of the gate valves on the air control box was changed to achieve a new amplitude of the tunnel oscillation.

17. Steps 14 through 16 were repeated.

18. At the end of each experiment, f_{nw} , ζ_w , f_{na} , and ζ_a were measured to verify the initial values.

In measuring the forces in the in-line direction, steps 1 through 4 were repeated. The force transducers were turned 90 degrees and pinned to measure the in-line force. Then the steps 5 through 17 were followed as before.

III. METHOD OF DATA ANALYSIS

A. INTRODUCTION

The recorded data consisted of the instantaneous values of the transverse displacement of the cylinder, lift force, and the acceleration of flow. Figures 19a through 19c show a sample of the traces of the above variables during two cycles of flow oscillation.

The data were subjected to extensive analysis in terms of the peak amplitudes of the force and cylinder displacement, their root-mean-square values, Fourier analysis, spectral analysis, Morison's equation [96], and finally, in terms of Duhamel's superposition integral.

B. ANALYSIS OF THE PEAK AMPLITUDES

The parameters D , K_s , f_{na} , f_{nw} , ζ_a , and ζ_w were recorded for each run. Then the peak values of the transverse force (lift force), F_{LM} ; peak values of the cylinder displacement, X_M ; and the periods T_f and T_c for the force and displacement, respectively, were evaluated over each half cycle of flow oscillation. Subsequently, the variables A_m , U_m , K , X_M/D , $U_m/f_n D$, and C_{LM} were calculated for further study. The coefficient C_{LM} is the peak lift coefficient and is given by

$$C_{LM} = \frac{F_{LM}}{\frac{1}{2} \rho U_m^2 L D} \quad (8)$$

where ρ is the density of the fluid; and L , the length of the cylinder.

C. DIGITIZATION OF THE DATA

The evaluation of the root-mean-square values of the various parameters, Fourier analysis, spectral analysis, Duhamel's superposition integral, and the use of Morison's equation required the careful digitization of the data.

In order to maintain a proper relationship between the phase and amplitude of a given variable a suitable frequency of digitization or digitization interval had to be chosen. Otherwise aliasing could occur which is a potential source of error in an analog to digital data conversion [103]. The maximum frequency resolvable is called the Nyquist frequency and is defined as

$$f_{NY} = \frac{1}{2\Delta t} \quad (9)$$

where Δt is the interval of digitization. The frequencies in the original data above this cut off frequency are folded back into the frequency range from zero to f_{NY} in an accordion pleated fashion. Therefore, in order to choose a suitable Δt the maximum frequency encountered in the experiments had to be known. The observation of the analog records showed that the highest frequencies encountered were in the range of 4 to 6 Hz.

In general, it is a good rule to select f_{NY} to be one-and-a-half or two times greater than the maximum anticipated frequency. Therefore, a Nyquist frequency of 10 Hz was chosen from which an interval of digitization of 0.05 seconds resulted. This corresponded to a 1.25 mm interval on the chart at its speed of 25 mm/sec. Any digitization interval below this value would have given correct results. The smallness of this interval is defined by the economy of the effort.

In case of the use of data in a spectral analysis the number of digitized data had to be N which is defined as

$$N = 2 \times 2^p \quad p = 1, 2, 3, 4, \dots$$

This consideration and others such as the ease of tapering led to an interval of digitization of 1.073 mm, equivalent to $\Delta t = 0.043$ seconds. This time interval is lower than the conservative value of 0.05 seconds.

The length of the records were different but never less than three cycles of tunnel oscillation which is about 18 seconds. This resulted in a resolution of $1/18 = 0.056$ Hz. The digitized records were long enough to satisfy all the assumptions inherent in the analysis.

The analog traces at a fixed tunnel amplitude were digitized by means of a Hewlett-Packard digitizer model 9874A which was linked to a Hewlett-Packard 9845A computer. The movement of a cursor by hand over the trace generated digitized coordinates of a given curve. The information was then stored either in files on tapes for use with the programs written for the HP computer or punched on cards to be used with an I.B.M. 360 computer.

D. EVALUATION OF THE ROOT-MEAN-SQUARE VALUES

The use of digitized data together with a suitable computer program yielded the rms values of the lift coefficient, $(C_L)_{rms}$, and the relative cylinder displacement, $(X)_{rms}/D$.

The record length for the evaluation of the rms values was at least three cycles of tunnel oscillation. A careful examination of the data has shown that a record length of three cycles was more than sufficient.

E. SPECTRAL ANALYSIS

As noted earlier, the nature of the lift force and cylinder-displacement traces were quite regular, particularly in the synchronization range. The quasi-harmonic shape of the said traces required a deterministic rather than random analysis. However, a knowledge of the frequency content of the oscillations was of primary importance in determining the modulations in the amplitude and frequency of the oscillation of the lift force and cylinder displacement. Evidently, only through spectral analysis can one decompose the force and displacement into their fundamental and subharmonics and draw conclusions regarding the energy content of each harmonic.

The following is a condensed description of the methodology.

If $x(t)$ is a periodic function of time t , with a period T_s , then it could always be expressed as an infinite trigonometric series of the form

$$x(t) = a_0 + \sum_{n=1}^{\infty} \left[a_n \cos\left(\frac{2\pi n t}{T_s}\right) + b_n \sin\left(\frac{2\pi n t}{T_s}\right) \right] \quad (10)$$

where

$$a_0 = \frac{1}{T_s} \int_0^{T_s} x(t) dt \quad (11)$$

$$a_n = \frac{2}{T_s} \int_0^{T_s} x(t) \cos\left(\frac{2\pi n t}{T_s}\right) dt \quad (12)$$

$$b_n = \frac{2}{T_s} \int_0^{T_s} x(t) \sin\left(\frac{2\pi n t}{T_s}\right) dt \quad (13)$$

The mathematical conditions for the convergence of Eq. (10) are extremely general and cover practically every conceivable engineering situation [104].

The Fourier series is a useful tool for determining the frequency content of a time-varying signal. However, the Fourier series always require a periodic time function. To overcome this shortcoming, Fourier evaluated his series as he let the period of the waveform approach infinity. Then the Fourier series given by Eq. (10) turns into a Fourier integral and Fourier coefficients represented by Eqs. (11), (12) and (13) become continuous functions of frequency, called Fourier transforms. Therefore, a Fourier integral may be regarded as the formal limit of a Fourier series as the period tends to infinity. It is customary to write the Fourier series in their complex form. Then one introduces the Fourier transforms defined by

$$F_x(f) = \int_{-\infty}^{\infty} x(t) e^{-i2\pi f t} dt \quad (\text{Forward Fourier transform}) \quad (14)$$

$$x(t) = \int_{-\infty}^{\infty} F_x(f) e^{i2\pi f t} df \quad (\text{Inverse Fourier transform}) \quad (15)$$

where

$$e^{\pm i2\pi f t} = \cos(2\pi f t) \pm i \sin(2\pi f t),$$

is known as the Kernel of the Fourier transform. Now $F_x(f)$ contains the amplitude and phase information at every frequency present in $x(t)$ without demanding that $x(t)$ be periodic. If the time history $x(t)$ of a sample function is not periodic it cannot be represented by a discrete Fourier series. Furthermore, for a stationary process, $x(t)$ goes on forever and the necessary condition

$$\int_{-\infty}^{\infty} |x(t)| dt < \infty \quad (16)$$

is not satisfied. Unless special precautions are taken, it is not therefore possible to evaluate the Fourier transform of $x(t)$ in order to obtain information about the frequency composition of the process. This difficulty can be overcome by Fourier analysing, not the sample function of the process itself, but rather its autocorrelation function $R_x(\tau)$.

The logic behind this approach is that the autocorrelation function gives information about the frequencies present in a random process indirectly. If the zero value of the process $x(t)$ is normalized (or adjusted) so that the mean value of the process is zero and it has no periodicity, then the autocorrelation function satisfies Eq. (16) and its Fourier transform could be written as

$$S_x(f) = \int_{-\infty}^{\infty} R_x(\tau) e^{-i2\pi f\tau} d\tau \quad (17)$$

The $S_x(f)$ is called mean square spectral density, energy density, or power spectrum. The last name originated from electrical engineering

because it is a measure of the power loss in a resistor. It can be shown that $S_x(f)$ is a real, even function of frequency, f and it is always positive [103, 105].

One sided spectral density is defined as

$$G_x(f) = 2 S_x(f) \quad (18)$$

It can be shown that

$$\sigma_x^2 = \int_0^{\infty} G_x(f) df \quad (19)$$

where σ_x^2 is the variance of the process [106].

The one sided cross spectrum is found from

$$G_{xy}(f) = 2 \int_0^{\infty} R_{xy}(\tau) e^{-i2\pi f\tau} d\tau \quad (20)$$

or

$$G_{xy}(f) = C_{xy}(f) - i Q_{xy}(f) \quad (21)$$

where $C_{xy}(f)$ is the co-spectrum. It is the real and in phase component. The $Q_{xy}(f)$ is the quad-spectrum and forms the imaginary part or out of phase component of $G_{xy}(f)$.

From Eq. (21), the phase difference between the process x and y is found to be

$$\alpha_{xy} = \tan^{-1} \frac{Q_{xy}(f)}{C_{xy}(f)} \quad (22)$$

If a finite record of length T_s is used, it can be shown [103] that an estimate of the cross-spectral density is given by

$$\hat{G}_{xy}(f, T_s) = 2 \frac{Y(n) X^*(n)}{\Delta f} \quad (23)$$

where X and Y represent the finite Fourier transforms of x and y respectively and X^* is the complex conjugate of X . Then an estimate for spectral density of a stationary process of finite length would be

$$\hat{G}_x(f, T_s) = 2 \frac{|X(n)|^2}{\Delta f} \quad (24)$$

where

$$X(n) = \frac{1}{2}(a_n - ib_n) \quad (25)$$

in which a_n and b_n are the Fourier coefficients given by Eqs. (11), (12), and (13). If N digitized data are used to evaluate a_n and b_n numerically then the computation time is proportional to N^2 . Even with high speed computers, computation of discrete Fourier transforms requires excessive machine time for large N . In 1965 Cooley and Tukey published their mathematical algorithm [107] which has become known as the "fast Fourier transform". The fast Fourier transform (F.F.T.) is a computational algorithm which reduces the computing time of a_n and b_n to a time proportional to $N \log N$. The idea of F.F.T. was first discovered by

Runge [108, 109] in 1903 who described essentially the computation of the F.F.T. algorithm as we know it today.

Any spectral estimate has only two degrees of freedom and the confidence interval turns out to be so large that it does not have any statistical meaning. Therefore, one deduces that the evaluation of only one $G_x(f, T_s)$ for a record length does not have any significance. There are several methods to increase the number of degrees of freedom. A simple method is to create an ensemble of records each of which has a record length T_s . If the length of the original record is long enough one can divide the record into k records each T_s seconds long. Now ensemble averaging improves the degrees of freedom, which in turn improves confidence, or spectral reliability of the spectral estimate then

$$\hat{G}(f, T_s) = \frac{1}{k} \sum_{k=1}^k \hat{G}(f, T_s, k) \quad (26)$$

where k is the number of sample function forming the ensemble and the degrees of freedom for each spectral estimate is now $\lambda = 2k$. The true spectrum is found as

$$G(f) = \lim_{\substack{T_s \rightarrow \infty \\ k \rightarrow \infty}} \frac{1}{k} \sum_{k=1}^k \hat{G}(f, T_s, k) \quad (27)$$

The use of this method requires that the process be ergodic. This means that the process must be stationary, i.e., for any sample function k , time average of the mean, autocorrelation and all other statistical averages do not differ when computed over different sample functions.

As it was mentioned earlier, the observation of the force and cylinder displacement traces revealed that the phenomenon repeated itself at almost every three cycles of flow oscillation for a given Keulegan-Carpenter number. This justified the assumption of ergodicity for the process.

Two or more sample functions each of which comprising at least three cycles of tunnel oscillations were used to evaluate spectral density of the process at a constant Keulegan-Carpenter number.

A flow chart of the program used to evaluate the spectral density is given in Fig. 23. The data was first "detrended" to remove any linear trend from the process. Then a cosine taper window was used to reduce the leakage and smoothen discontinuities at the "joints" at the two ends of the records.

In addition to the spectral density for each data set, other statistical averages such as variance, standard deviation, skewness, and kurtosis were estimated. Integration of spectral density, using Eq. (19), was performed to compare the result against variance which was evaluated directly from digitized data. The closeness of these two was also a good check for the goodness of spectral estimate.

F. IN LINE FORCE

The drag coefficient C_d and the inertia coefficient C_m for the in-line force were evaluated in order to determine the effect of the cross-flow oscillation of the cylinder on the in-line force. Data reduction for the forces in-line with the direction of the ambient flow was based on Morison's equation [96] and the Fourier analysis. The in-line force, consisting of the drag force F_d and the inertia force F_i , is assumed

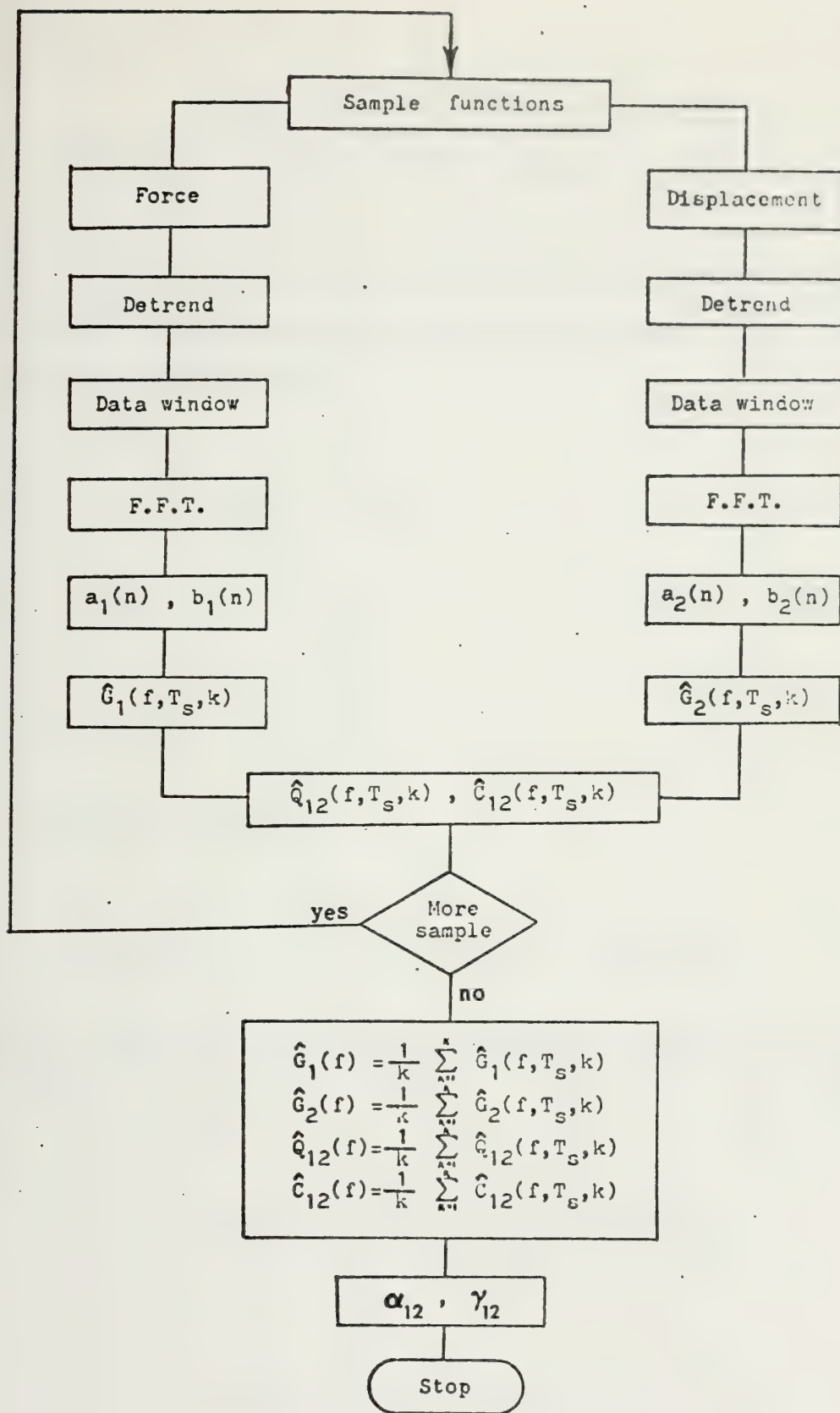


Fig. 23 Flow chart of the computer program for the evaluation of the spectral density.

to be given by

$$F = F_d + F_i = \frac{1}{2} C_d L D \rho |U| U + \frac{1}{4} C_m L D^2 \pi \rho \frac{dU}{dt} \quad (28)$$

in which C_d and C_m represent respectively the drag and inertia coefficients and U is the instantaneous velocity of the ambient flow. For an harmonic flow represented by

$$U = -U_m \cos \theta \quad (29)$$

where

$$\theta = \frac{2\pi t}{T},$$

equation (28) may be written as

$$\frac{F}{\frac{1}{2} \rho U_m^2 D L} = -C_d |\cos \theta| \cos \theta + C_m \frac{\pi^2}{K} \sin \theta \quad (30)$$

The Fourier averages of C_d and C_m were evaluated from (30) by Keulegan and Carpenter as [111]

$$C_d = -\frac{3}{4} \int_0^{2\pi} \frac{F_m}{\rho U_m^2 D L} \cos \theta d\theta \quad (31)$$

$$C_m = \frac{2\pi^3}{K} \int_0^{2\pi} \frac{F_m}{\rho U_m^2 D L} \sin \theta d\theta \quad (32)$$

in which F_m represents the measured force.

The in-line and lift forces were measured by two force transducers at each end of the cylinder while it was oscillating in the transverse direction. The three channel recorder with three strip chart paper was used to record forces and the flow oscillation. Figures 24 and 25 show sample in-line and transverse force traces. The in-line force was then digitized every 0.1 seconds and the digitized data, along with other parameters such as D , L , ν , and A_m , were fed into a computer program to evaluate C_d and C_m from Eqs. (31) and (32).

G. DUHAMEL'S SUPERPOSITION INTEGRAL

One of the methods used to investigate the relationship between the instantaneous force and displacement in a linear, oscillating, system is the so-called Duhamel's superposition integral. Assume that the oscillation of the cylinder is represented by

$$M \ddot{X} + 2 M \zeta \omega_n \dot{X} + k_s X = F_L(t) \quad (33)$$

where $F_L(t)$ is the instantaneous lift force. One can imagine that the force $F_L(t)$ is composed of a series of impulses [111]. Then through the use of the convolution or superposition integral one can evaluate the instantaneous response of the system to the force $F_L(t)$ from [111]

$$\begin{aligned} X = & \left(X_0 - \frac{1}{M\omega_n} \int_0^t \frac{F(t) e^{-\zeta\omega_n(t-t_v)}}{\sqrt{1-\zeta^2}} \sin \sqrt{1-\zeta^2} \omega_n t_v dt_v \right) \cos \omega_n t \\ & + \left(\frac{\dot{X}_0}{\omega_n} + \frac{1}{M\omega_n} \int_0^t \frac{F(t) e^{-\zeta\omega_n(t-t_v)}}{\sqrt{1-\zeta^2}} \cos \sqrt{1-\zeta^2} \omega_n t_v dt_v \right) \sin \omega_n t \quad (34) \end{aligned}$$

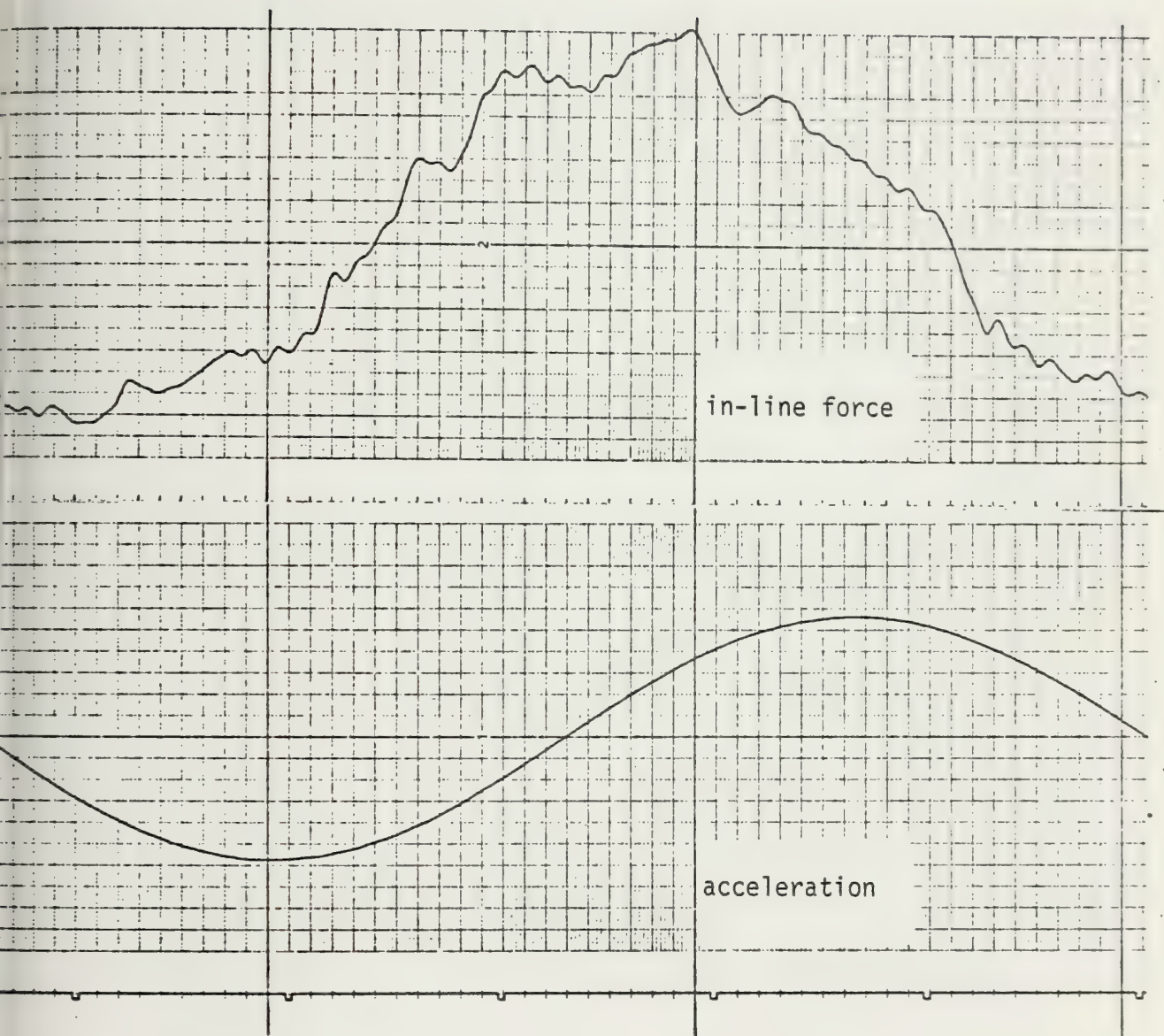


Fig. 24 A sample of the in-line force trace.

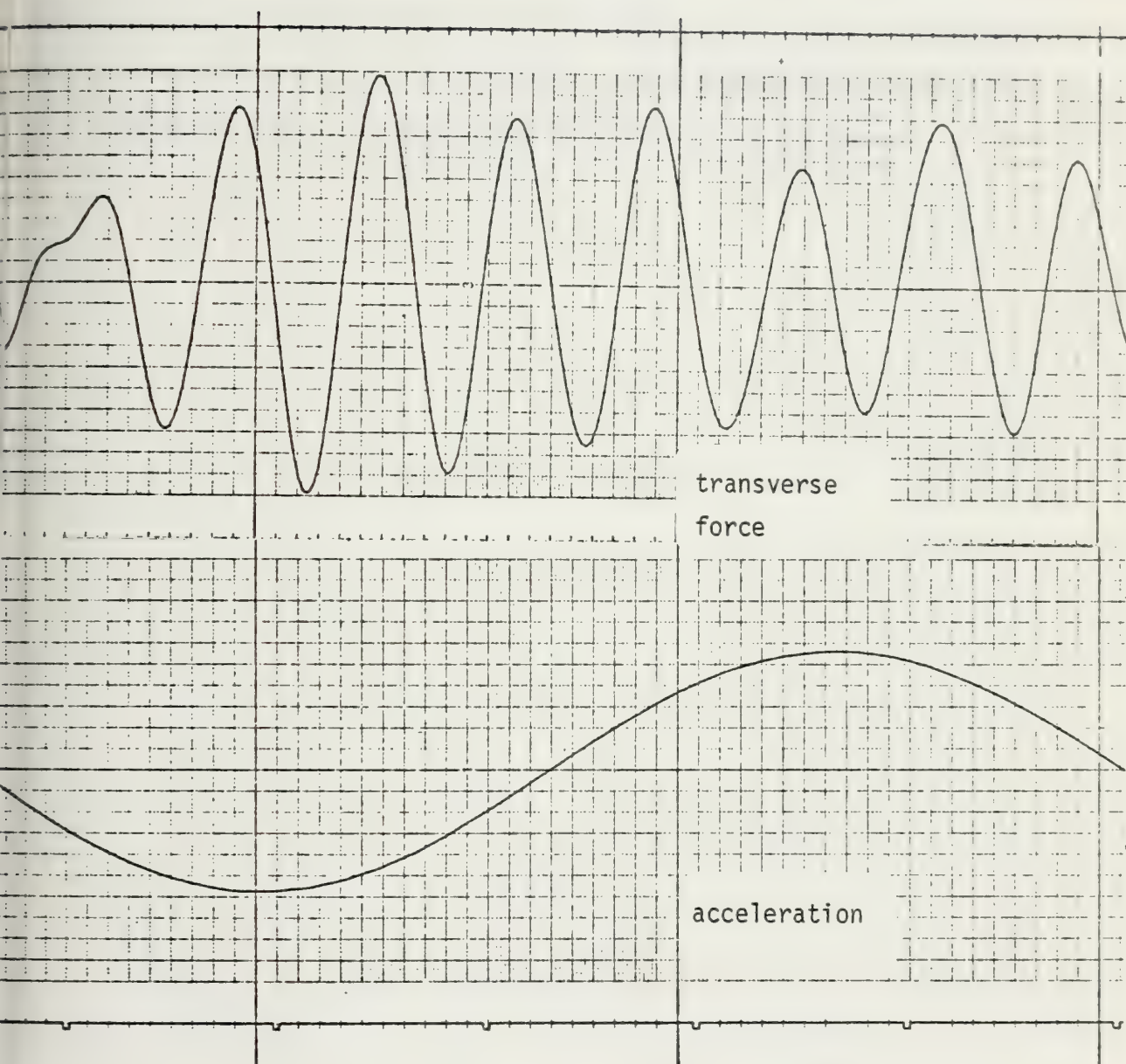


Fig. 25 A sample of the transverse force trace.

in which X_0 and \dot{X}_0 denote the initial condition and t_v is the variable time.

For this purpose, the lift force trace was digitized every .02 seconds and used as the input to Eq. (34) along with other parameters characterizing the oscillating system such as ζ , D , M , etc. A computer program then performed the calculations. This computation served also as a confirmation for the consistency of the lift force data.

IV. RESULTS

A. INTRODUCTION

The experimental results will now be reported, showing first the dependence of the relative displacement and lift coefficient on the flow parameters, and, secondly, the analysis of the data through the use of the Fourier analysis, spectral analysis, and Duhamel's integral. Lastly, the in-line force acting on transversely oscillating cylinders will be presented.

B. REPRESENTATIVE RELATIVE DISPLACEMENTS AND LIFT COEFFICIENTS

The variation of the relative displacement X_M/D as a function of $K = U_m T/D$, $U_r = U_m/f_{nw} D$, f_f/f_{nw} , and f_c/f_{nw} is shown in Figs. 26 through 29 for a 3 in. smooth cylinder. Data for other representative smooth and rough cylinders are shown in Figs. 30 through 45 in Appendix A. In the foregoing, U_m represents the maximum velocity of flow during a cycle; f_f , the frequency of the transverse-force oscillations between two successive peaks; f_{nw} , the natural frequency of the cylinder in still water; and f_c , the frequency of the cylinder oscillations. The relative roughness for all rough cylinders was $k_c/D = 1/100$ where k_c is the average sand-roughness height.

The variation of the rms values of X/D with K , U_r , f_f/f_{nw} , and f_c/f_{nw} for the 3 in. smooth cylinder is shown in Figs. 46 through 49. Similar data for other cylinders are shown in Figs. 50 through 65 in Appendix B. The peak amplitudes of the lift coefficient are shown in Figs. 66 through 69 as a function of K , U_r , f_f/f_{nw} , and f_f/f_c for the 3 in. smooth cylinder.

Data for other cylinders are shown in Figs. 70 through 85 in Appendix C. The rms values of C_L for the 3 in. cylinder are shown in Figs. 86 through 89 for the 3 in. cylinder. The remainder is shown in Figs. 90 through 105 in Appendix D.

The data presented in the figures cited above exhibit certain characteristics which will be discussed below. Firstly, all the plots showing the peak-amplitude values of the relative amplitude and the lift coefficient show considerable scatter. This is partly due to the amplitude and phase modulations in the force and displacement traces and partly due to the inherently random nature of the vortex shedding in steady and harmonic flow about stationary and oscillating cylinders. The rms values of the displacement and force exhibit much smoother variation with respect to the parameters K , U_r , f_f/f_{nw} , and f_f/f_c . The data span a broad range of Keulegan-Carpenter numbers. Within this range the relative amplitude shows one dominant and, at times, one secondary peak. For example, Fig. 26 shows that X_M/D reaches a maximum value of 0.27 at a Keulegan-Carpenter number of about 55. A second and considerably smaller peak occurs at about $K = 135$ (see Figs. 26 and 46). The region in which the first peak occurs is called the primary region of synchronization and the region in which the secondary peak occurs is called secondary synchronization. A tertiary synchronization region observed in steady flow past oscillating cylinders has not been found in the harmonically oscillating flow. Clearly the primary synchronization region extends over a small range of K values. Outside the synchronization region the cylinder continues to oscillate at small amplitudes as a body subjected to forced oscillations by shedding of the vortices. The dependence of the primary synchronization region on

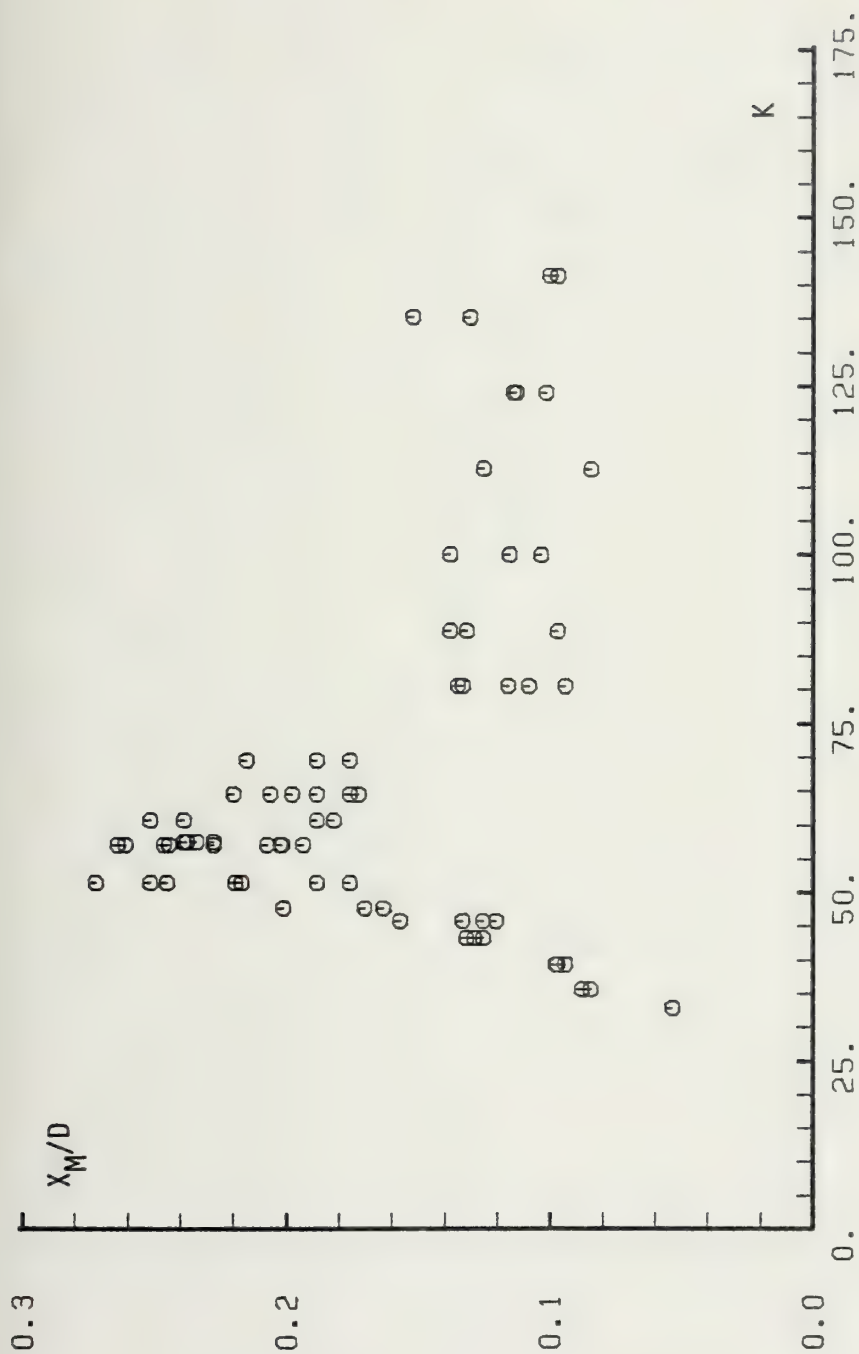


Fig. 26 X_M/D versus K for 3 in. smooth cylinder, $\zeta = 0.052$.

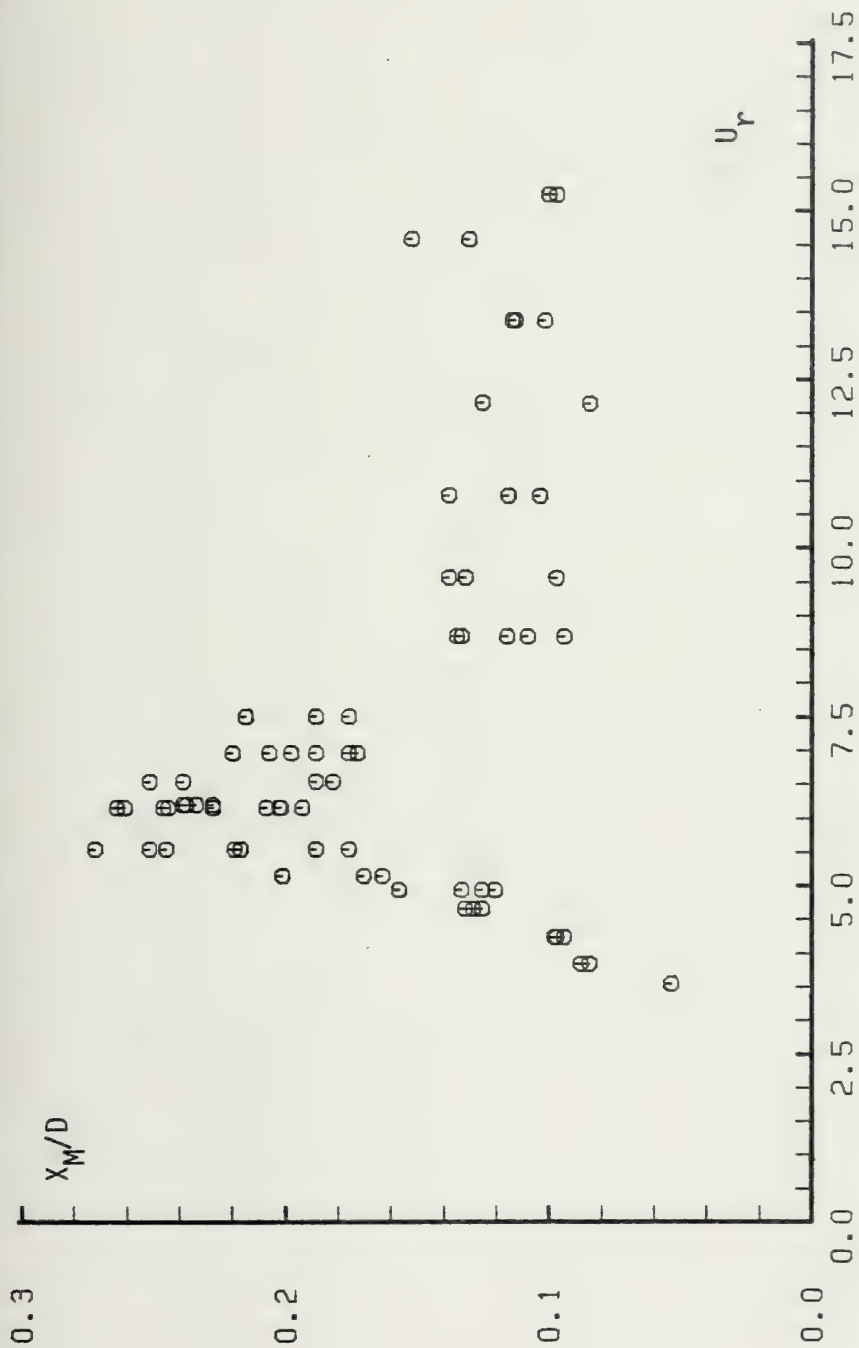


Fig. 27 X_M/D versus U_r for 3 in. smooth cylinder, $z = 0.052$.

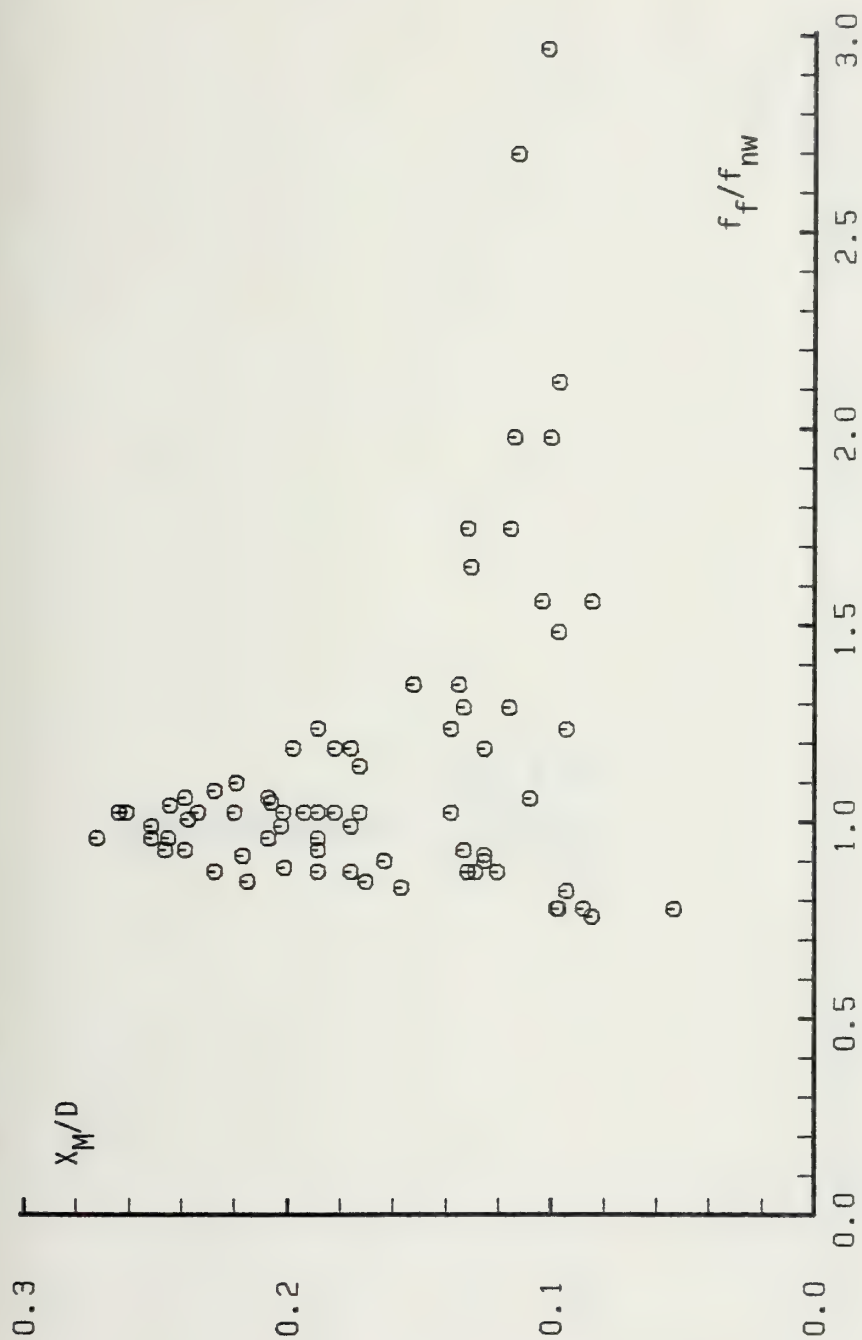


Fig. 28 X_M/D versus f_f/f_{nw} for 3 in. smooth cylinder, $\zeta = 0.052$

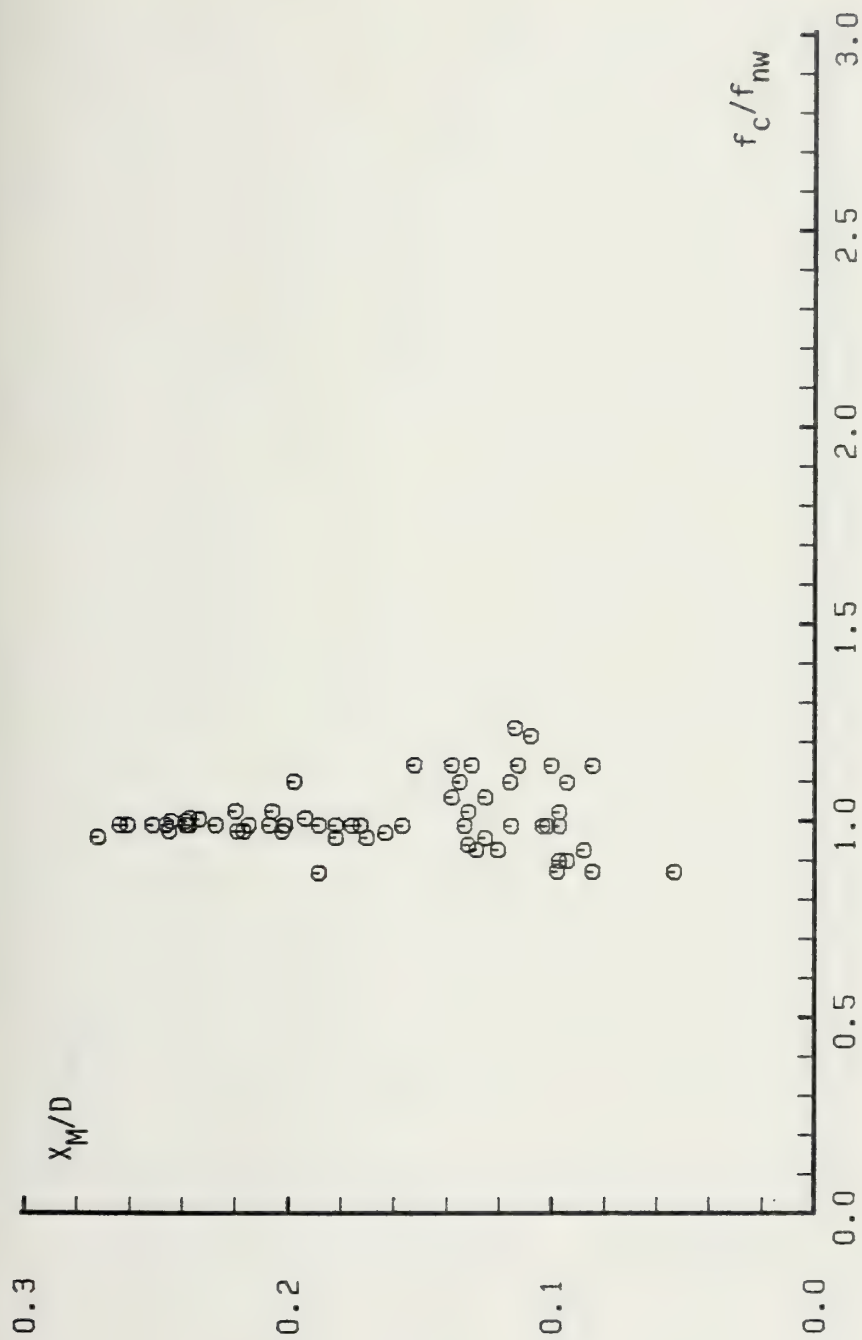


Fig. 29 X_M/D versus f_c/f_{nw} for 3 in. smooth cylinder, $z = 0.052$

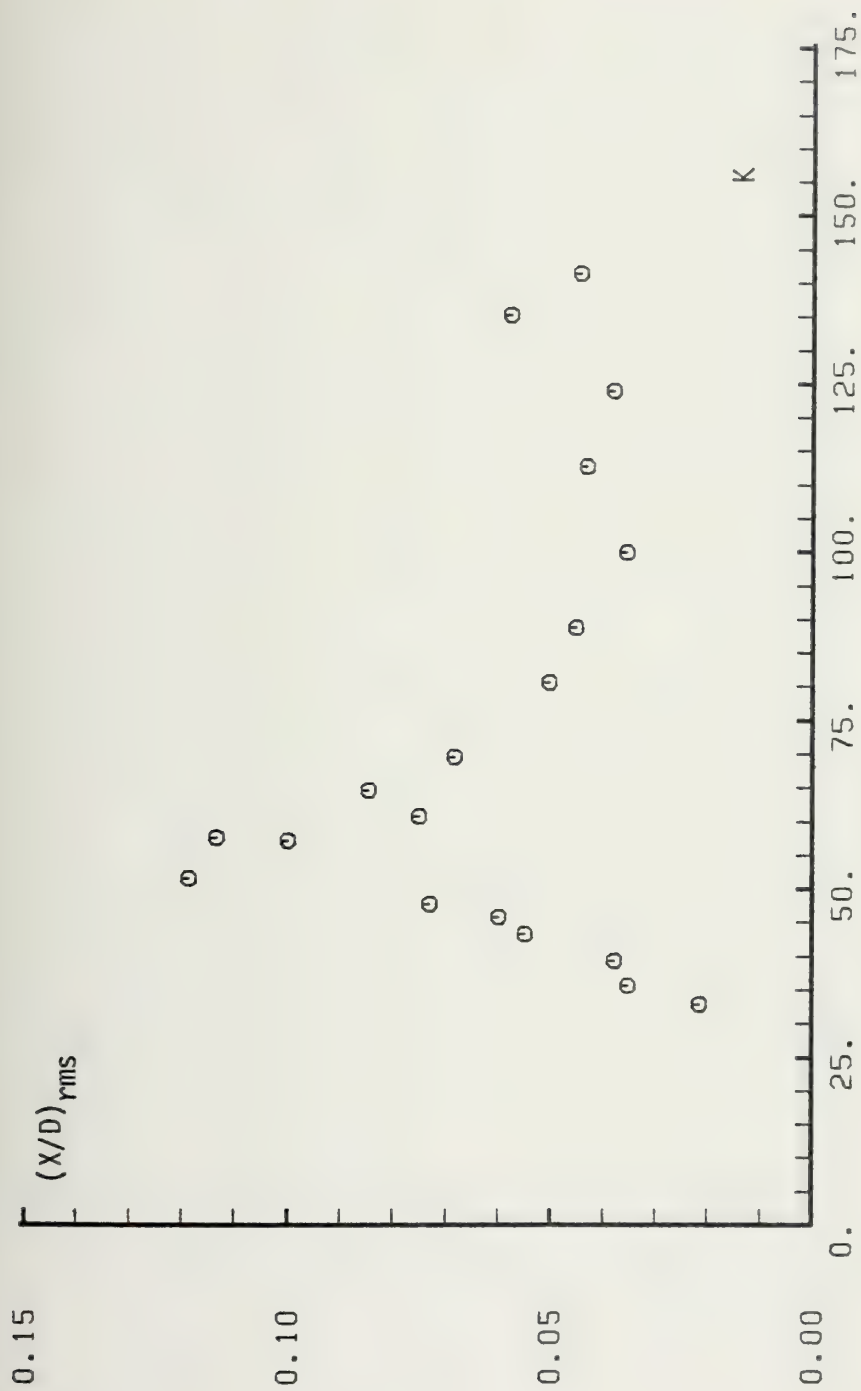


Fig. 46 $(X/D)_{rms}$ versus K for 3 in. smooth cylinder, $\zeta = 0.052$.

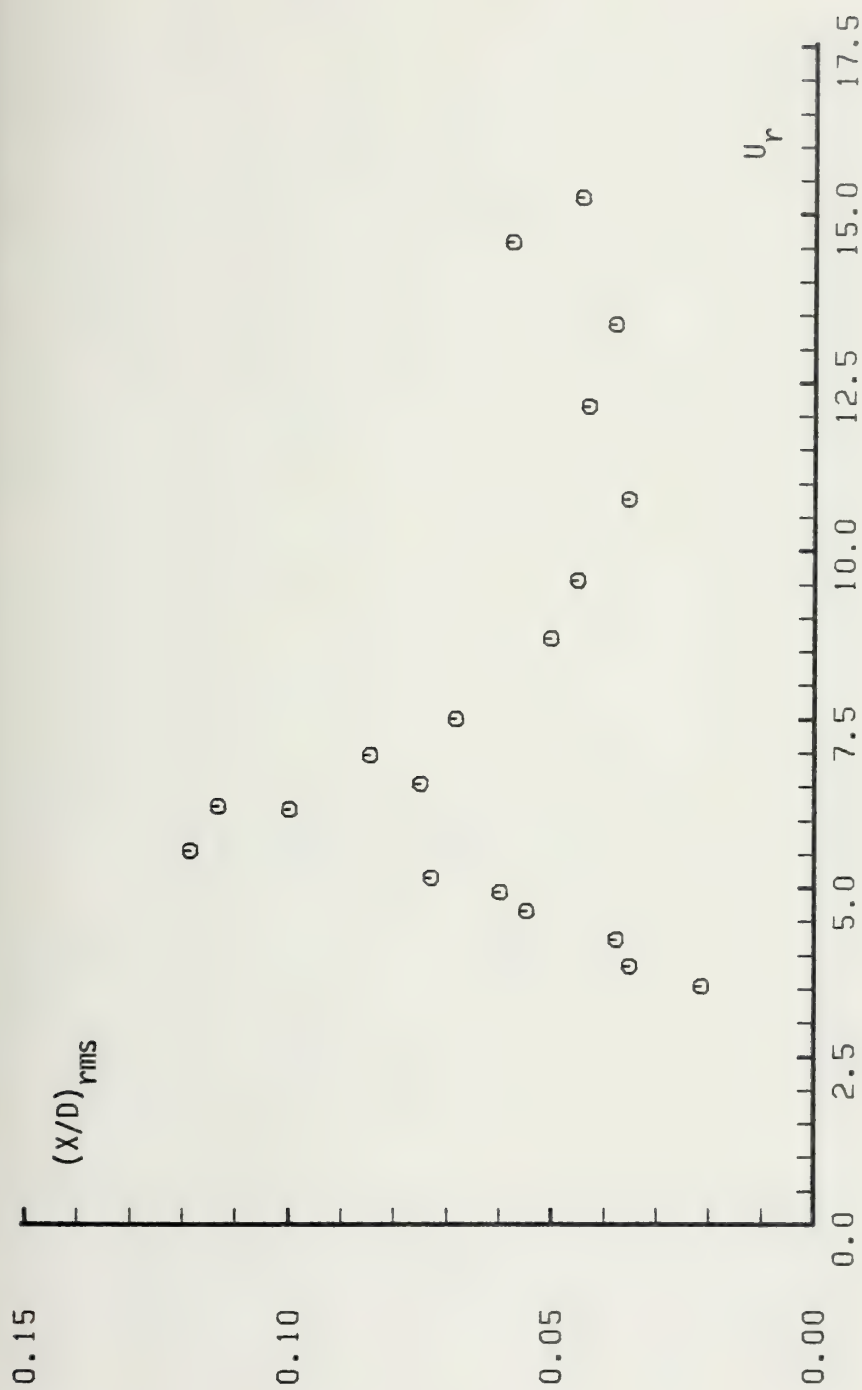


Fig. 47 $(X/D)_{rms}$ versus U_r for 3 in. smooth cylinder, $z = 0.052$.

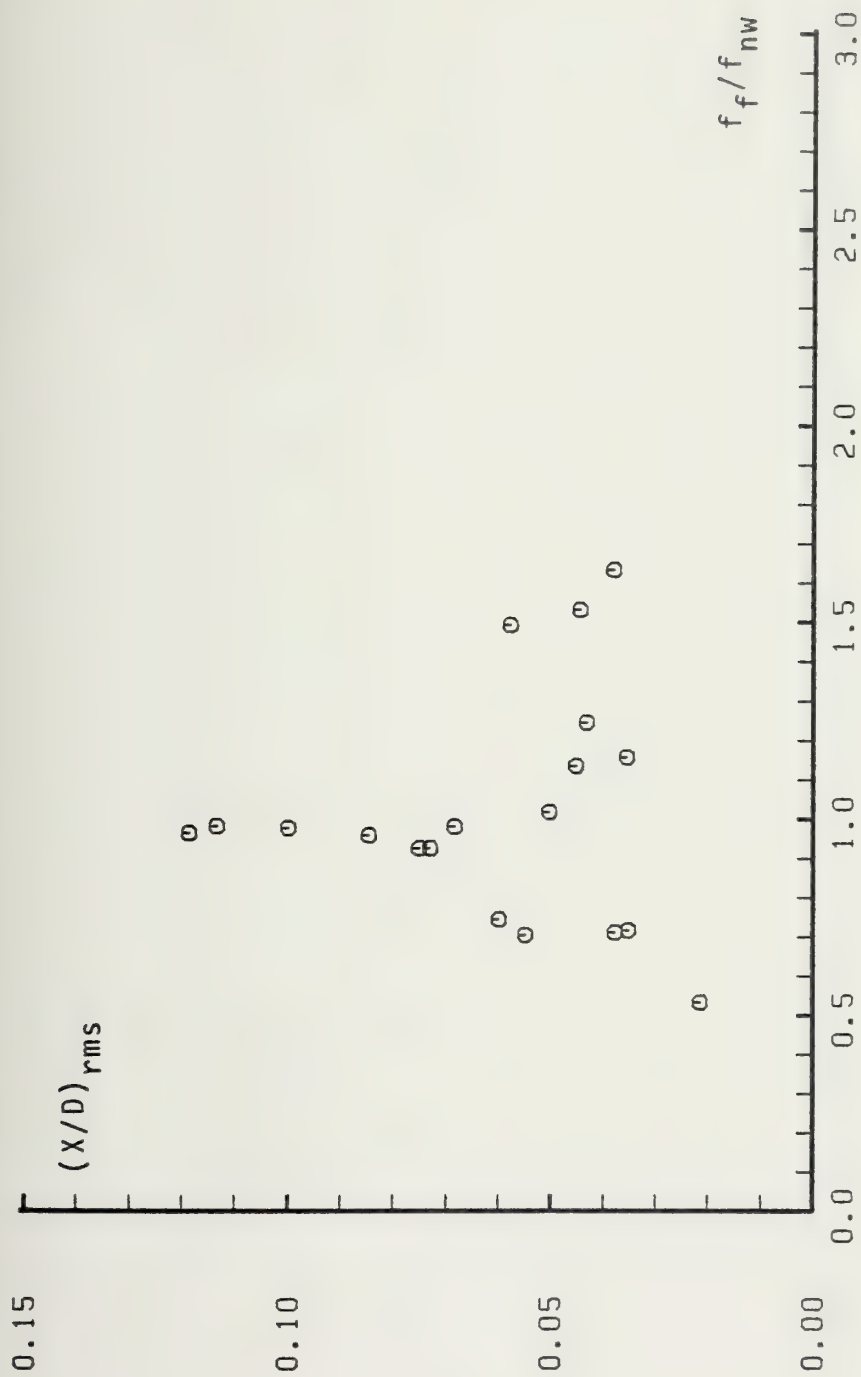


Fig. 48 $(X/D)_{rms}$ versus f_f/f_{nw} for 3 in. smooth cylinder,
 $\zeta = 0.052$.

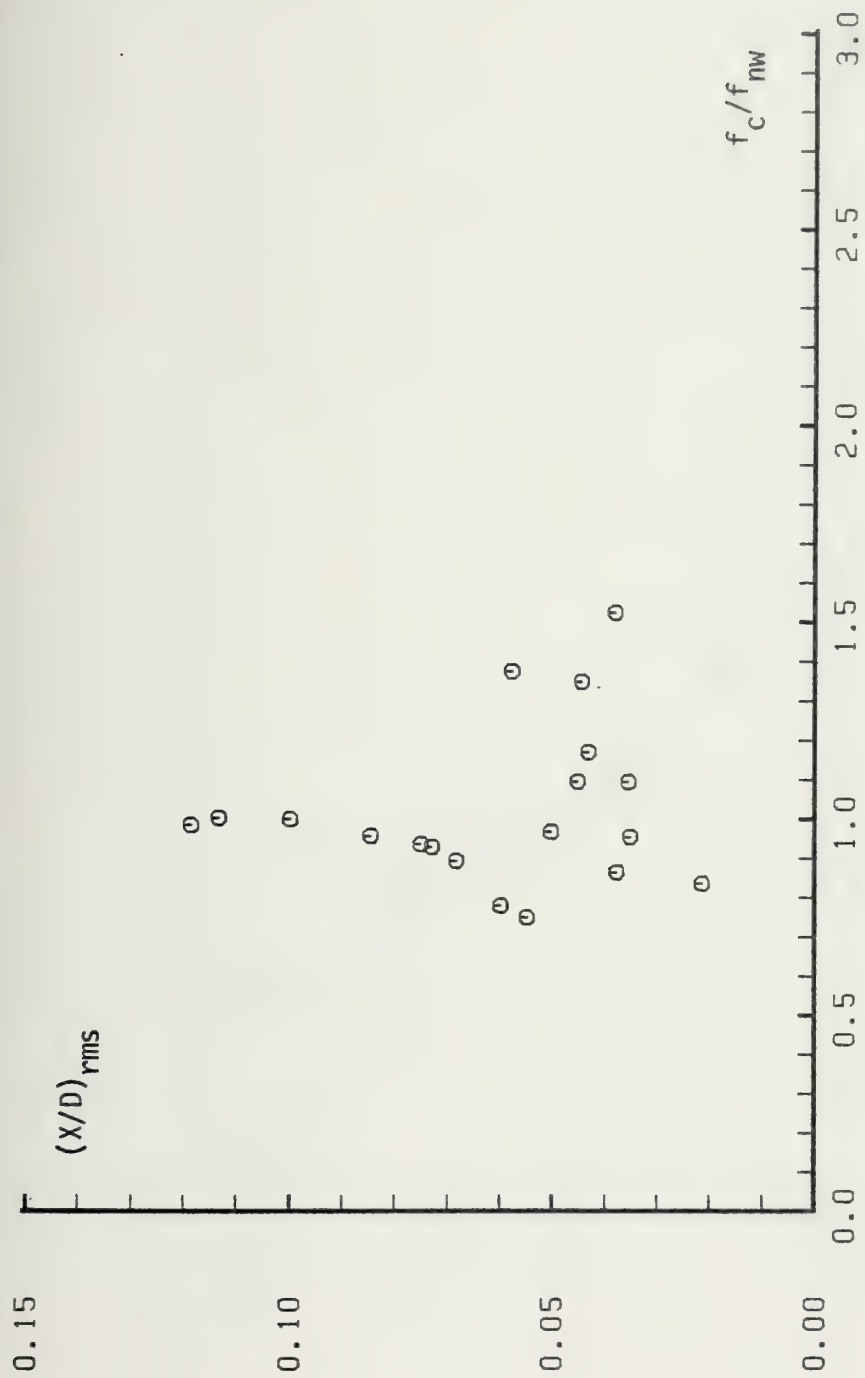


Fig. 49 $(X/D)_{rms}$ versus f_c/f_{nw} for 3 in. smooth cylinder, $z = 0.052$.

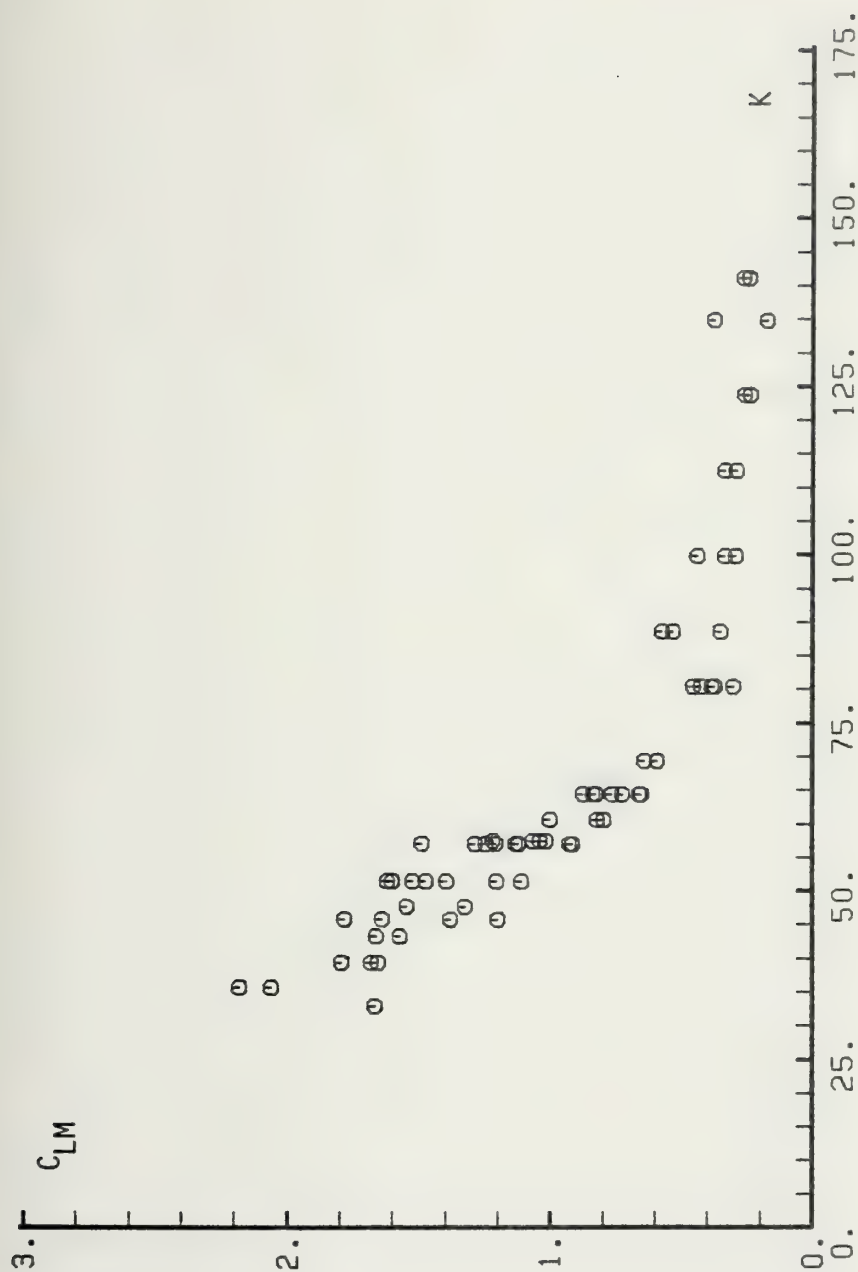


Fig. 66 C_{LM} versus K for 3 in. smooth cylinder, $\zeta = 0.052$.

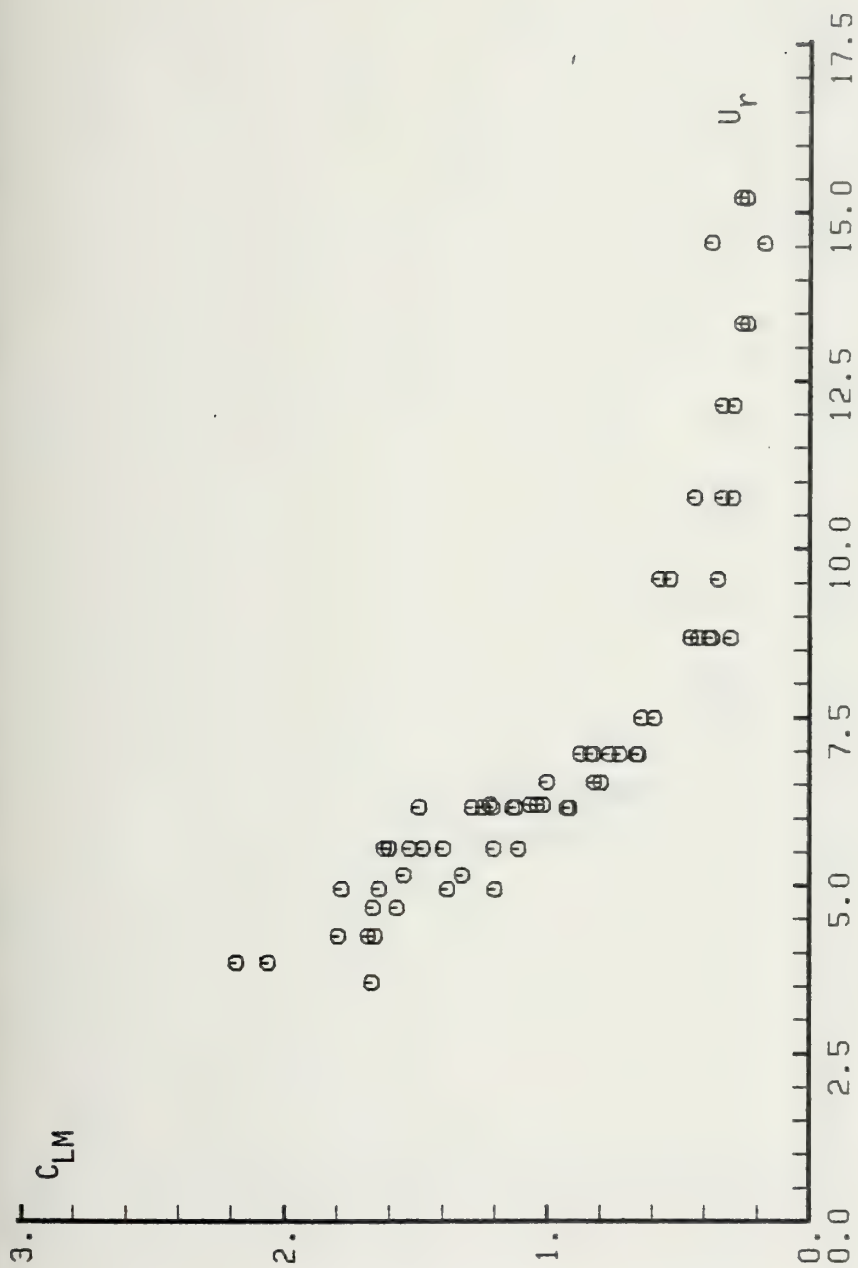


Fig. 67 C_{LM} versus U_r for 3 in. smooth cylinder, $z = 0.052$.

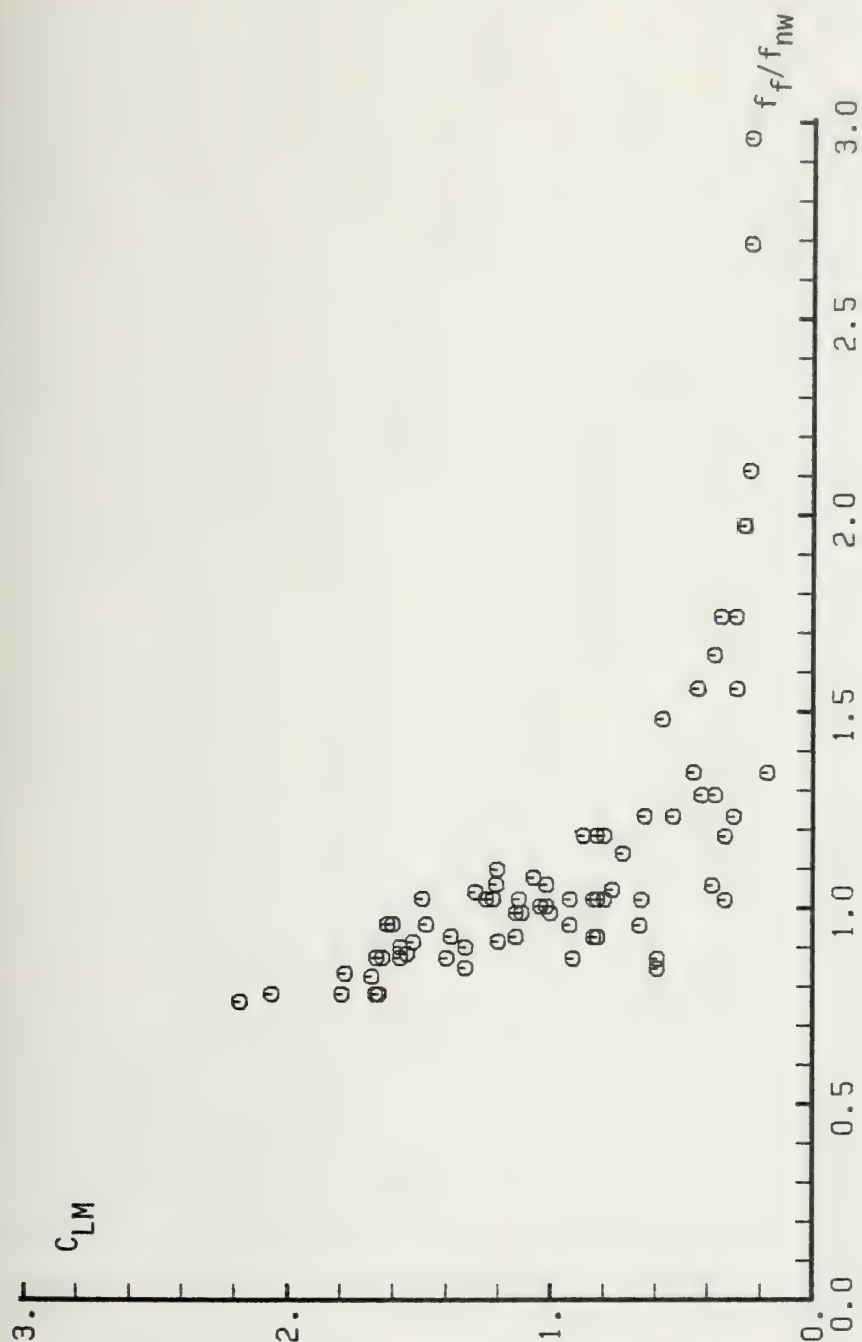


Fig. 68 C_{LM} versus f_f/f_{nw} for 3 in. smooth cylinder, $z = 0.052$

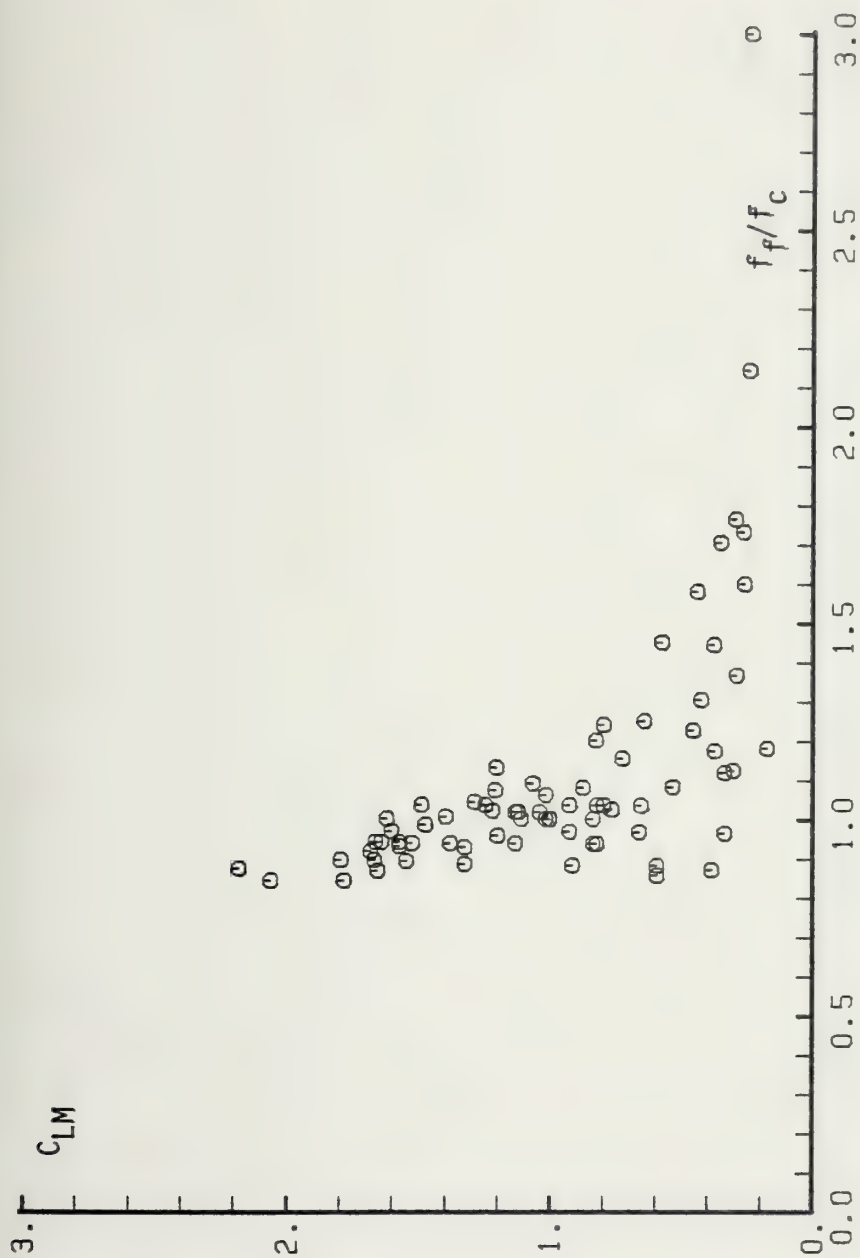


Fig. 69 C_{LM} versus f_f/f_c for 3 in. smooth cylinder, $z = 0.052$

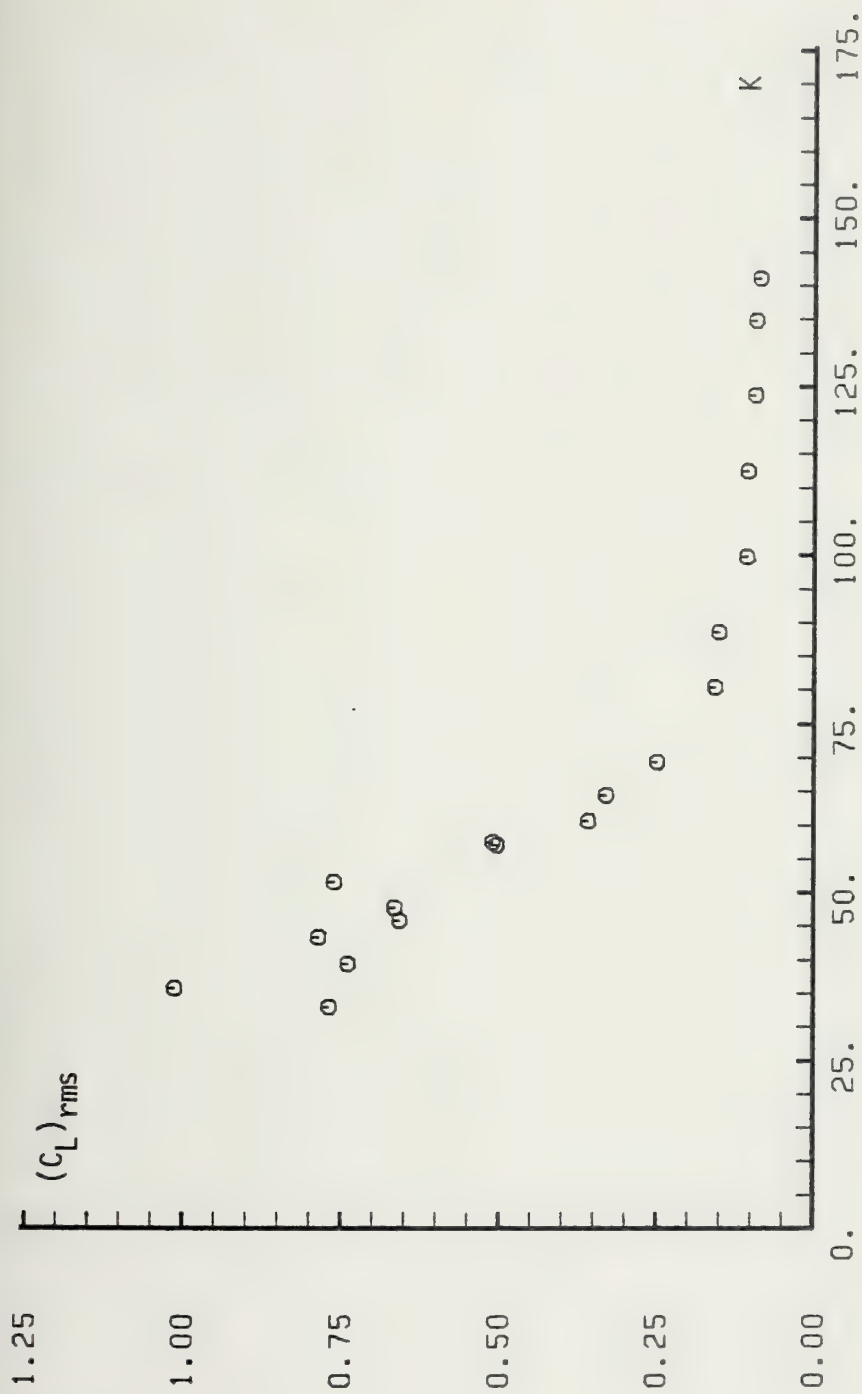


Fig. 86 $(C_L)_{rms}$ versus K for 3 in. smooth cylinder, $z = 0.052$

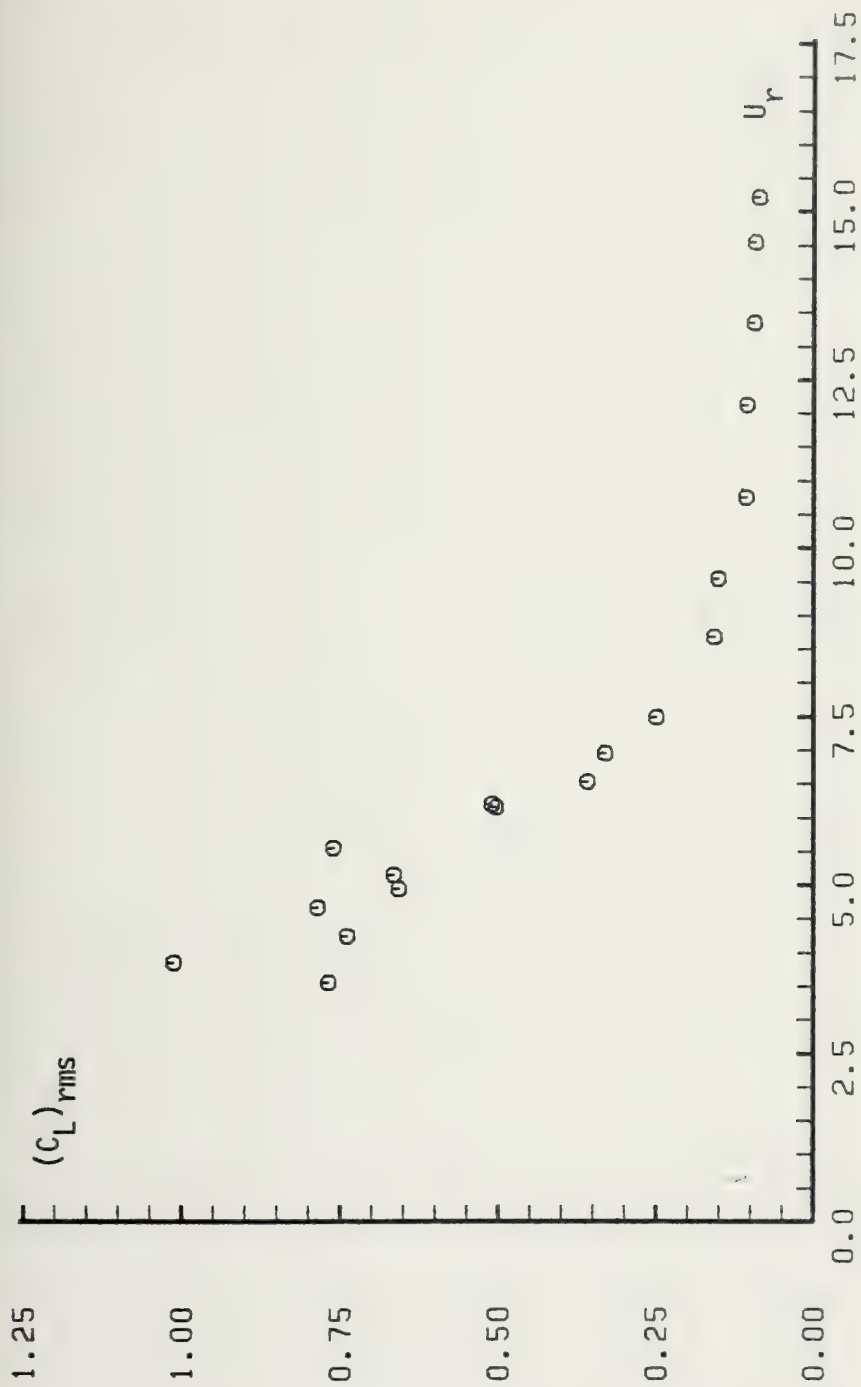


Fig. 87 $(C_L)_{rms}$ versus U_r for 3 in. smooth cylinder, $z = 0.052$

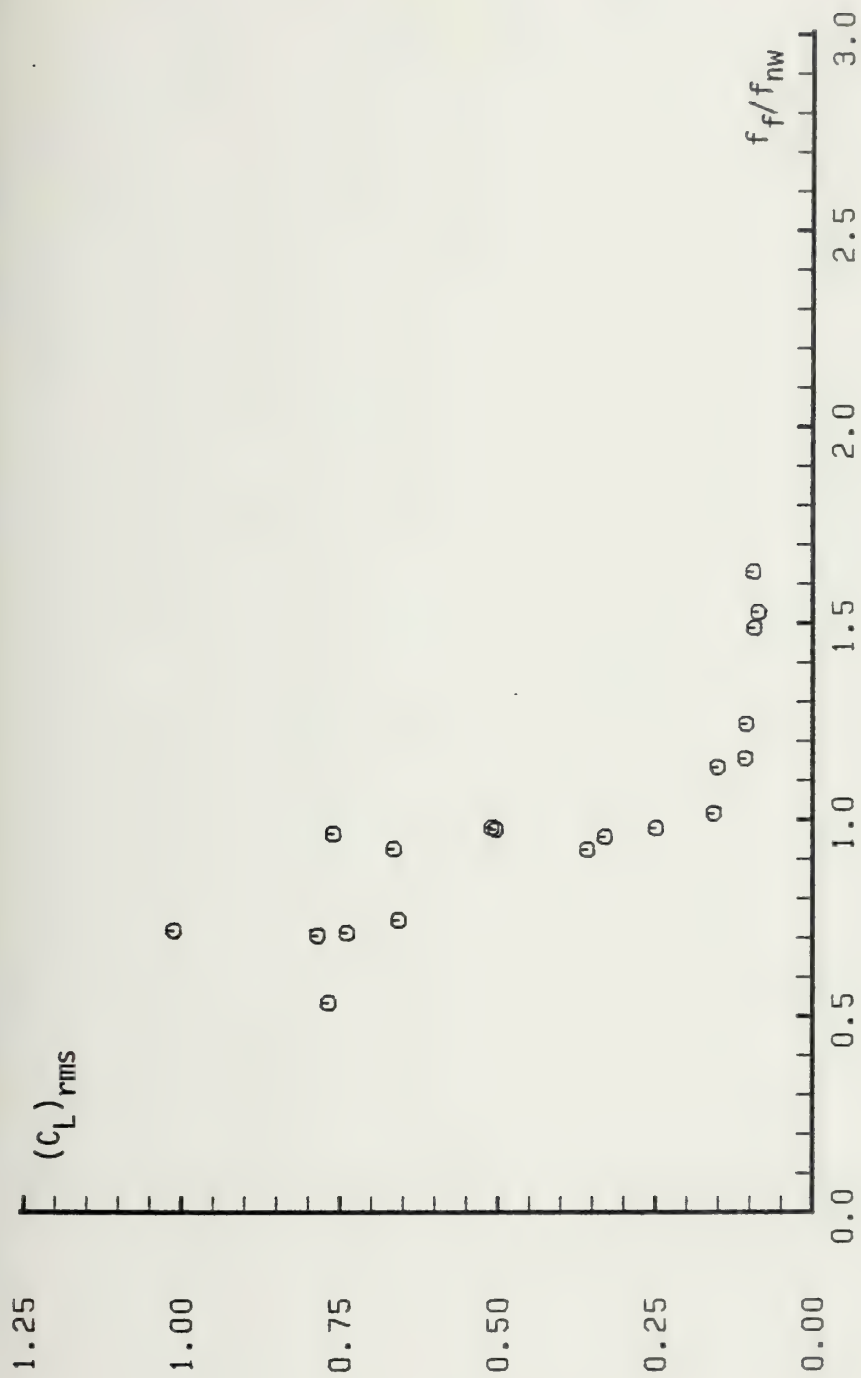


Fig. 88 $(c_L)_{rms}$ versus f_f/f_{nw} for 3 in. smooth cylinder, $z = 0.052$

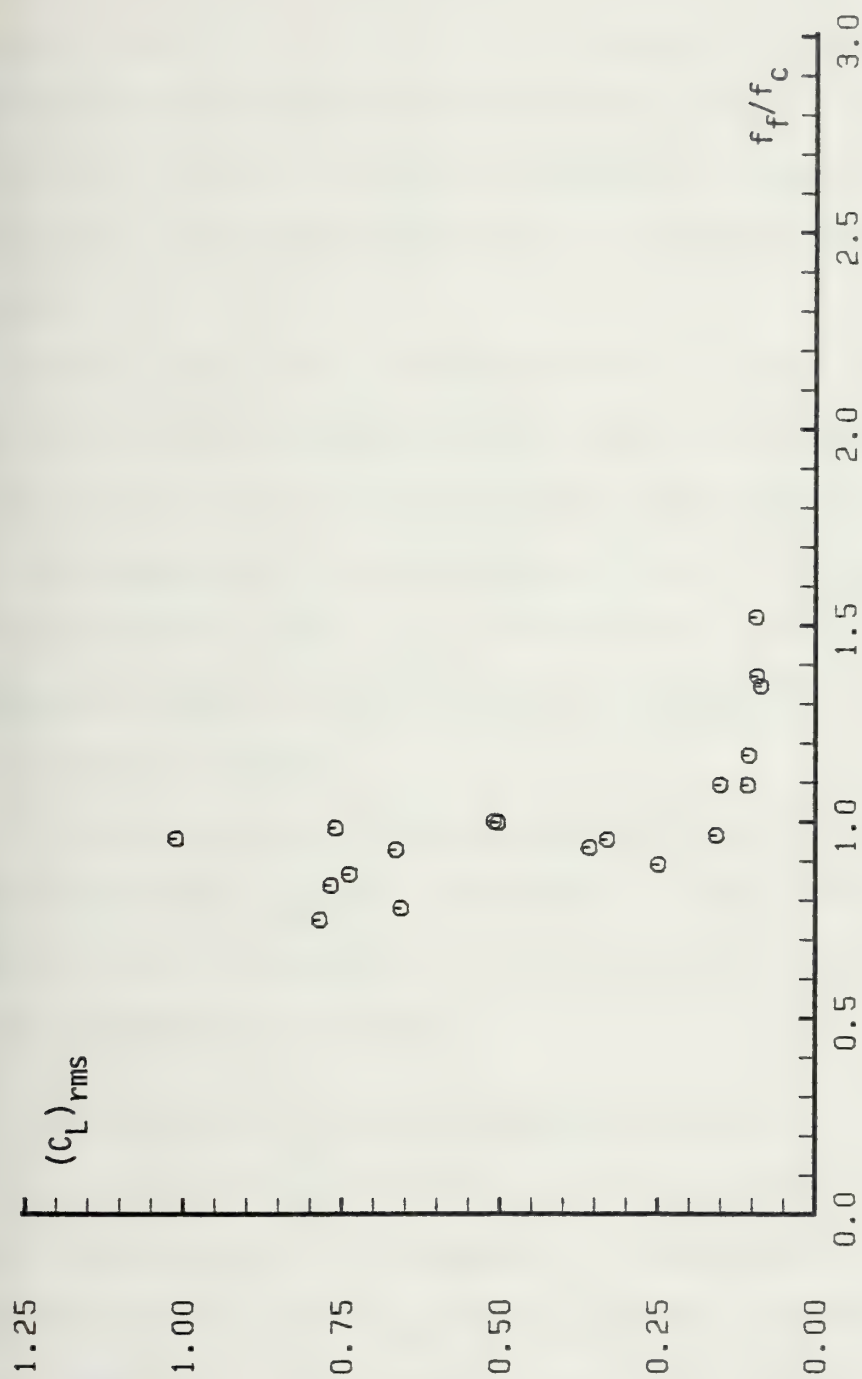


Fig. 89 $(C_L)_{rms}$ versus f_f/f_c for 3 in. smooth cylinder, $z = 0.052$

the reduced velocity $U_m/f_{nw} D$ is seen clearly in figures similar to Figs. 27 and 47. The primary synchronization (referred to hereafter as the synchronization) occurs at U_r values characteristic of those encountered in steady flows [see Fig. 3 where $V/(2\pi f_{nw} D) \approx 1$]. The frequency ratios of f_f/f_{nw} and f_c/f_{nw} (see Figs. 28 and 29 and Figs. 48 and 49) show that synchronization takes place when the frequency of force oscillations nearly coincides with the natural frequency of the cylinder. Furthermore, the cylinder oscillates at a frequency close to its natural frequency.

The lift coefficient at synchronization is several times larger than that in the non-synchronization region (see, for example, Figs. 66-69 and Figs. 86-89). As will be noted later, the said lift coefficient is 2.75 times that for the stationary cylinder at the corresponding Keulegan-Carpenter number. The amplification of the lift force is a consequence of the non-linear interaction between the flow and the cylinder as discussed in Chapter I.

As noted earlier, the random nature of the vortex shedding gives rise to modulations in both displacement and force traces. It is, therefore, useful to examine the relative influence of the harmonics of the displacement and lift force.

C. FOURIER ANALYSIS OF THE SYNCHRONIZATION REGION

When a signal is periodic over T_s it is convenient to use a Fourier series representation. The dependence of the Fourier coefficients on the pertinent dimensionless groups may then be used to describe the signal completely. Even when the signal is not completely regular, it is still useful to investigate the contributions to it, associated with

various harmonics of the wave frequency. Thus, if the displacement and force signals are considered as given approximately by

$$X(t) = \sum_{n=1}^{\infty} \bar{X}_n \cos(2\pi nft/T + \phi_n) \quad (35)$$

and

$$C_L(t) = \sum_{n=1}^{\infty} \bar{C}_{Ln} \cos(2\pi nft/T) \quad (36)$$

in which \bar{X}_n and \bar{C}_{Ln} are the effective Fourier components and may be deduced through the use of a suitable computer subroutine.

Figures 106 through 113 show the normalized displacement and their corresponding normalized Fourier coefficients for all smooth and rough cylinders. An examination of the Fourier-coefficient plot shows that the predominant frequency invariably occurs at $f = 9f_w = 9/T$ where T is the period of flow oscillation in the tunnel. The experiments by Sawaragi [99] have also shown that the predominant frequency is equal to a multiple of the flow oscillation frequency. The relationship between the predominant frequency and Strouhal number will be discussed shortly. Figures 106 through 113 also show that there are secondary harmonics which are considerably smaller than the predominant harmonic. A correct representation of the phase and amplitude modulations of the displacement requires the use of at least two or three harmonics. Figures 114 through 121 show representative normalized force traces and the corresponding normalized Fourier coefficients.

Once again it is found that the predominant frequency of the lift force is $f_f = 9 f_w$. Also, there are relatively strong higher harmonics

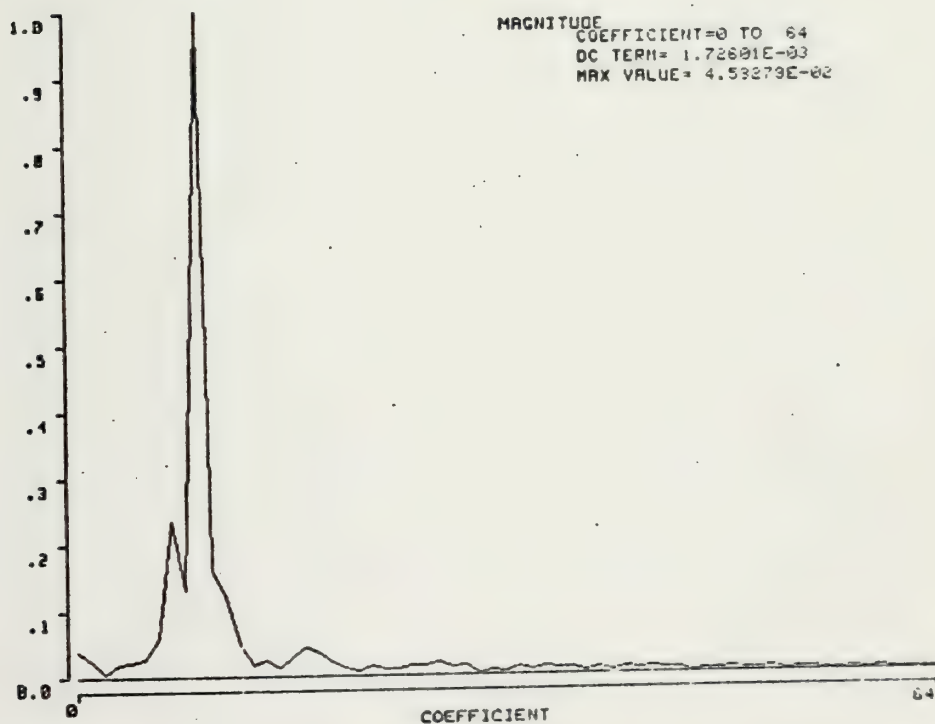
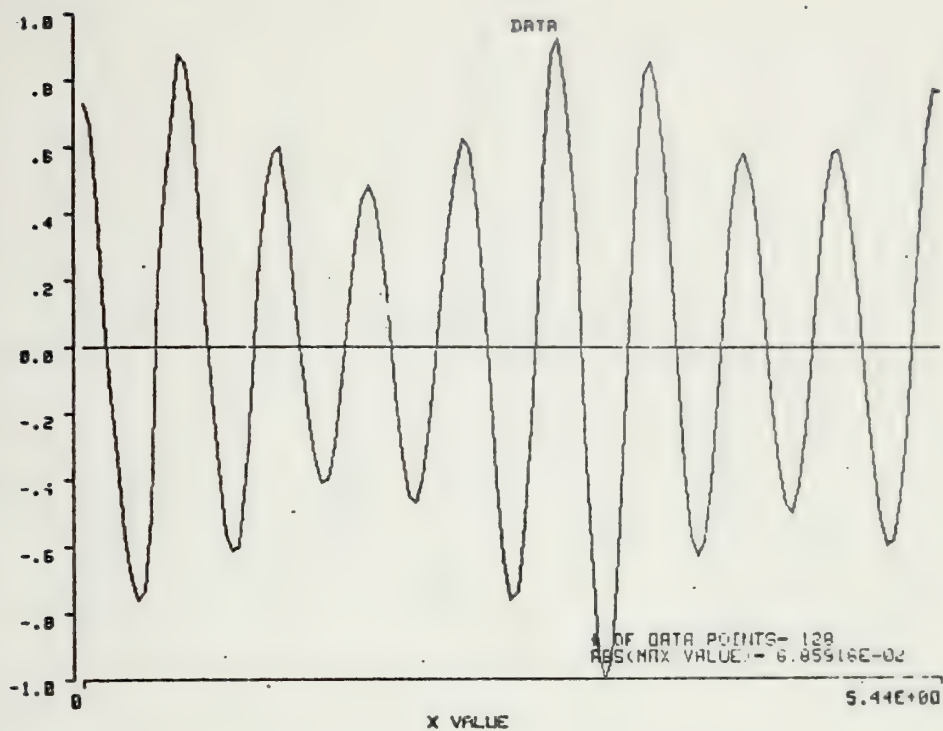


Fig. 106 Normalized displacement and Fourier coefficients for 3 in. smooth cylinder, $\zeta = 0.052$.

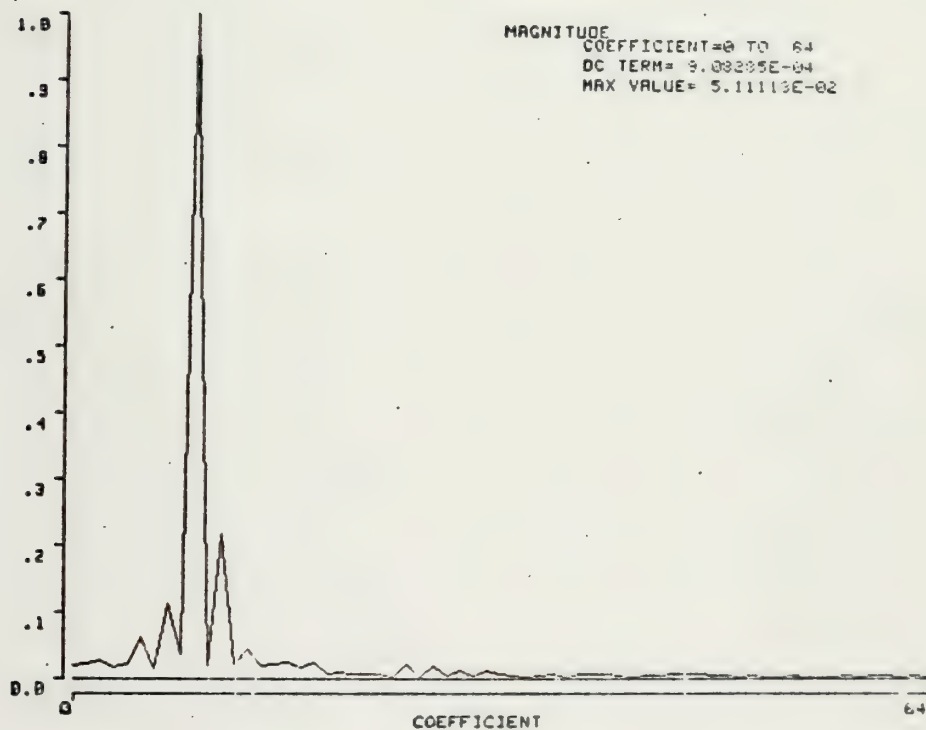
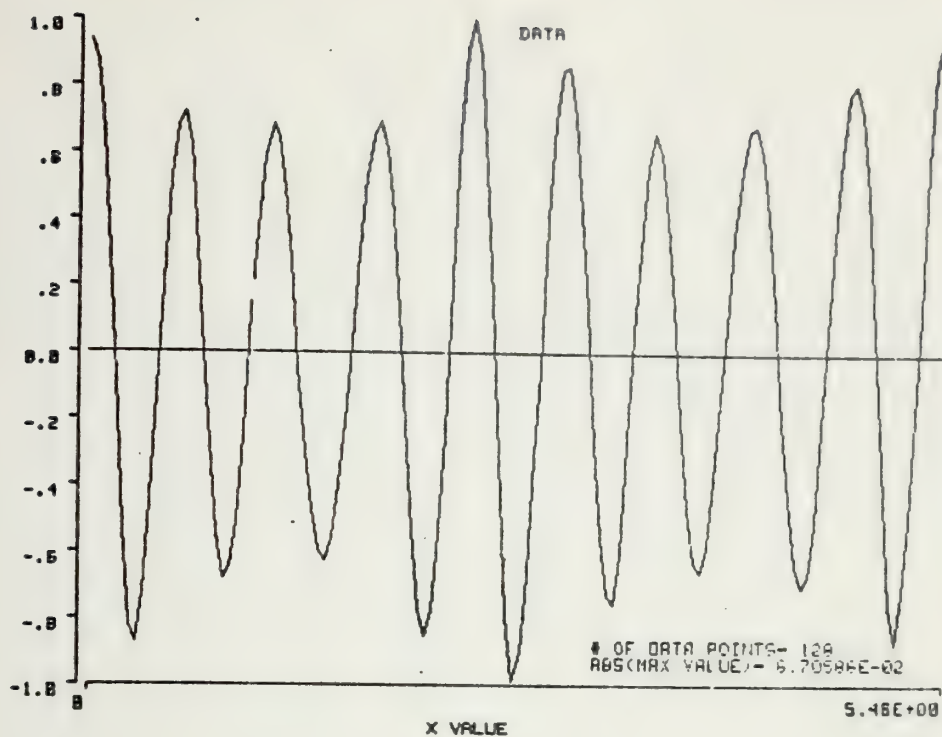


Fig. 107 Normalized displacement and Fourier coefficients for 3 in. rough cylinder, $\zeta = 0.067$.

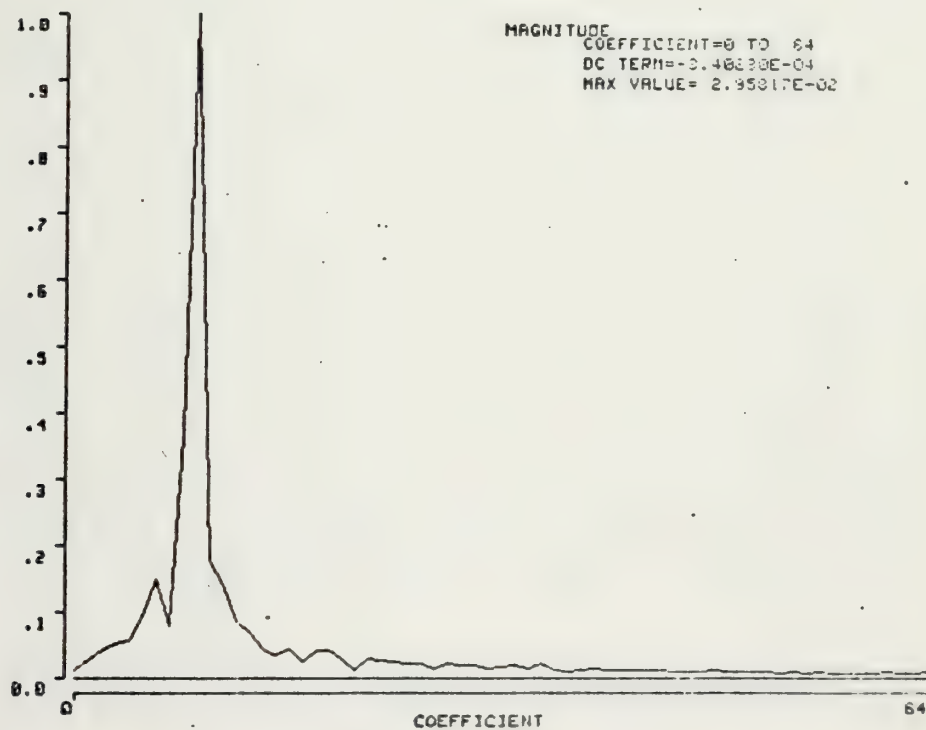
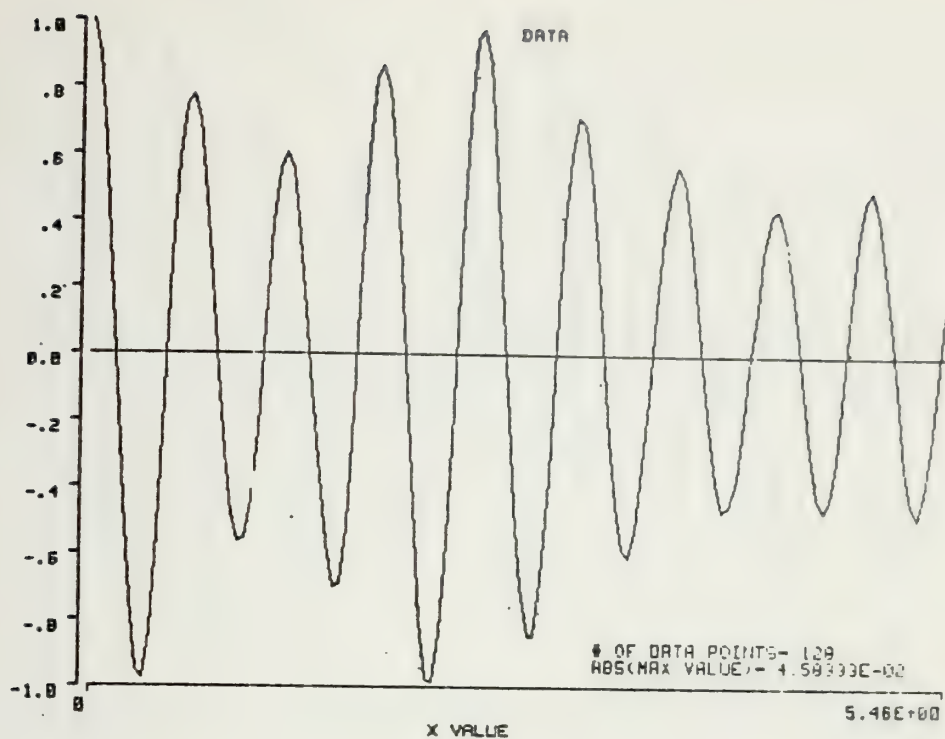


Fig. 108 Normalized displacement and Fourier coefficients for 4 in. smooth cylinder, $\zeta = 0.046$.

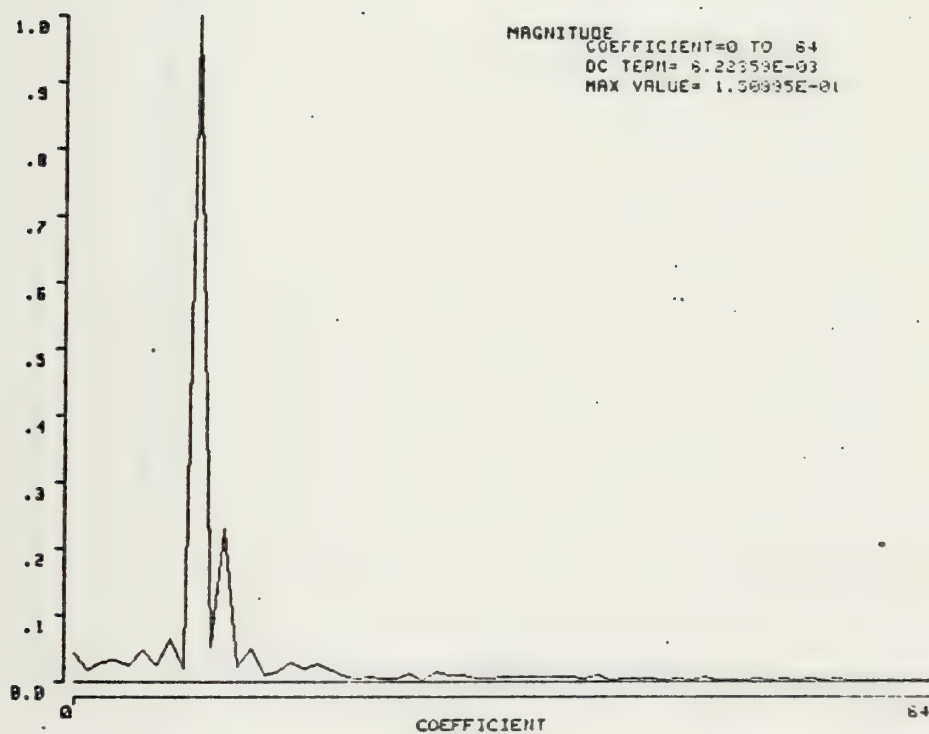
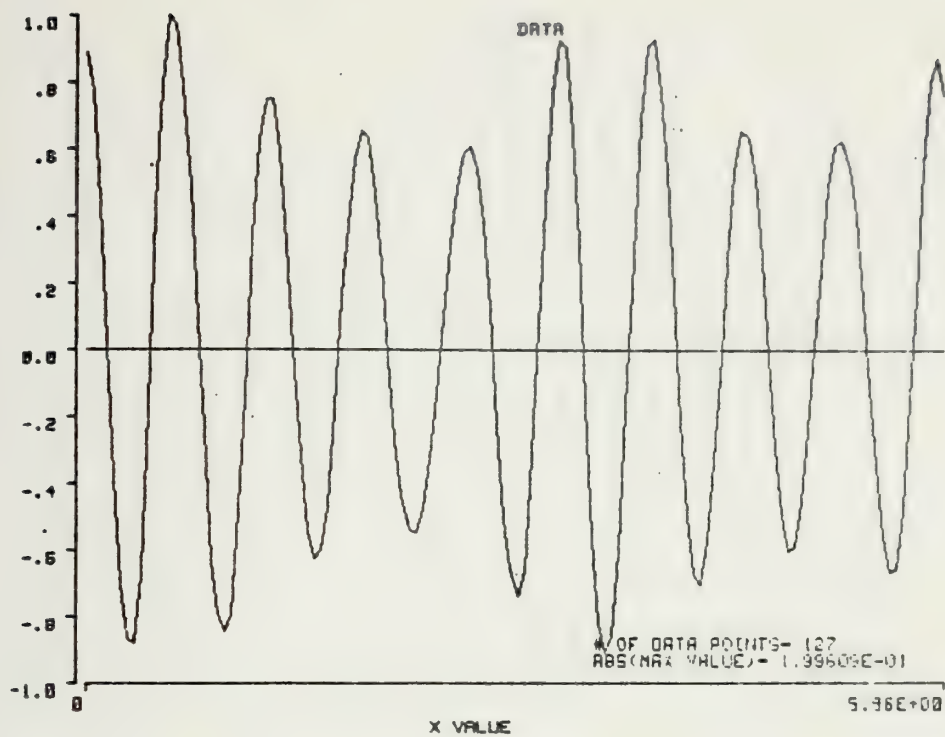


Fig. 109 Normalized displacement and Fourier coefficients for 4 in. rough cylinder, $\zeta = 0.030$.

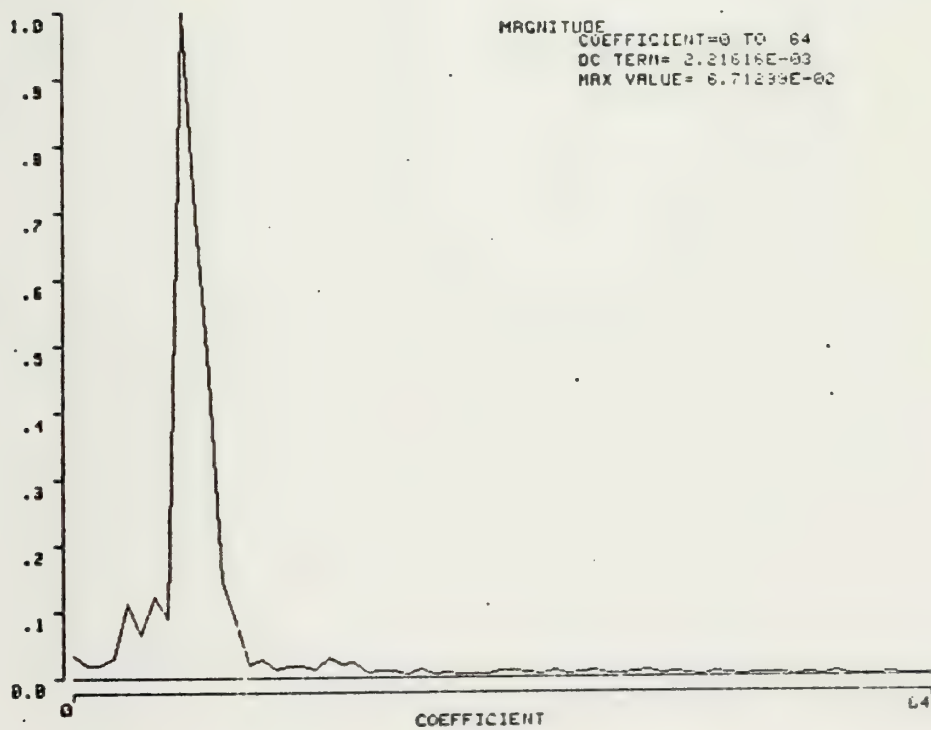
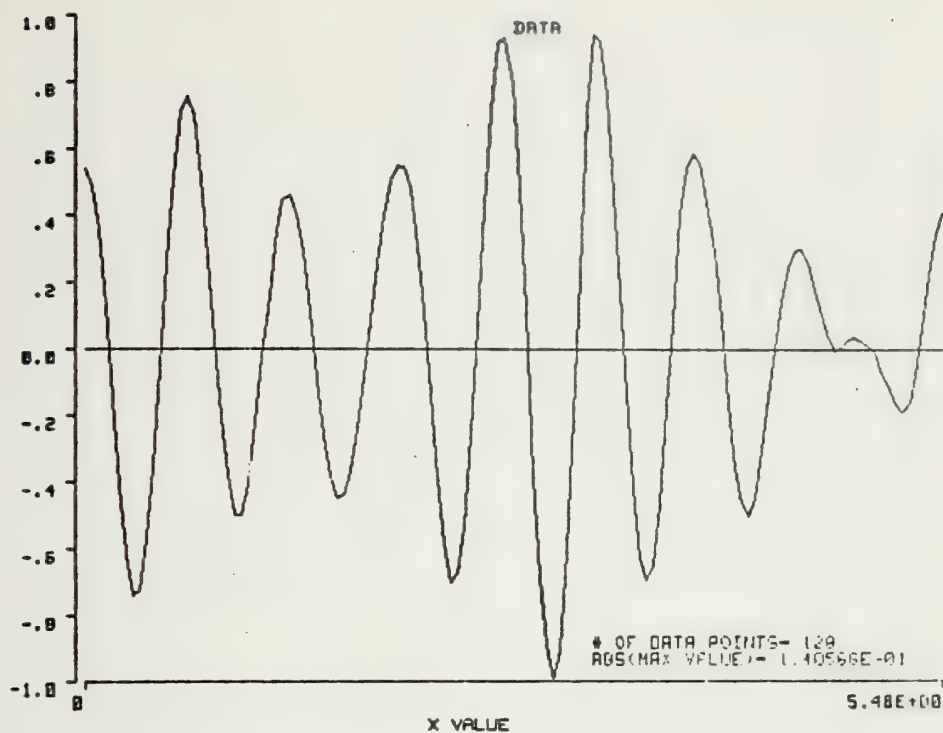


Fig. 110 Normalized displacement and Fourier coefficients for 4 in. rough cylinder, $\zeta = 0.060$.

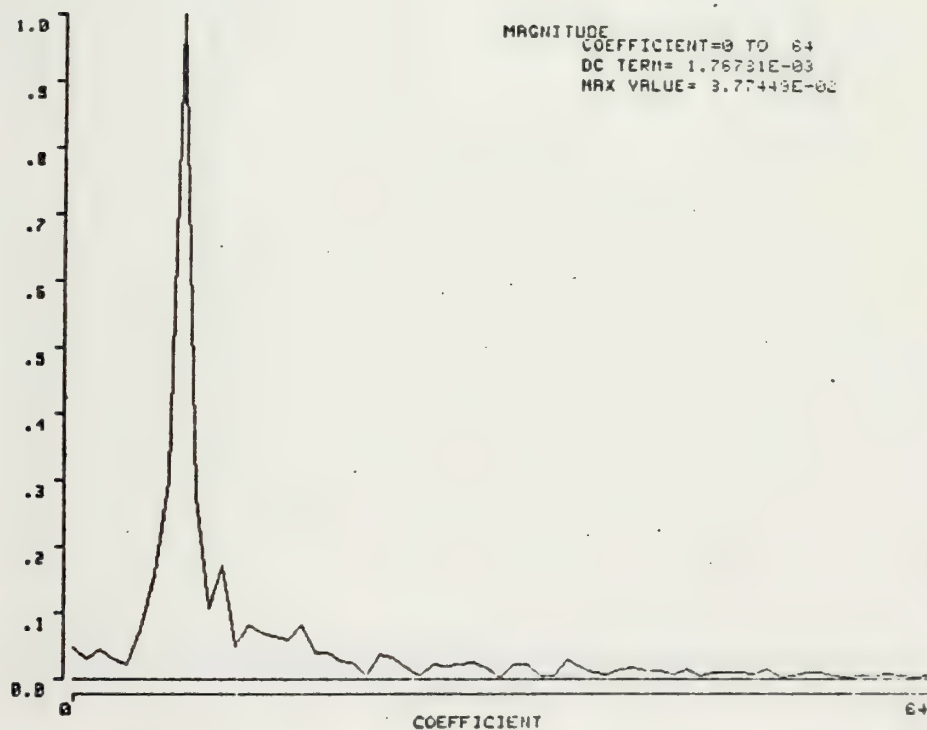
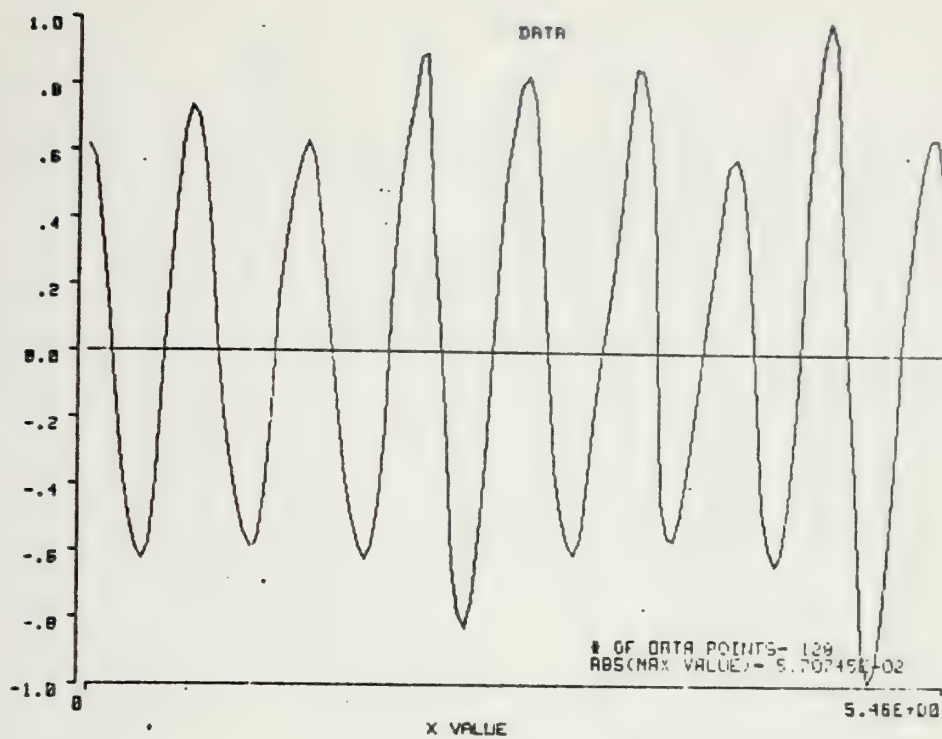


Fig. 111 Normalized displacement and Fourier coefficients for 5 in. smooth cylinder, $\zeta = 0.067$.

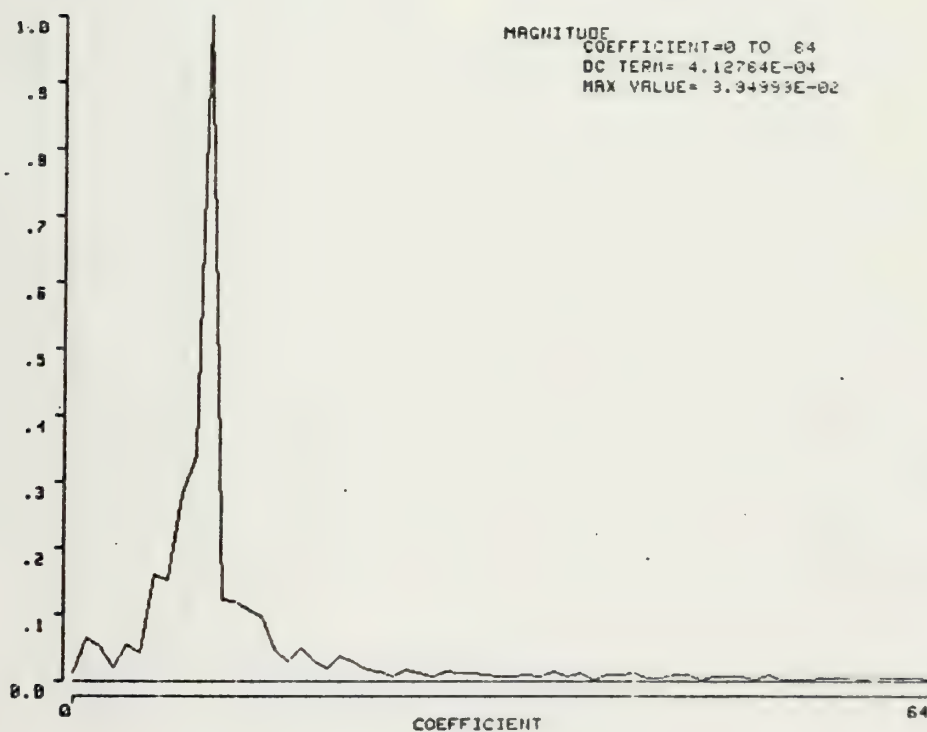
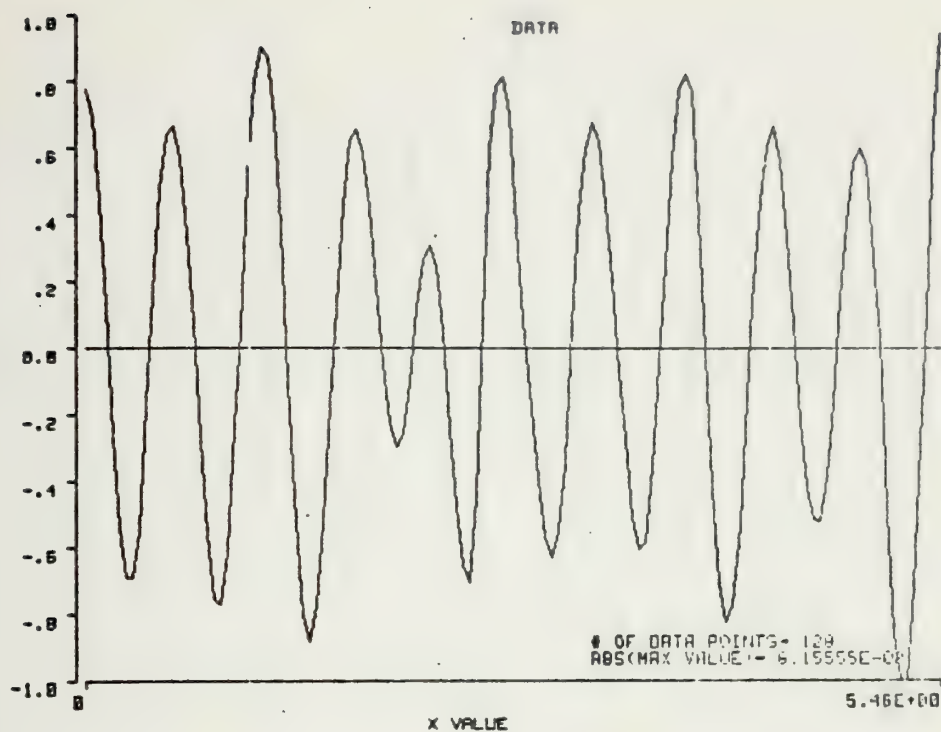


Fig. 112 Normalized displacement and Fourier coefficients for 5 in. smooth cylinder, $\zeta = 0.055$.

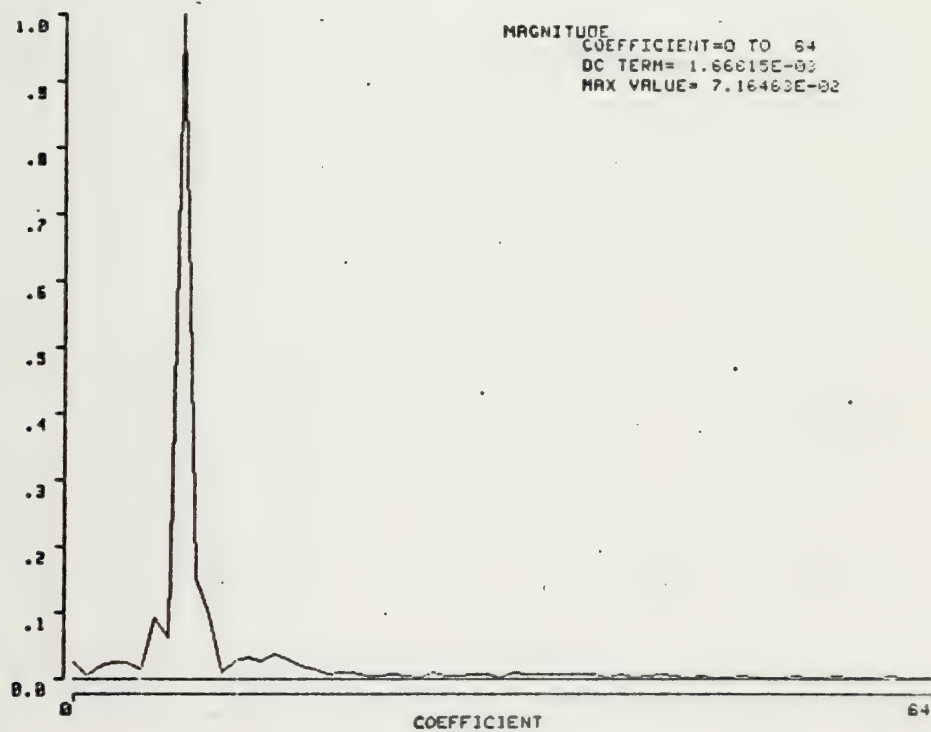
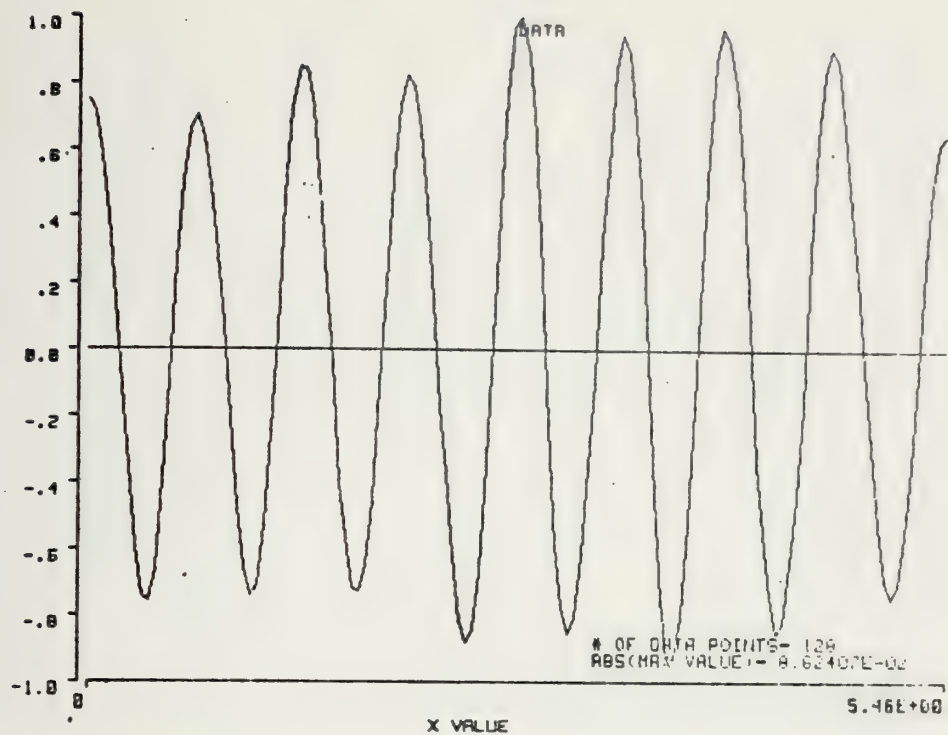


Fig. 113 Normalized displacement and Fourier coefficients for 5 in. smooth cylinder, $\zeta = 0.054$, (with lead blocks).

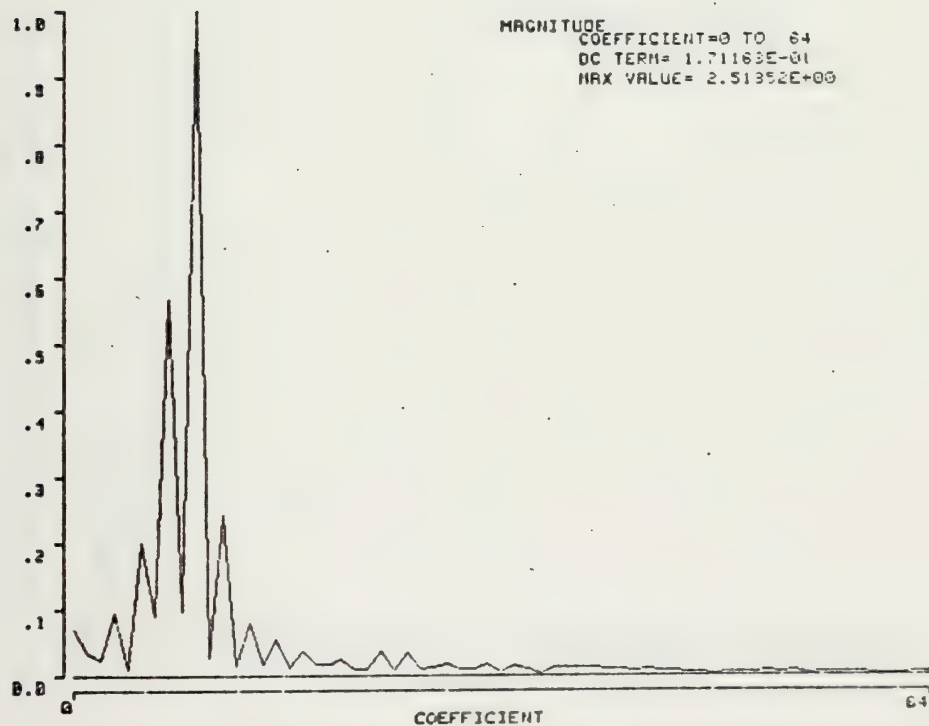
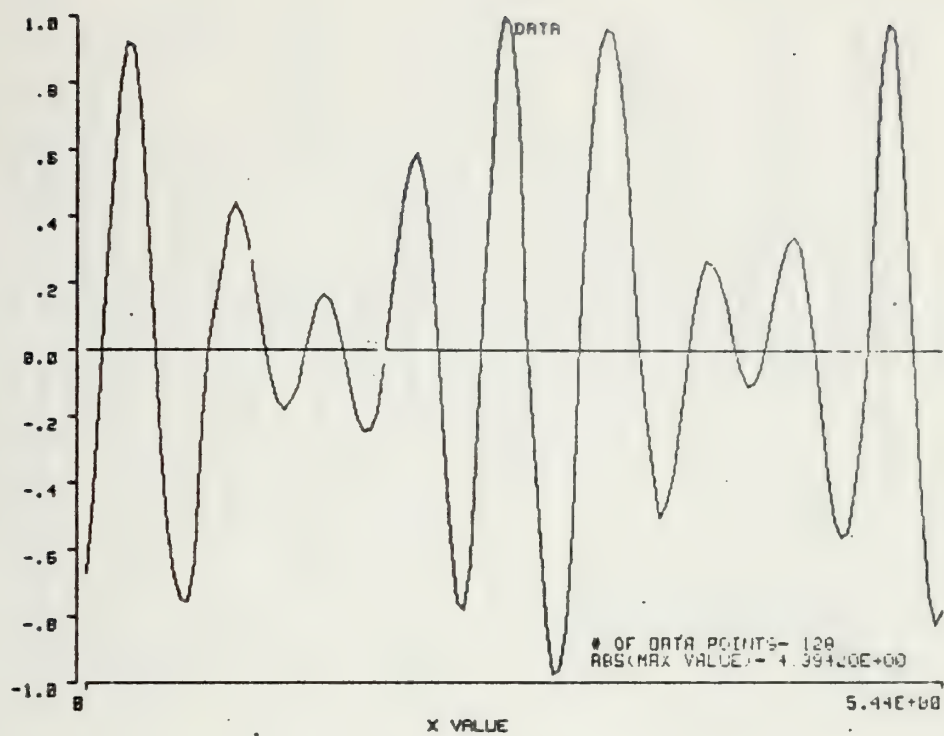


Fig. 114 Normalized lift force and Fourier coefficients for 3 in. smooth cylinder, $\zeta = 0.052$.

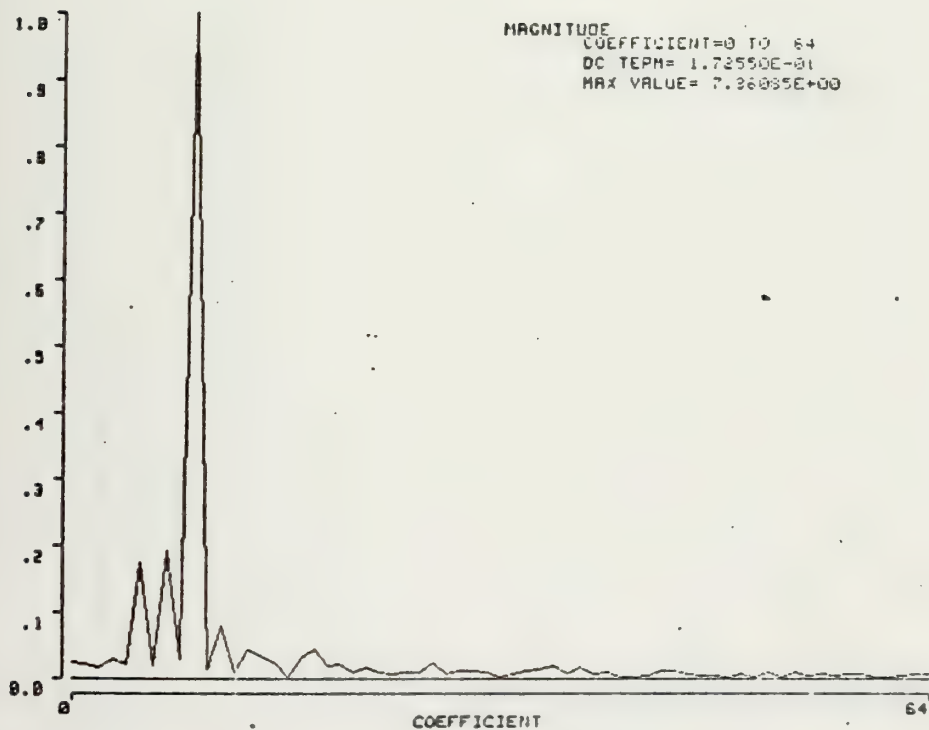
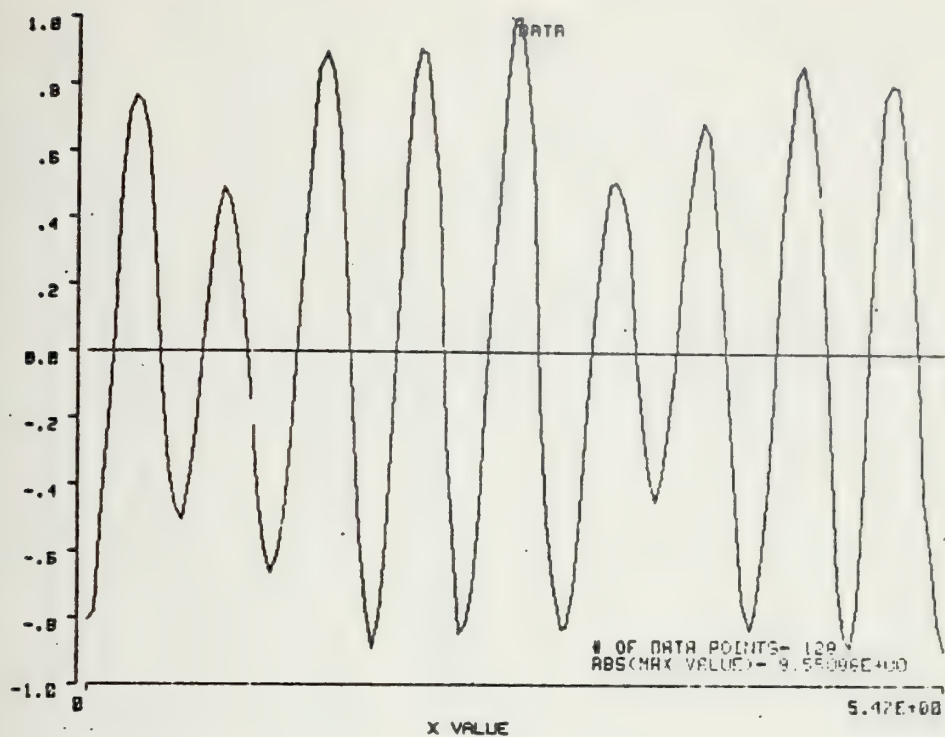


Fig. 115 Normalized lift force and Fourier coefficients for 3 in. rough cylinder, $\zeta = 0.067$.

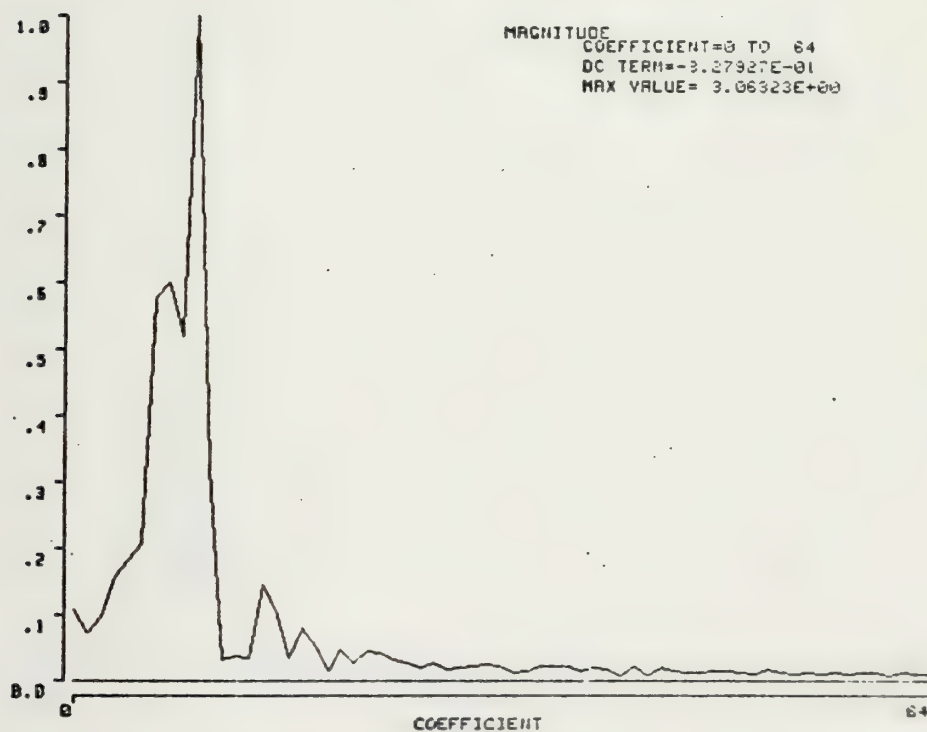
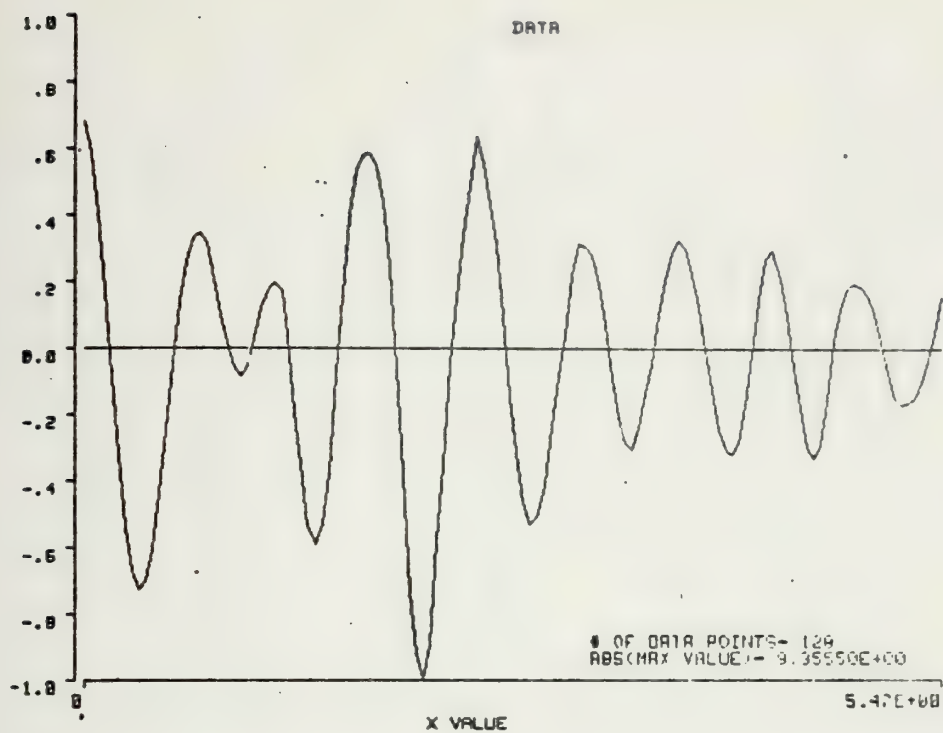


Fig. 116 Normalized lift force and Fourier coefficients for 4 in. smooth cylinder, $\zeta = 0.046$.

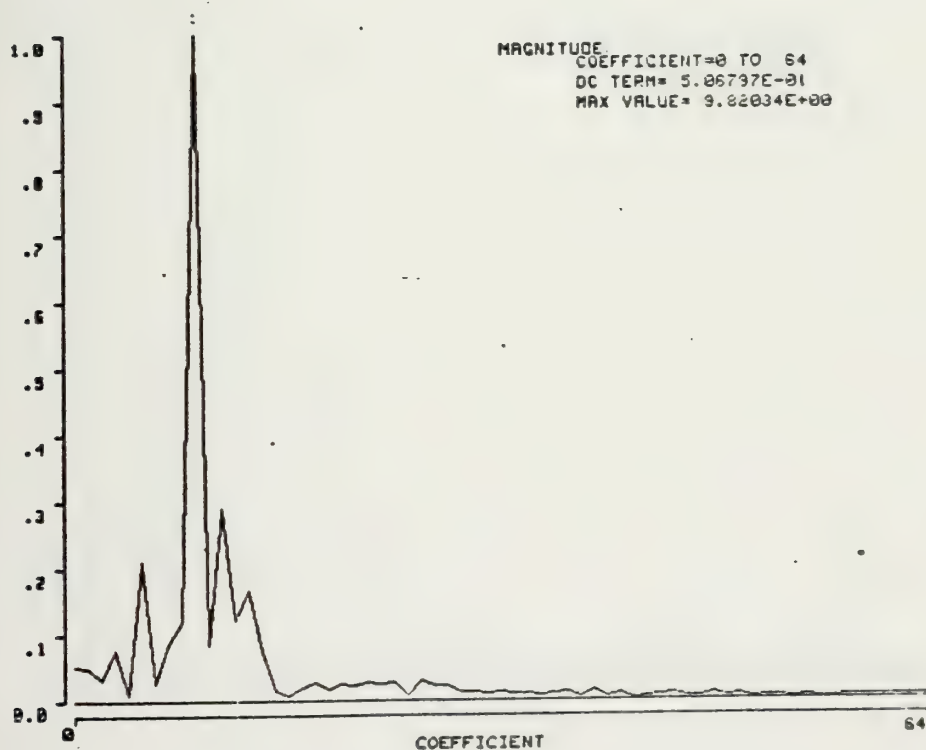
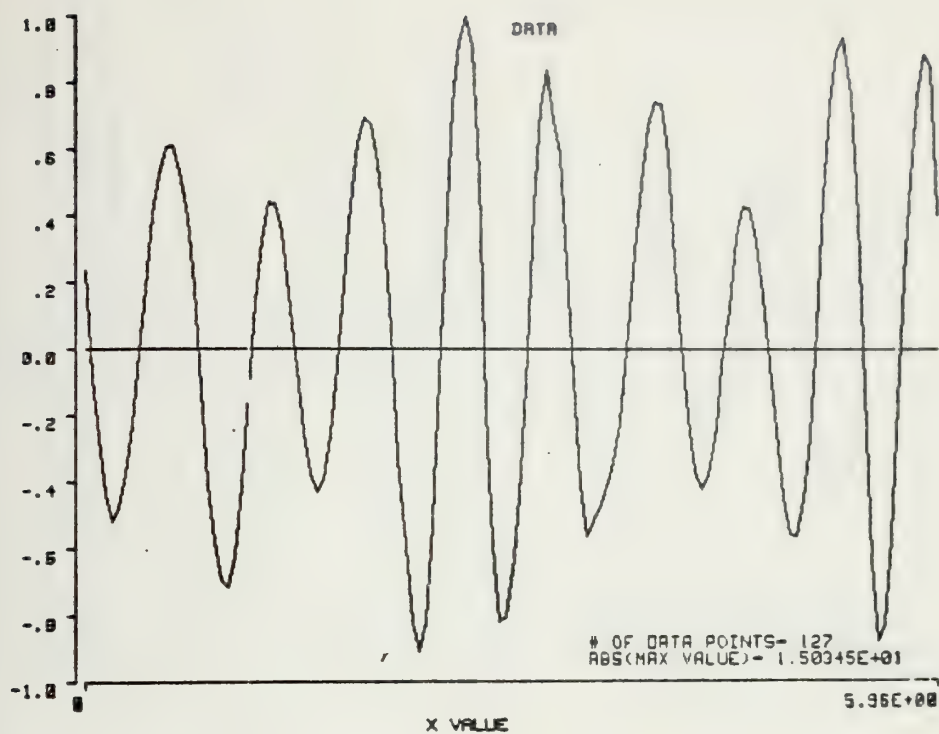


Fig. 117 Normalized lift force and Fourier coefficients for 4 in. rough cylinder, $\zeta = 0.060$.

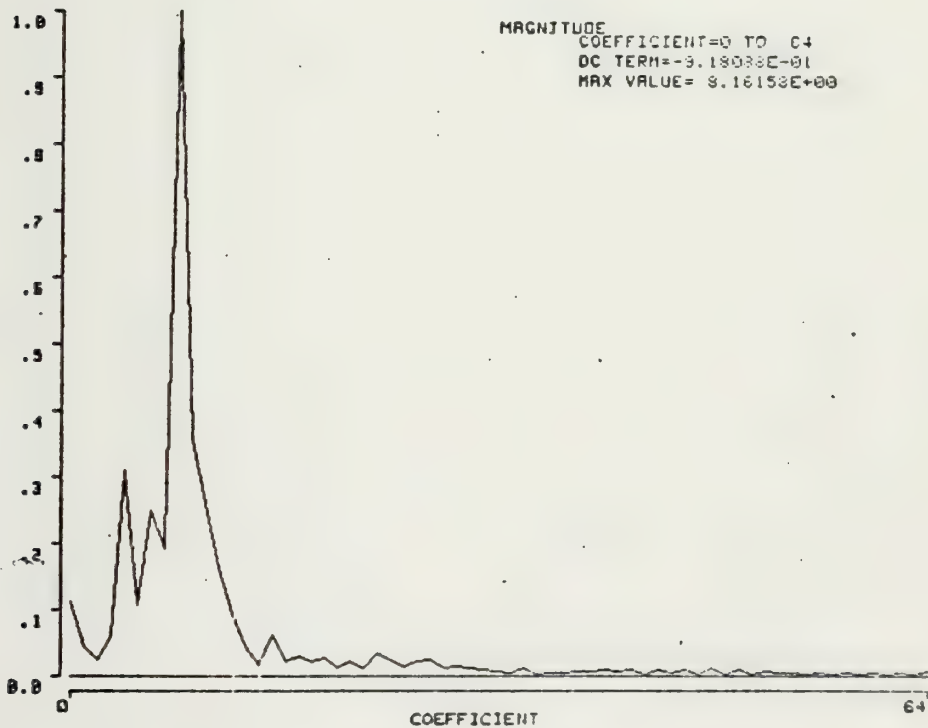
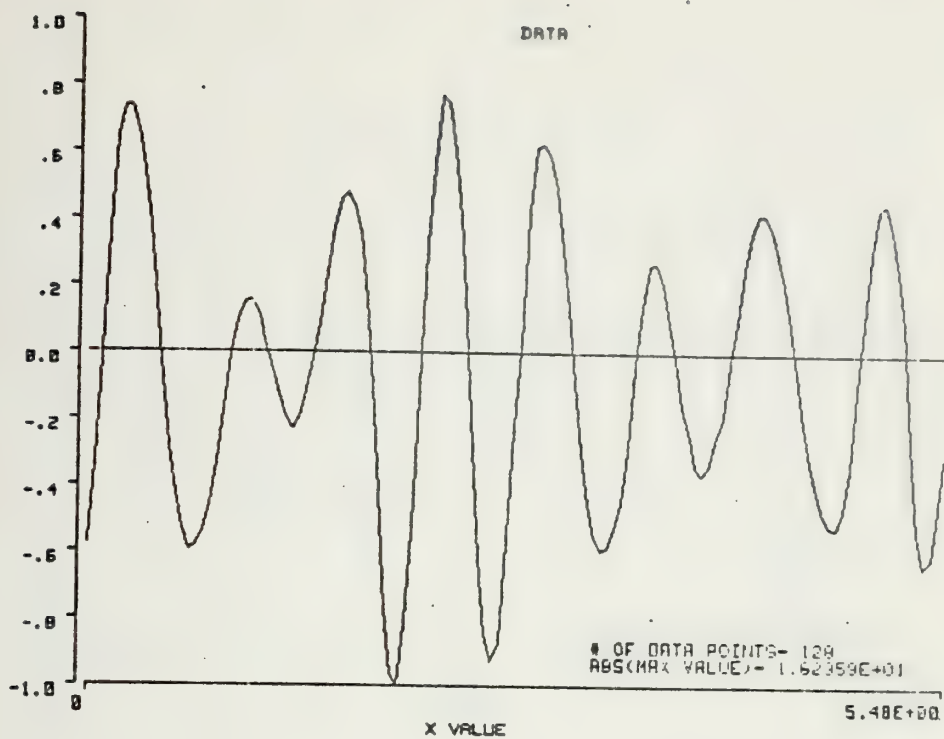


Fig. 118 Normalized lift force and Fourier coefficients for 4 in. rough cylinder, $\zeta = 0.030$.

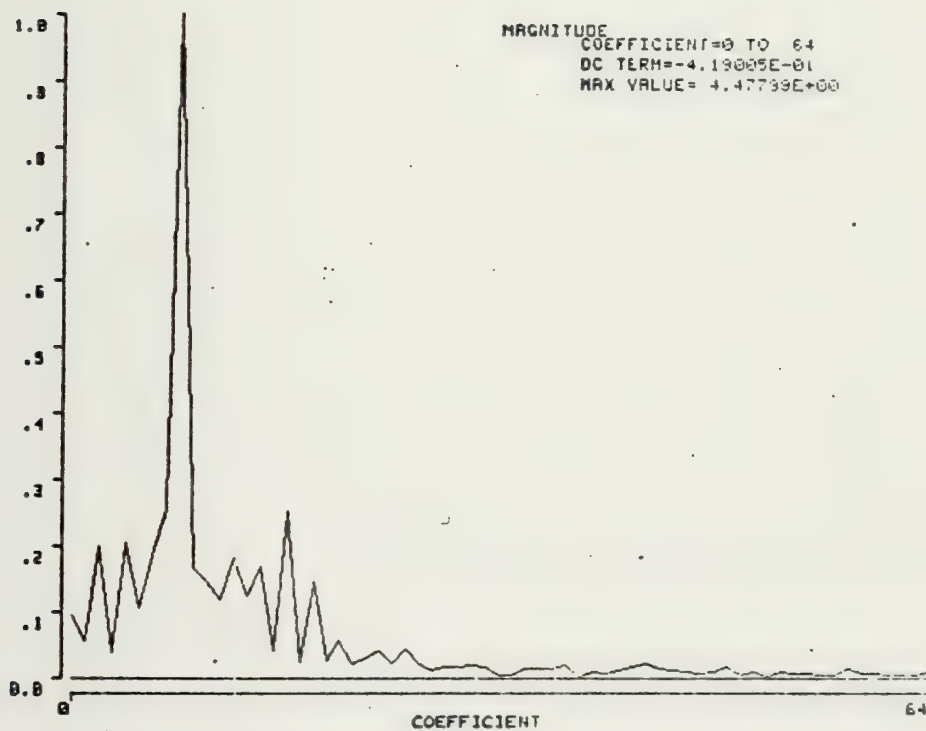
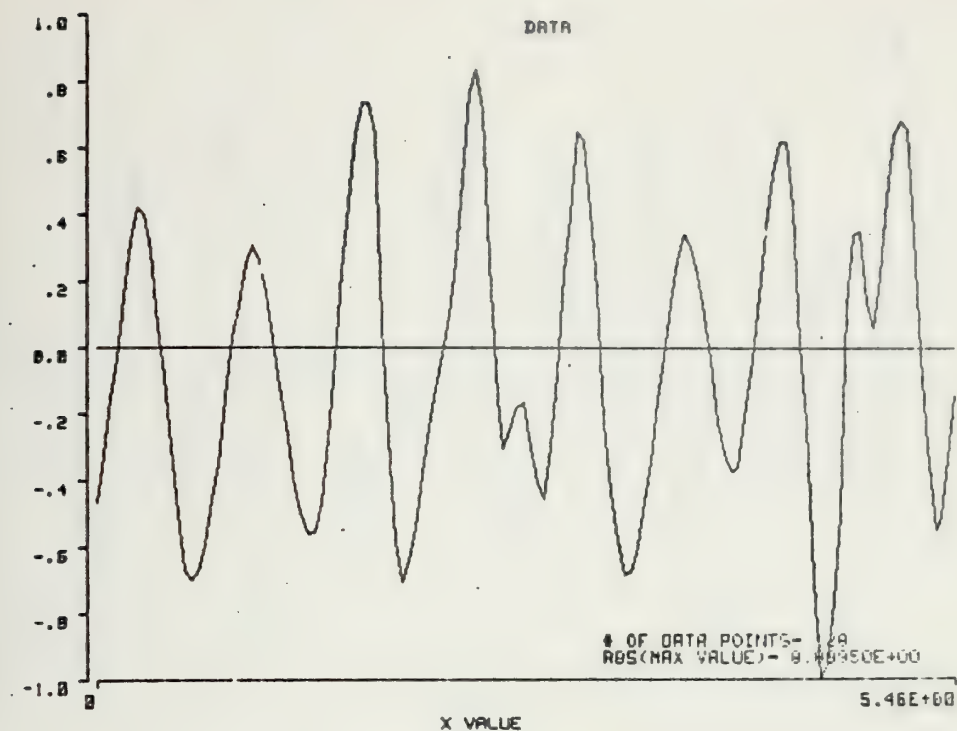


Fig. 119 Normalized lift force and Fourier coefficients for 5 in. smooth cylinder, $\zeta = 0.061$, (with lead blocks).

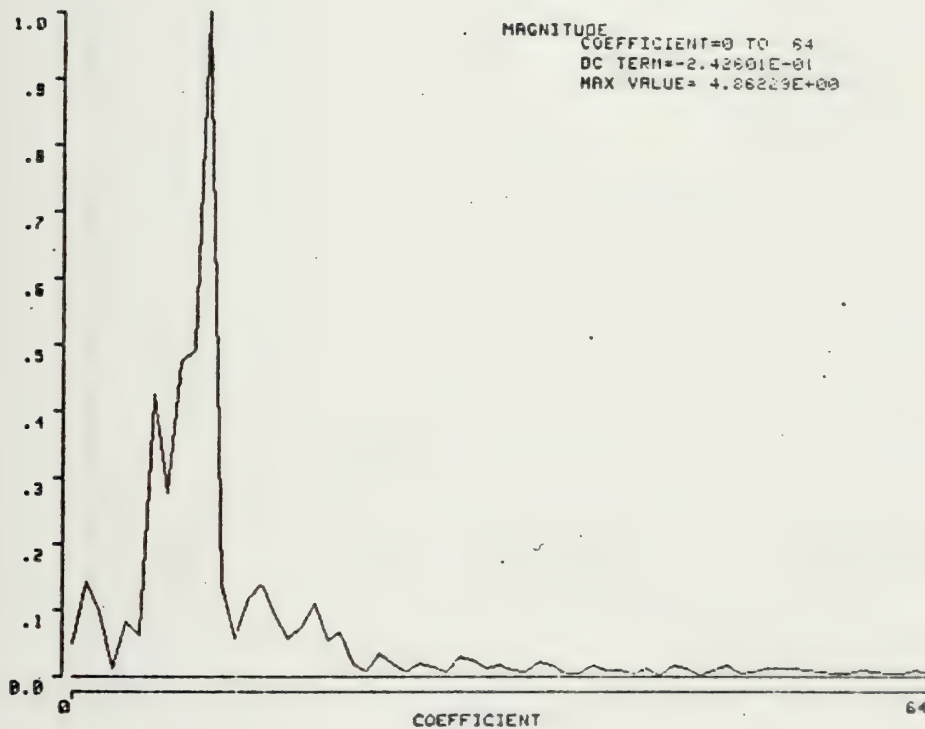
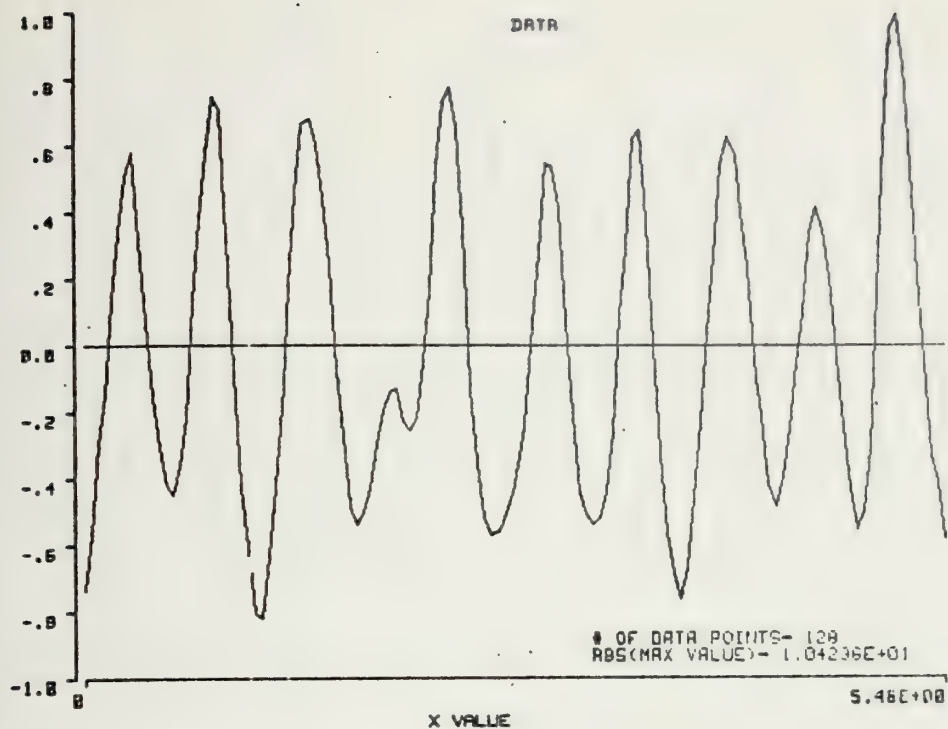


Fig. 120 Normalized lift force and Fourier coefficients for 5 in. smooth cylinder, $\zeta = 0.055$, (with lead blocks).

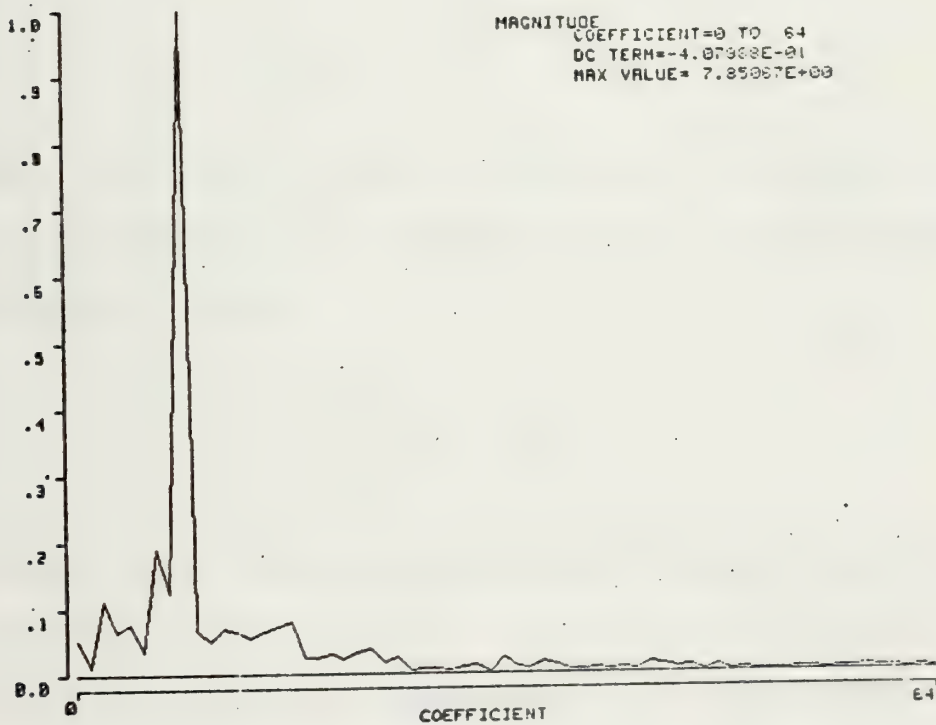
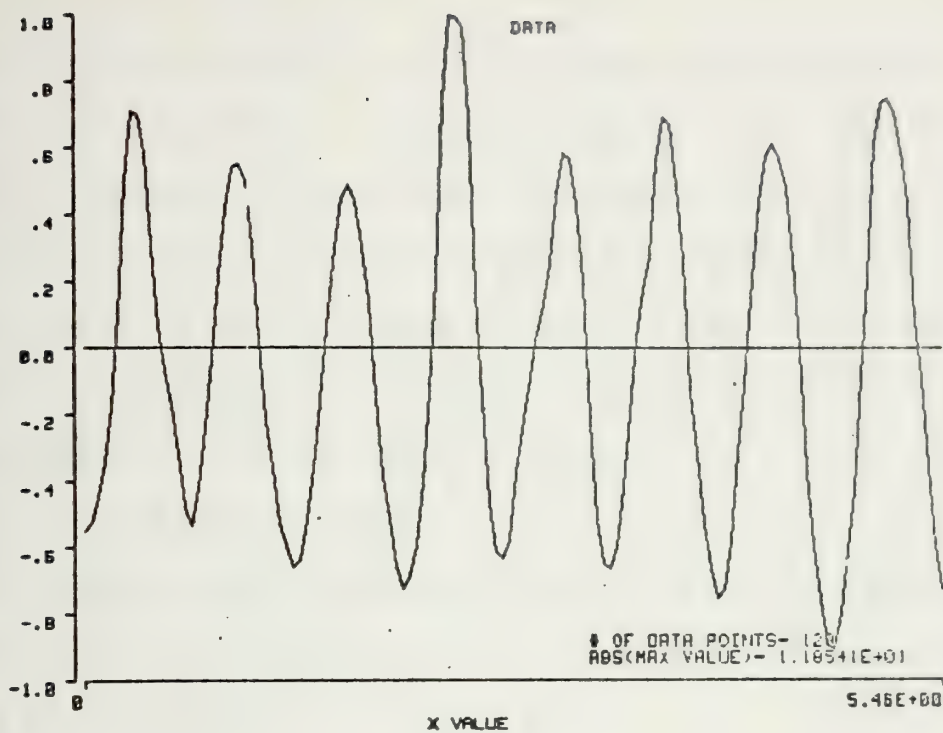


Fig. 121 Normalized lift force and Fourier coefficients for 5 in. smooth cylinder, $\zeta = 0.054$, (with lead blocks).

on either side of the predominant frequency. It is found that the instantaneous lift force, as well as displacement, may be represented fairly well through the use of their predominant and two or three additional, most significant, harmonics. Figures 122a through 122c show the Fourier representation of a sample displacement trace for a 4 in. rough cylinder with one, two, and three Fourier components, respectively. Similar results for the force trace are shown in Figs. 123a - 123e. Evidently, the displacement is fairly well represented by the first three components. The force trace for the particular cylinder required the use of four Fourier components.

The occurrence of the predominant frequency at $9f_w$ is not without a reason. If the Strouhal number is defined in terms of the maximum velocity U_m , then one has

$$S = \frac{f_v D}{U_m} \quad (37)$$

which varies from about 0.1 to 0.23 during a cycle in harmonic flow. Multiplying the numerator and the denominator by T , the period of the flow oscillation, one has

$$S = \frac{f_v D T}{U_m T} = \frac{f_v T}{K} \quad (38)$$

It is fully realized that the vortex shedding frequency f_v does not remain constant throughout the cycle. In fact, f_v is largest near the instant of U_m and decreases as U approaches zero. Consequently, the fundamental question as to which representative vortex shedding frequency

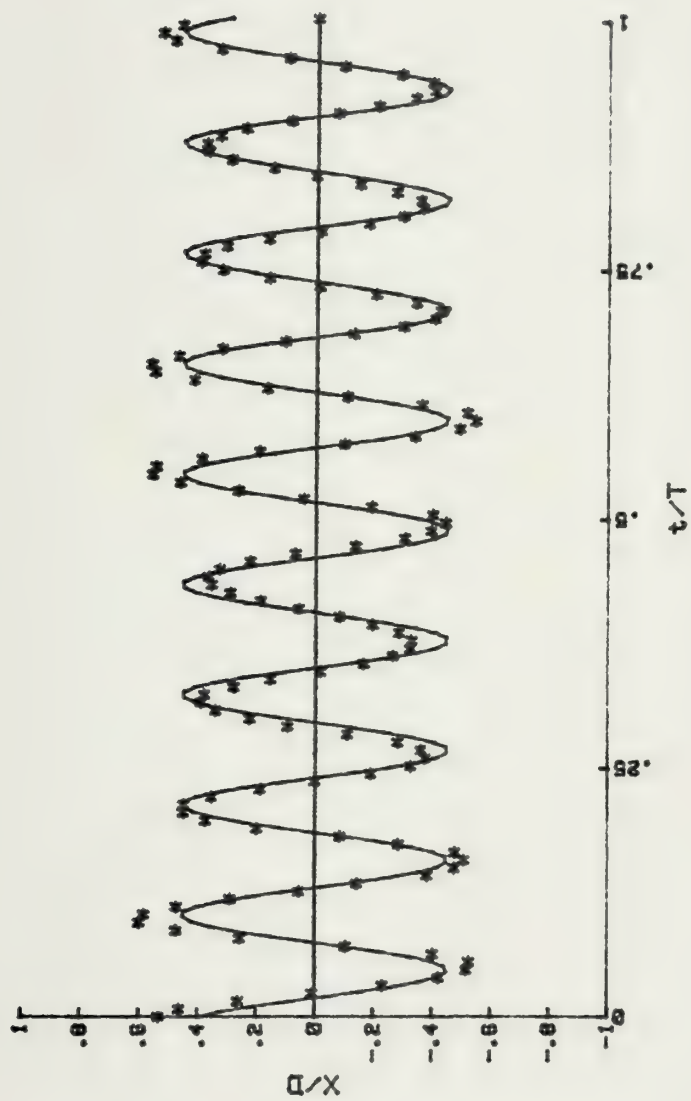


Fig. 122a Predominant harmonic representation of the displacement trace for a 4 in. rough cylinder, $\zeta = 0.030$.

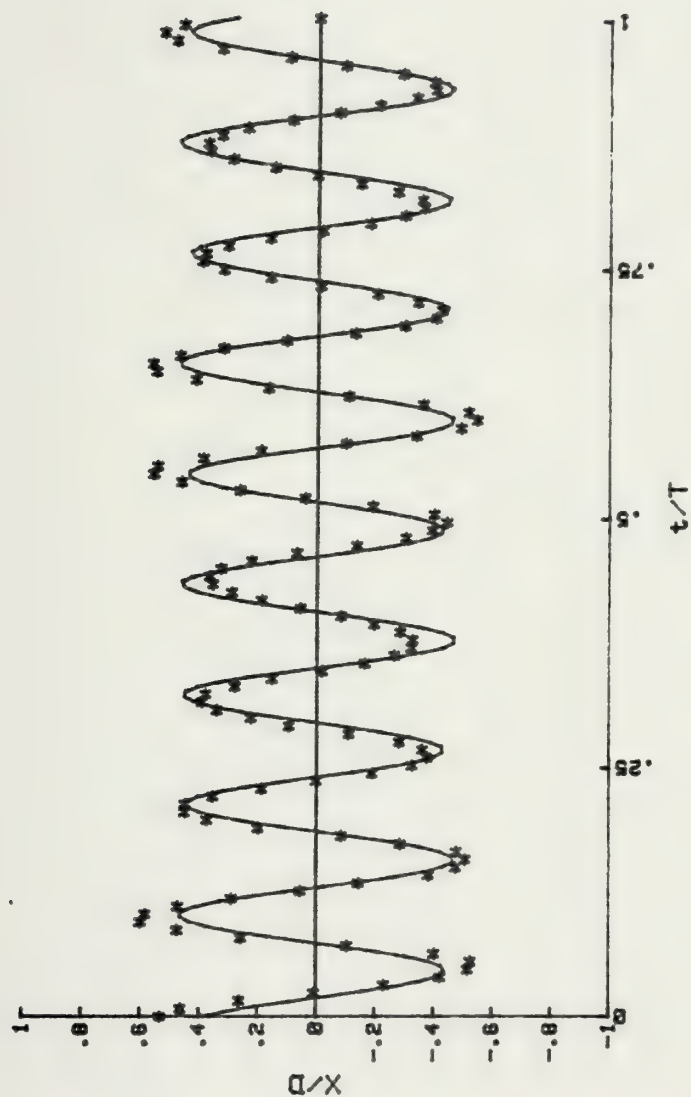


Fig. 122b Two-term Fourier series representation of the displacement trace for a 4 in. rough cylinder, $\zeta = 0.030$.

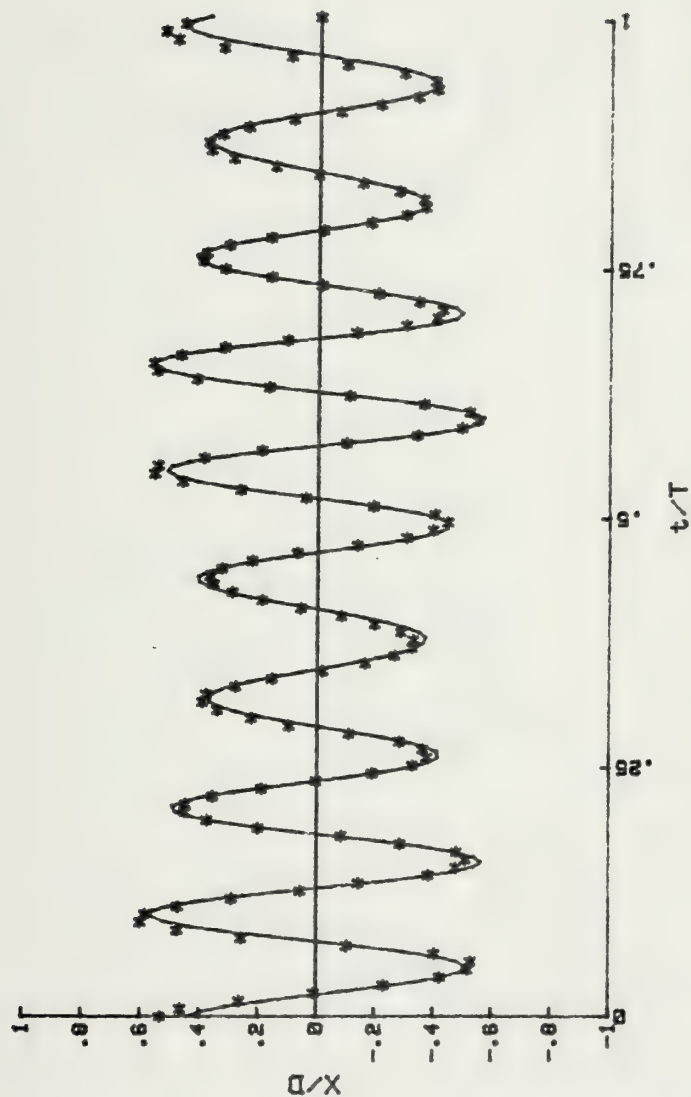


Fig. 122c Three-term Fourier series representation of the displacement trace for a 4 in. rough cylinder, $\zeta = 0.030$.

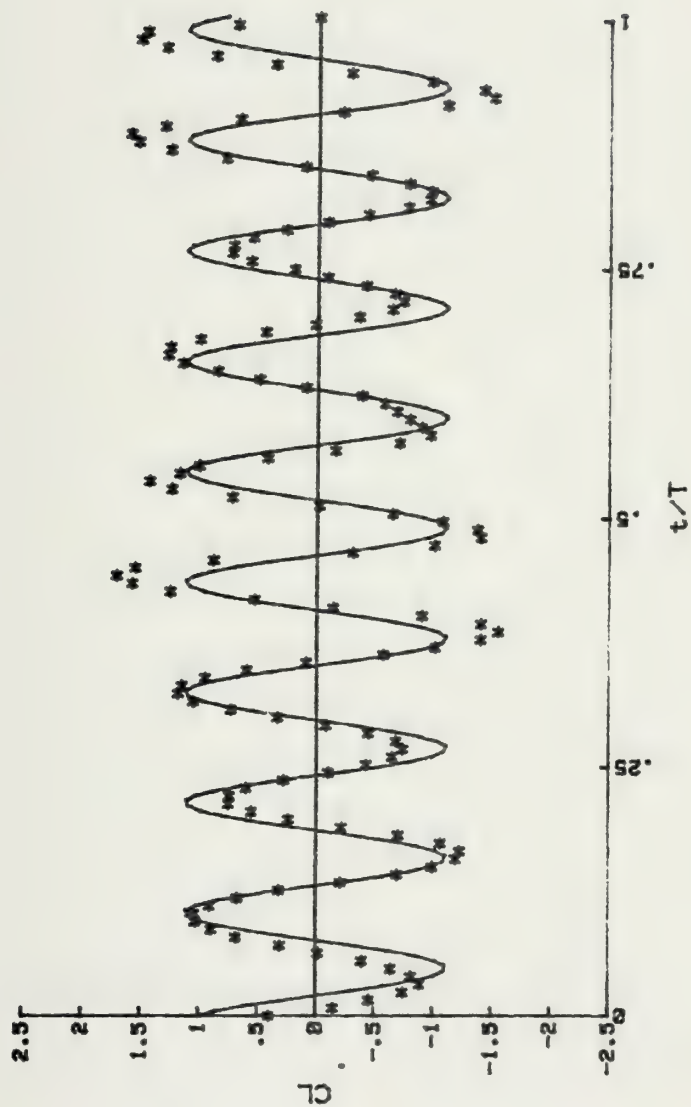


Fig. 123a Predominant harmonic representation of the force trace for a 4 in. rough cylinder, $\zeta = 0.030$.

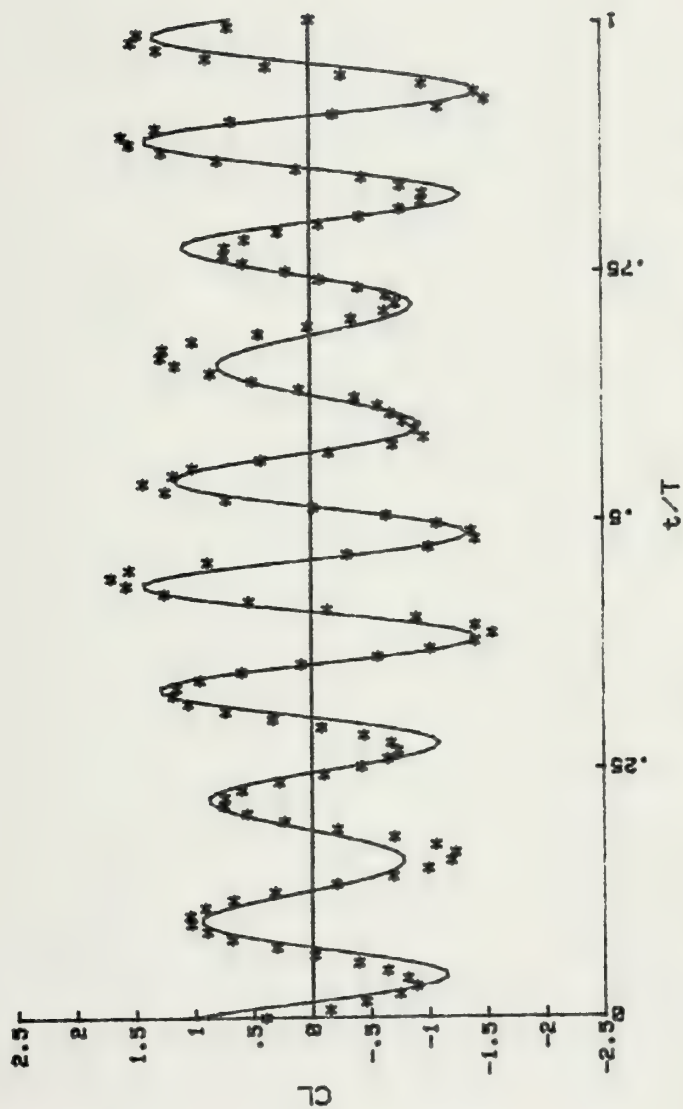


Fig. 123b Two-term Fourier series representation of the force trace for a 4 in. rough cylinder, $\zeta = 0.030$.

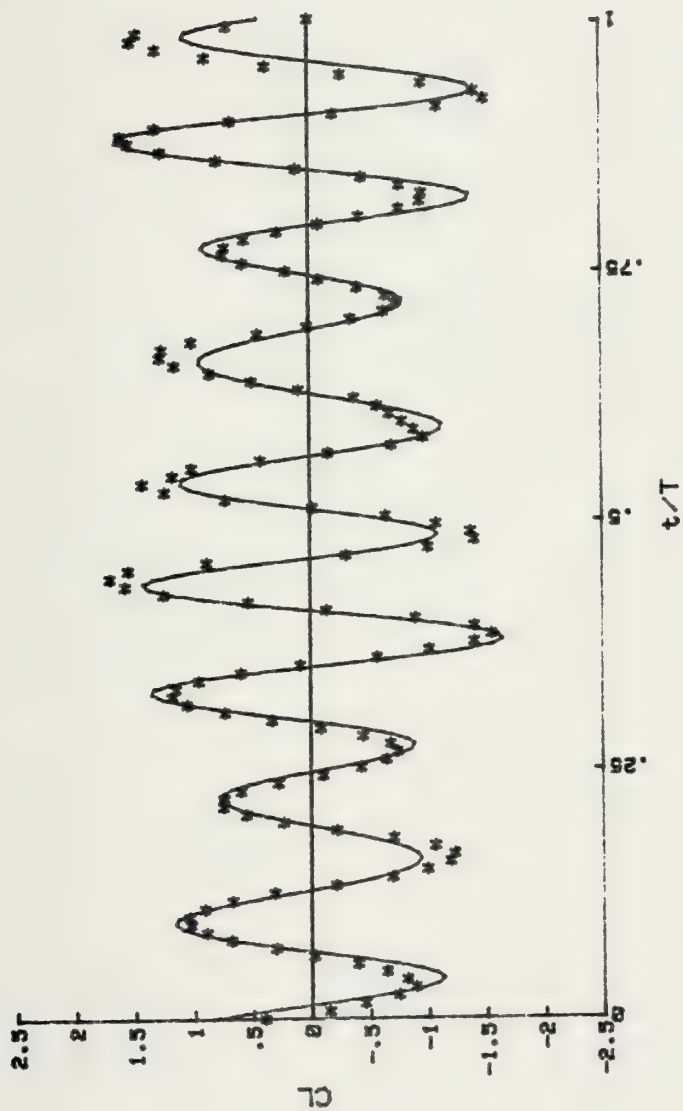


Fig. 123c Three-term Fourier series representation of the force trace for a 4 in. rough cylinder, $\zeta = 0.030$.

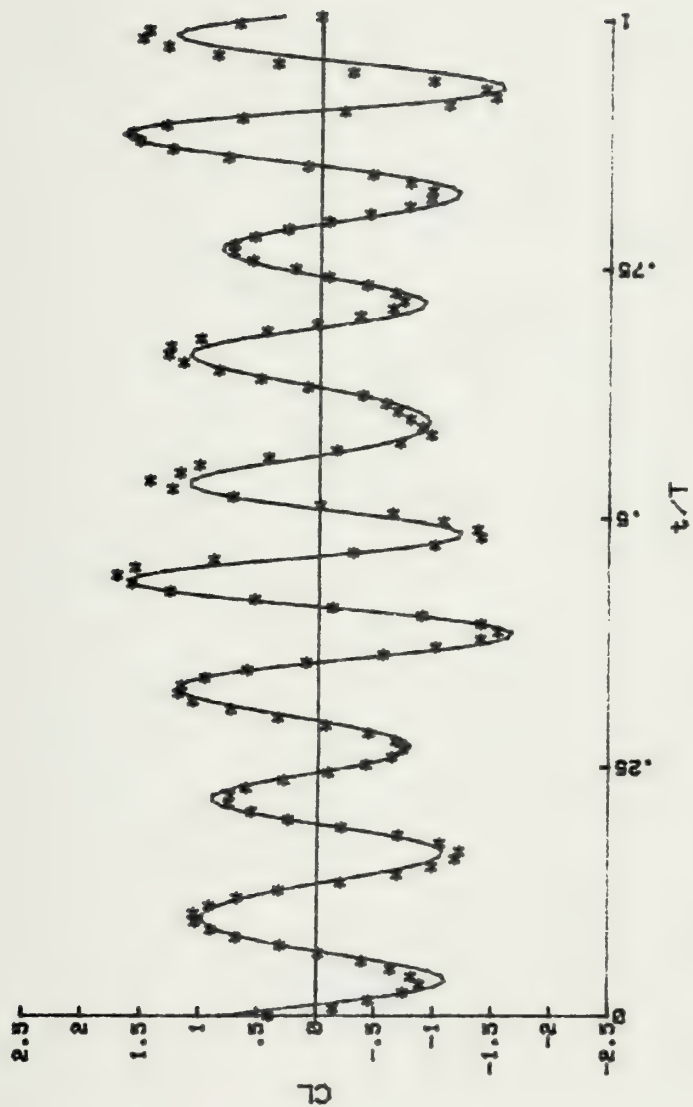


Fig. 123d Four-term Fourier series representation of the force trace for a 4 in. rough cylinder, $\zeta = 0.030$.

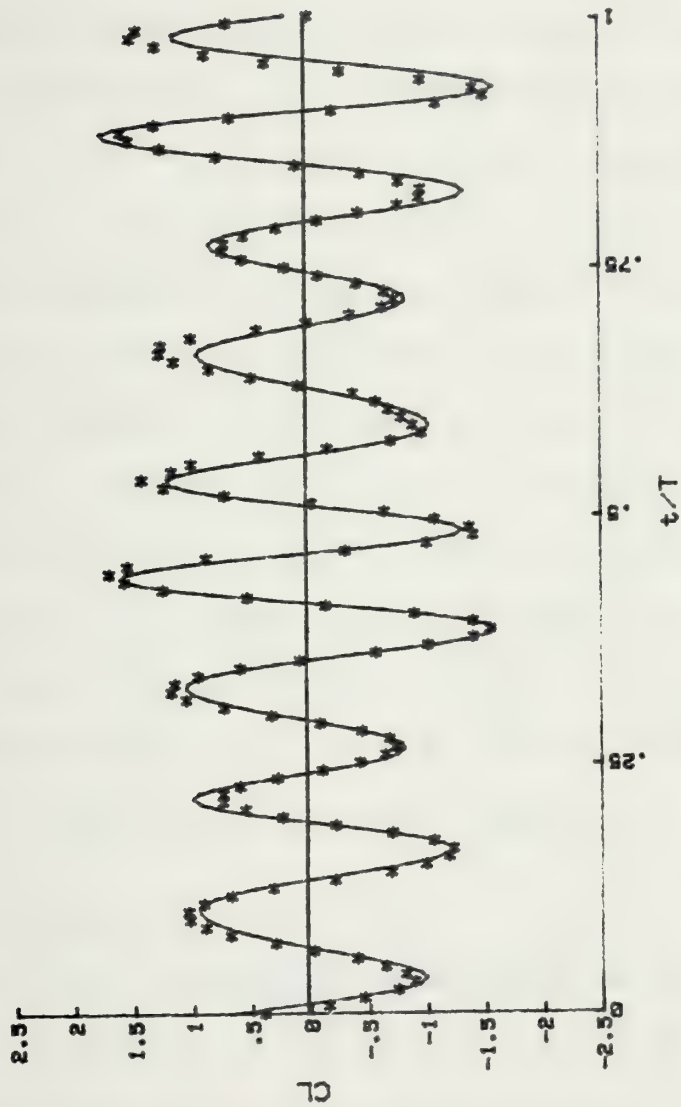


Fig. 123e Five-term Fourier series representation of the force trace for a 4in. rough cylinder, $\zeta = 0.030$.

the cylinder oscillation synchronizes may be answered only through the Fourier analysis. Replacing f_v by N/T one has $SK = N$. In the present investigation the synchronization occurs in the range of Kelulegan-Carpenter numbers from about 48 to 60. With $N = 9$, one has $S = 0.15 - 0.18$. Using a value of $S = 0.16$ for the perfect synchronization (at which the displacement is maximum) one finds $K = 56$. In other words, the cylinder undergoes synchronized oscillations when the natural frequency of the cylinder coincides with the vortex shedding frequency based on a Strouhal number of 0.16, as verified by the experiments. Consequently the integer N may be smaller or larger depending on the Keulegan-Carpenter number at which synchronization is realized. For example, for a cylinder whose natural frequency is twice the flow oscillation frequency ($N = 2$), the synchronization takes place at $K = 12.5$. This result is in conformity with the results of Sawaragi [99]. However, the Keulegan-Carpenter number in his experiments is based on the rms value of the wave induced velocities along the vertical cylinder. Thus, an exact verification of the corresponding results is not possible. Finally, it should be noted that the use of the rms value of the flow velocity and the frequency at which perfect synchronization takes place results in $S = 0.22$.

D. SPECTRAL ANALYSIS

The spectral density, coherence, and phase at perfect synchronization are shown in Figs. 124 and 125 for the 3 in. smooth and 4 in. rough cylinders. Similar results in the non-synchronization region are shown in Figs. 126 and 127 for a representative value of $K = 80$. The spectral density for a broad range of K values for the 3 in. cylinder is shown in Figs. 128 through 143 in Appendix E. Similar data for the 4 in. rough cylinder are shown in Figs. 144 through 158 in Appendix F.

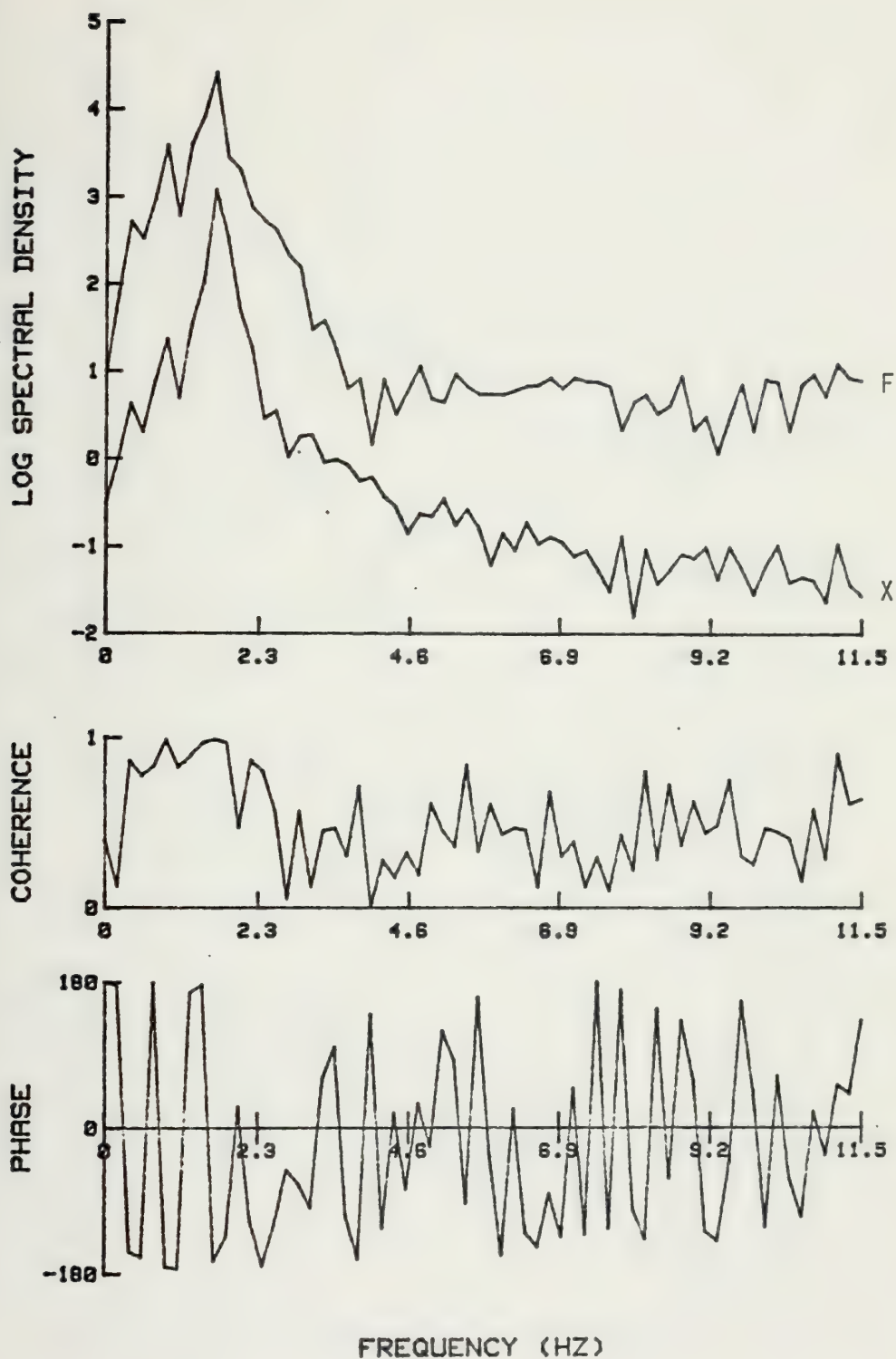


Fig. 124 Spectral analysis for a 3 in. smooth cylinder at resonance, $\zeta = 0.052$, $K = 51$.

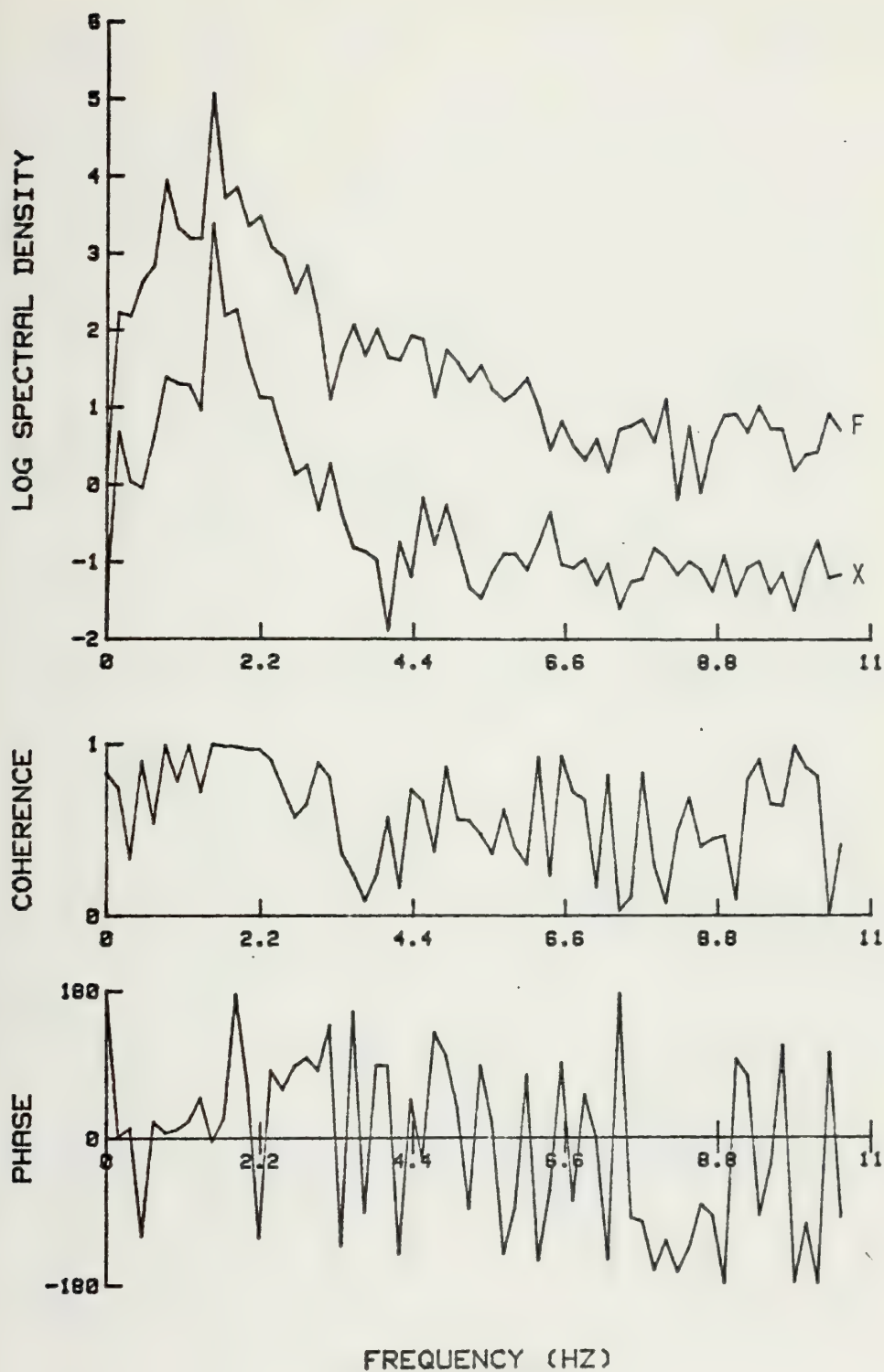


Fig. 125 Spectral analysis for a 4 in. rough cylinder at resonance, $\zeta = 0.030$, $K = 49$.

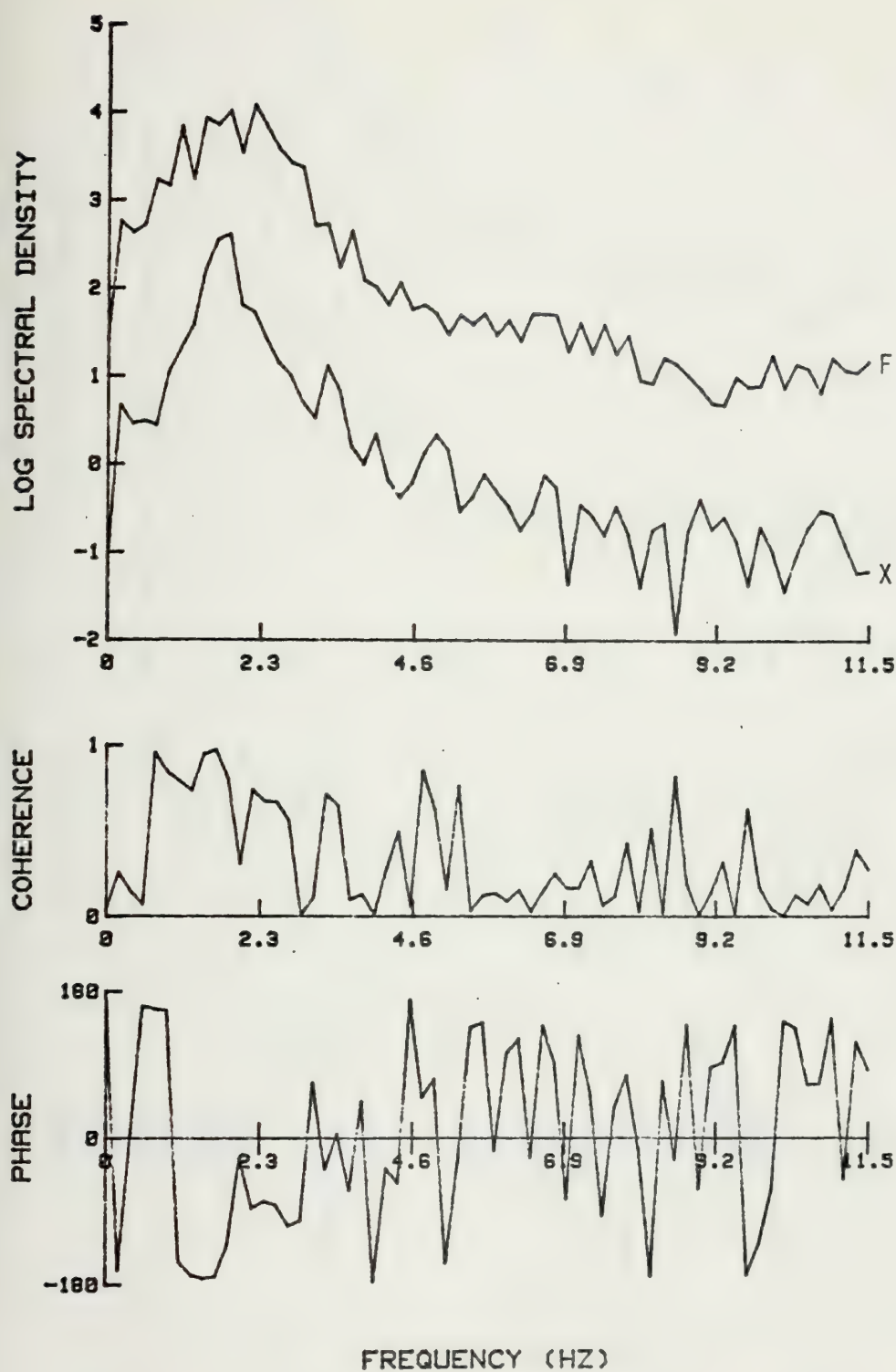


Fig. 126 Spectral analysis for a 3 in. smooth cylinder,
 $\zeta = 0.052$, $K = 80$.

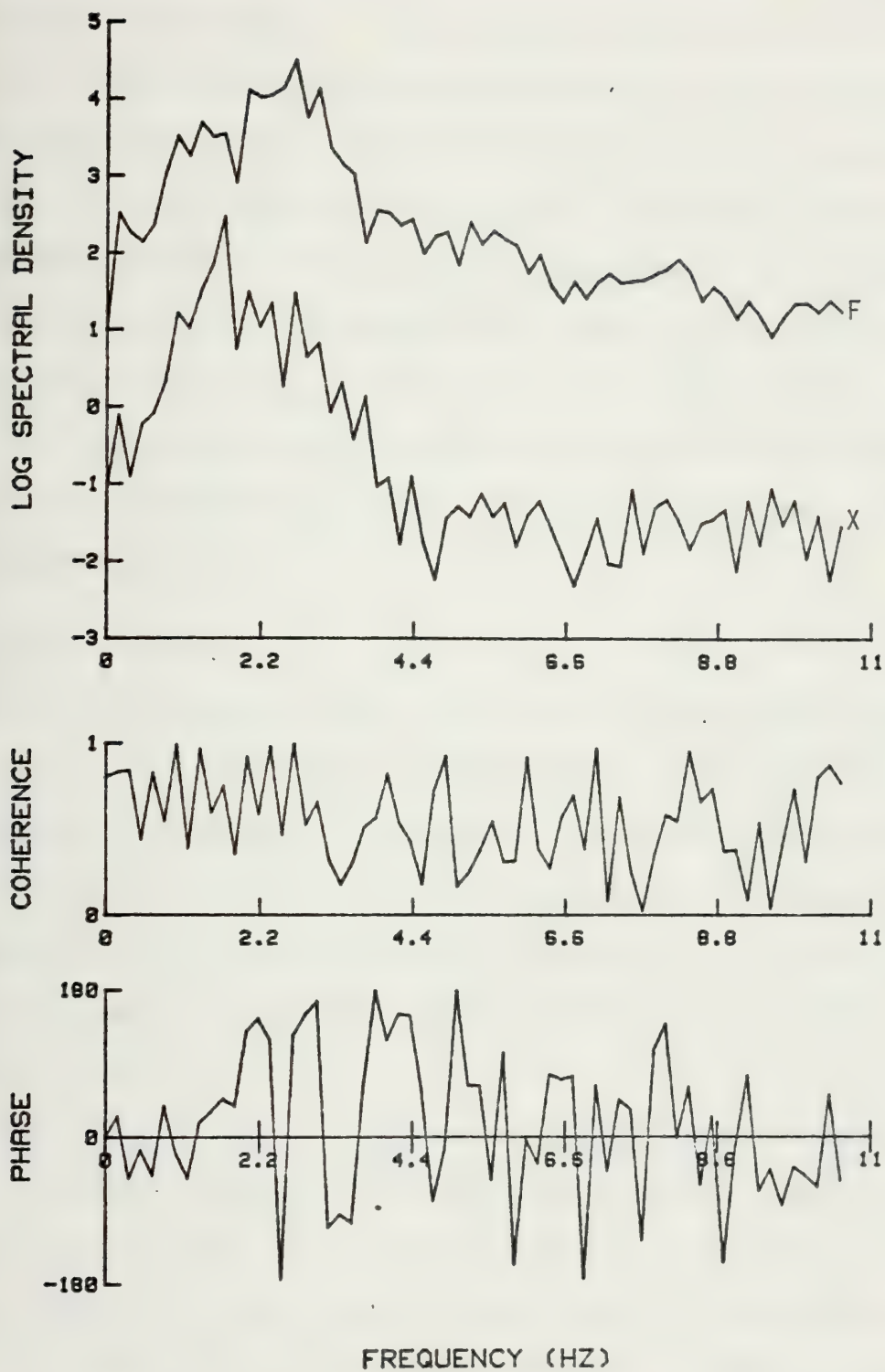


Fig. 127 Spectral analysis for a 4 in. rough cylinder,
 $\zeta = 0.030$, $K = 80$.

It is clear from Figs. 124 and 125 that the spectral density is sharply defined at synchronization and the force and displacement peaks occur at the same frequency. Furthermore, the coherence is nearly perfect. In the non-synchronized region the spectral density for the force becomes broad band and the peaks of the displacement and force do not occur at the same frequency as seen from Figs. 126 and 127. The peak of the displacement is relatively better defined and continues to occur near the natural frequency of the cylinder ($f_{nw} = 1.69$ for the 3 in. smooth cylinder and $f_{nw} = 1.54$ for the 4 in. rough cylinder). The results of the spectral analysis confirm the findings of the Fourier analysis that at resonance the force and displacement maximums occur at the same frequency.

E. DUHAMEL'S INTEGRAL

Figures 159 through 163 show a comparison of the measured and calculated values of the instantaneous displacement as a function of time. The measured force shown in the upper half of each figure was used as input in Duhamel's integral, as given by Eq. (34). The close agreement between the measured and calculated displacements is an indication of the proper measurement of the various quantities such as mass, damping ratio, frequency, etc.

A sensitivity analysis was carried out by varying the frequency f_n in Eq. (34) while maintaining all other input parameters unaltered. The purpose of this analysis was partly to explore whether the natural frequency of the oscillating cylinder remained equal to that determined in still water and whether the prediction of Duhamel's integral strongly depended on the natural frequency. The implication of the equivalence

of the natural frequency of the cylinder undergoing transverse oscillations in harmonic flow to that in still fluid is that the added mass of the synchronized cylinder is identical to the displaced mass of the cylinder. If, on the other hand, the natural frequency of the synchronized cylinder were to be higher than that in still water, one would conclude that the added mass of the synchronized cylinder is smaller than its displaced mass. Extensive calculations with various values of the natural frequency have shown that the natural frequency of the synchronized cylinder is 5 percent larger than that for the natural frequency in still water. The difference between the two frequencies may be partly due to the experimental errors and partly due to the difference between the actual added mass and displaced mass. King [112] conducted a series of experiments in still water (by plucking a cantilevered cylinder) and also in flowing water at the fundamental mode of the flow-excited vibrations. From a comparison of the measured frequencies he concluded that the still-water and flow-excited frequencies are virtually equal, i.e., the added mass is unaffected by streaming flow. Apparently, this conclusion is valid only at the resonance condition. The results of the present investigation also showed that the added mass is relatively unaffected by the harmonically oscillating flow. One must, however, note that the best agreement between the measured and calculated displacement is obtained with a natural frequency approximately 5 percent larger than the still-water natural frequency.

The foregoing also points out the important fact that a simple comparison of the natural frequencies measured in still water and in flowing water at resonance is not sufficient for an accurate assessment of the

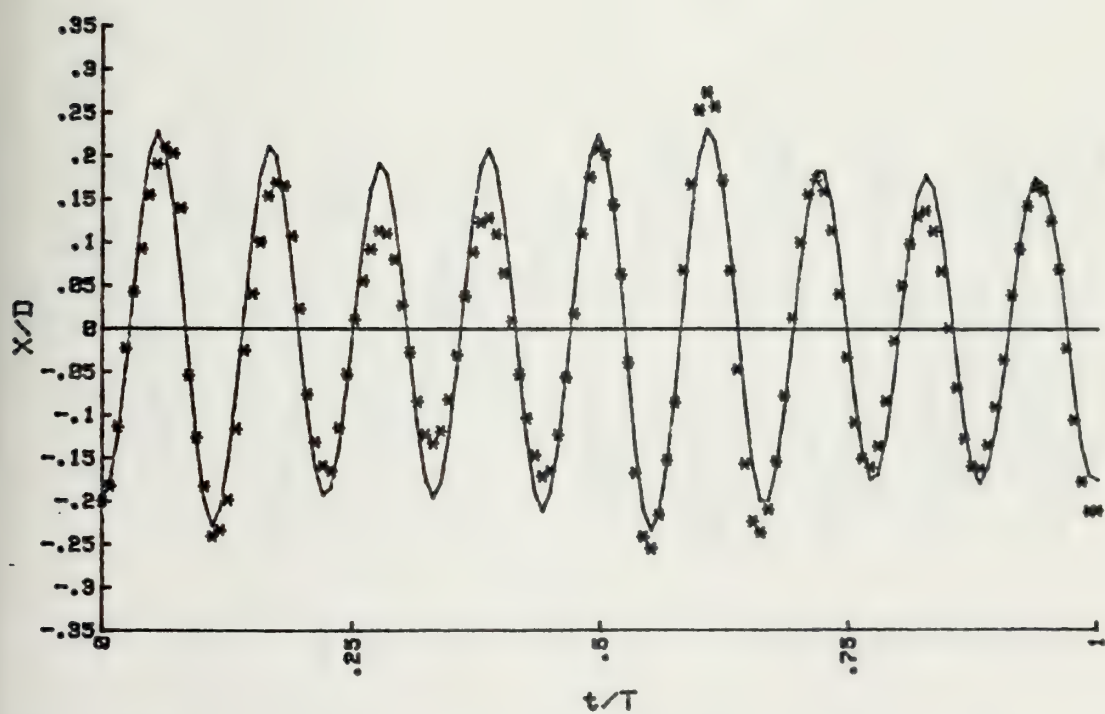
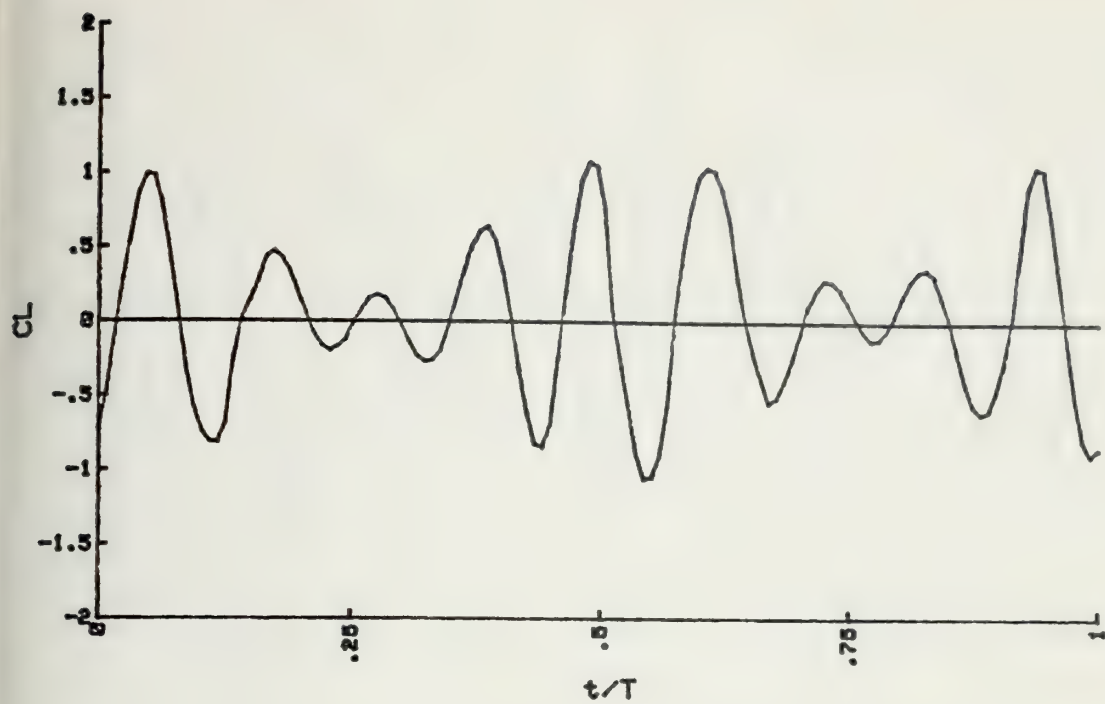


Fig. 159 Comparison of measured and calculated displacement by Duhamel's integral for a 3 in. smooth cylinder, $\zeta = 0.052$.

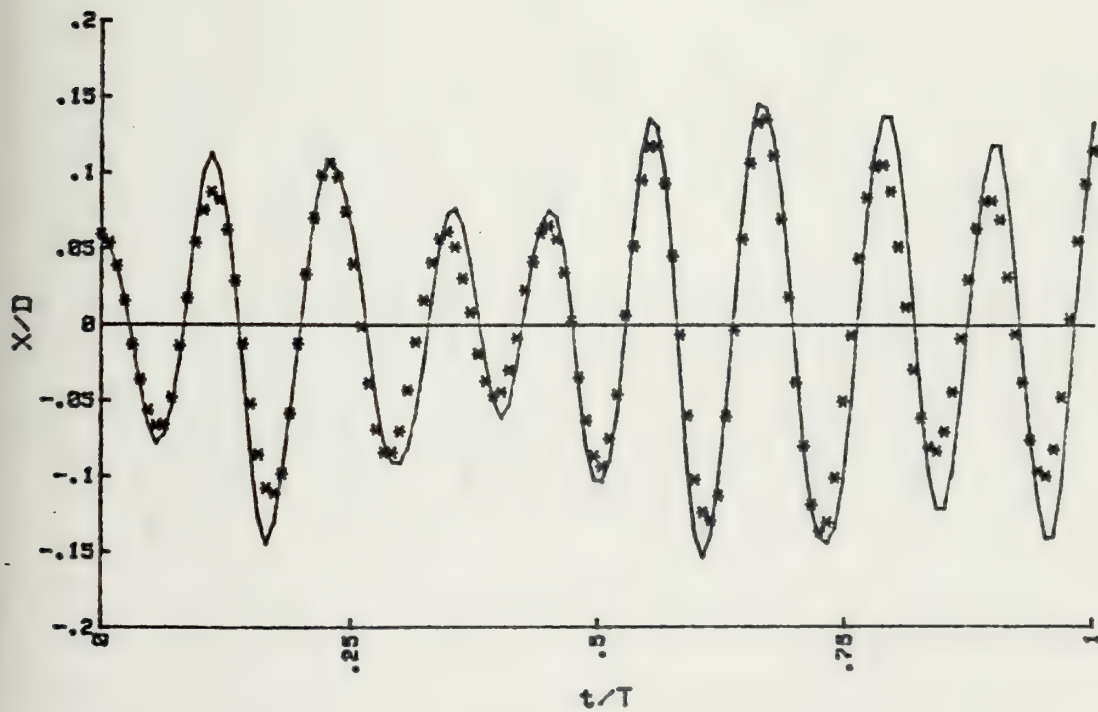
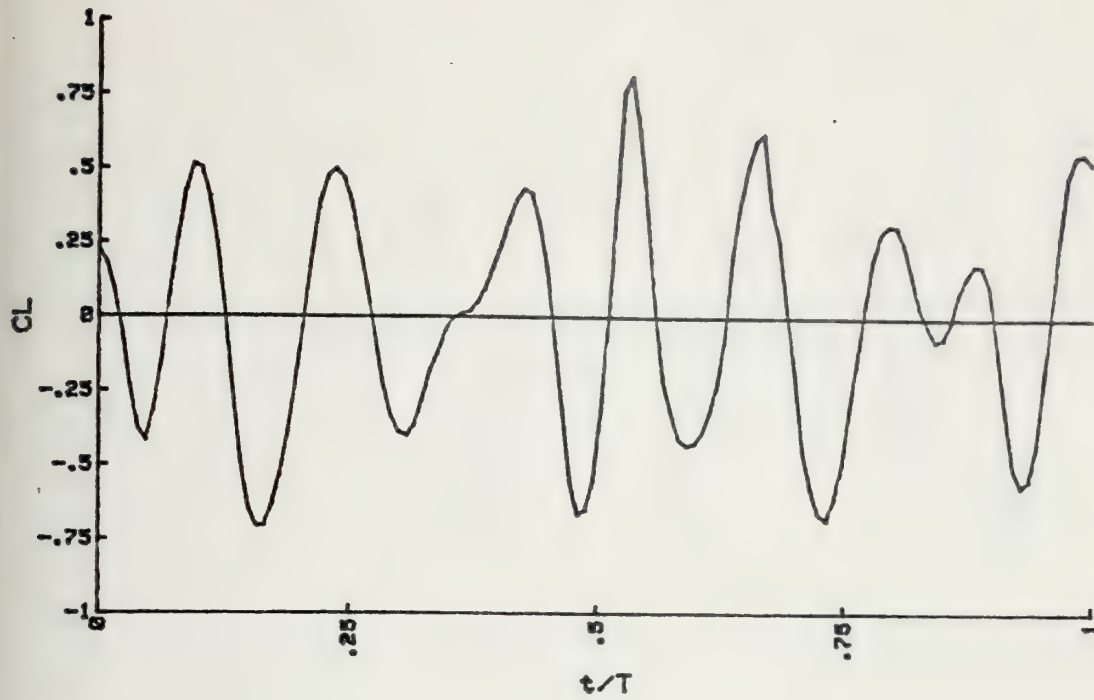


Fig. 160 Comparison of measured and calculated displacement by Duhamel's integral for a 4 in. smooth cylinder, $\zeta = 0.046$.

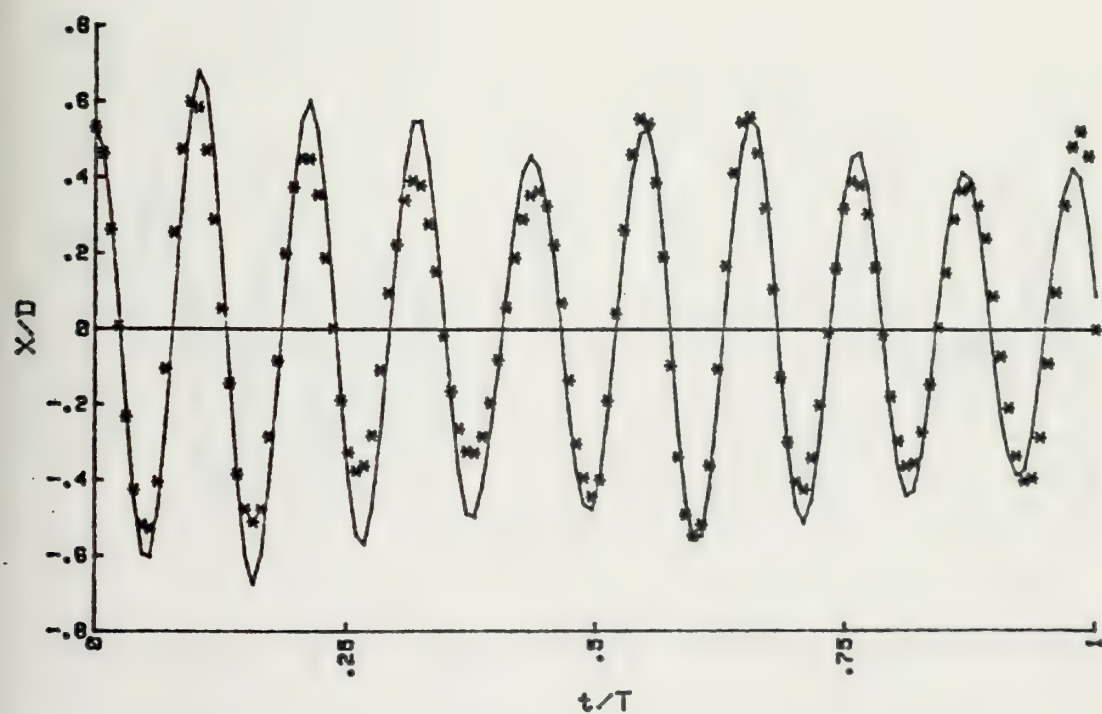
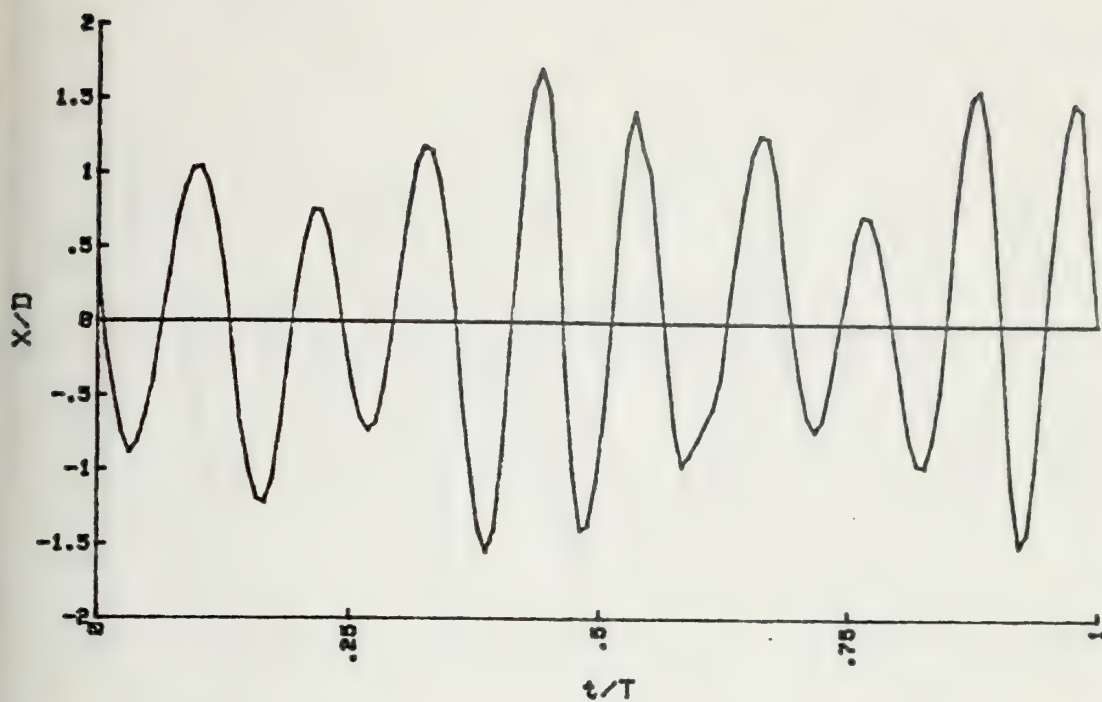


Fig. 161 Comparison of measured and calculated displacement by Duhamel's integral for a 4in. rough cylinder, $\zeta = 0.030$.

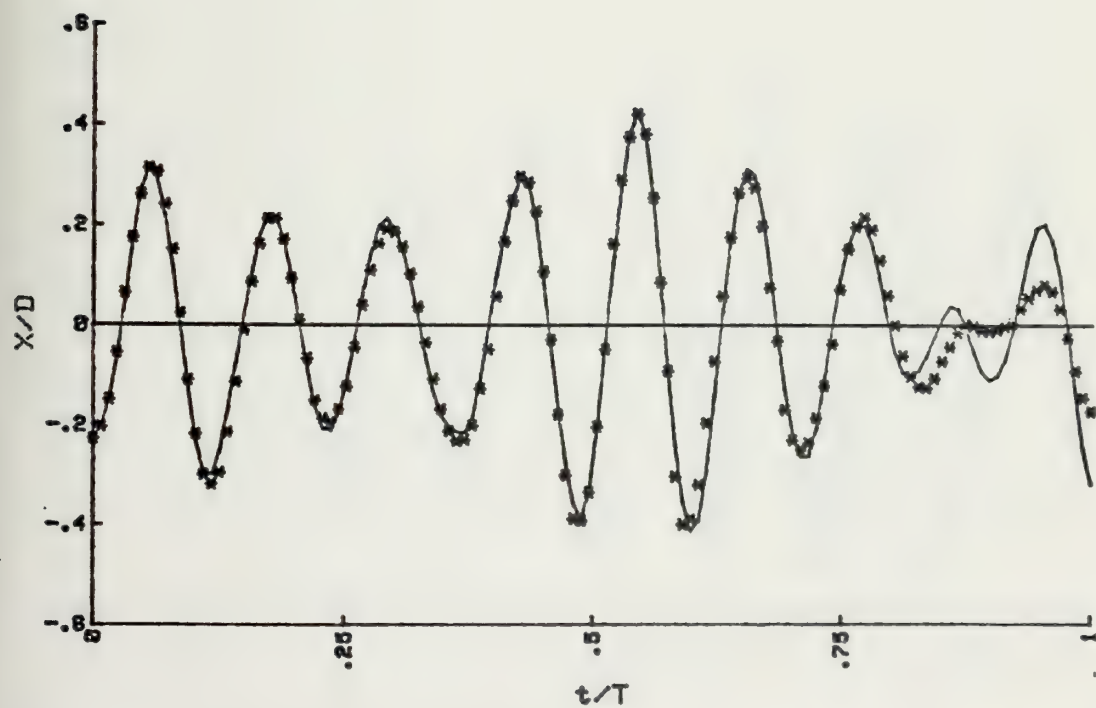
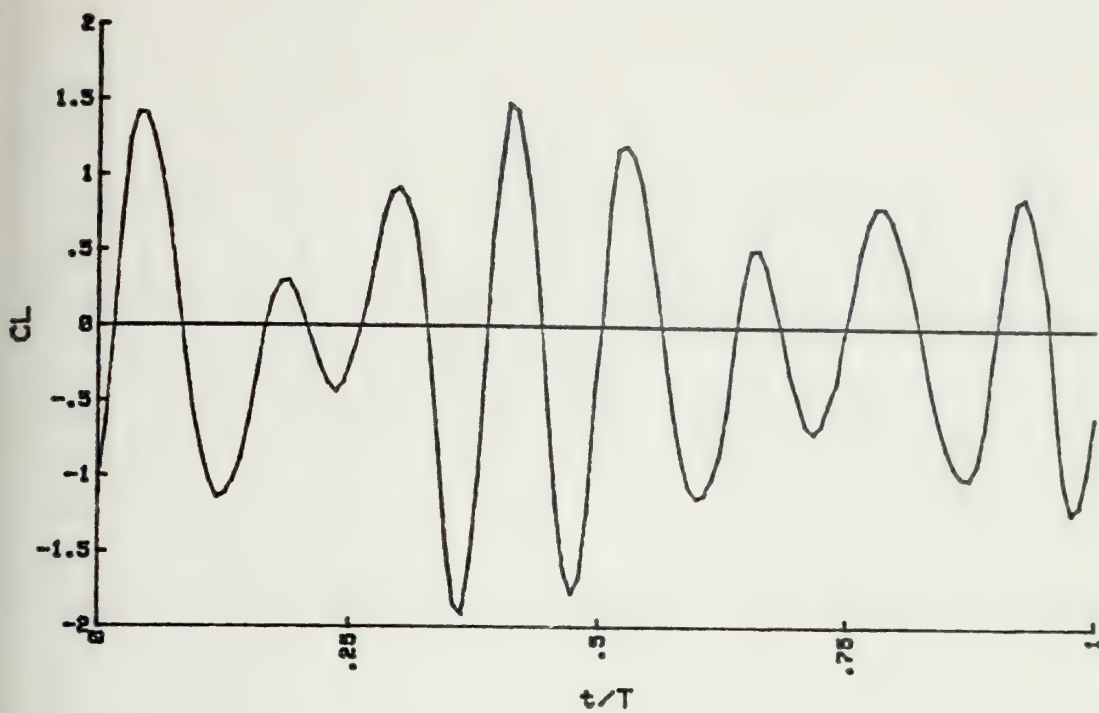


Fig. 162 Comparison of measured and calculated displacement by Duhamel's integral for a 4in. rough cylinder, $\zeta = 0.060$.

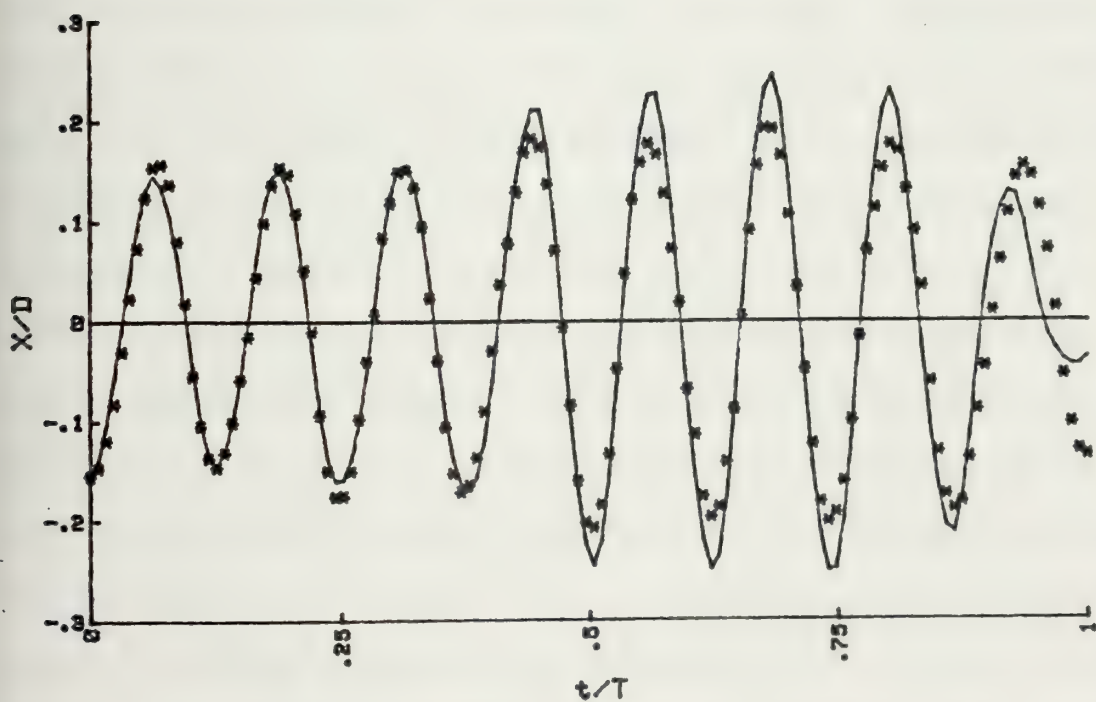
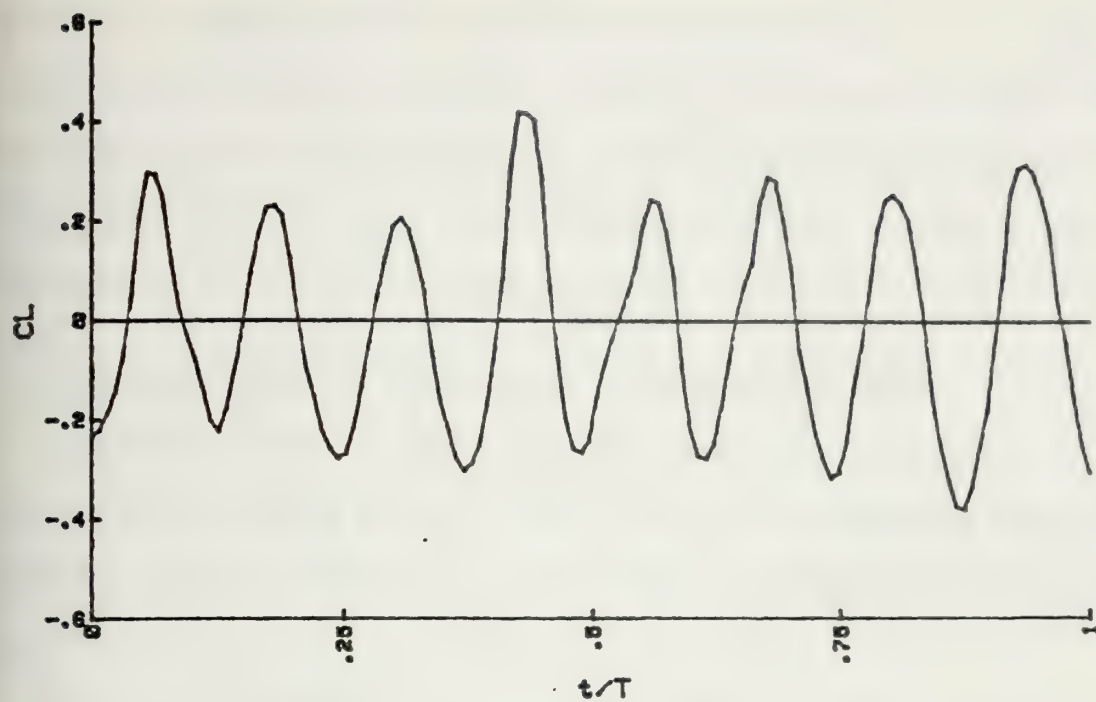


Fig. 163 Comparison of measured and calculated displacement by Duhamel's integral for a 5in. smooth cylinder, $\zeta = 0.054$.

variation or lack of variation of the added mass. The use of Duhamel's integral is a more reliable method for the determination of the natural frequency at resonance. Be that as it may, it is rather surprising that the added mass of a body oscillating, at its natural frequency, in a fluid otherwise at rest, is nearly the same with that undergoing synchronized oscillations in a fluid in motion.

F. DRAG COEFFICIENT FOR TRANSVERSELY OSCILLATING CYLINDERS

Experiments with cylinders undergoing transverse oscillations in steady flow have shown that [113] the in-line force increases with X/D since the cylinder presents a larger apparent projected area to the mean flow.

From an engineering viewpoint, the significance of the magnitude of the in-line force is that a cylinder or cable excited by the flow to oscillate in the transverse direction may be subjected to in-line forces larger than those assumed in its design. Furthermore, the deflections caused by the in-line force of sufficiently flexible cylinders tend to couple with transverse oscillations and affect not only the magnitude of the transverse oscillations but also the path of the cylinder motion. It is because of these reasons that the in-line force acting on the cylinders undergoing oscillations in the transverse direction to the harmonic flow has been measured. The drag coefficient has been determined through the use of Eq. (31) and is shown in Figs. 164 through 166 for three representative cylinders. Also shown in these figures are the mean lines for the drag coefficient of the corresponding stationary cylinders. In general, the oscillating-cylinder drag coefficients are larger than those for the stationary cylinder. However the increase is not as dramatic as in the case of steady flow about vibrating cylinders [114].

The inertia coefficient C_m has also been evaluated and it was found that it did not differ from that for stationary cylinders. This is primarily because of the fact that at Keulegan-Carpenter numbers larger than about 30 the in-line force is primarily drag dominated and the effect of the inertial force is negligible [see Eq. (30)].

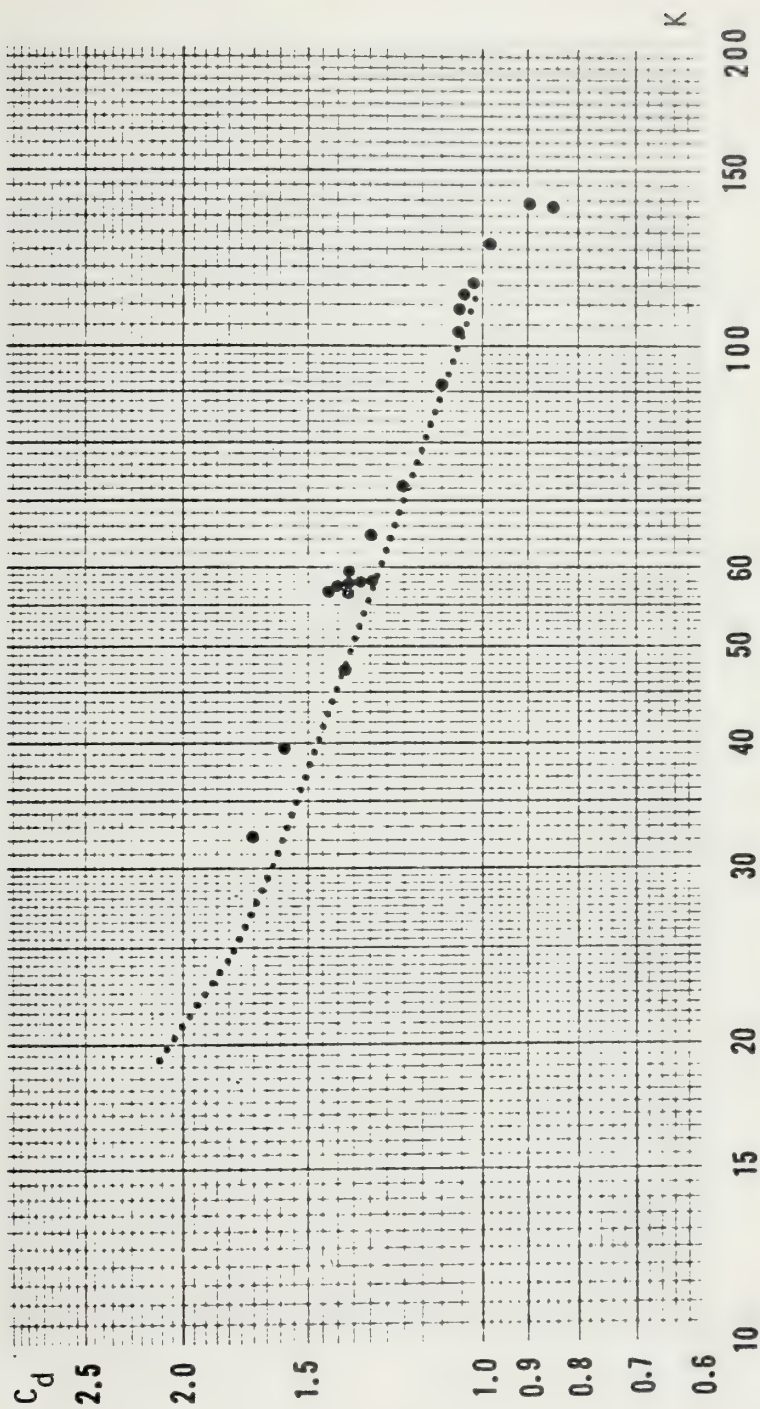


Fig. 164 C_d versus K for a 3 in. smooth cylinder, $\zeta = 0.052$.

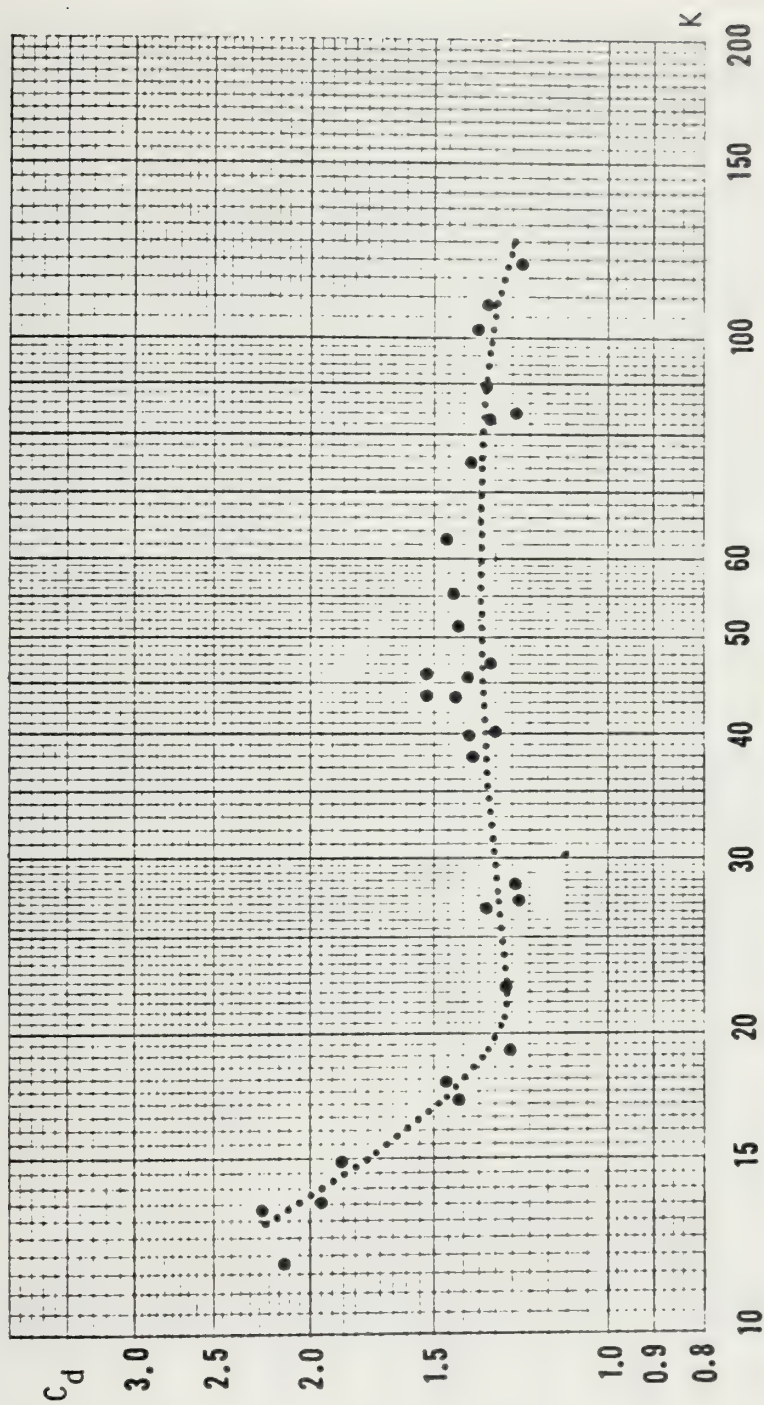


Fig. 165 C_d versus K for a 3 in. rough cylinder, $z = 0.067$.

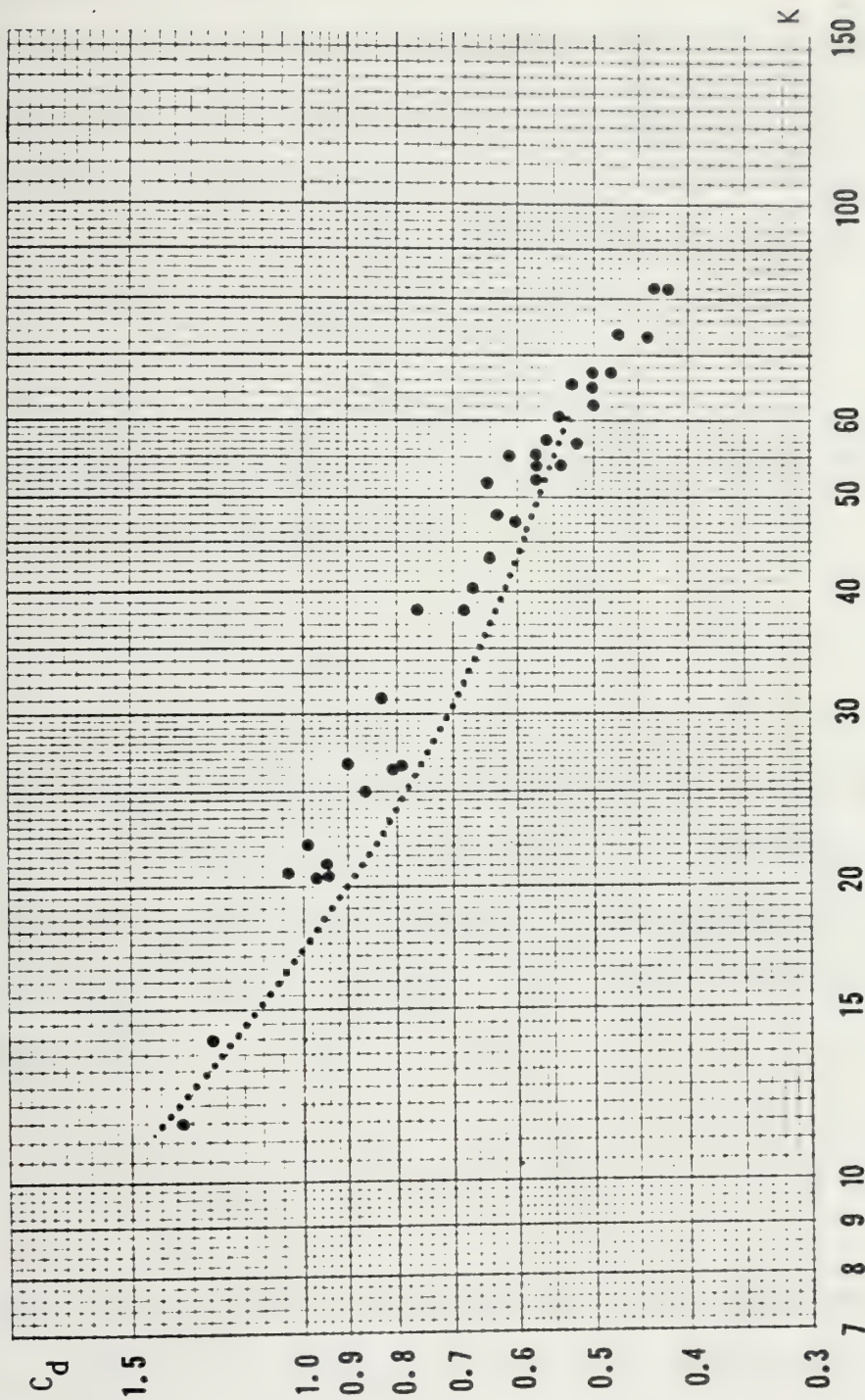


Fig. 166 C_d versus K for a 5 in. smooth cylinder, $\zeta = 0.055$.

V. ANALYSIS AND DISCUSSION OF RESULTS

A. INTRODUCTION

In the following, the results obtained with various analyses and models will be compared with those obtained experimentally. First the general equation of motion will be presented and then the oscillator model of Hartlen and Currie [87] will be discussed with reference to the experimental data presented in the previous chapter.

B. EQUATION OF MOTION AND COMPARISON OF RESULTS

The equation of motion for an elastically-mounted and linearly-damped cylinder may be written as

$$M \ddot{X} + 2 M \omega_n \zeta \dot{X} + K_S = F_L(t) \quad (39)$$

where X represents the transverse displacement of the cylinder; M , the mass of the cylinder plus the displaced mass; ζ , the damping ratio in still water; ω_n , the natural frequency of the synchronized cylinder; K_S , the spring constant; and $F_L(t)$, the exciting force. $F_L(t)$ may be presented by

$$F_L(t) = \frac{1}{2} \zeta D L (C_L^\circ)_{rms} U_m^2 C_L(t)/(C_L^\circ)_{rms} \quad (40)$$

in which $(C_L^\circ)_{rms}$ is the lift coefficient for the stationary cylinder at the corresponding Keulegan-Carpenter number and Reynolds number.

The ratio $C_L(t)/(C_L^\circ)_{rms}$ represents the amplification of the lift force

at or in the neighborhood of perfect synchronization. Even during the period of nearly perfect synchronization the exciting force does not retain a constant amplitude and frequency. This fact has already been demonstrated through the use of the Fourier analysis. In general, it is necessary to consider the harmonics of the lift force. Rewriting Eq. (36), one has

$$C_L(t) = \sum_{n=1}^{\infty} \bar{C}_{Ln} \cos(2\pi n f_f t/T) \quad (36 - \text{repeated})$$

Inserting $C_L(t)$ in Eqs. (39) and (40), one obtains a differential equation which may be solved by assuming

$$X(t) = \sum_{n=1}^{\infty} \bar{X}_n \cos(2\pi n f_f t/T + \phi_n) \quad (35 - \text{repeated})$$

The general solution of Eq. (39) is given by

$$\frac{X}{D} = \sum_{n=1}^{\infty} \frac{\frac{1}{2} \left[\frac{\rho L D^2}{M} (C_L^\circ)_{\text{rms}} \right] \left(\frac{U_m}{\omega_n D} \right)^2 \bar{C}_{Ln} / (C_L^\circ)_{\text{rms}}}{\left\{ \left[1 - \left(\frac{n\omega_f}{\omega_n} \right)^2 \right]^2 + \left(2\zeta \frac{n\omega_f}{\omega_n} \right)^2 \right\}^{1/2}} \cos(n\omega_f t/T + \phi_n) \quad (41)$$

The relative amplitude \bar{X}_n/D is thus given by

$$\frac{\bar{X}_n}{D} = \frac{\frac{1}{2} \left[\frac{\rho L D^2}{M} (C_L^\circ)_{\text{rms}} \right] \left(\frac{U_m}{\omega_n D} \right)^2 \bar{C}_{Ln} / (C_L^\circ)_{\text{rms}}}{\left\{ \left[1 - \left(\frac{n\omega_f}{\omega_n} \right)^2 \right]^2 + \left(2\zeta \frac{n\omega_f}{\omega_n} \right)^2 \right\}^{1/2}} \quad (42)$$

Finally, the phase angle reduces to

$$\phi_n = -\tan^{-1} \left[\frac{2 \zeta \frac{n\omega_f}{\omega_n}}{1 - \left(\frac{n\omega_f}{\omega_n} \right)^2} \right] \quad (43)$$

The amplification ratios $\bar{C}_{Ln}/(C_L^\circ)_{rms}$ have been evaluated for the fundamental and two harmonics through the use of the Fourier-decomposed exciting force. The results have shown that the said ratio for the predominant harmonics at synchronization are given by

$$C_{Lp_1}/(C_L^\circ)_{rms} = 2.75 \pm 0.15 \quad (44a)$$

$$C_{Lp_2}/(C_L^\circ)_{rms} = 1.15 \pm 0.10 \quad (44b)$$

$$C_{Lp_3}/(C_L^\circ)_{rms} = 0.70 \pm 0.07 \quad (44c)$$

$$(C_L(t))_{rms}/(C_L^\circ)_{rms} = 2.80 \pm 0.20 \quad (44d)$$

in which p_i represents the predominant harmonics (see Figs. 114-121).

The $(C_L^\circ)_{rms}$ values for the corresponding stationary cylinders were taken from the data presented in [101].

It is rather remarkable that the amplification ratios at synchronization remain fairly constant in spite of the wide range of the test parameters. Consequently, they can be used with confidence in the prediction of the relative amplitude of the cylinder oscillations. It should be noted, in passing, that there is, at present, no theoretical means to predict the amplitude ratios. The use of the Navier-Stokes

equations is limited to very small Reynolds numbers. The discrete-vortex model is limited to steady flow about stationary and oscillating cylinders [10]. It is not currently possible to apply the discrete-vortex model to the hydroelastic oscillation of cylinders in harmonically oscillating flow. This is primarily because of the difficulty of the determination of the numerous and mobile separation points on the cylinder. Consequently, one must rely on the experimentally determined values of the amplification ratios in predicting the cylinder response.

Equations (44a) through (44c) together with Eq. (41) have been used to predict the response of all the cylinders. Figures 167 and 168 show two of these plots where the predicted and measured responses are seen to compare reasonably well. Similar comparisons with all other cylinders proved to be equally satisfactory.

A critical examination of the relative significance of the second and third harmonics on the cylinder response has shown that the response is largely determined by the predominant harmonic. This has already been anticipated because of the fact that the second and third harmonics of the relative displacement are an order of magnitude smaller than the predominant harmonic (see Figs. 106-113). Assuming that the fundamental harmonic of the exciting force is representable by $(C_L)_{rms}$ and that $\omega_f \approx \omega_n$ at synchronization, Eq. (42) reduces to

$$\frac{\bar{X}}{D} = \frac{(U_m/f_n D)^2 [(C_L)_{rms}/(C_L^o)_{rms}]}{16\pi^2 M\zeta / [\zeta L D^2 (C_L^o)_{rms}]} \quad (45)$$

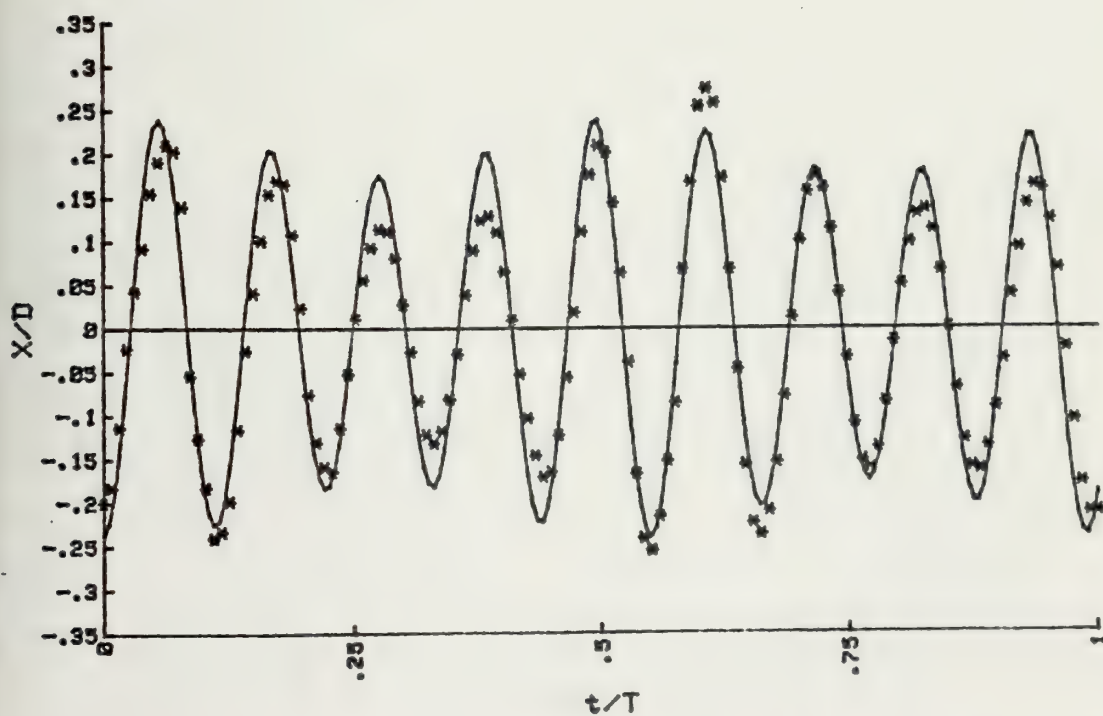
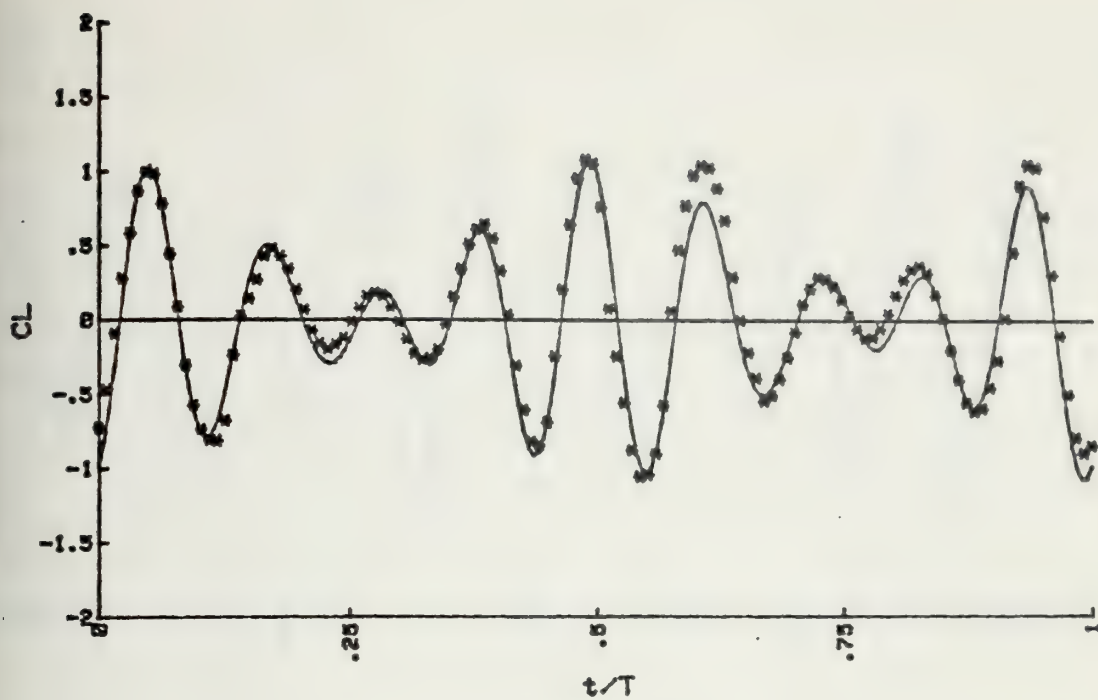


Fig. 167 Measured and predicted response for a 3 in. smooth cylinder, $\zeta = 0.052$.

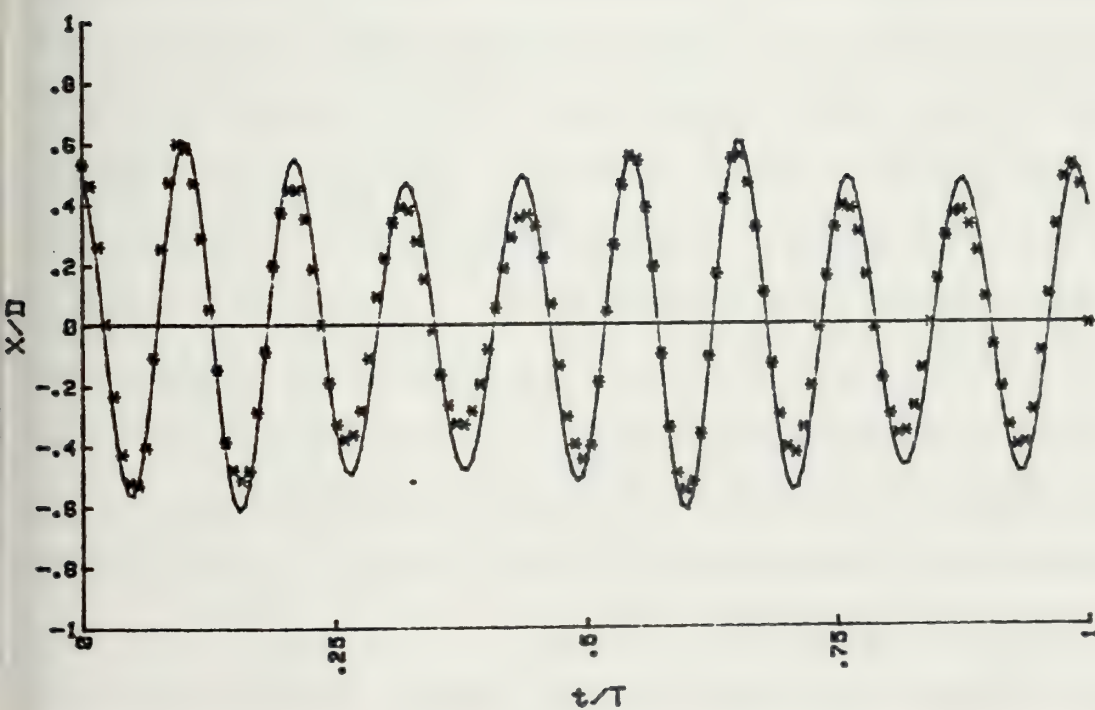
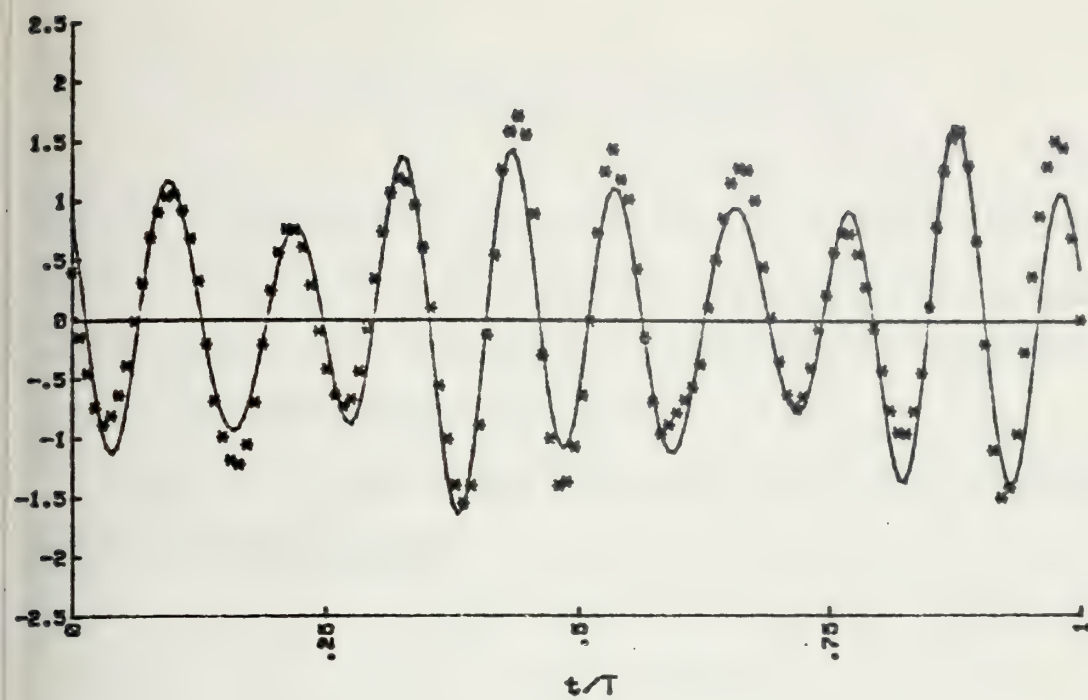


Fig. 168 Measured and predicted response for a 4 in. rough cylinder, $\zeta = 0.030$.

A comparison of Eqs. (44a) and (44d) shows that

$$(C_L)_{rms}/(C_L^\circ)_{rms} \cong C_{Lp1}/(C_L^\circ)_{rms} \quad (46)$$

Thus, it is reasonable to expect that Eq. (45) will yield the fundamental harmonic of the relative displacement fairly accurately. As noted earlier, higher order harmonics of \bar{X}/D are an order of magnitude smaller and certainly quite negligible.

Equation (45) shows that a relationship should exist between \bar{X}/D and the response parameter

$$R_p = \frac{M \zeta}{\rho D^2 L (C_L^\circ)_{rms}} \quad (47)$$

for both smooth and rough cylinders. Figure 169 shows the relationship between \bar{X}/D and R_p for all test cylinders. The relationship between the two parameters is rather remarkable in view of the fact that only the fundamental harmonic of the exciting force has been used and it was assumed that $\omega_f \cong \omega_n \cong \omega_{nw}$. Figure 169 also shows that the response of a given body to a given flow must necessarily depend on the starting dynamical conditions, i.e., on the dynamics of the same flow past the same body when the latter is held stationary. The use of a response parameter given by $M\zeta/(\rho LD^2)$, as done previously by others [3], without $(C_L^\circ)_{rms}$ could not have correlated the response for all smooth and rough cylinders. In fact, initially, the experiments were conducted with smooth cylinders. It was supposed that roughness will complicate the matters further. Contrary to this supposition, roughness and the

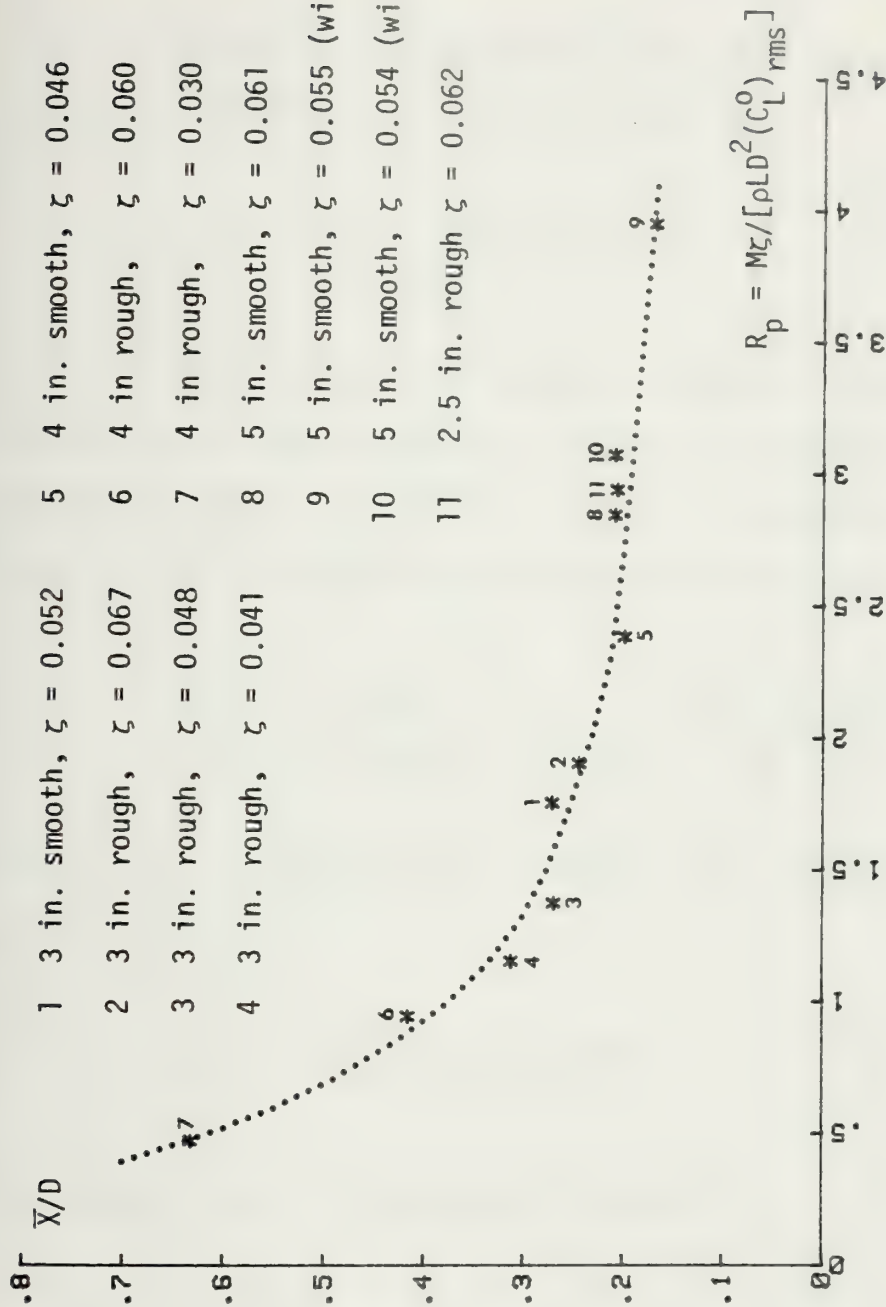


Fig. 169 \bar{X}/D versus response parameter R_p

consideration of the starting dynamical conditions helped to delineate the most important parameter governing the hydroelastic oscillations of cylinders.

As noted in Chapter I, researchers have used different definitions for the response parameter. One such definition is

$$\Delta_r = \frac{M \zeta}{\rho L D^2} (8 \pi^2 S^2) \quad (48)$$

This particular parameter has been extensively used in correlating the data obtained in steady flow about oscillating cylinders. A semi-empirical analysis by Iwan and Blevins [1,89] related the relative amplitude in steady flow at perfect synchronization to Δ_r by

$$\frac{\bar{X}}{D} = \frac{0.44}{\Delta_r + 11.94 S^2} \left[0.3 + \frac{4.52 S}{\Delta_r + 11.94 S^2} \right]^{1/2} \quad (49)$$

Griffin, Skop, and Ramberg [61] proposed a least-squares fit to the existing data as

$$\frac{\bar{X}}{D} = 1.29 / [1 + 0.43 \Delta_r]^{3.35} \quad (50)$$

Finally, Sarpkaya [10, 73] theoretically obtained

$$\frac{\bar{X}}{D} = 9.56 (C_L^\circ)_{\text{rms}} / [1.94 + \Delta_r^2 / (C_L^\circ)_{\text{rms}}^2]^{1/2} \quad (51)$$

in which $\Delta_r / (C_L^\circ)_{\text{rms}}$ is related to R_p by

$$\frac{\Delta_r}{(C_L^\circ)_{rms}} = R_p (8 \pi^2 S^2) \quad (52)$$

Thus, the variation of \bar{X}/D with R_p or $\Delta_r/(C_L^\circ)_{rms}$ in harmonic flow may be compared with that in steady flow through the use of Eq. (51). Figure 170 shows such a comparison for all the data obtained in the present investigation. It is rather surprising that not only the response in steady flow but also that in harmonic flow is fairly well represented by Eq. (51). It is of importance to note that in plotting the data shown in Fig. 170 $(C_L^\circ)_{rms}$ values appropriate to each cylinder have been used [see Eq. (45)].

In summary, it has been shown that the synchronization in harmonic flow occurs over a range of $U_m/f_n D$ values from 5.0 to 7.5 (see Figs. 47, 51, 55, 59, 63), with perfect synchronization at $U_m/f_n D \approx 5.6$. The amplification factor for the predominant harmonic is about 2.75, and the response is a unique function of the response parameter R_p or $\Delta_r/(C_L^\circ)_{rms}$ for all smooth and rough cylinders. The effect of the Keulegan-Carpenter number and the Reynolds number on the cylinder response is imbedded in the dependence of $(C_L^\circ)_{rms}$ on the starting dynamical conditions, i.e., on the dependence of $(C_L^\circ)_{rms}$ on K and Re . Finally, the predominant harmonic of the response is an order of magnitude larger than those of the higher order harmonics, which enable one to determine the response through the use of a relatively simple analysis. The modulations in amplitude and phase of the response is quite well predicted both by a generalized solution based on the Fourier decomposition of the exciting force and by a straightforward application of the Duhamel's integral.

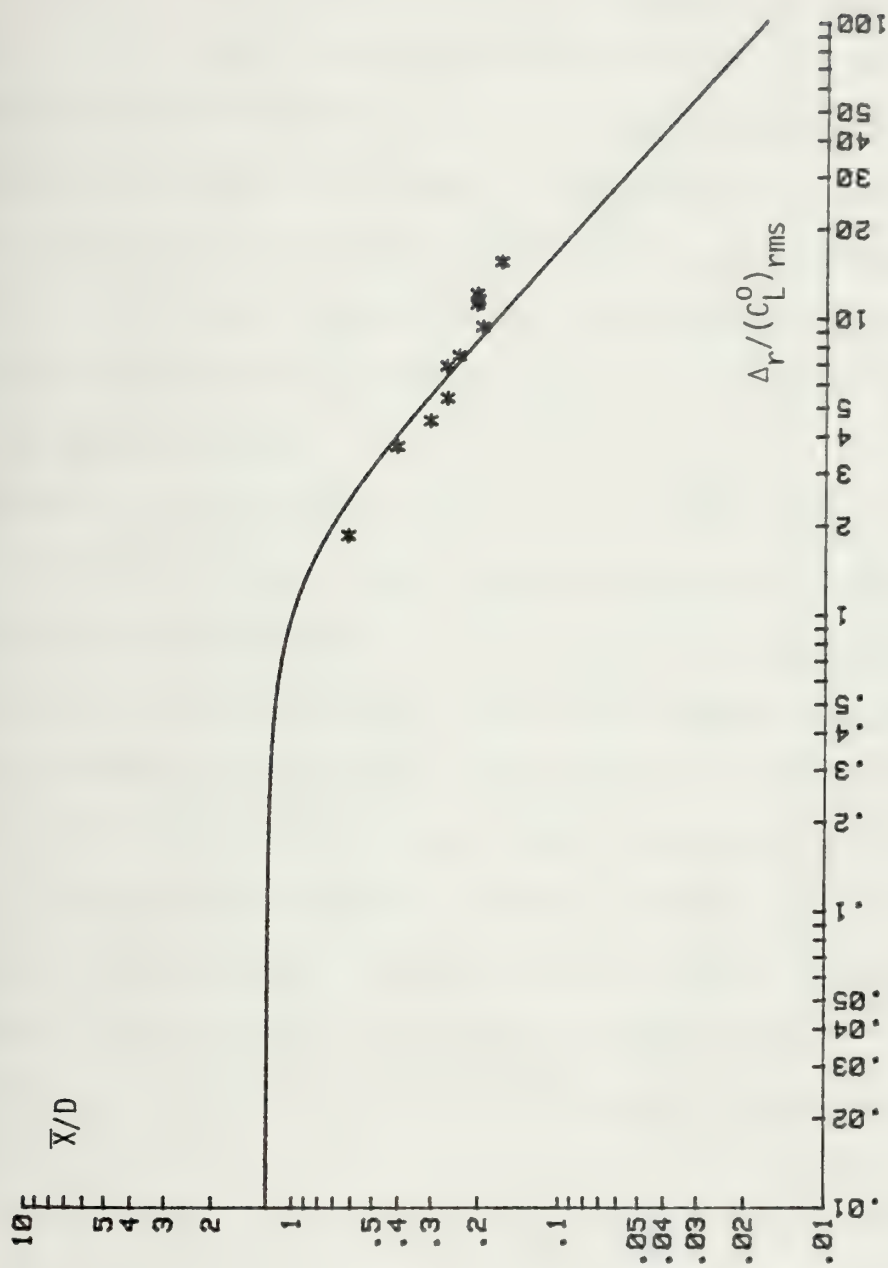


Fig. 170 Comparison of cylinder oscillation in harmonic and steady flow.

C. APPLICATION OF THE WAKE-OSCILLATOR MODEL

Several mathematical models have been proposed [86-91]; (see also [2, 55, 71, 92] for additional models) in an attempt to simulate and/or explain some of the experimental results summarized in Chapter I. These models do not include the analysis of the flow field and the fluid-mechanical arguments invoked in their evaluation are not altogether convincing. Thus their worth should be measured not so much by their capacity to obtain functional relations among significant parameters that lead to the basic understanding of the phenomenon but by their ability to produce results which are qualitatively similar to those obtained experimentally.

The most noteworthy among the oscillator models is the one proposed by Hartlen and Currie [87] where a van der Pol-type soft nonlinear oscillator for the lift force is coupled to the body motion by a linear-dependence on cylinder velocity. This model is based partly on a suggestion by Birkhoff and Zarantonello [23], mentioned earlier in connection with the estimation of the Strouhal number, and by Bishop and Hassan [56] in connection with their now classic experiments with oscillating cylinders in uniform flow. The model has its roots in mechanics and electricity rather than in the equations of fluid motion.

The pair of equations which result from this concept are

$$\ddot{x}_r + 2 \zeta \dot{x}_r + x_r = a_0 \Omega_0^2 C_L \quad (53)$$

$$\ddot{C}_L - \alpha \Omega_0 \dot{C}_L + \left(\frac{\gamma}{\Omega_0}\right) \dot{C}_L^3 + \Omega_0^2 C_L = B \dot{x}_r \quad (54)$$

in which

$$\begin{aligned}
 X_r &= X/D, & \dot{X}_r &= \frac{dX}{d\tau}, & \tau &= \omega_n t \\
 a_0 &= \frac{\rho D^2 L}{8 \pi^2 S_0^2 M} \\
 S_0 &= f_0 D/V \\
 \Omega_0 &= f_0/f_n
 \end{aligned} \tag{55}$$

where f_0 is the frequency of vortex shedding by a stationary cylinder in steady flow of velocity V and S_0 is the corresponding Strouhal number. The parameters α and γ are the van der Pol coefficients and B is the interaction parameter.

In Equation (54), first and fourth terms generate a simple harmonic oscillator of normalized frequency Ω_0 , the second term (the so-called negative lift damping) provides the growth of C_L , and the third term prevents unlimited growth. The fifth term provides the feedback from the body motion to the fluid motion and hence to the lift force. Equation (54) is not the only form which could provide the desired variation of C_L , but it is the simplest.

Of the three parameters (α , γ and B), two must be chosen to provide the best fit to the data. This is not too unusual and all other models require some retrofitting to experiment. The ratio α/γ is related to the amplitude of the steady-state oscillation of the lift force by [87]

$$C_L^o = \sqrt{4\alpha/3\gamma} \tag{56}$$

which is the solution of Eq. (54) for

$$\chi_r = 0.$$

Experiments in steady flow have shown that [56] in large-amplitude, steady-state, vortex-induced oscillation, the displacement and exciting force have nearly sinusoidal forms and oscillate at the same frequency ω_c , close to ω_n , with a phase angle ϕ . Thus

$$x_r = \bar{X}_r \sin(\Omega_c \tau) \quad (57)$$

and

$$C_L = \bar{C}_L \sin(\Omega_c \tau + \phi) \quad (58)$$

Substituting Eqs. (57) and (58) in Eq. (53) and equating to zero the resulting coefficients of $\sin(\Omega_c \tau)$ and $\cos(\Omega_c \tau)$, Hartlen and Currie [87] obtained

$$(1 - \Omega_c^2) \bar{X}_r = a_0 \Omega_0^2 \bar{C}_L \cos \phi \quad (59)$$

$$2 \zeta \bar{X}_r = a_0 \Omega_0^2 \bar{C}_L \sin \phi \quad (60)$$

Likewise, substituting Eqs. (57) and (58) in Eq. (62), dropping terms arising from \dot{C}_L^3 , and using Eqs. (59) and (60), one has

$$\Omega_0 = \Omega_c \left[1 - \frac{2 a_0 B \zeta \Omega_c^2}{(1 - \Omega_c^2)^2 + 4 \zeta^2 \Omega_c^2} \right]^{-1/2} \quad (61)$$

which shows that $\Omega_c < \Omega_0$ or $f_c < f_0$.

Hartlen and Currie applied their analysis to a comparison with Jones, et al., [17], data ($Re = 3.6 \times 10^5$ to 1.9×10^7 , $\bar{X}_r = 0.08$) with good qualitative results. However, some doubt has been raised [8] as to whether the oscillations had reached synchronization and whether an amplitude of $\bar{X}_r = 0.08$ was sufficiently greater than the threshold amplitude [44, 62] necessary to bring about synchronization. Furthermore, Jones, et al, data did not show an increase in drag in the transcritical range of Reynolds numbers.

Hartlen and Currie also used Ferguson's [63] data for the circular cylinder and obtained the results shown in Fig. 171. These results are in qualitative agreement with those shown in Fig. 3. There are however, some important quantitative differences:

1. In Feng's data (Fig. 3) the cylinder is seen to continue to oscillate at $\omega_c \cong \omega_n$ on both sides of the region outside the lock-in range. This feature is not presented in Fig. 171.
2. The force and response maximums occur in Fig. 3 at about the same V_r -value. In Fig. 171, \bar{C}_L remains constant over a broad range of synchronization, reaching a maximum at a V_r -value considerably smaller (relative to the width of the lock-in range) than that for \bar{X}_r . The explanation of these discrepancies and the relationship between the particular changes in the wake and/or the elastic system which trigger the hysteresis remained unresolved.

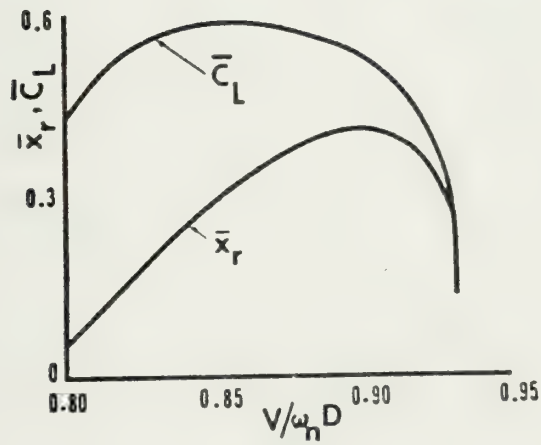
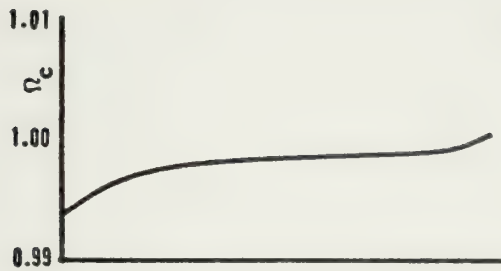


Fig. 171 Response characteristics in steady flow as predicted by Hartlen and Currie model [87].

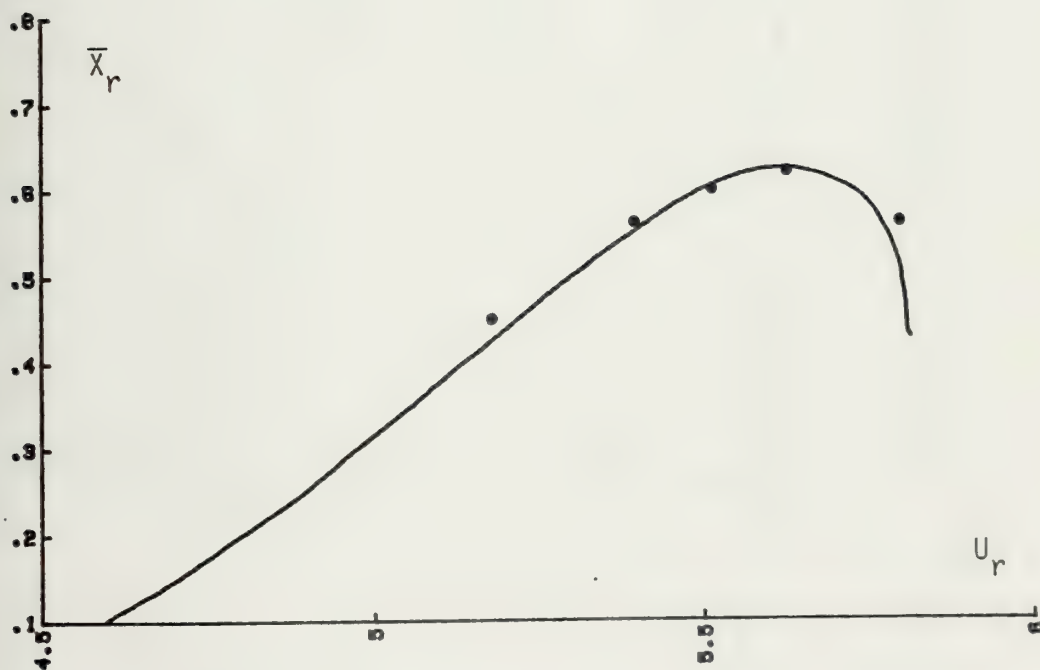
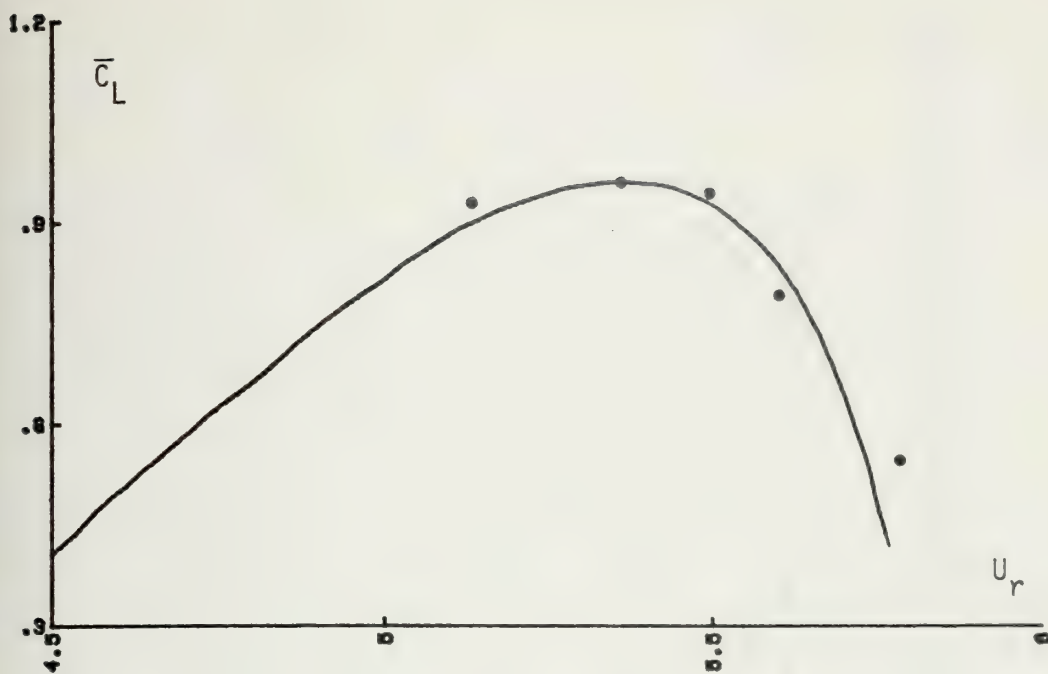


Fig. 172a \bar{C}_L and \bar{X}_r versus U_r in harmonic flow as predicted by Hartlen and Currie model.

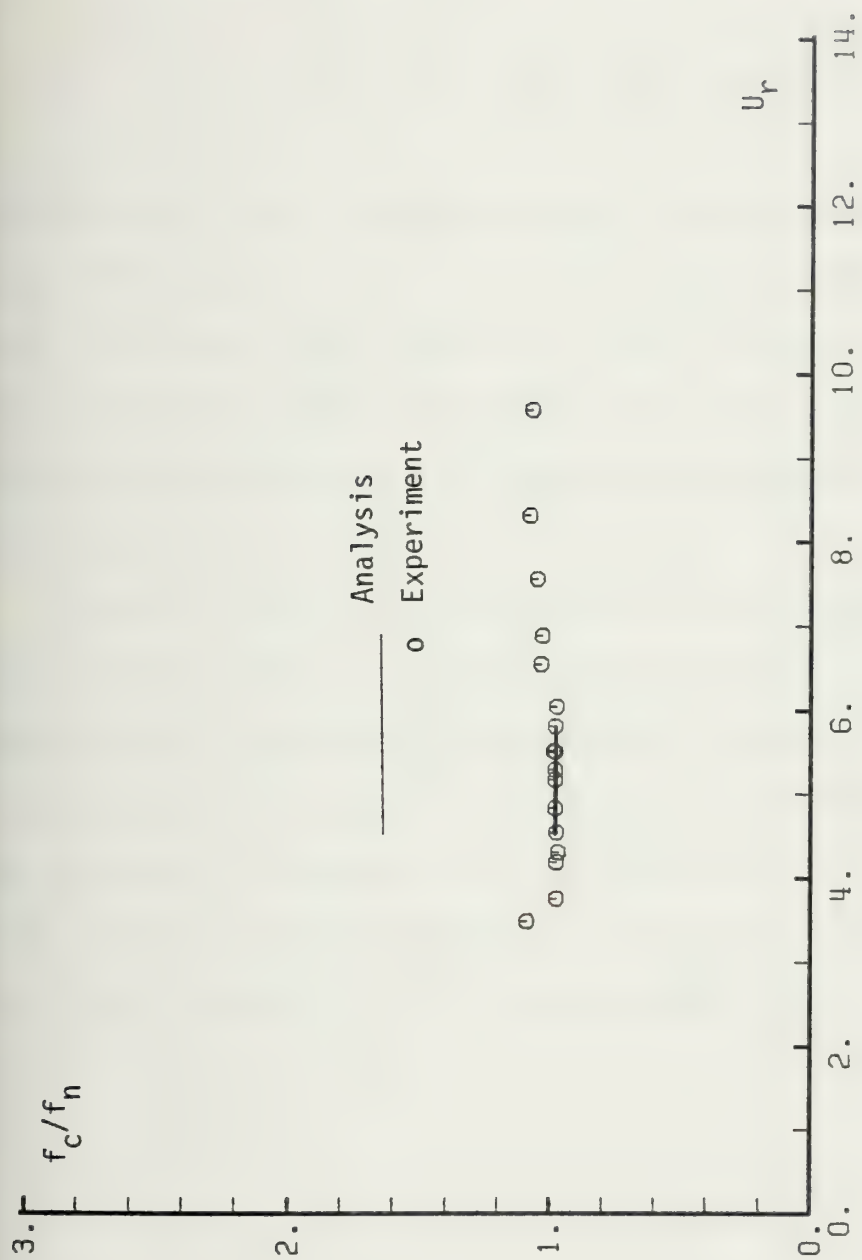


Fig. 172b f_c/f_n versus U_r in harmonic flow as predicted by Hartlen and Currie model.

In spite of its shortcomings, Hartlen and Currie model has been applied to the hydroelastic oscillations of cylinders in harmonic flow through the use of Eqs. (53), (54) and

$$C_L(t) = \bar{C}_{Lp_1} \sin(\Omega_c \tau + \phi) \quad (62)$$

The parameters α and B have been chosen to provide the best fit to the data. Representative results for a 4 in. rough cylinder are shown in Figs. (172a) and (172b). Apparently, the judicious selection of the two independent parameters provides a fairly good agreement between the data and the predictions of the model near synchronization. Calculations with other cylinders yielded similar results.

As noted earlier, this model does not include the analysis of the flow field and gives no clues regarding the values of α , γ , or B . Nevertheless, it is worthy of consideration because of its ability to predict the general trend of the data once α and B are chosen through the use of two data points on the response curve. Additional attempts made to improve the oscillator model by making $B\dot{X}_r$ term in Eq. (54) a non-linear function of \dot{X}_r will not be presented here.

VI. CONCLUSIONS

The theoretical and experimental investigation of the hydroelastic oscillations of smooth and rough circular cylinders in harmonic flow warranted the following conclusions:

1. An elastically-mounted cylinder may undergo synchronized oscillations when the reduced velocity $U_r = U_m/f_n D$ is in the range of 5.0 to 7.5.
2. Perfect synchronization, at which the response is maximum, occurs at $U_r \cong 5.6$.
3. Synchronized oscillations occur at an average Strouhal number of 0.16.
4. In the region of synchronous oscillations, the rms of the lift coefficient and the amplitude of the predominant harmonic of the normalized lift force are amplified by a factor of about 2.75 relative to that for a stationary cylinder in harmonic flow at the corresponding Keulegan-Carpenter number and Reynolds number.
5. The Fourier and spectral analyses of the exciting force and response, in the resonance region, show that the exciting force is well represented by its three most important harmonics and the response, by the predominant harmonic alone.
6. The analysis relating the governing parameters predicts fairly accurately the response of both the smooth and rough cylinders in the synchronous region.
7. The measured instantaneous values of the cylinder response are in excellent agreement with those predicted through the use of the Duhamel's integral.

8. The wake oscillator model of Hartlen and Currie, as applied to harmonic flow about transversely-oscillating cylinders, predicts fairly accurately the general behavior of the force and response data provided that the two free parameters of the model are chosen judiciously.
9. Outside the synchronization region the cylinders continue to oscillate, with very small amplitudes, at nearly their natural frequency.
10. The analyses and the data presented herein are sufficient to predict not only the range of occurrence of hydroelastic oscillations of elastically-mounted cylinders in harmonic flow but also to evaluate the amplitudes of the exciting force and the response.

APPENDIX A

PEAK RELATIVE AMPLITUDES AS A FUNCTION OF K , U_r , f_f/f_{nw} , and f_c/f_{nw}

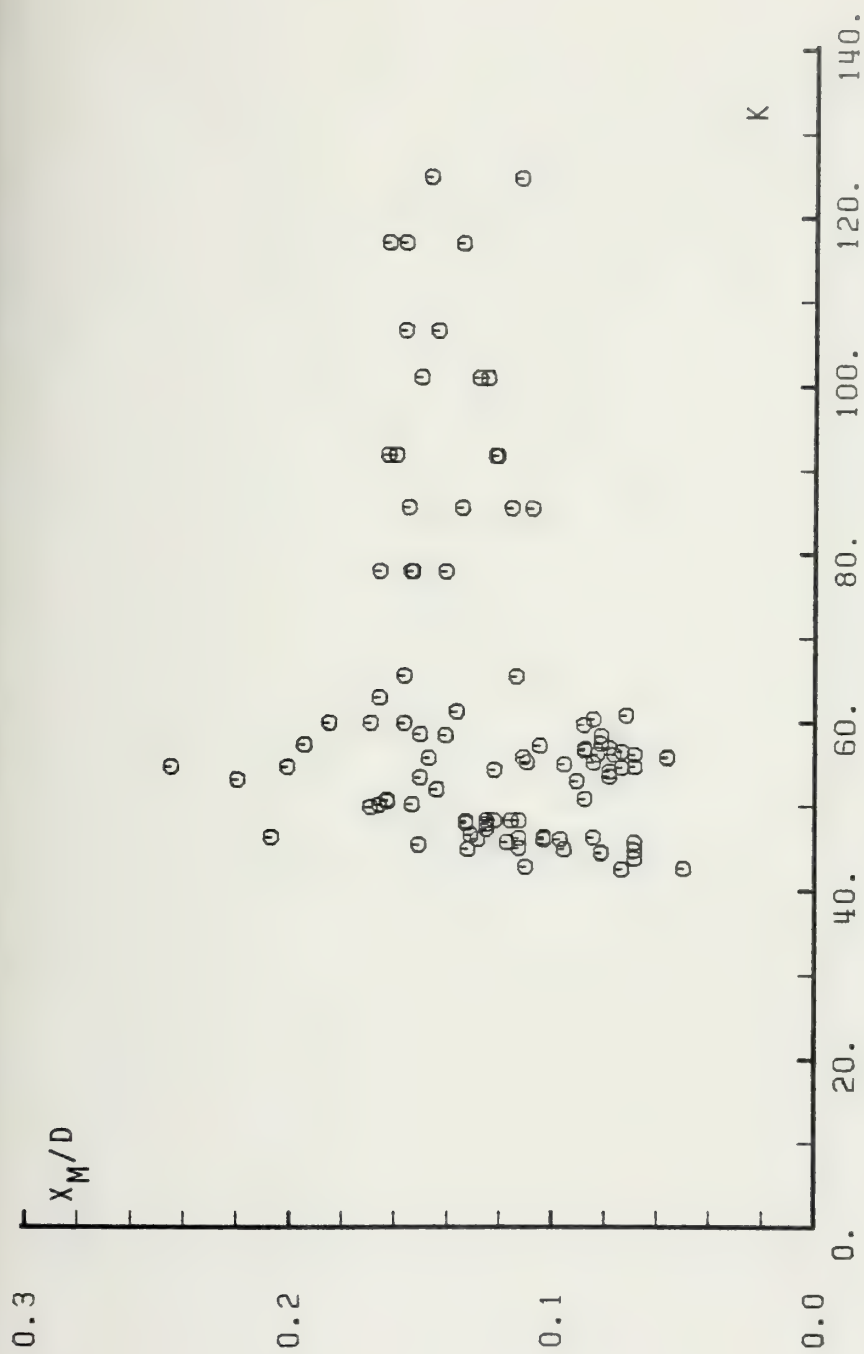


Fig. 30 X_M/D versus K for 3 in. rough cylinder, $\zeta = 0.067$.

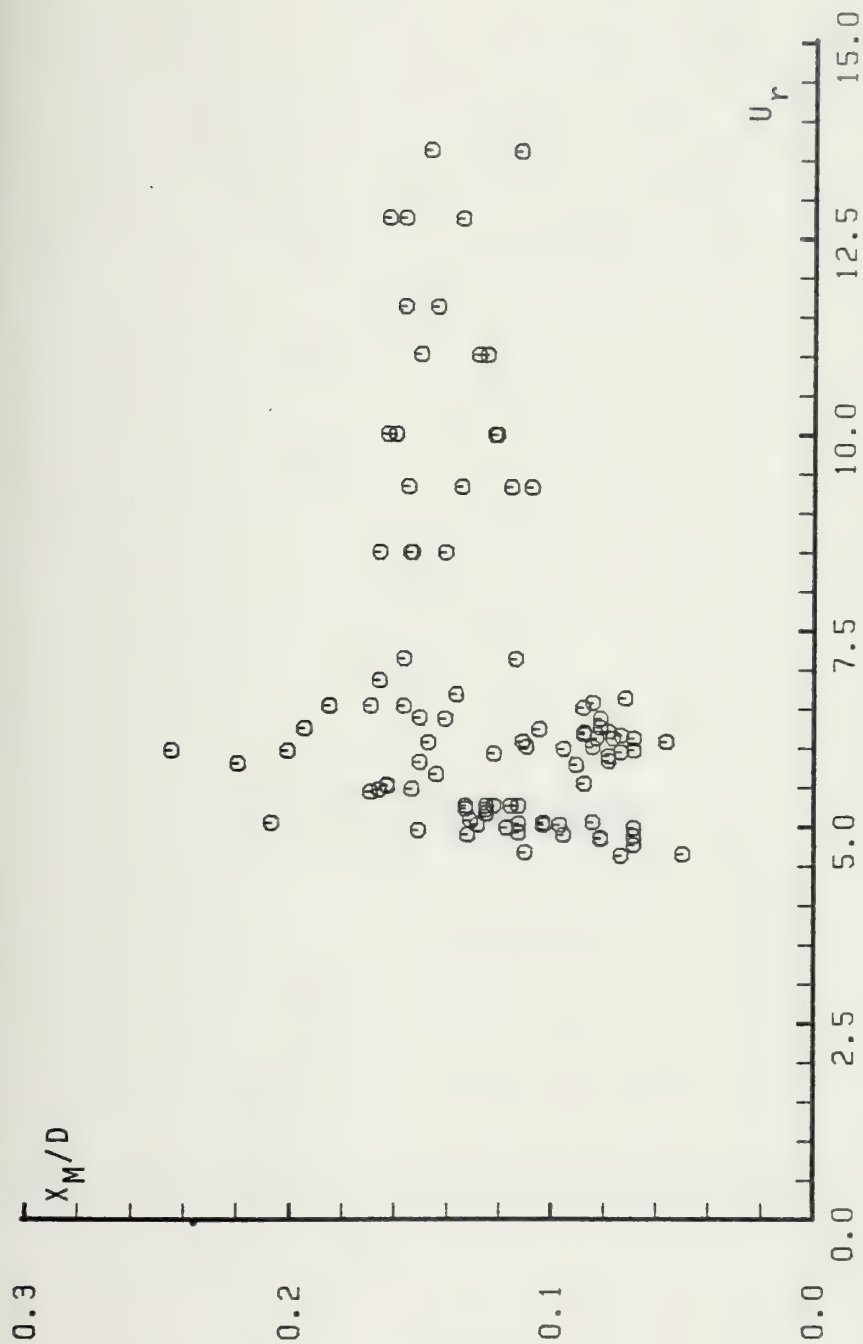


Fig. 37 X_M/D versus U_r for 3 in. rough cylinder, $z = 0.067$.

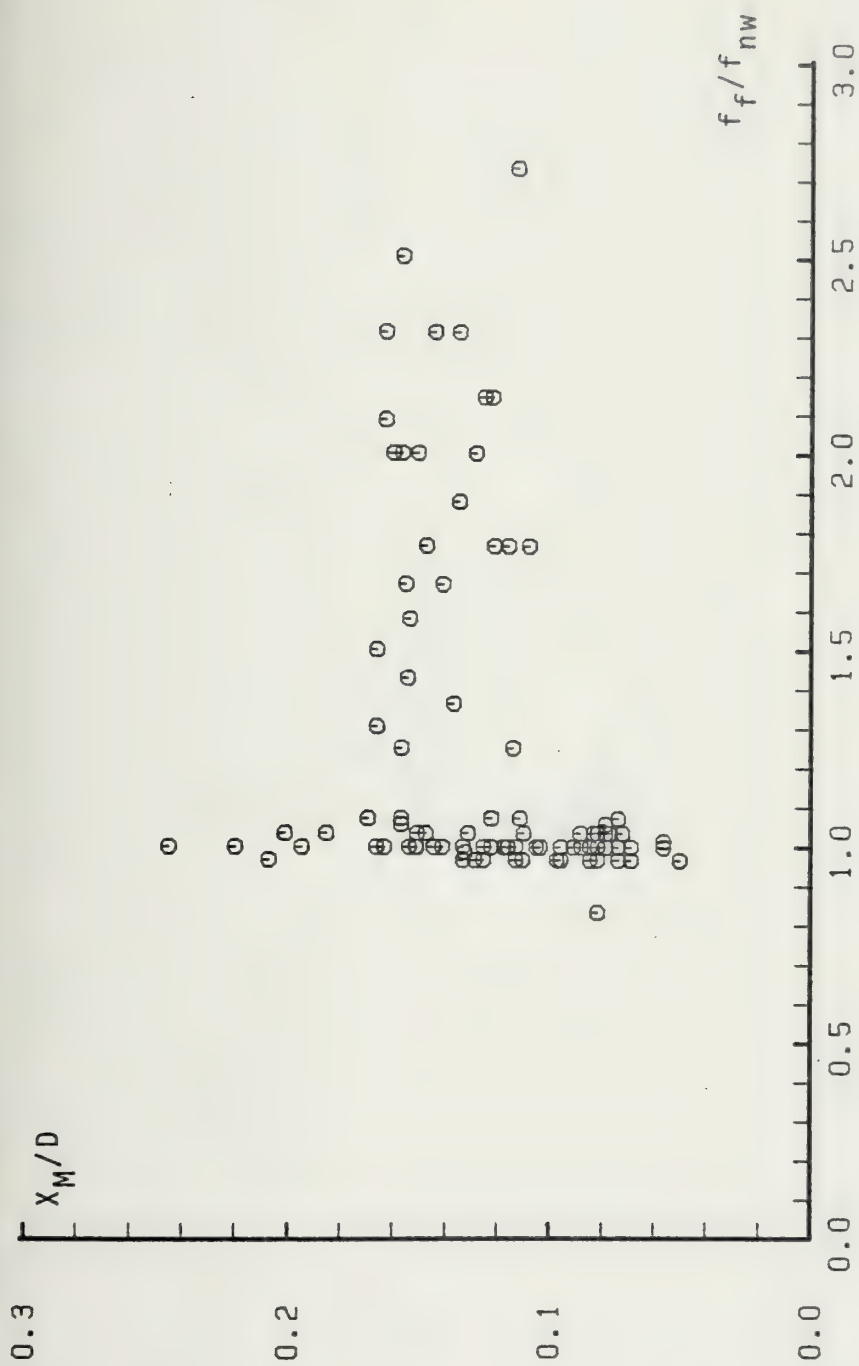


Fig. 32 X_M/D versus f_f/f_{nw} for 3 in. rough cylinder, $\zeta = 0.067$.

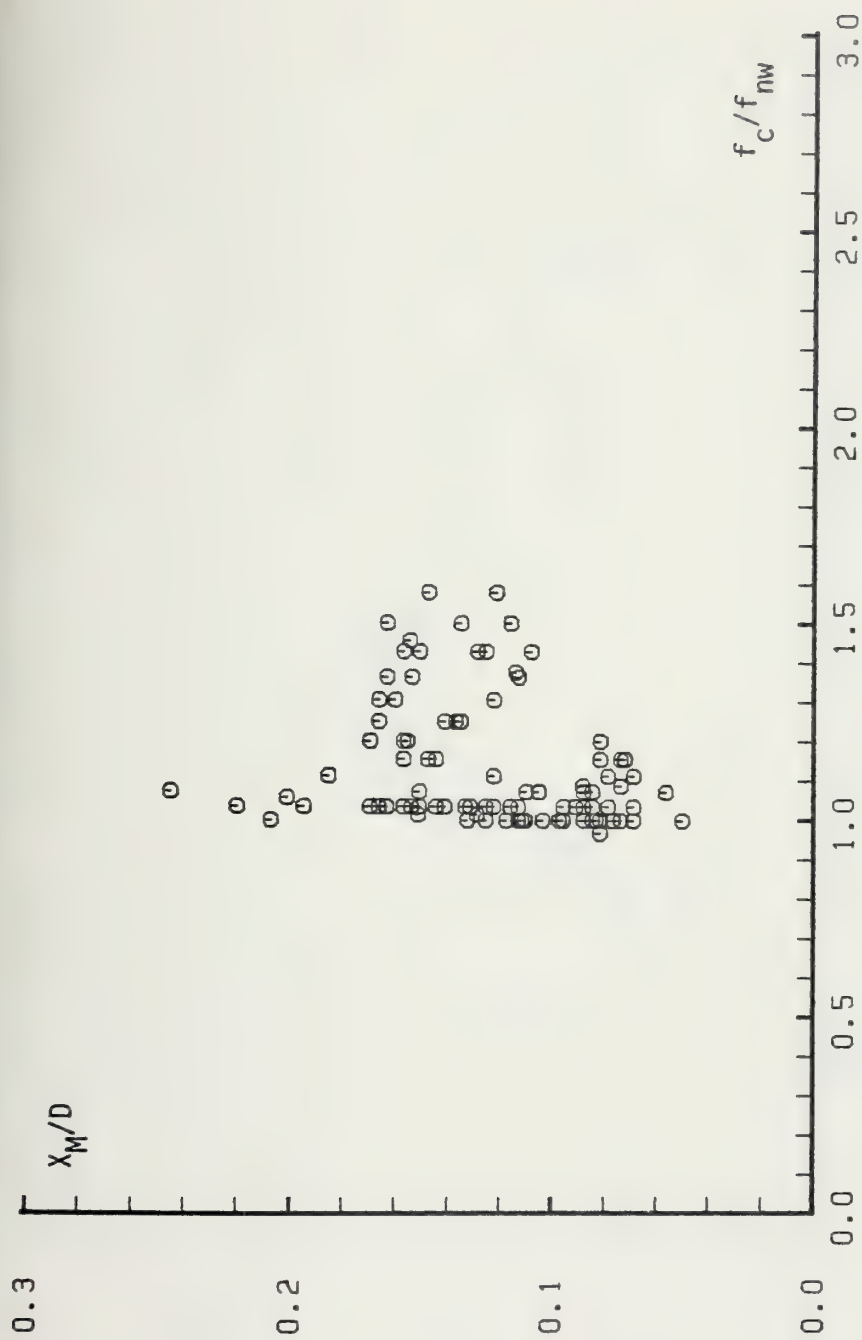
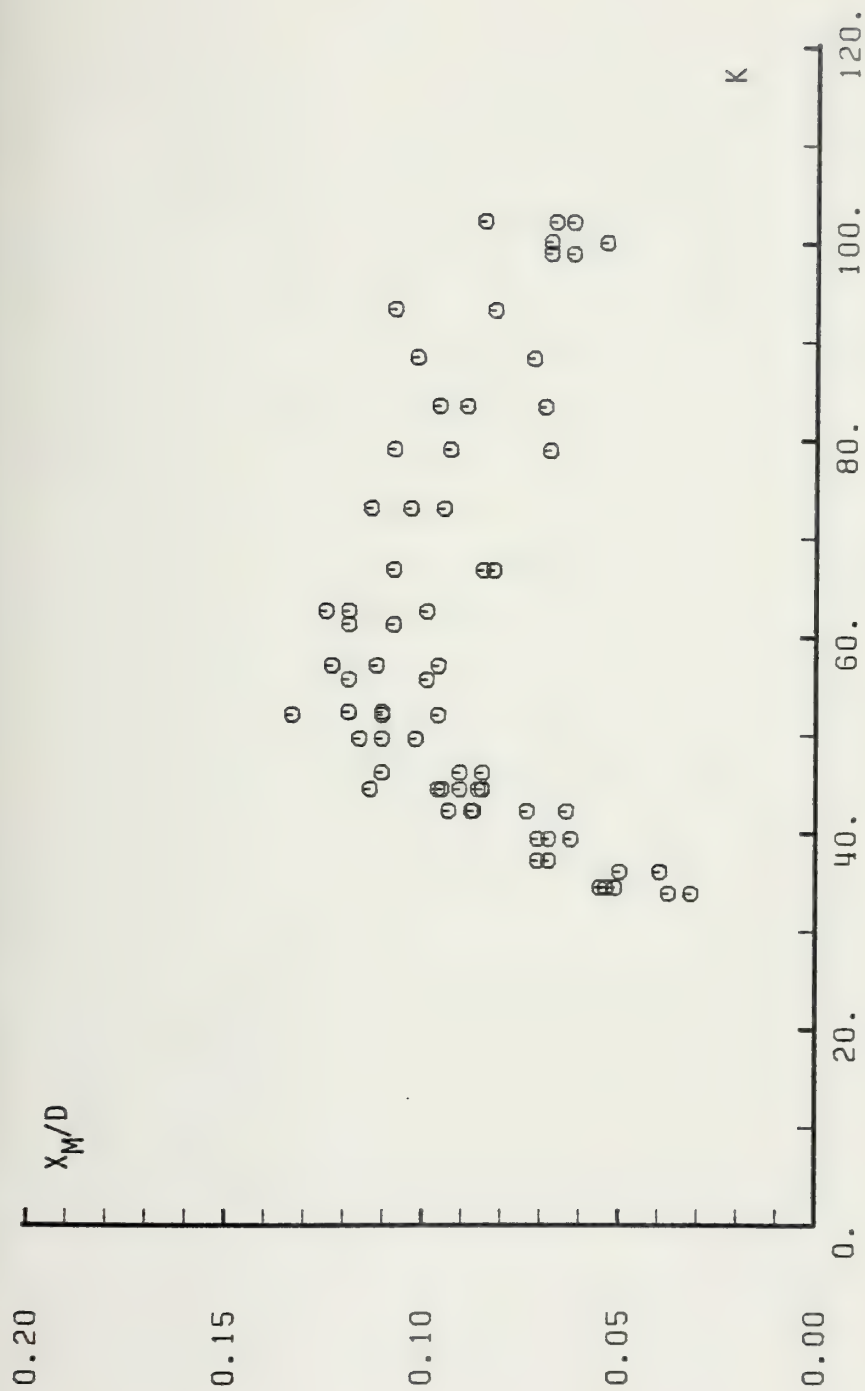


Fig. 33 X_M/D versus f_c/f_{nw} for 3 in. rough cylinder, $\zeta = 0.067$.



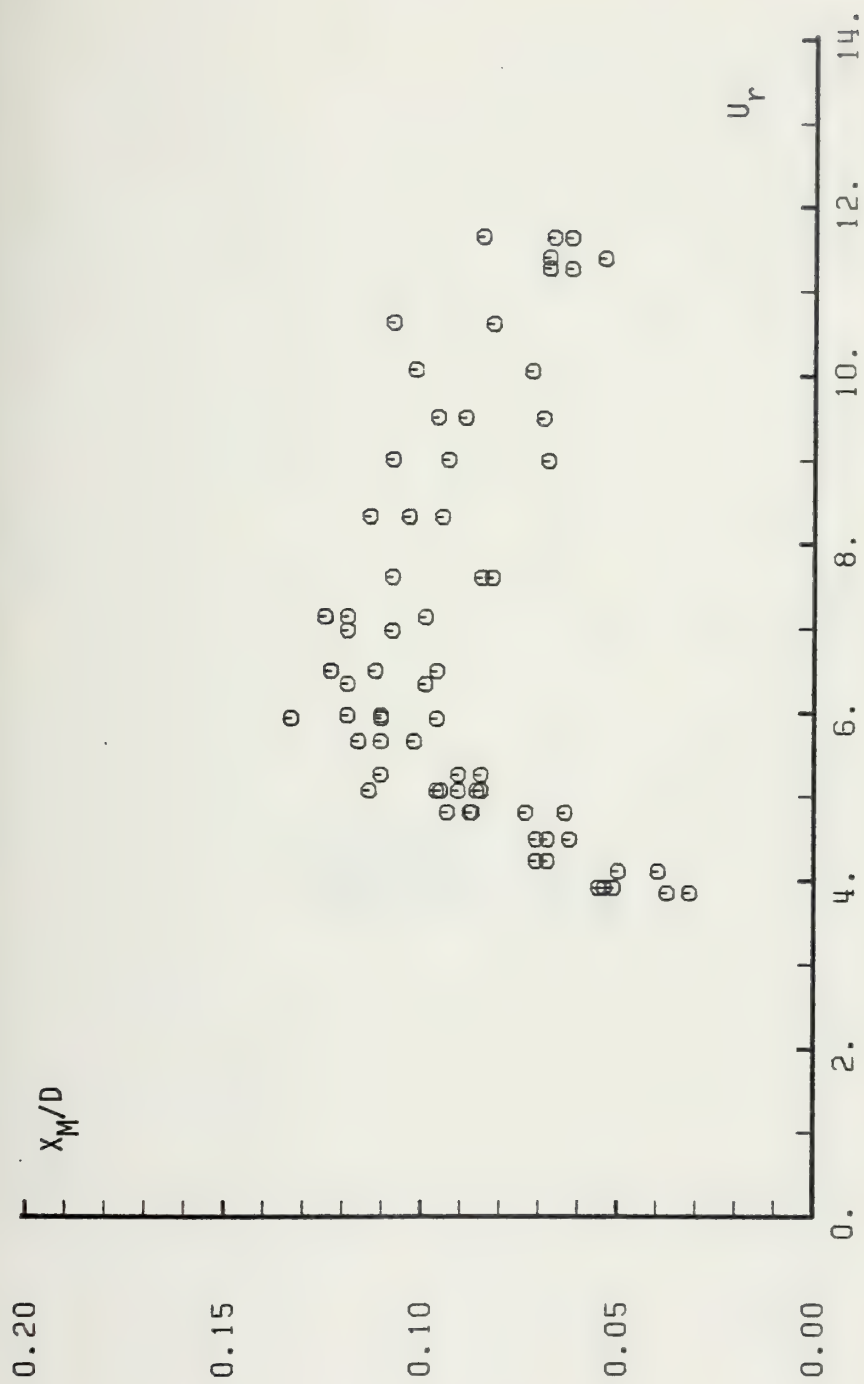


Fig. 35 X_M/D versus U_r for 4 in. smooth cylinder, $\zeta = 0.046$.

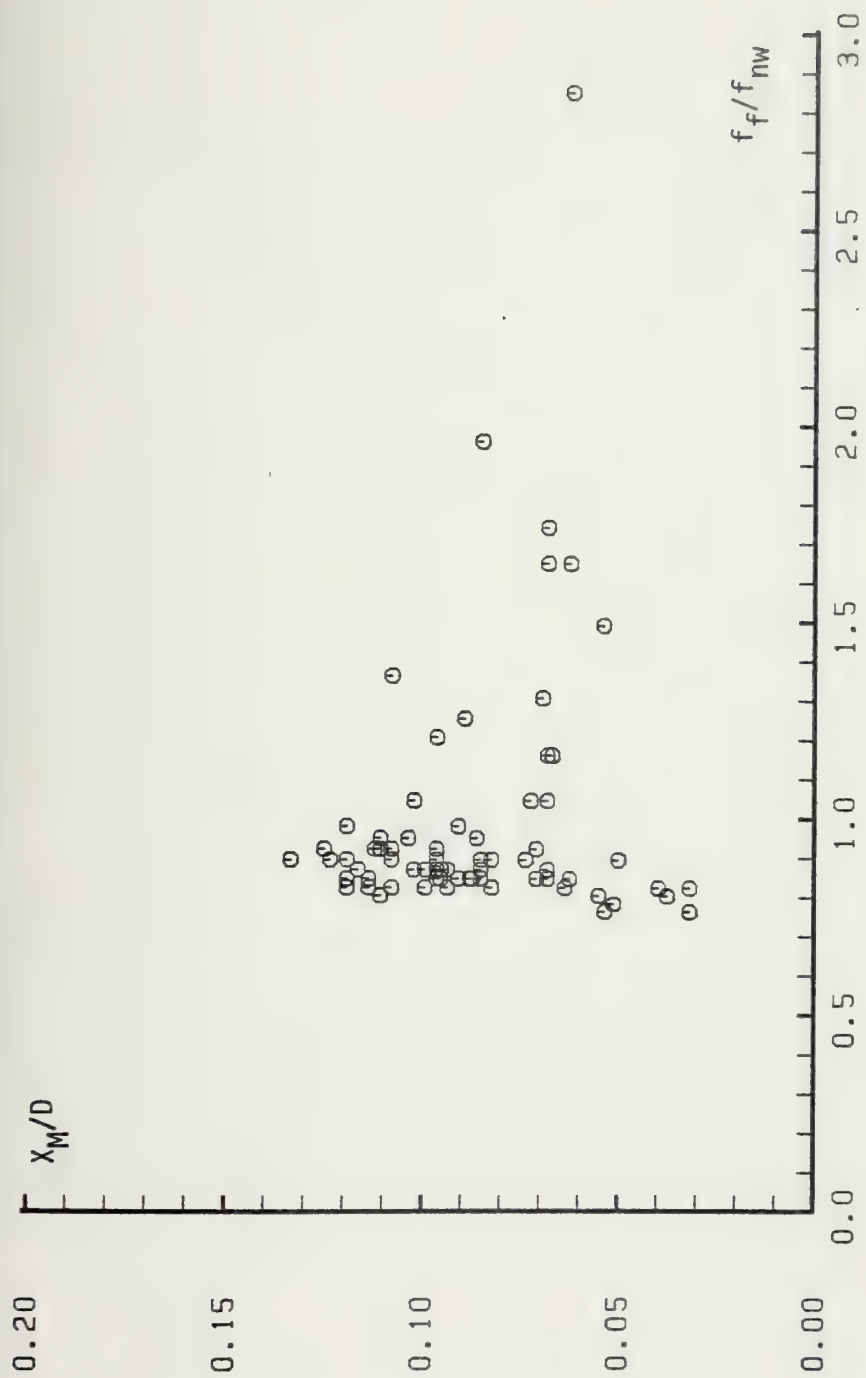


Fig. 36 X_M/D versus f_f/f_{nw} for 4 in. smooth cylinder, $\zeta = 0.046$.

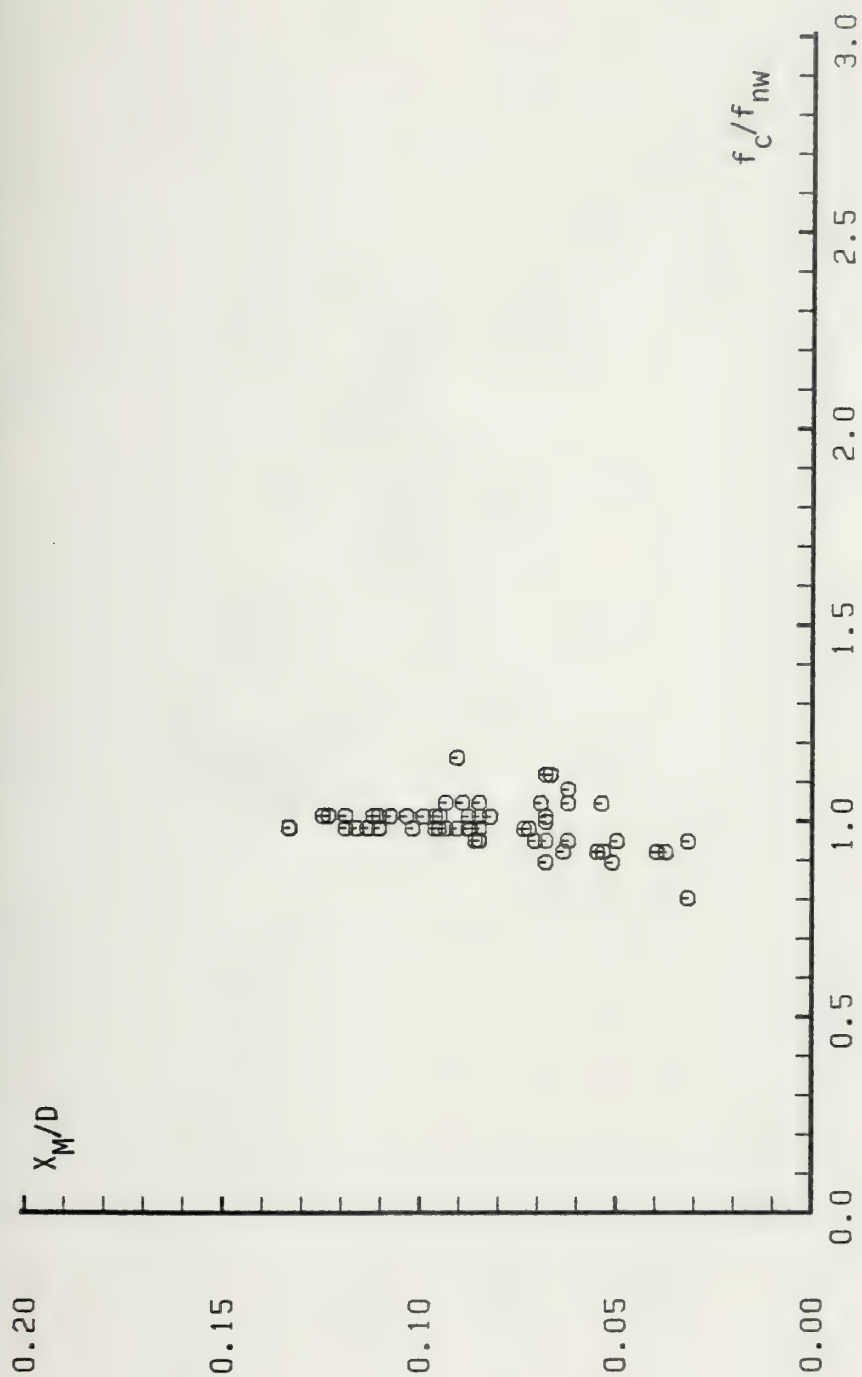


Fig. 37 X_M/D versus f_C/f_{nw} for 4 in. smooth cylinder, $\zeta = 0.046$.

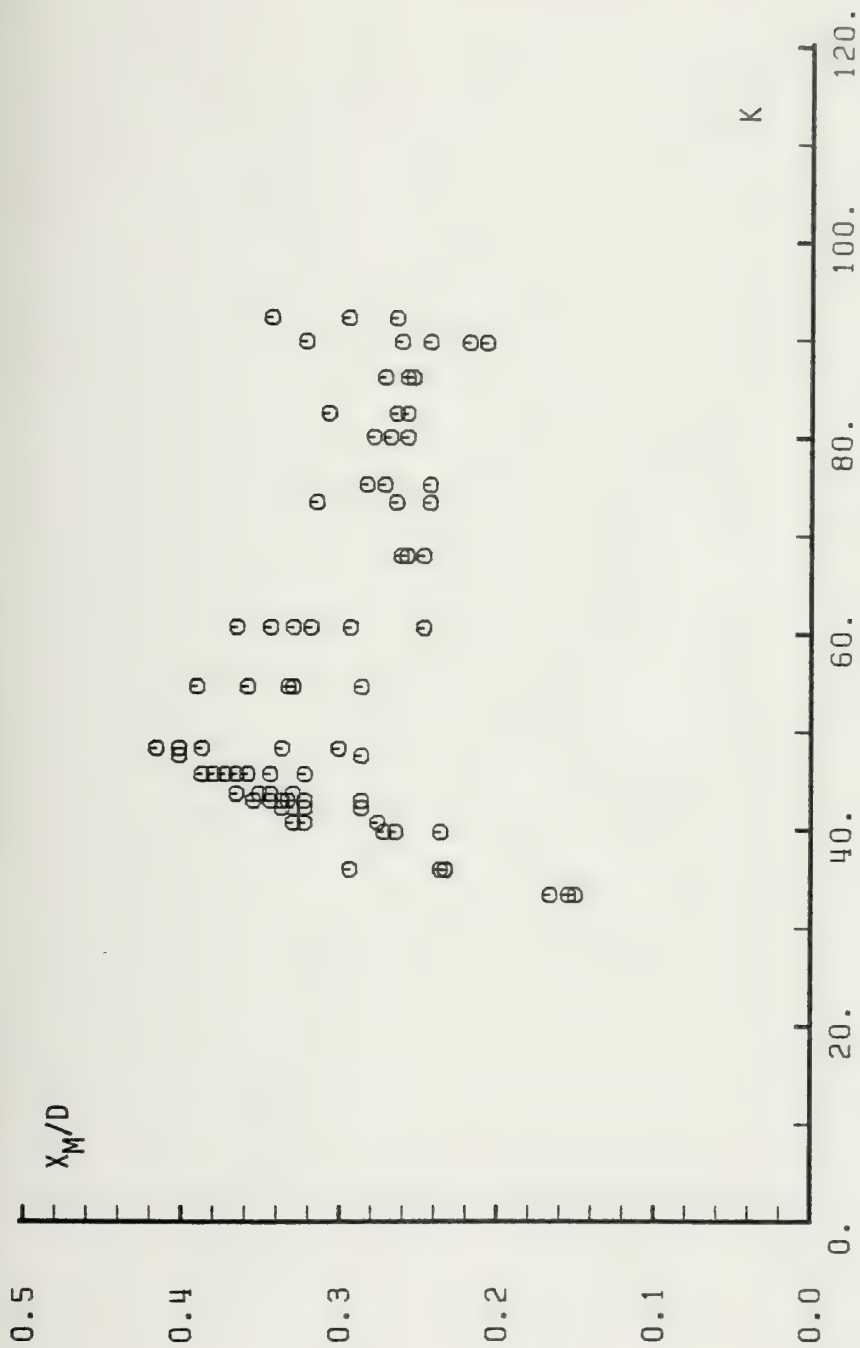


Fig. 38 X_M/D versus K for 4 in. rough cylinder, $\zeta = 0.060$.

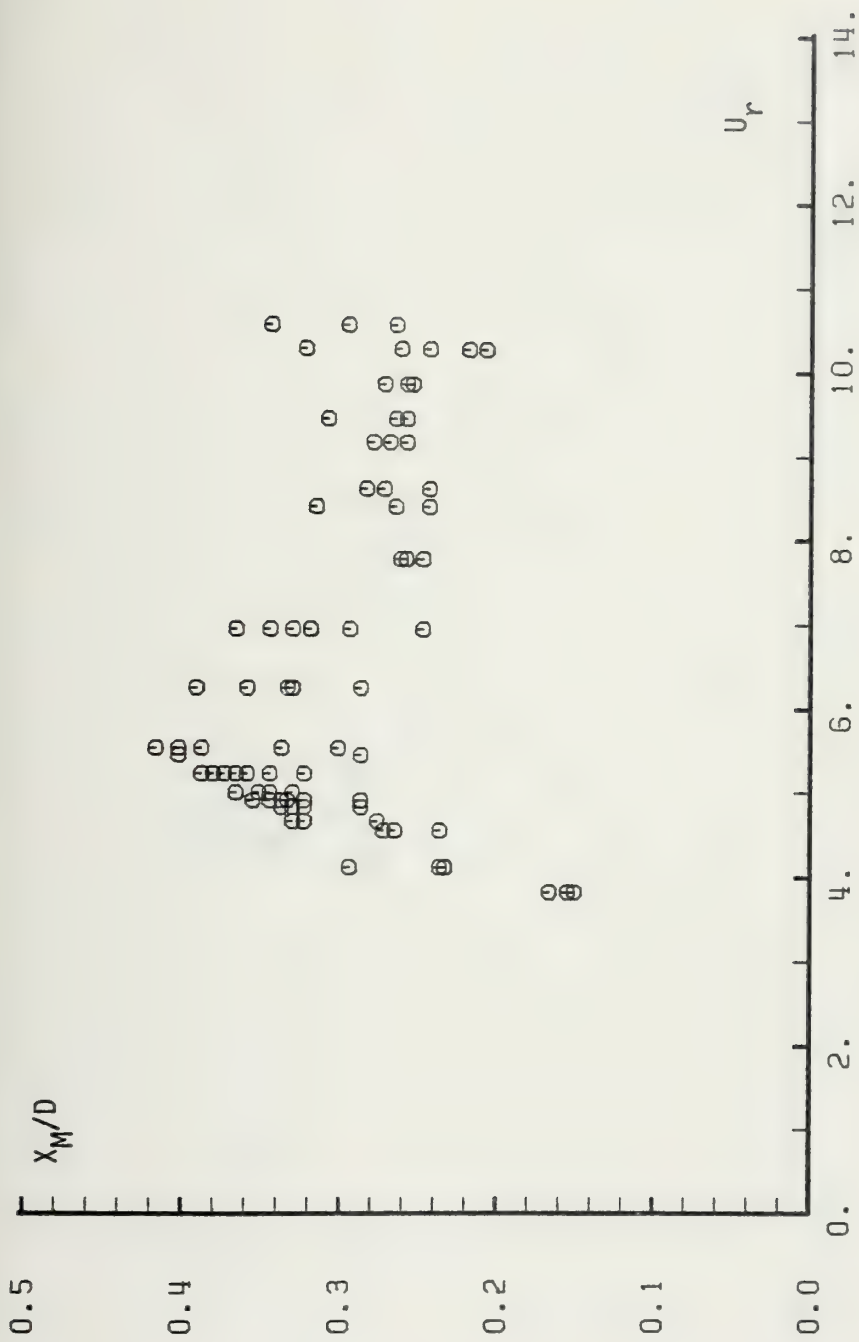


Fig. 39 X_M/D versus U_r for 4 in. rough cylinder, $\zeta = 0.060$.

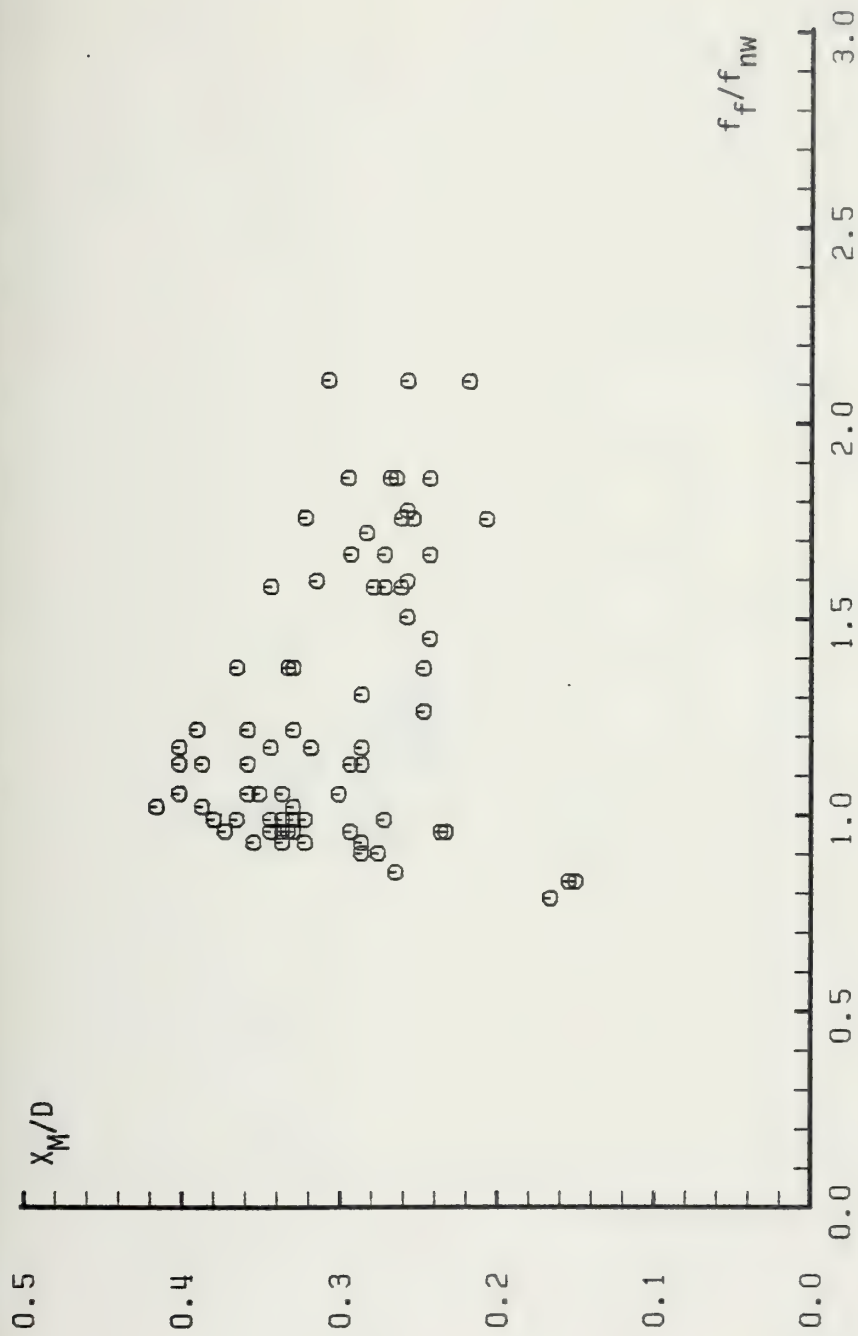


Fig. 40 X_M/D versus f_f/f_{nw} for 4 in. rough cylinder, $\zeta = 0.060$.

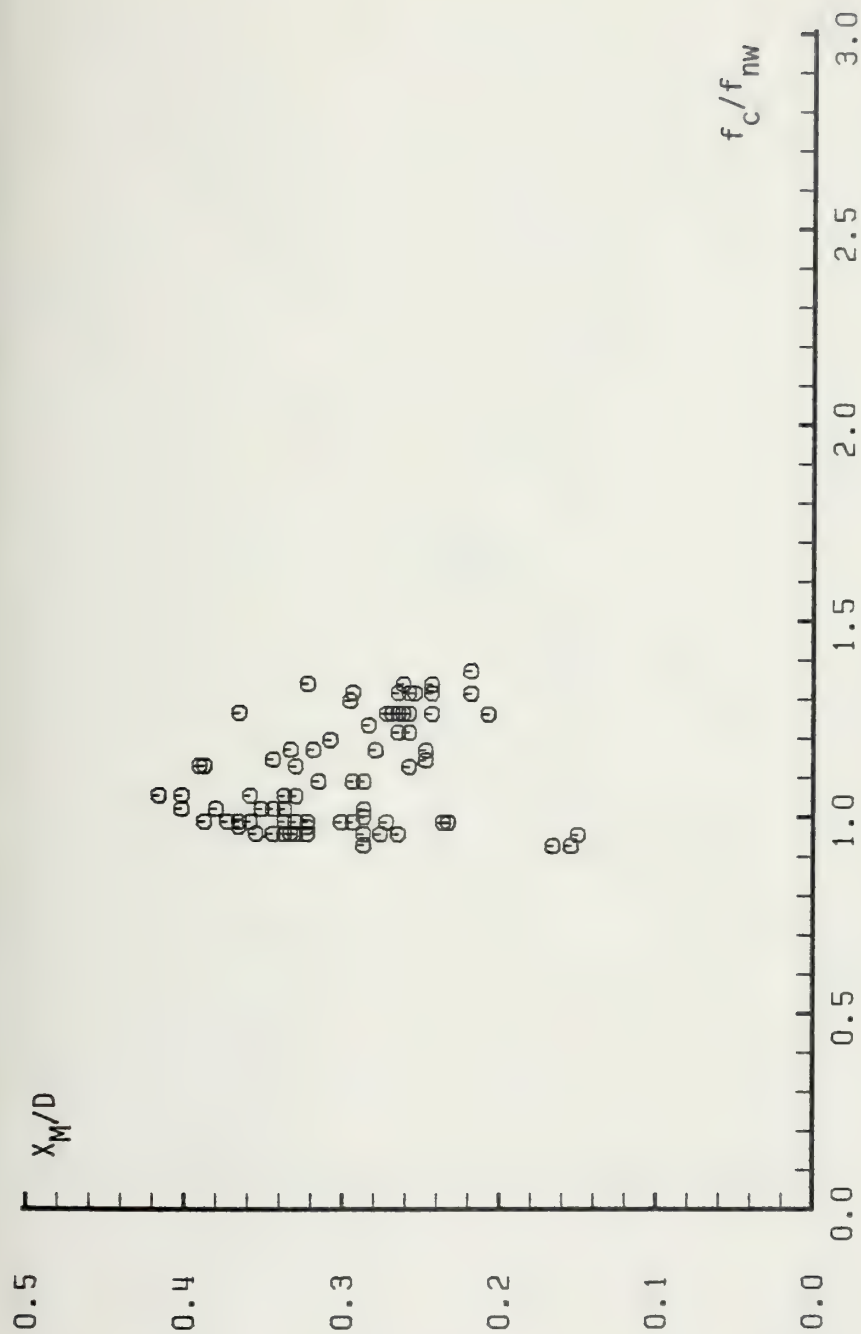


Fig. 41 X_M/D versus f_c/f_{nw} for 4 in. rough cylinder, $\zeta = 0.060$.

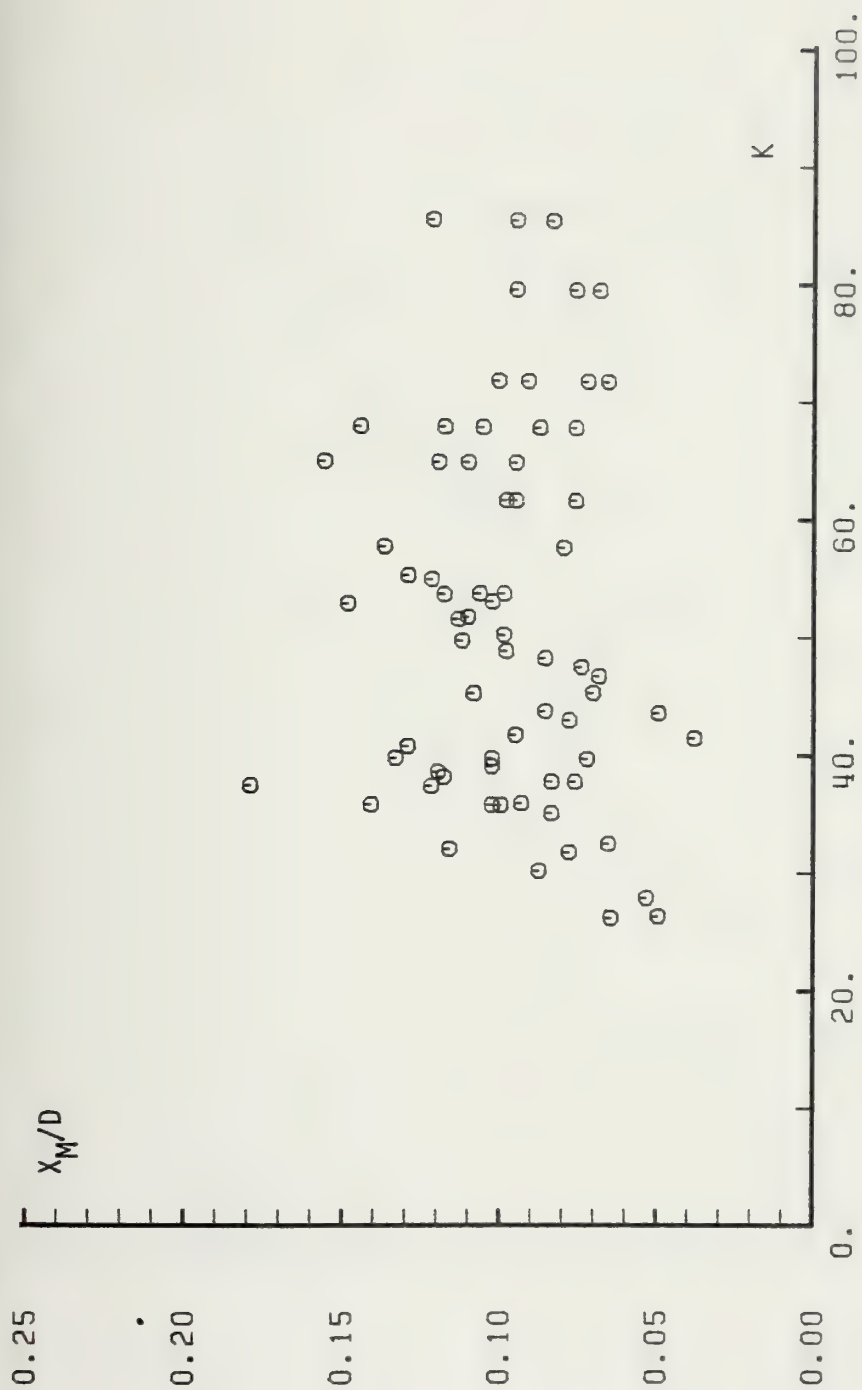


Fig. 42 X_M/D versus K for 5 in. smooth cylinder, $\zeta = 0.055$.

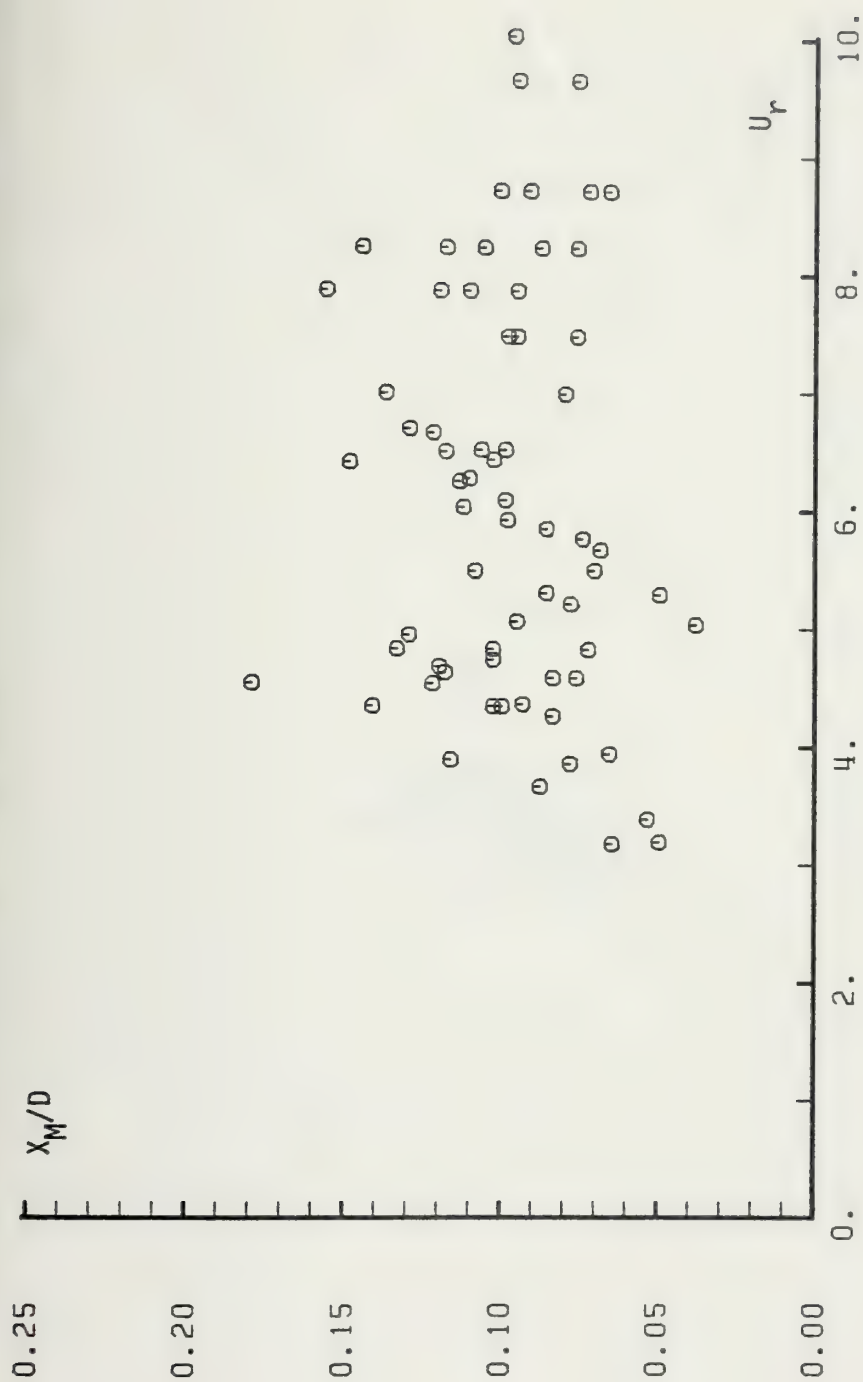


Fig. 43 X_M/D versus U_r for 5 in. smooth cylinder, $\zeta = 0.055$.

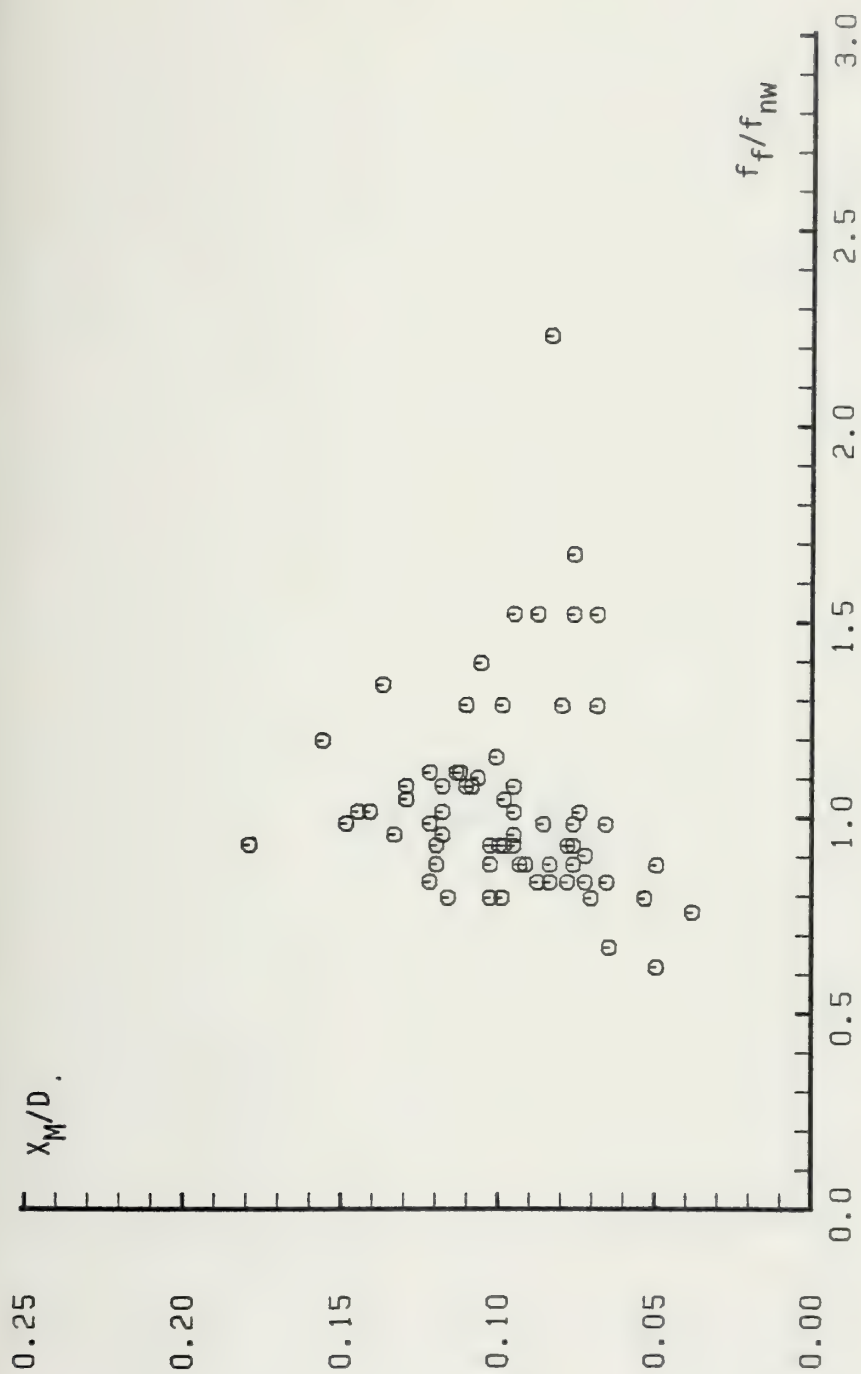


Fig. 44 X_M/D versus f_f/f_{nw} for 5 in. smooth cylinder, $z = 0.055$.

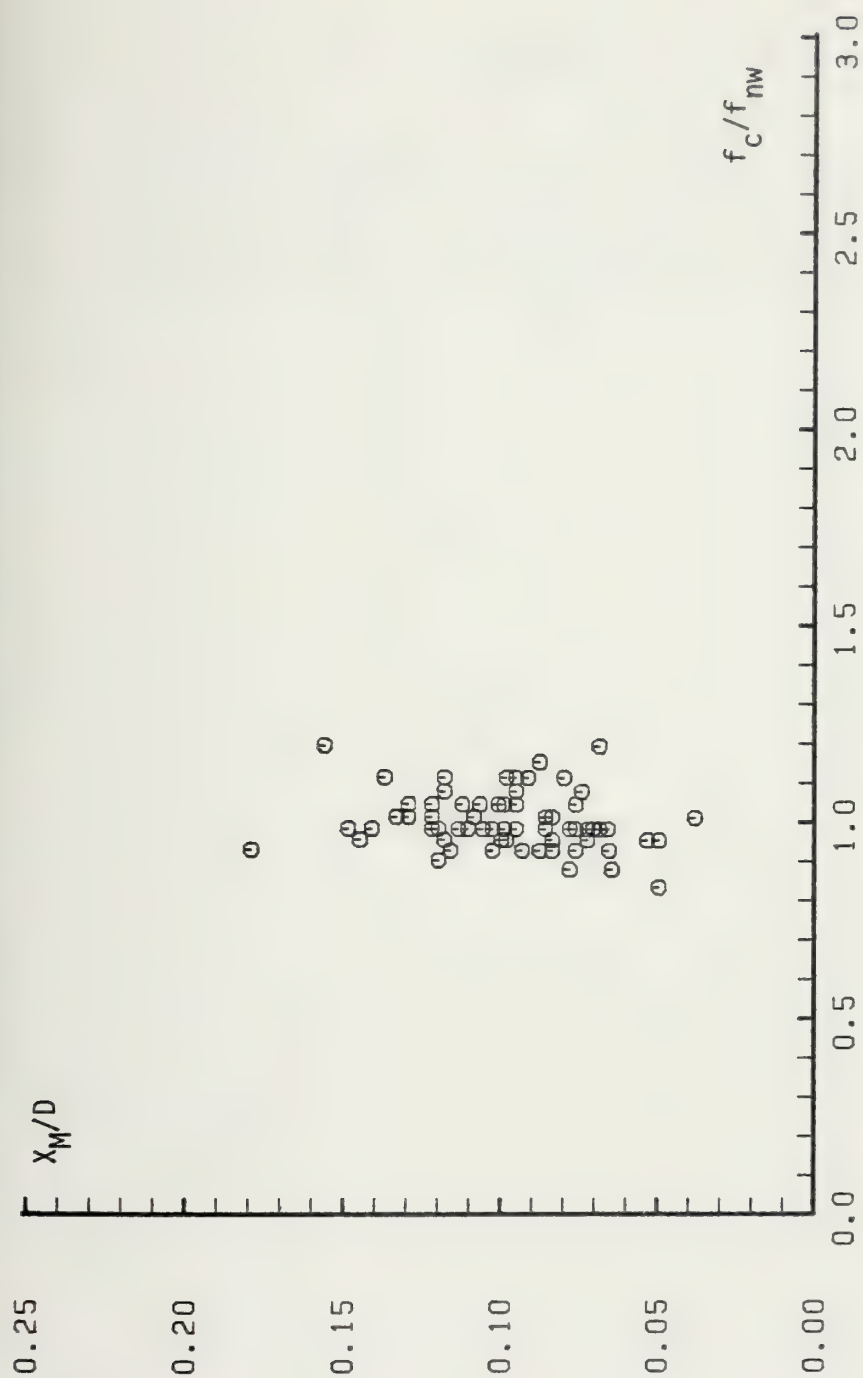


Fig. 45 X_M/D versus f_c/f_{nw} for 5 in. smooth cylinder, $z = 0.055$.

APPENDIX B

ROOT-MEAN-SQUARE VALUES OF THE RELATIVE AMPLITUDES
AS A FUNCTION OF K , U_r , f_f/f_{nw} , and f_c/f_{nw}

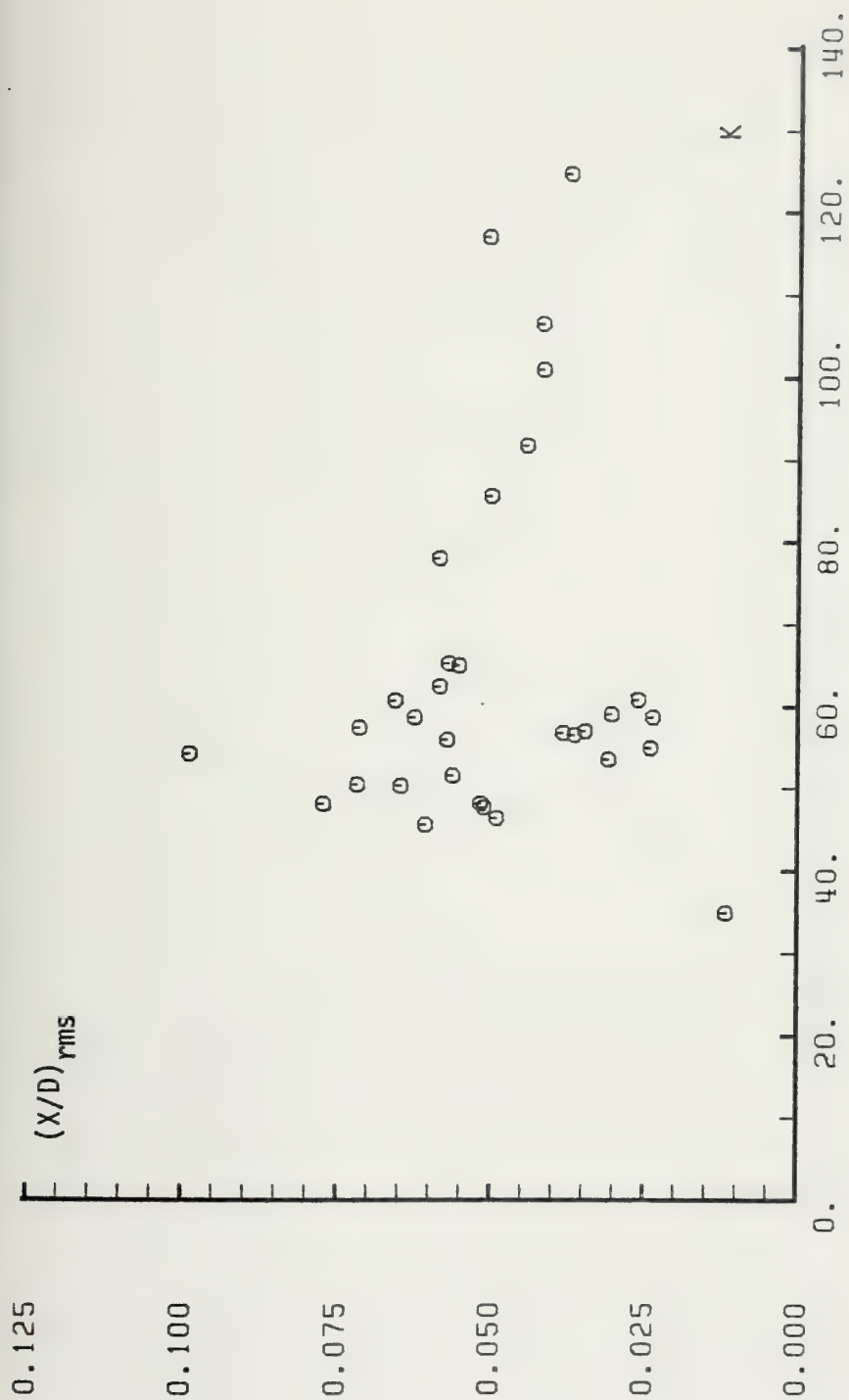


Fig. 50 $(X/D)_{rms}$ versus K for 3 in. rough cylinder, $\zeta = 0.067$.

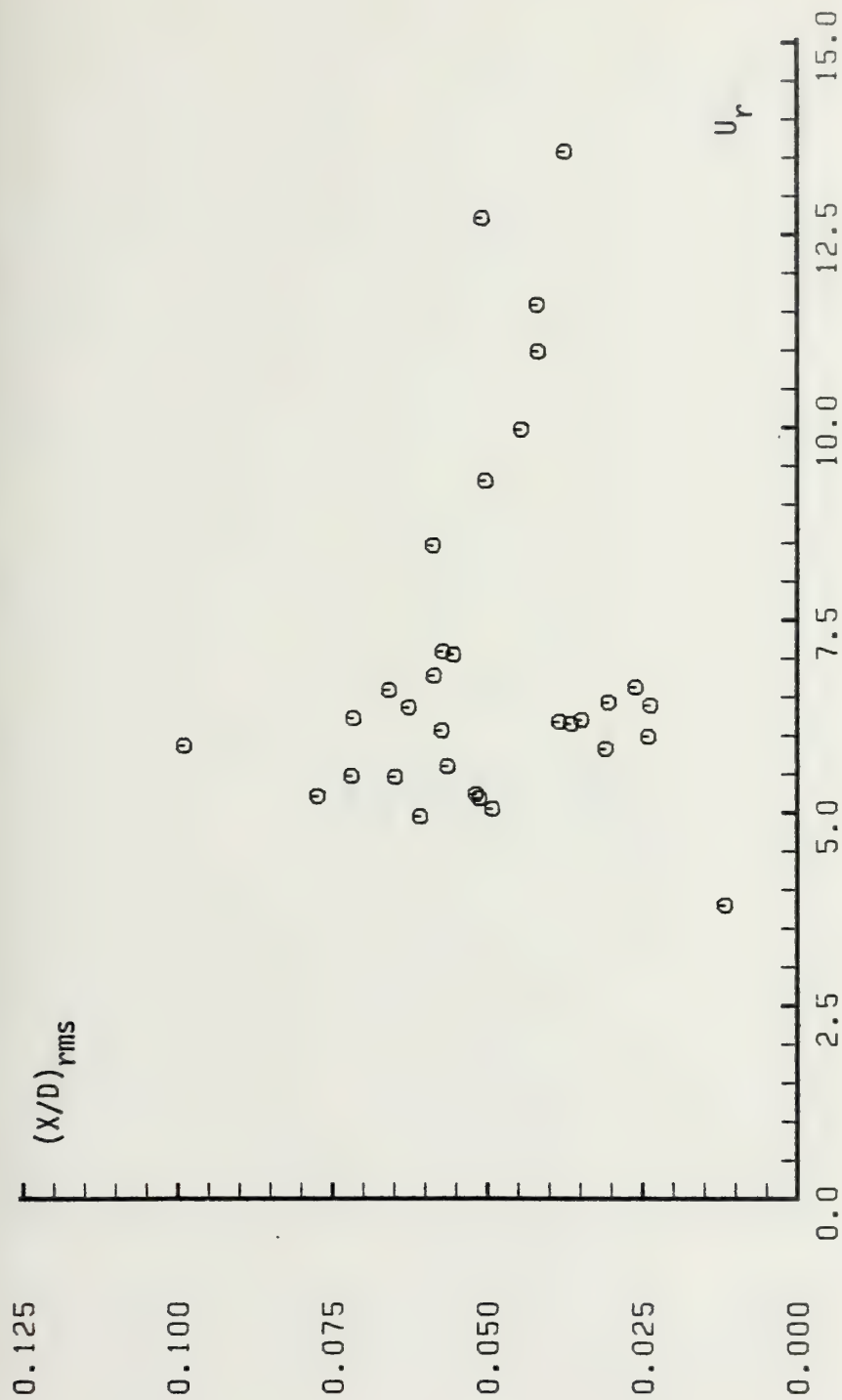


Fig. 51 $(X/D)_{rms}$ versus U_r for 3 in. rough cylinder, $\zeta = 0.067$.

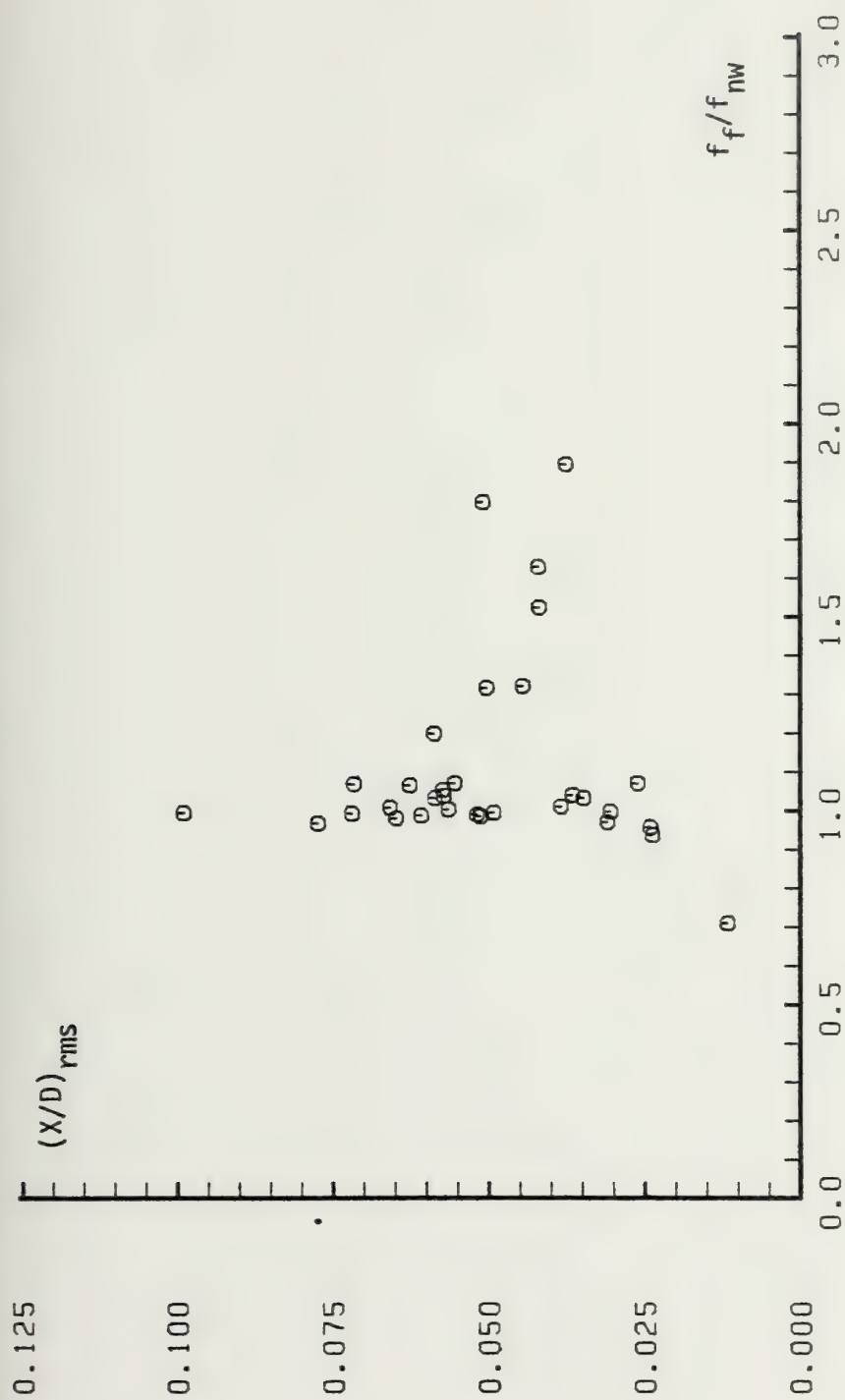


Fig. 52 $(X/D)_{rms}$ versus f_f/f_{nw} for 3 in. rough cylinder, $\zeta = 0.067$.

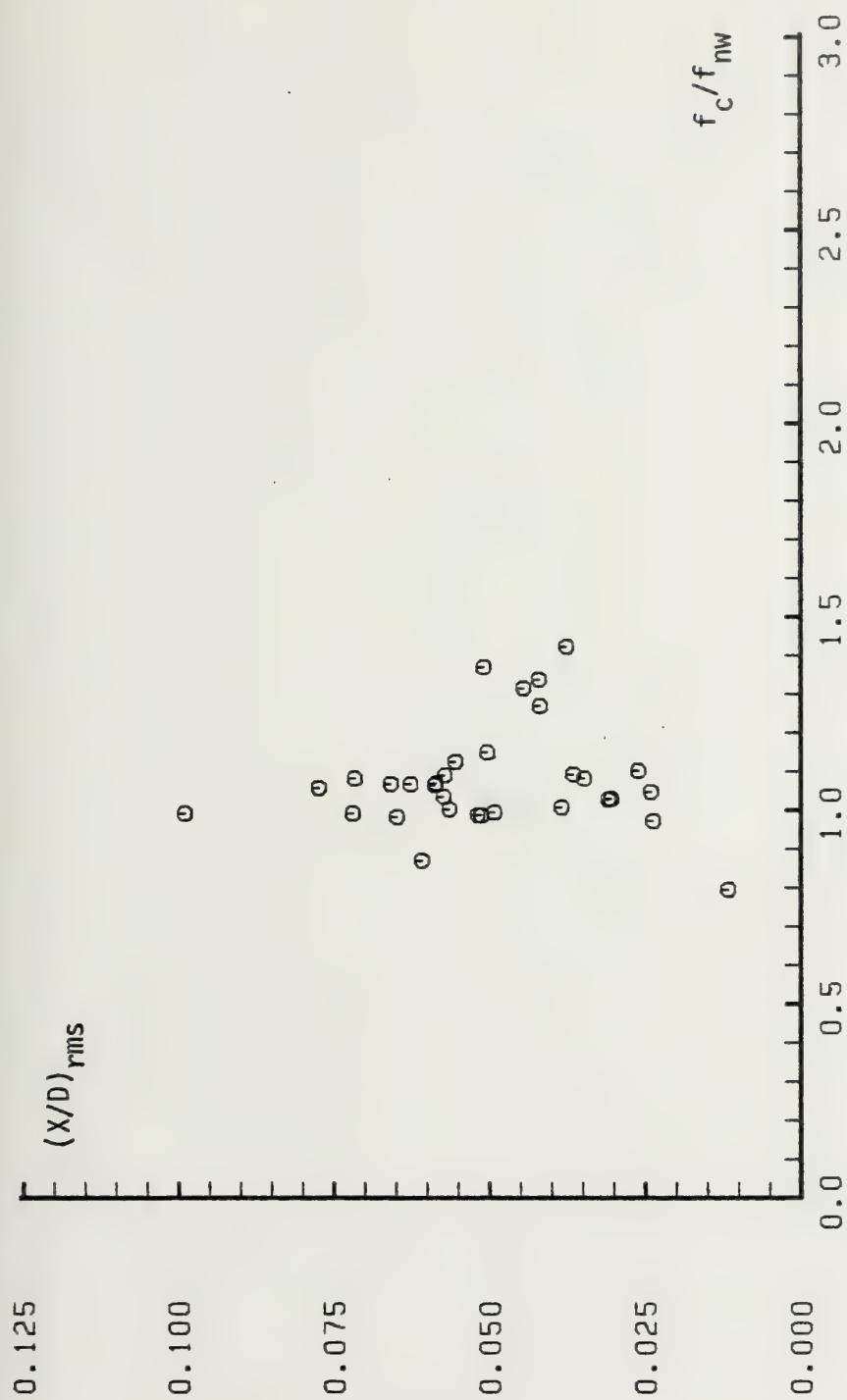


Fig. 53 $(X/D)_{rms}$ versus f_c/f_{nw} for 3 in. rough cylinder, $\zeta = 0.067$.

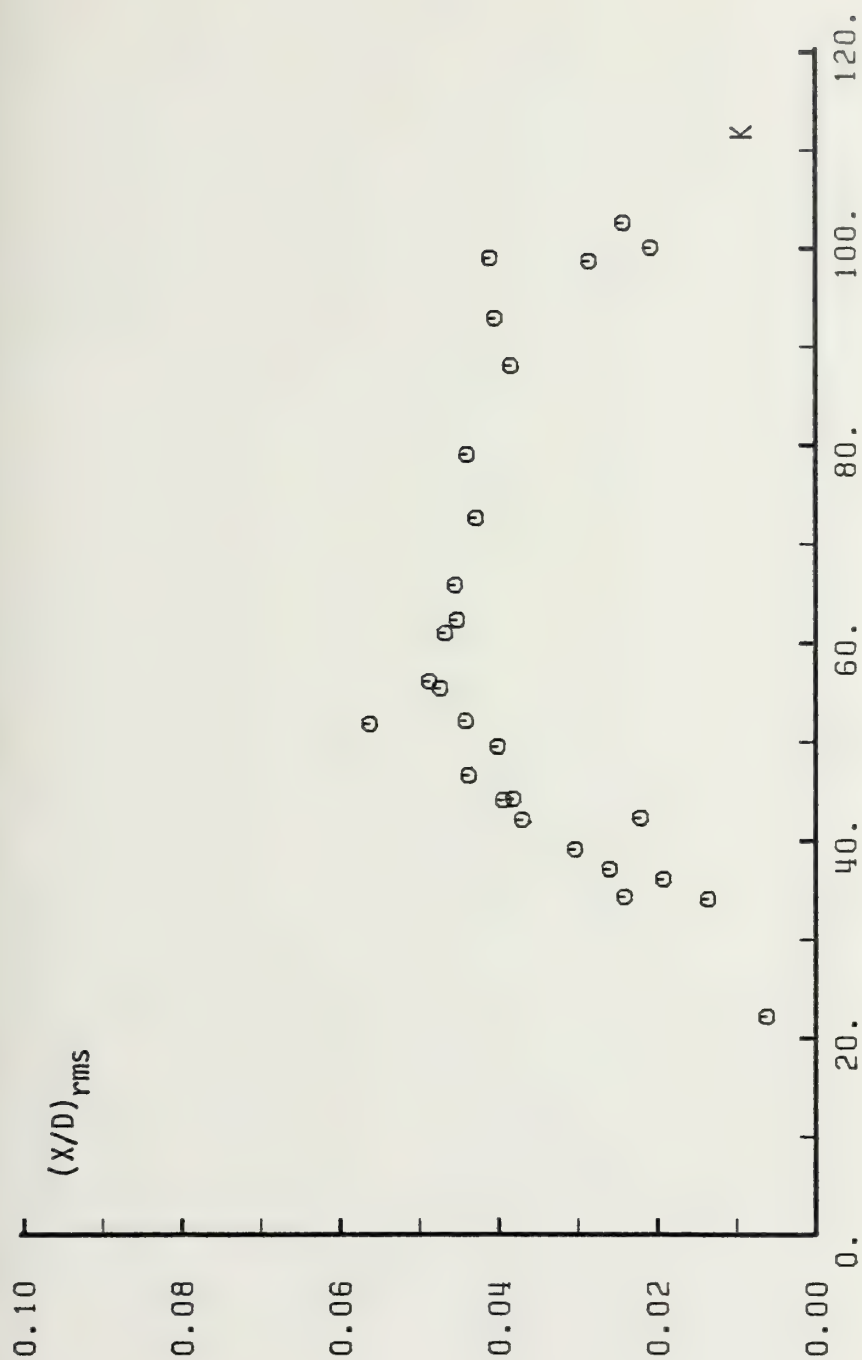


Fig. 54 $(X/D)_{rms}$ versus K for 4 in. smooth cylinder, $\zeta = 0.046$.

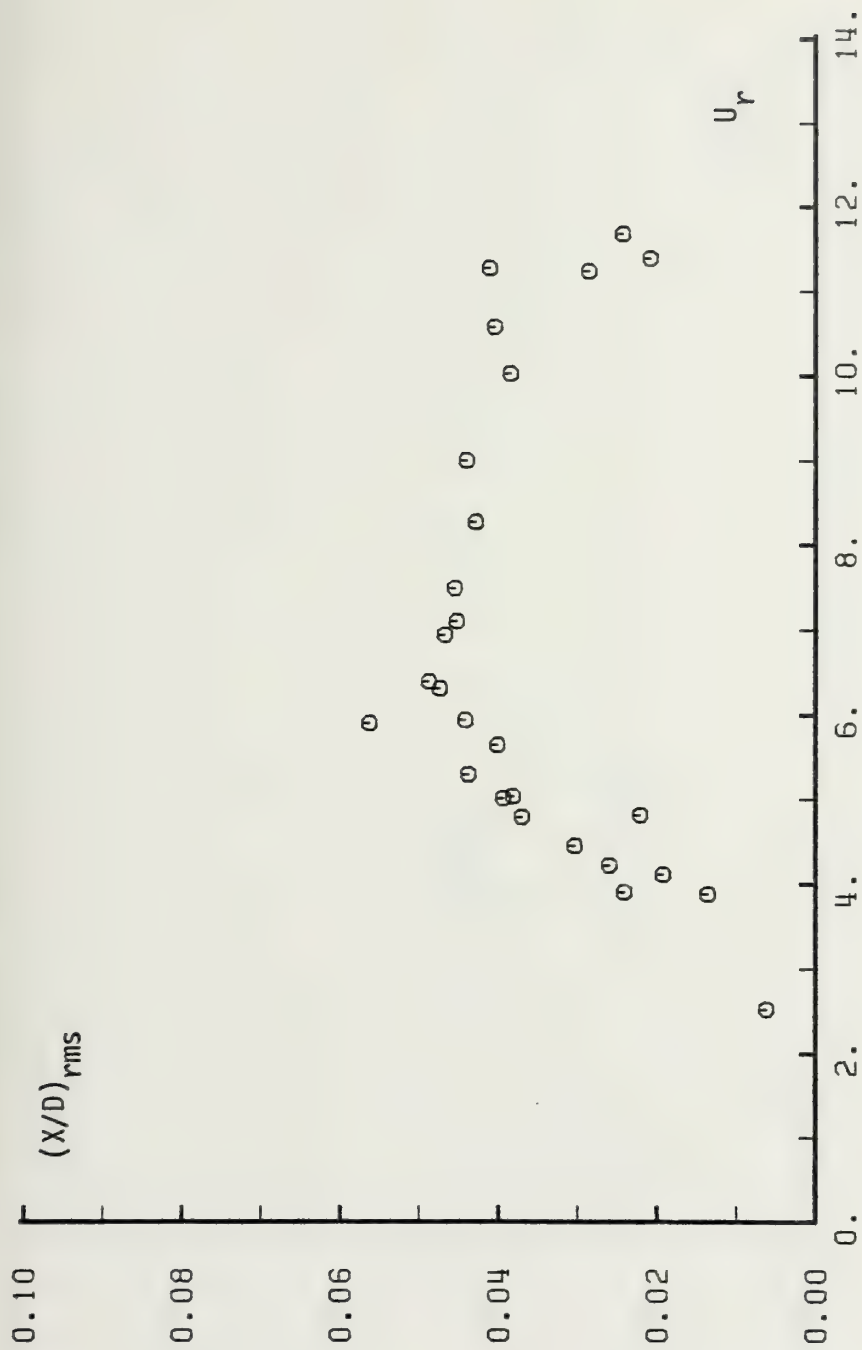


Fig. 55 $(X/D)_{rms}$ versus U_r for 4 in. smooth cylinder, $z = 0.046$.

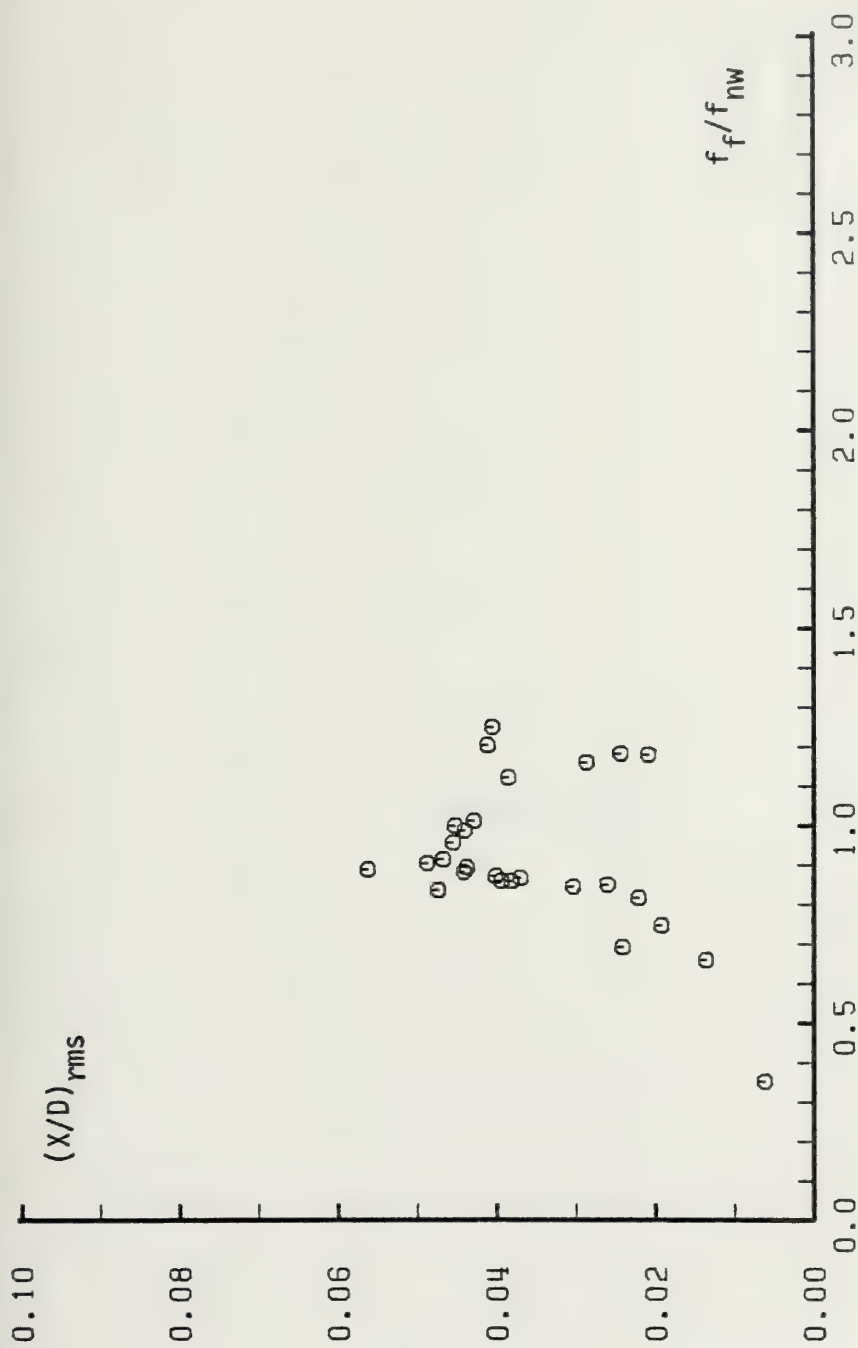


Fig. 56 $(X/D)_{rms}$ versus f_f/f_{nw} for 4 in. smooth cylinder, $\zeta = 0.046$.

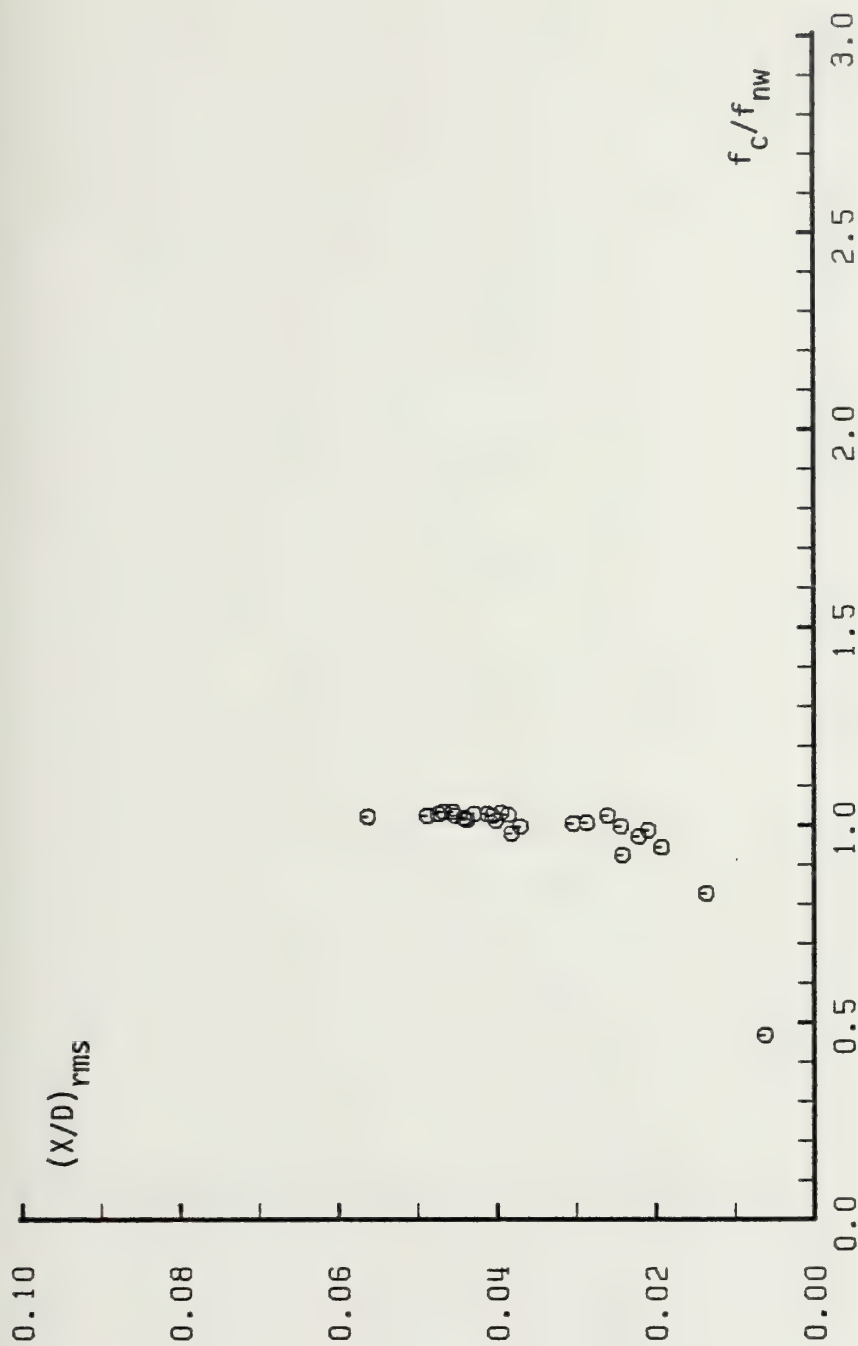


Fig. 57 $(X/D)_{rms}$ versus f_c/f_{nw} for 4 in. smooth cylinder, $\zeta = 0.046$.

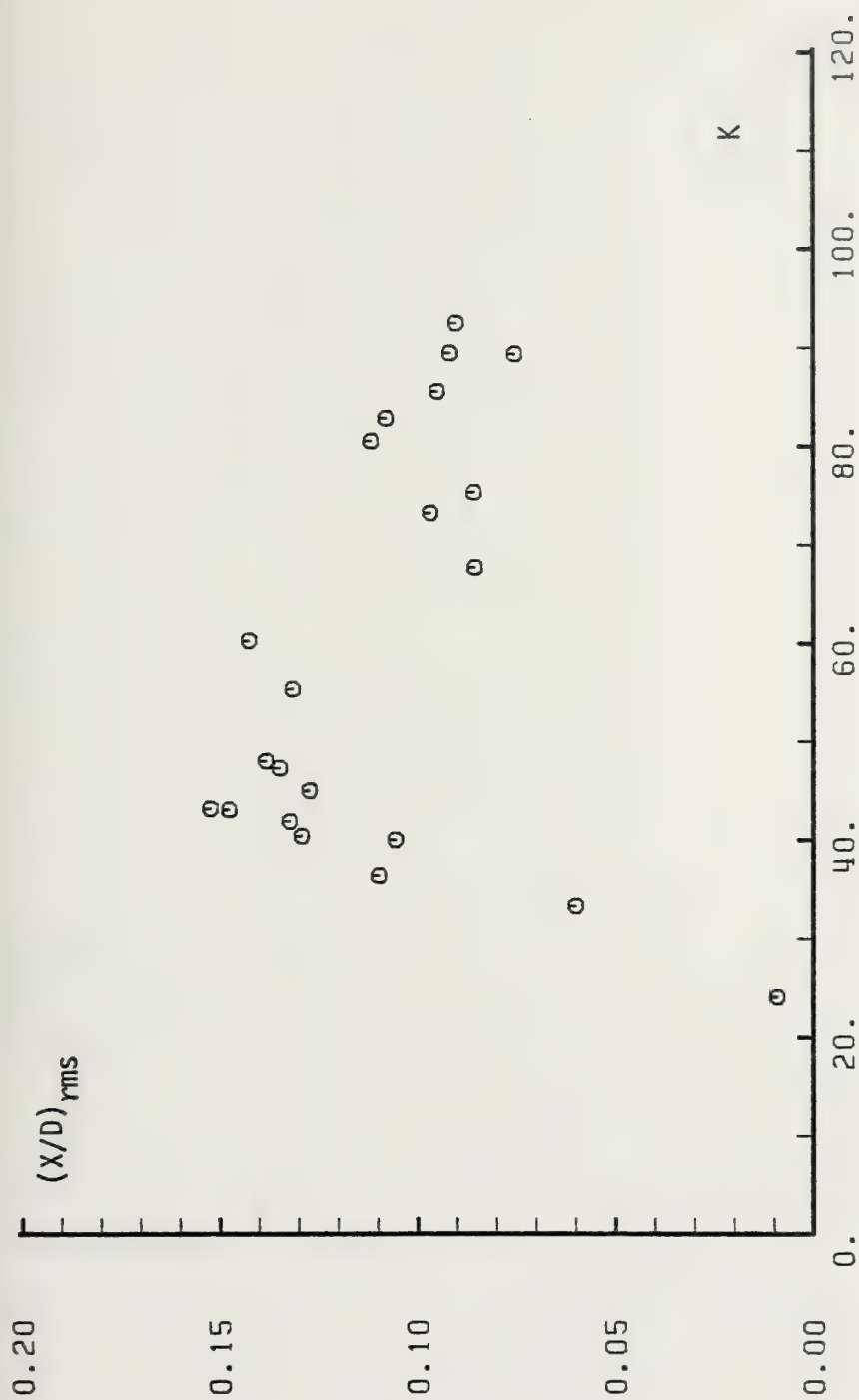


Fig. 58 $(X/D)_{rms}$ versus K for 4 in. rough cylinder, $\zeta = 0.060$.

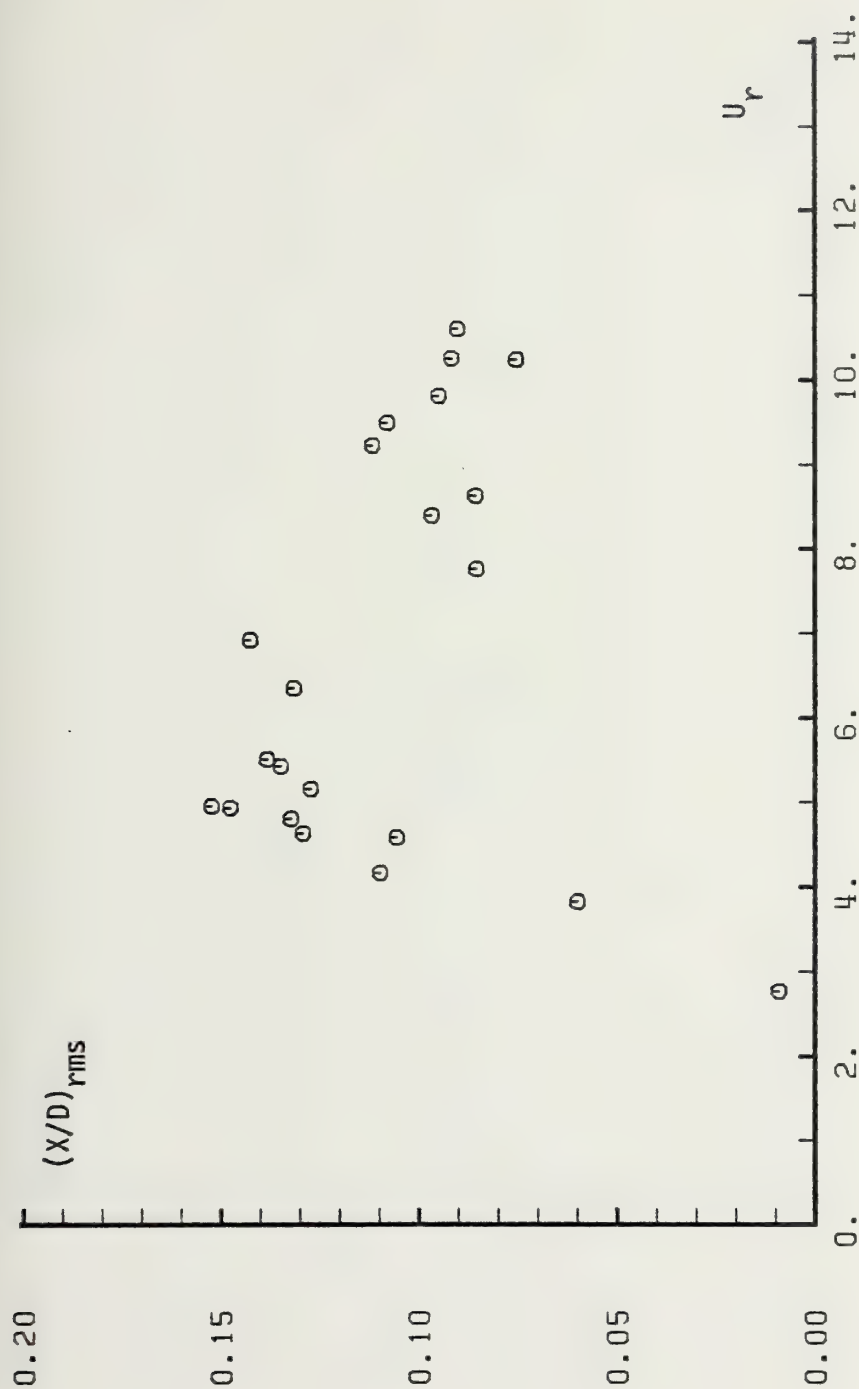


Fig. 59 $(X/D)_{rms}$ versus U_r for 4 in. rough cylinder, $\zeta = 0.060$.

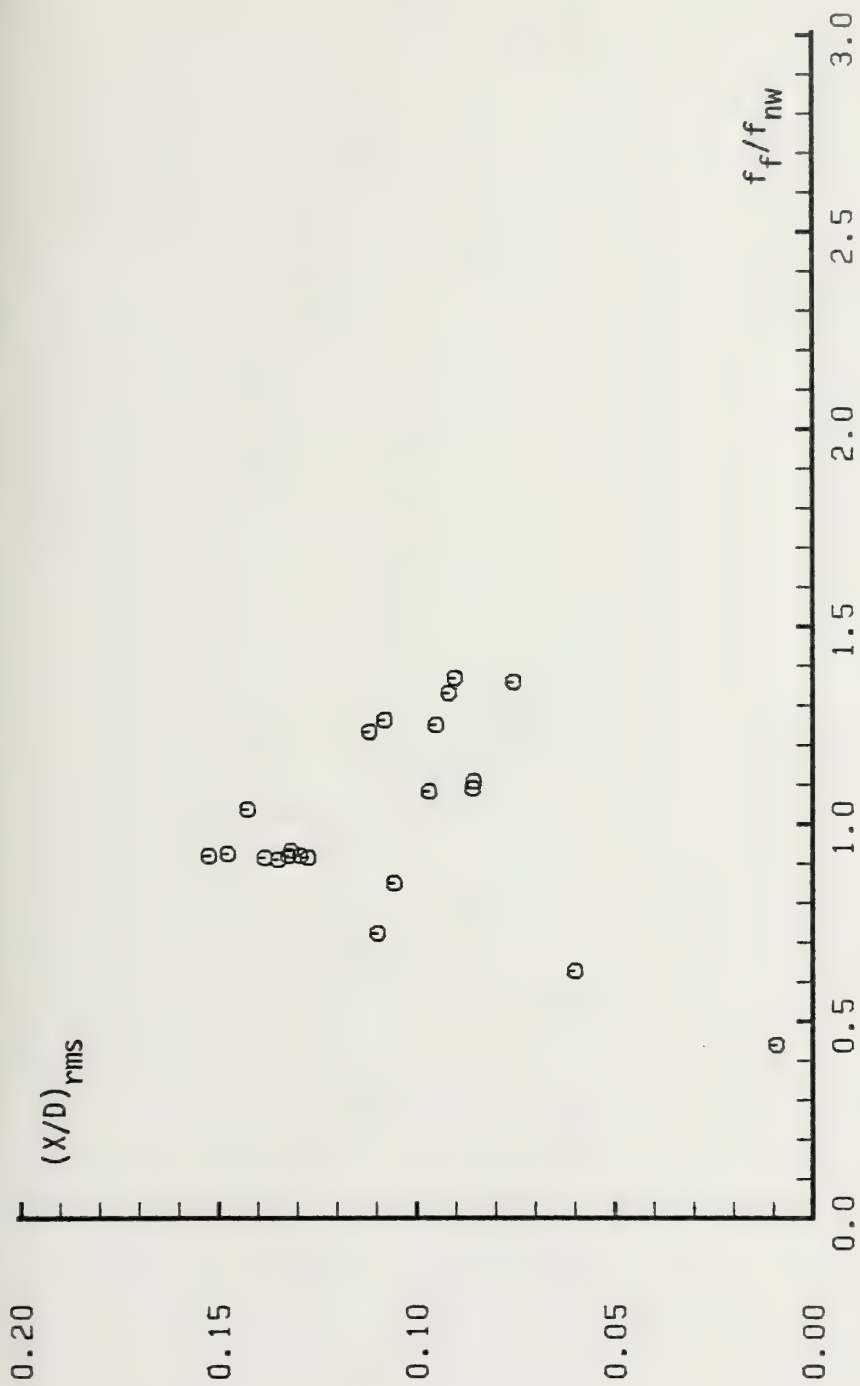


Fig. 60 $(X/D)_{rms}$ versus f_f/f_{nw} for 4 in. rough cylinder, $\zeta = 0.060$.

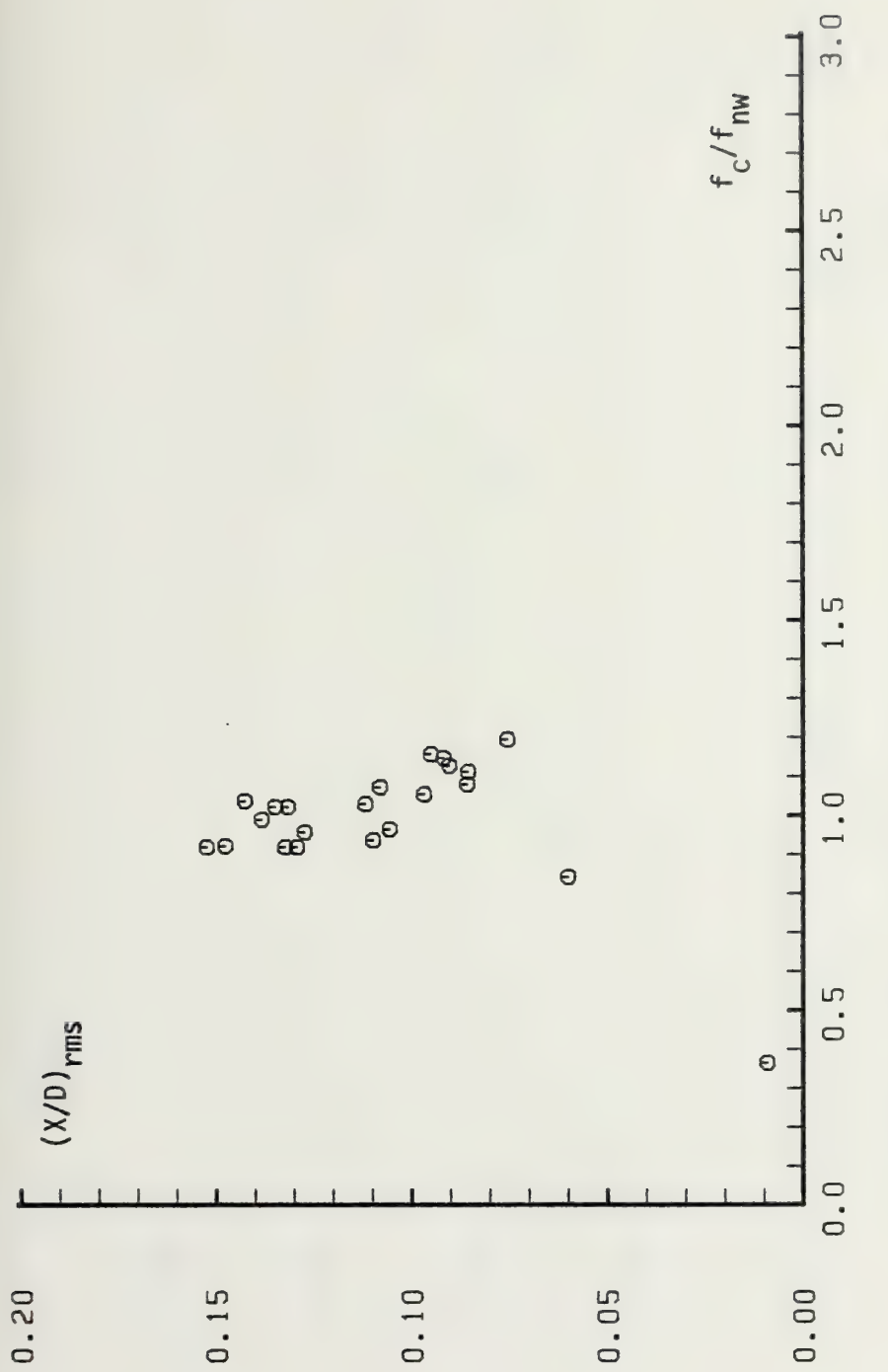


Fig. 61 $(X/D)_{rms}$ versus f_c/f_{nw} for 4 in. rough cylinder, $\zeta = 0.060$.

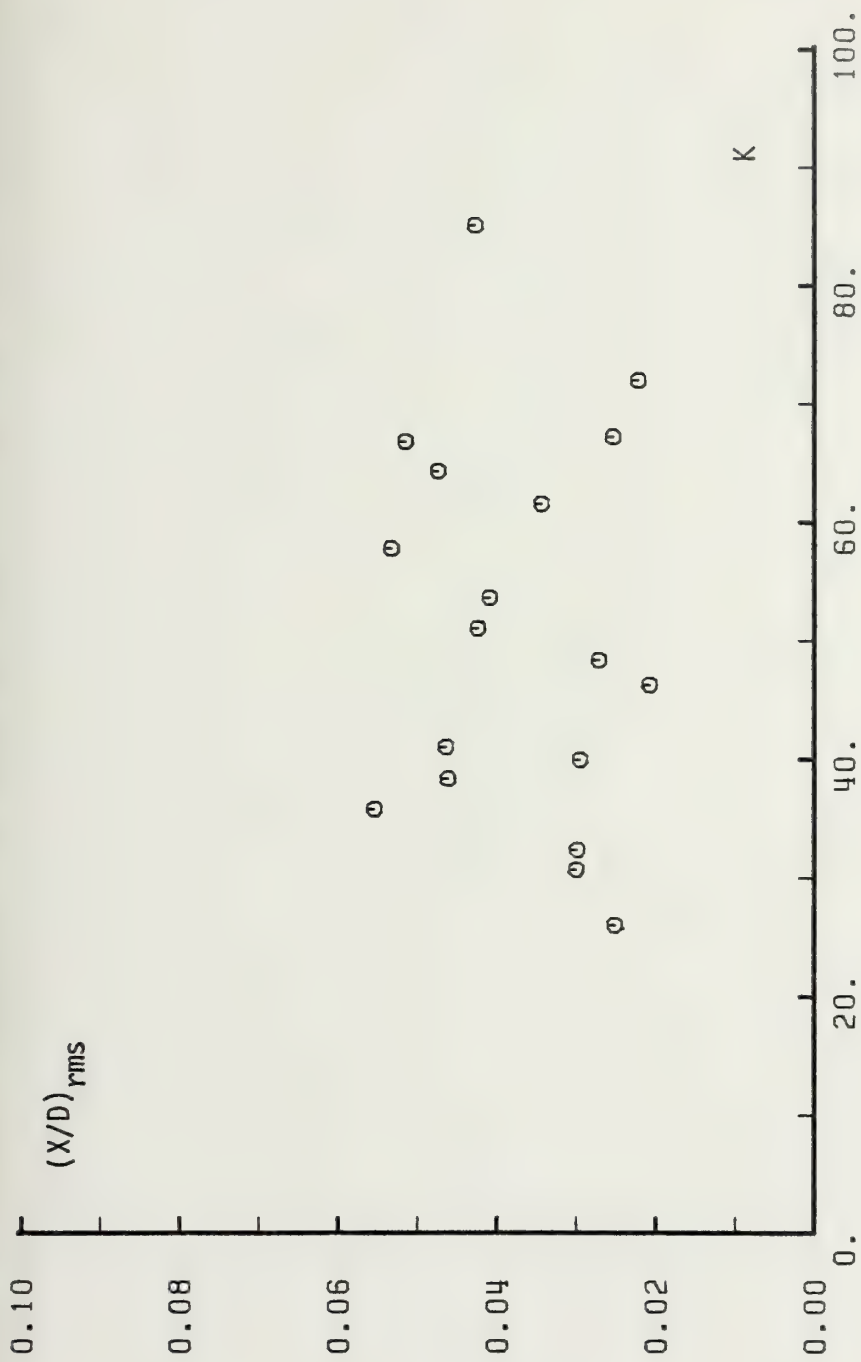


Fig. 62 $(X/D)_{rms}$ versus K for 5 in. smooth cylinder, $\zeta = 0.055$.

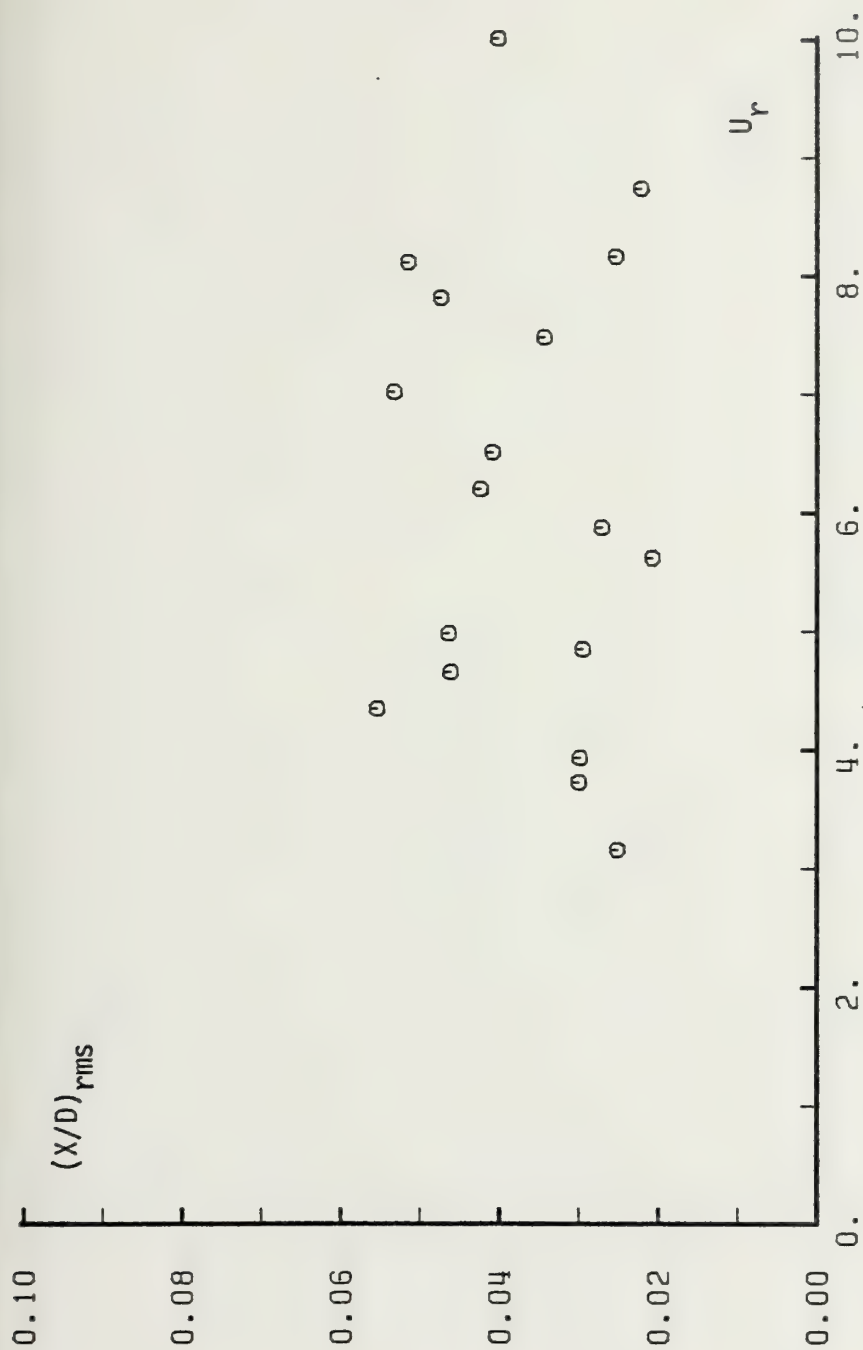


Fig. 63 $(X/D)_{rms}$ versus U_r for 5 in. smooth cylinder, $z = 0.055$.

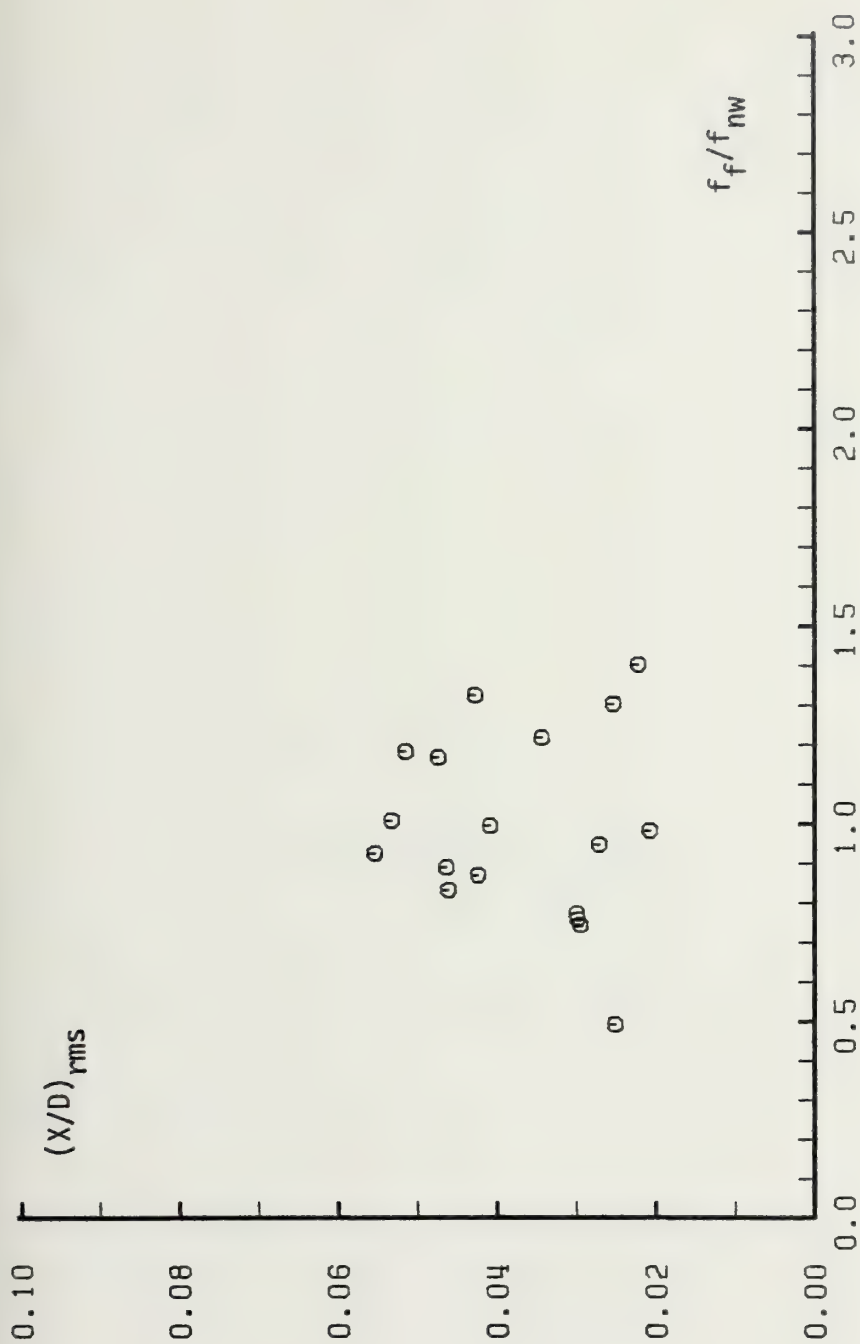


Fig. 64 $(X/D)_{\text{rms}}$ versus f_f/f_{nw} for 5 in. smooth cylinder, $\zeta = 0.055$.

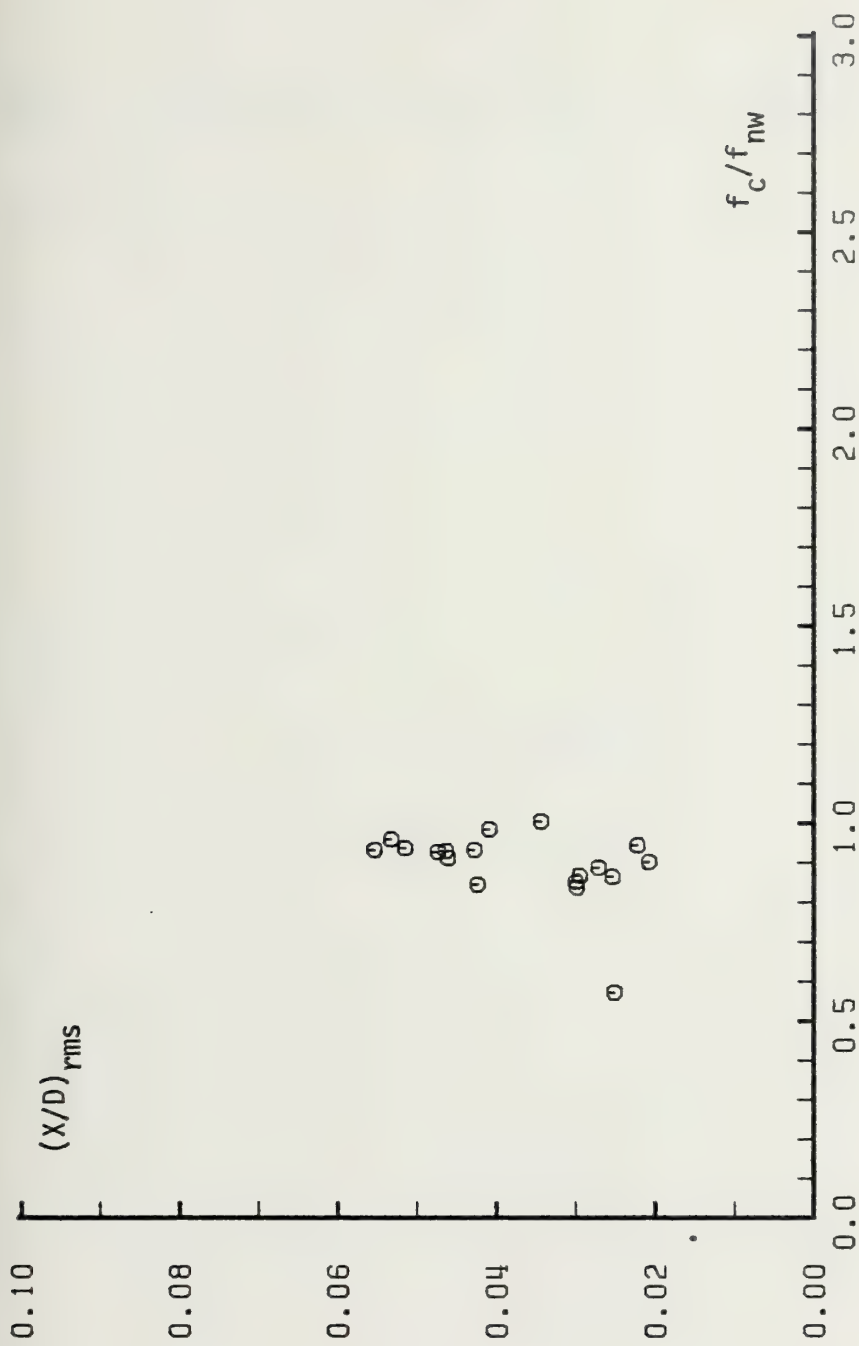


Fig. 65 $(X/D)_{rms}$ versus f_c/f_{nw} for 5 in. smooth cylinder, $\zeta = 0.055$.

APPENDIX C

PEAK LIFT COEFFICIENTS AS A FUNCTION OF K , U_r , f_f/f_{nw} , and f_f/f_c

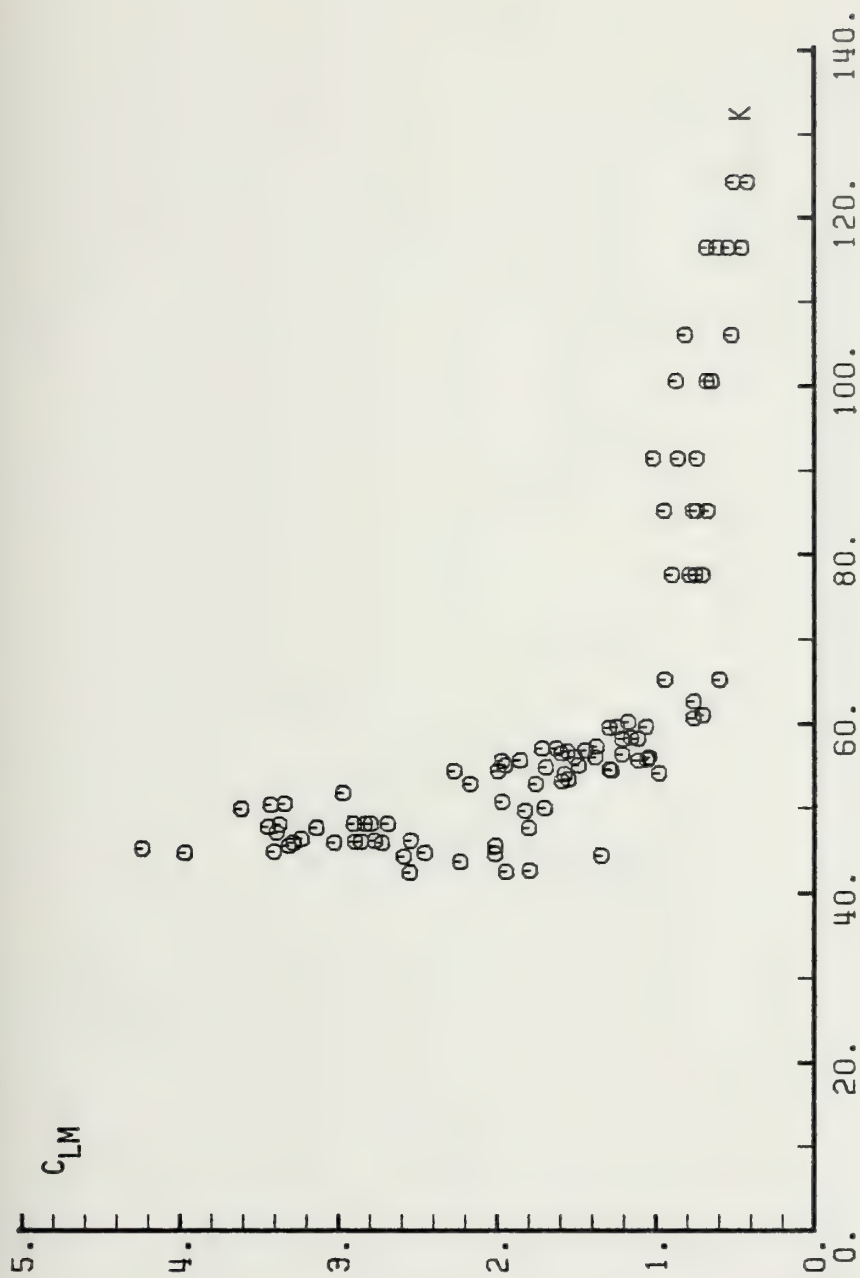


Fig. 70 C_{LM} versus K for 3 in. rough cylinder, $\zeta = 0.067$.

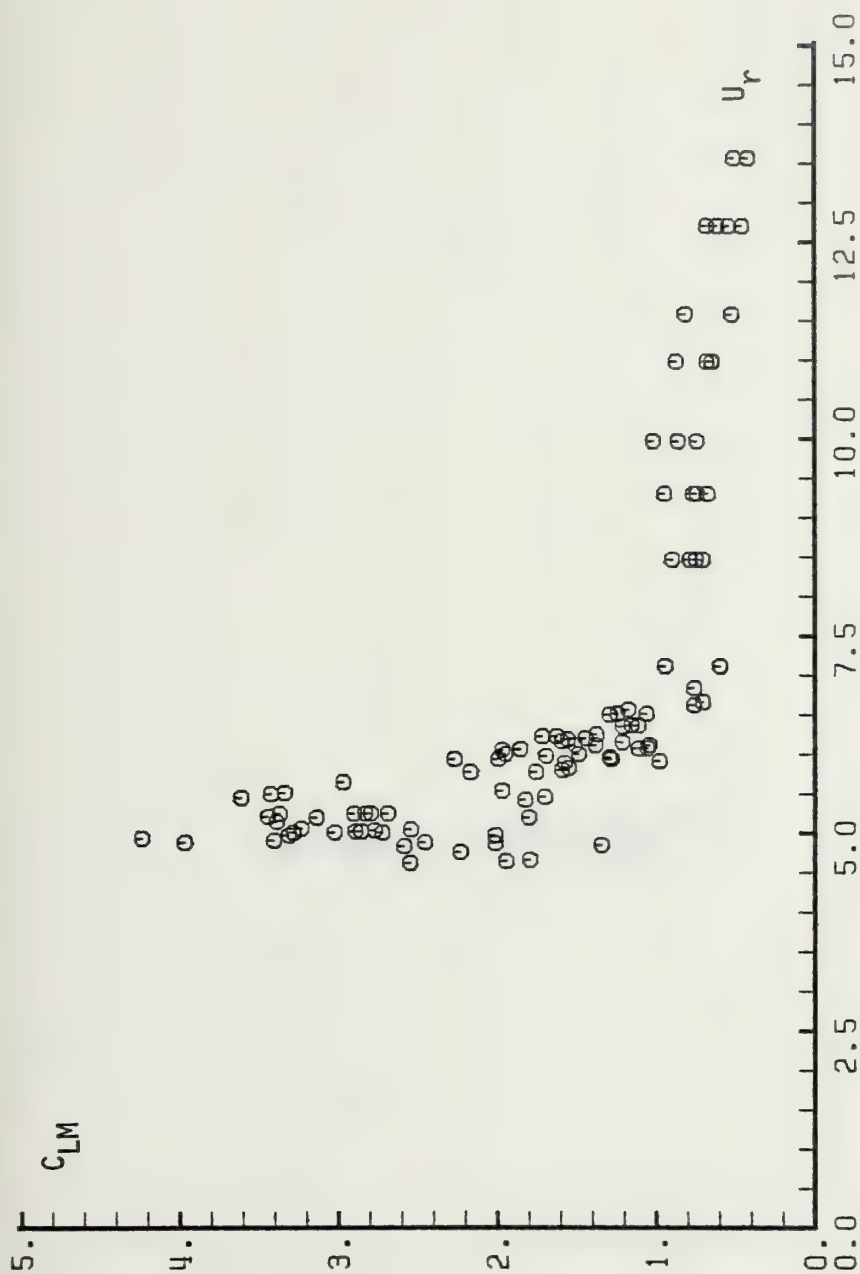


Fig. 71 C_{LM} versus U_r for 3 in. rough cylinder, $z = 0.067$.

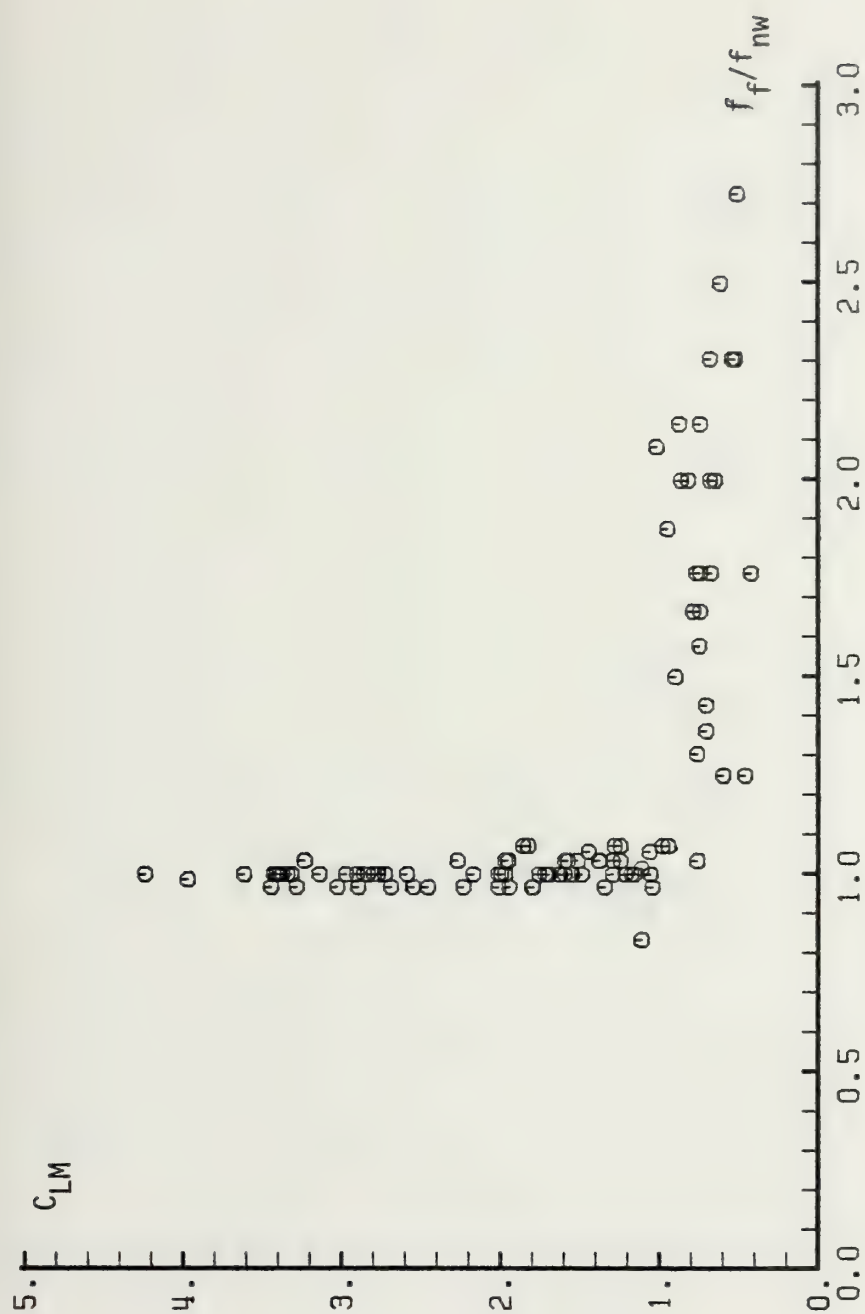


Fig. 72 C_{LM} versus f_f/f_{nw} for 3 in. rough cylinder, $z = 0.067$.

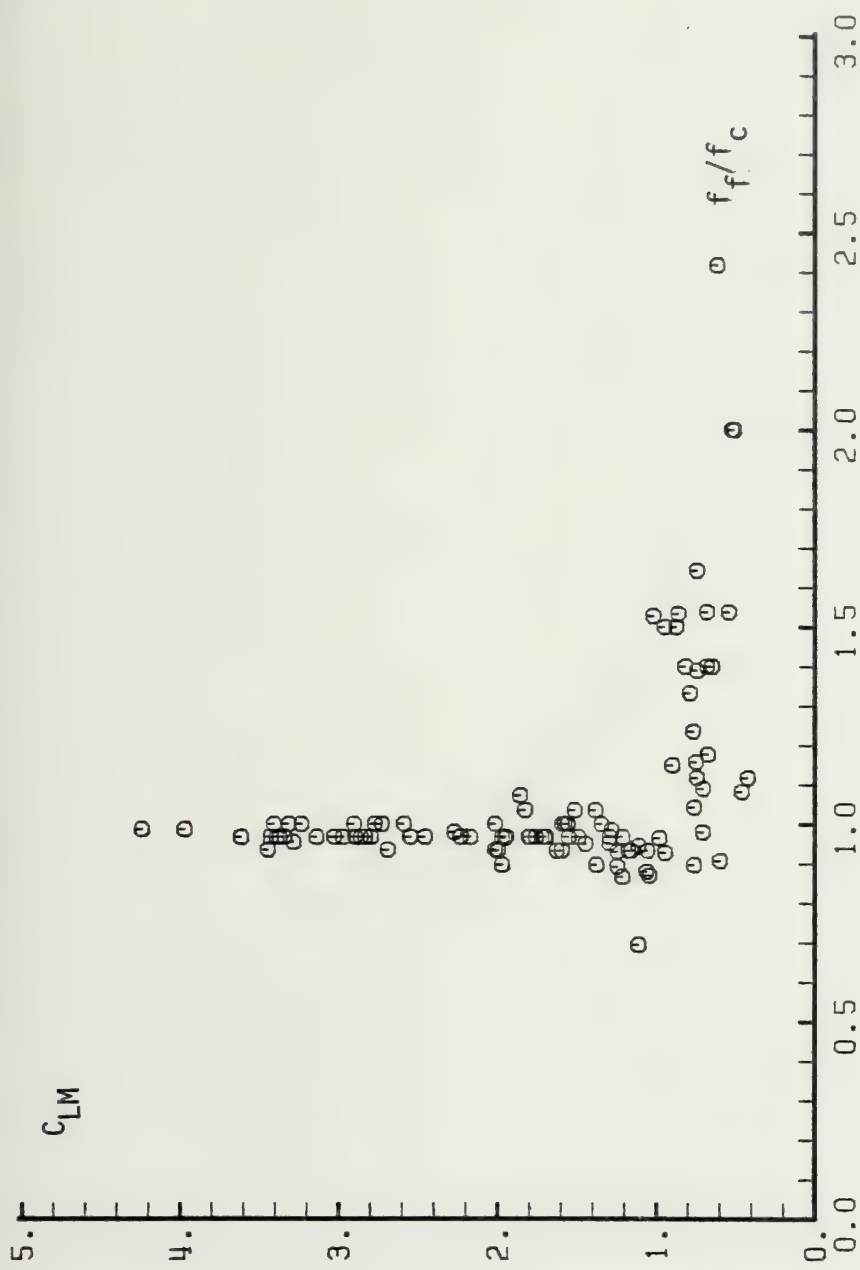


Fig. 73 C_{LM} versus f_f/f_c for 3 in. rough cylinder, $\zeta = 0.067$.

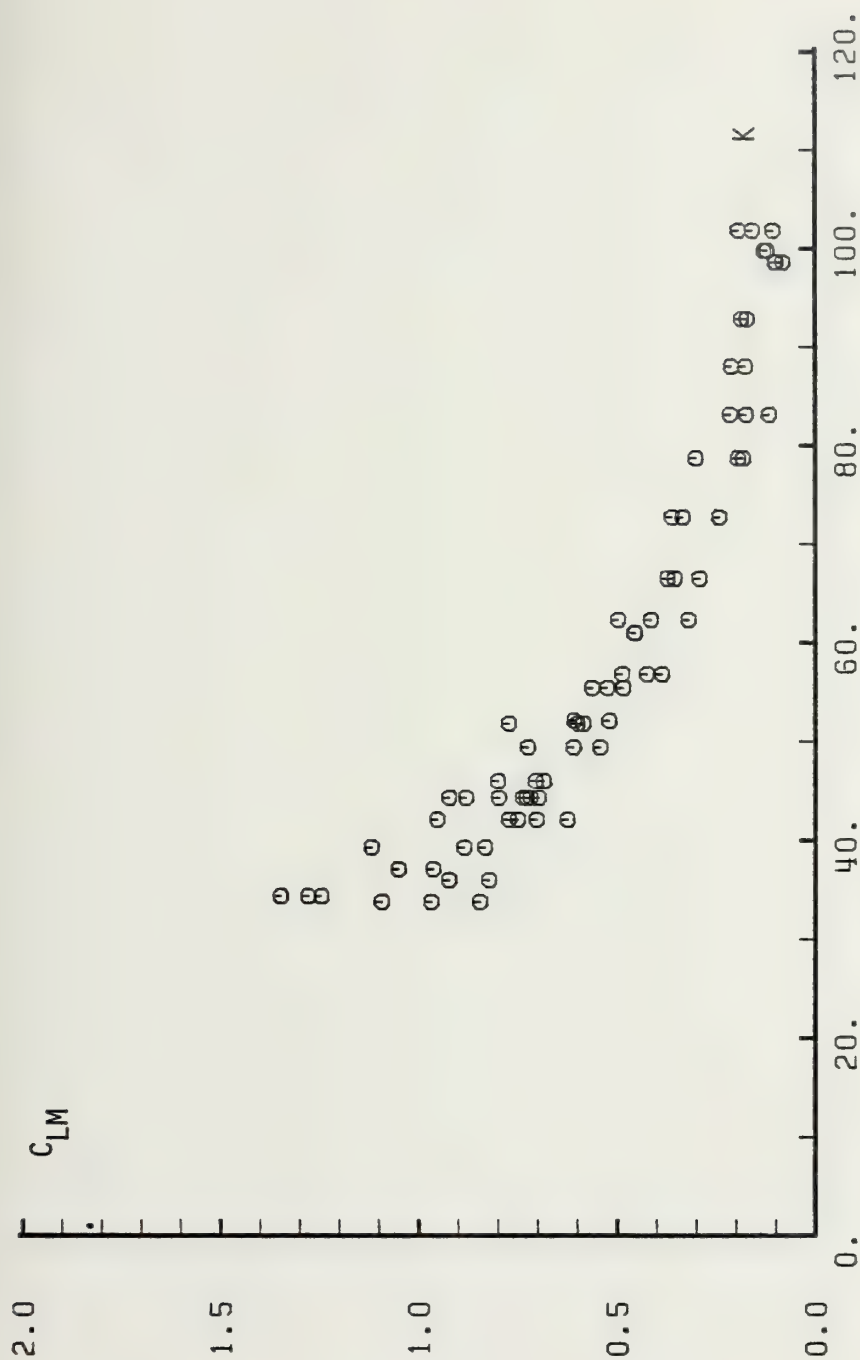


Fig. 74 C_{LM} versus K for 4 in. smooth cylinder, $z = 0.046$.

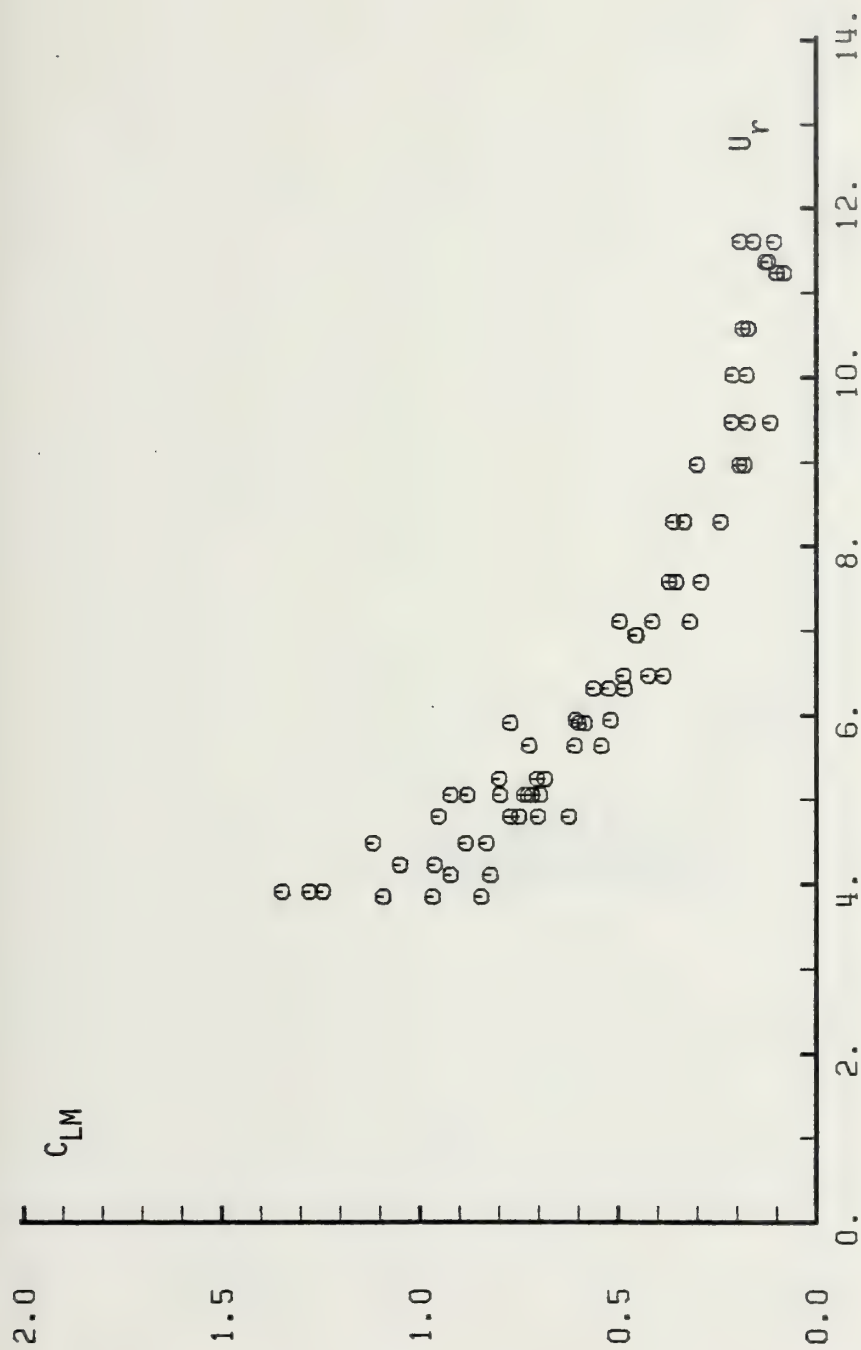


Fig. 75 C_{LM} versus U_r for 4 in. smooth cylinder, $\zeta = 0.046$.

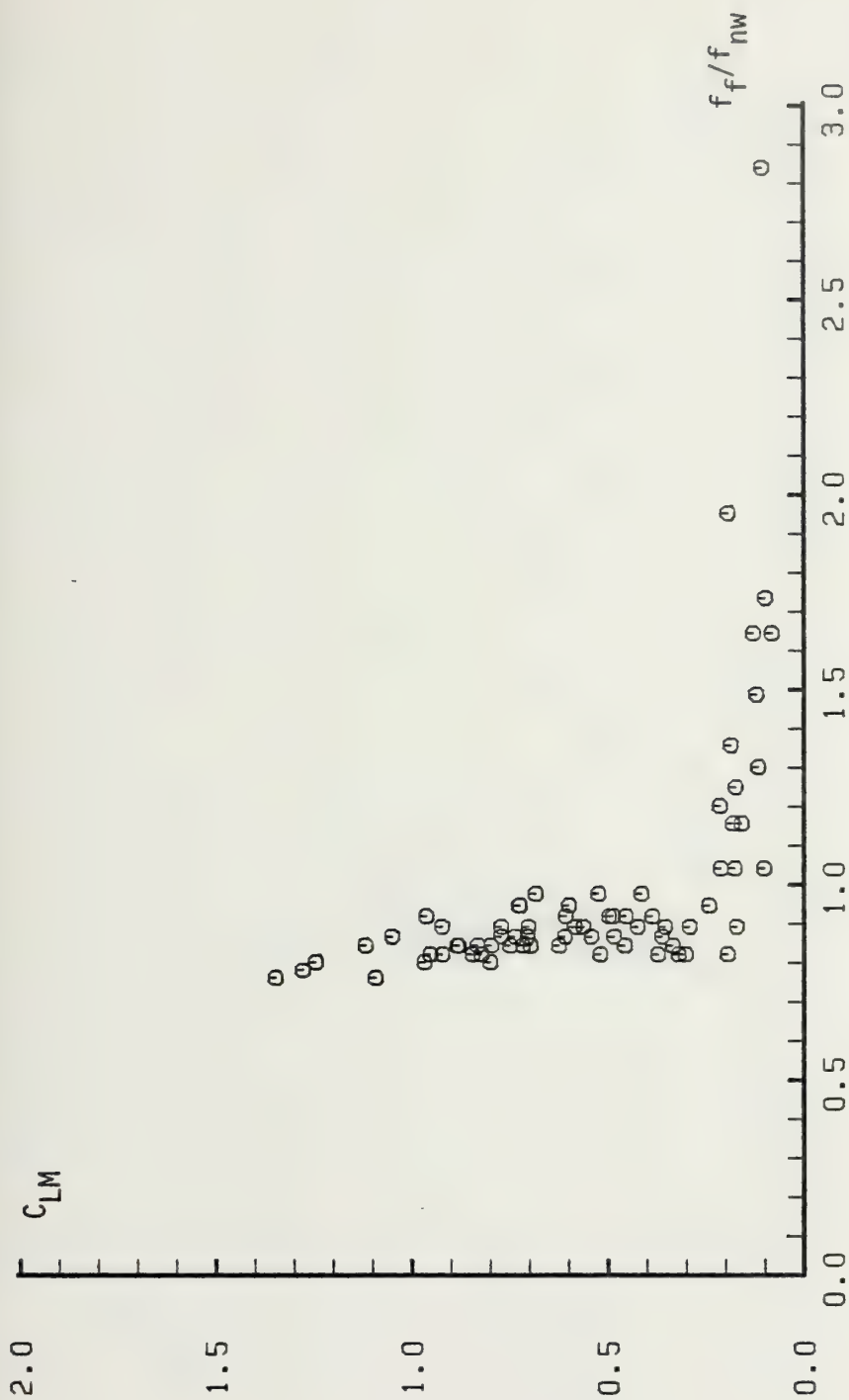


Fig. 76 C_{LM} versus f_f/f_{nw} for 4 in. smooth cylinder, $\zeta = 0.046$.

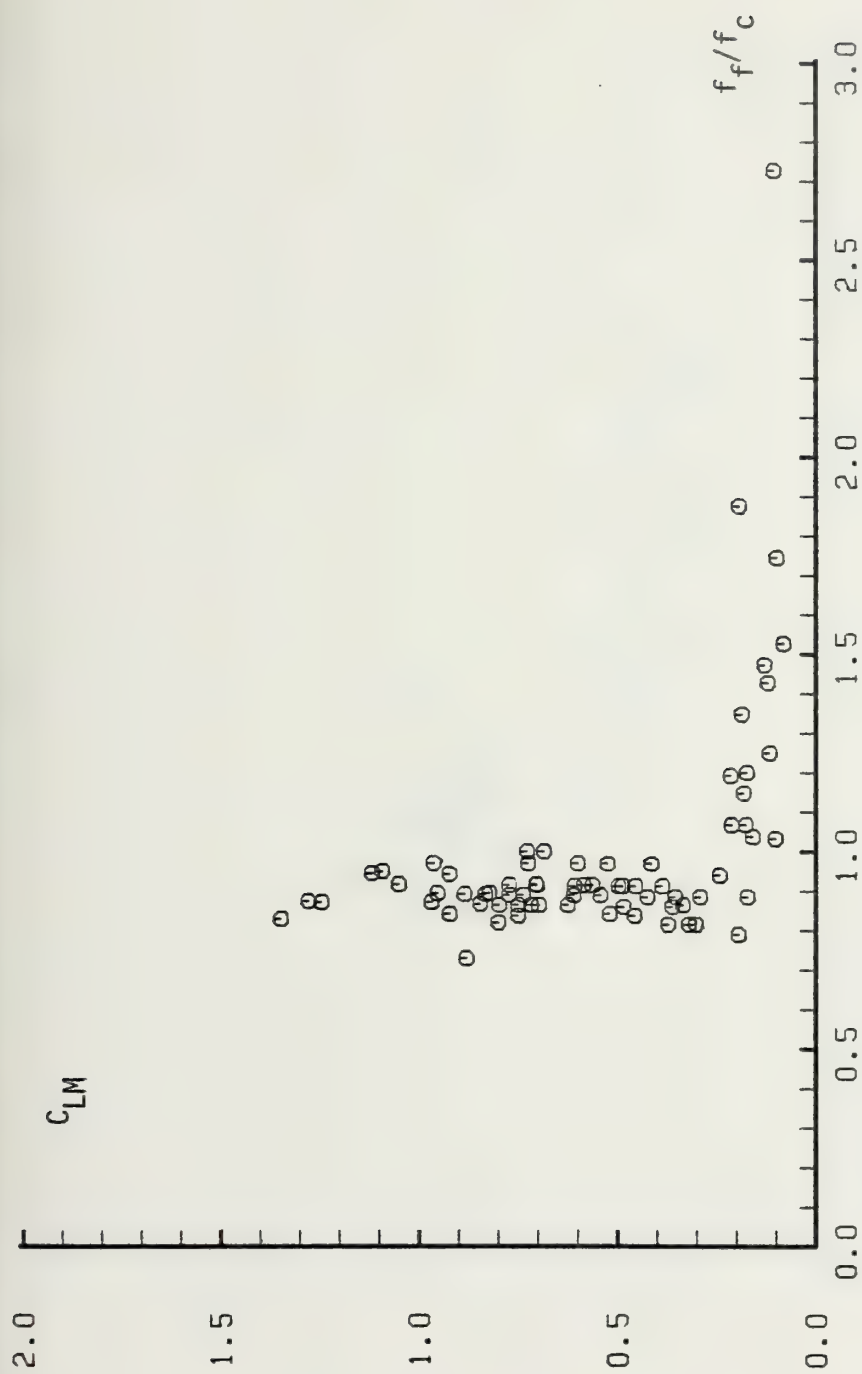


Fig. 77 C_{LM} versus f_f/f_c for 4 in. smooth cylinder, $\zeta = 0.046$.

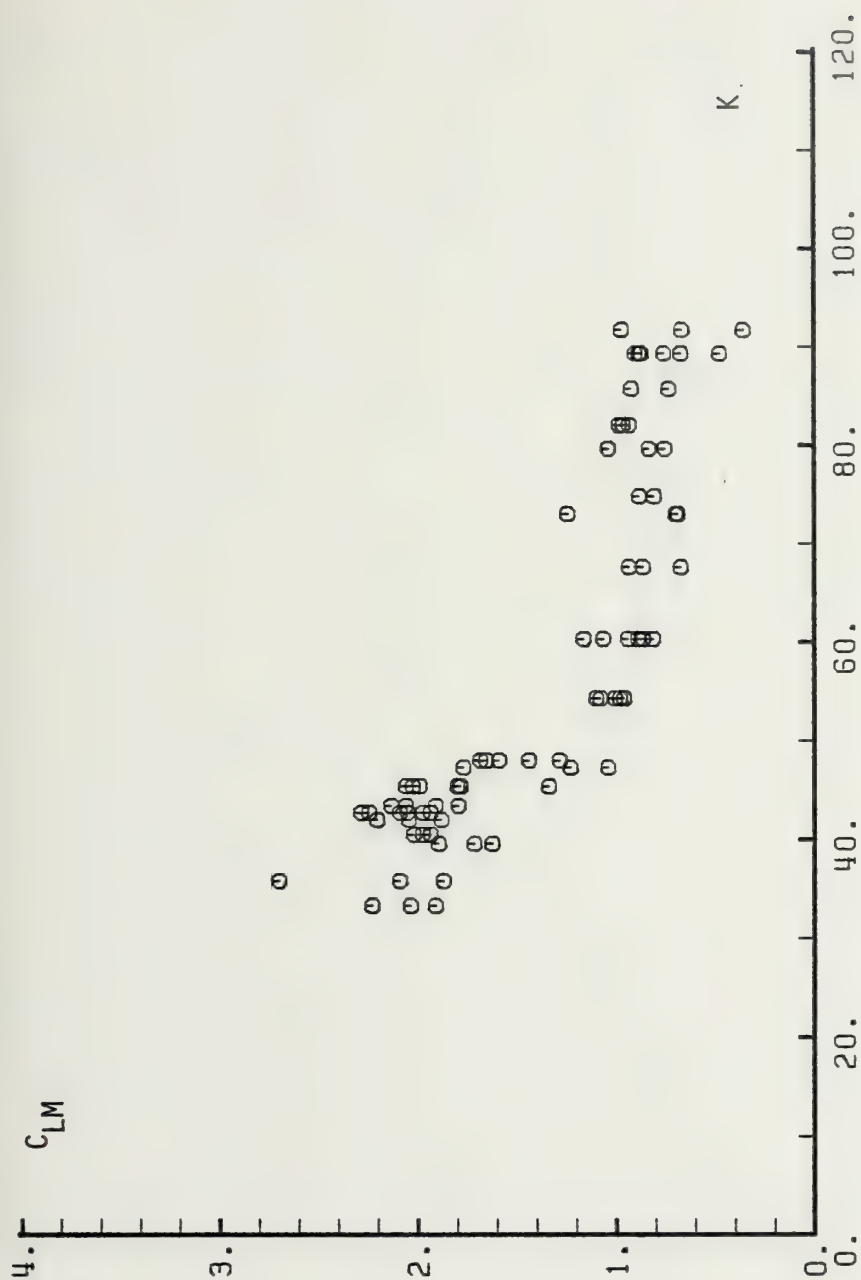


Fig. 78 C_{LM} versus K for 4 in. rough cylinder, $z = 0.060$.

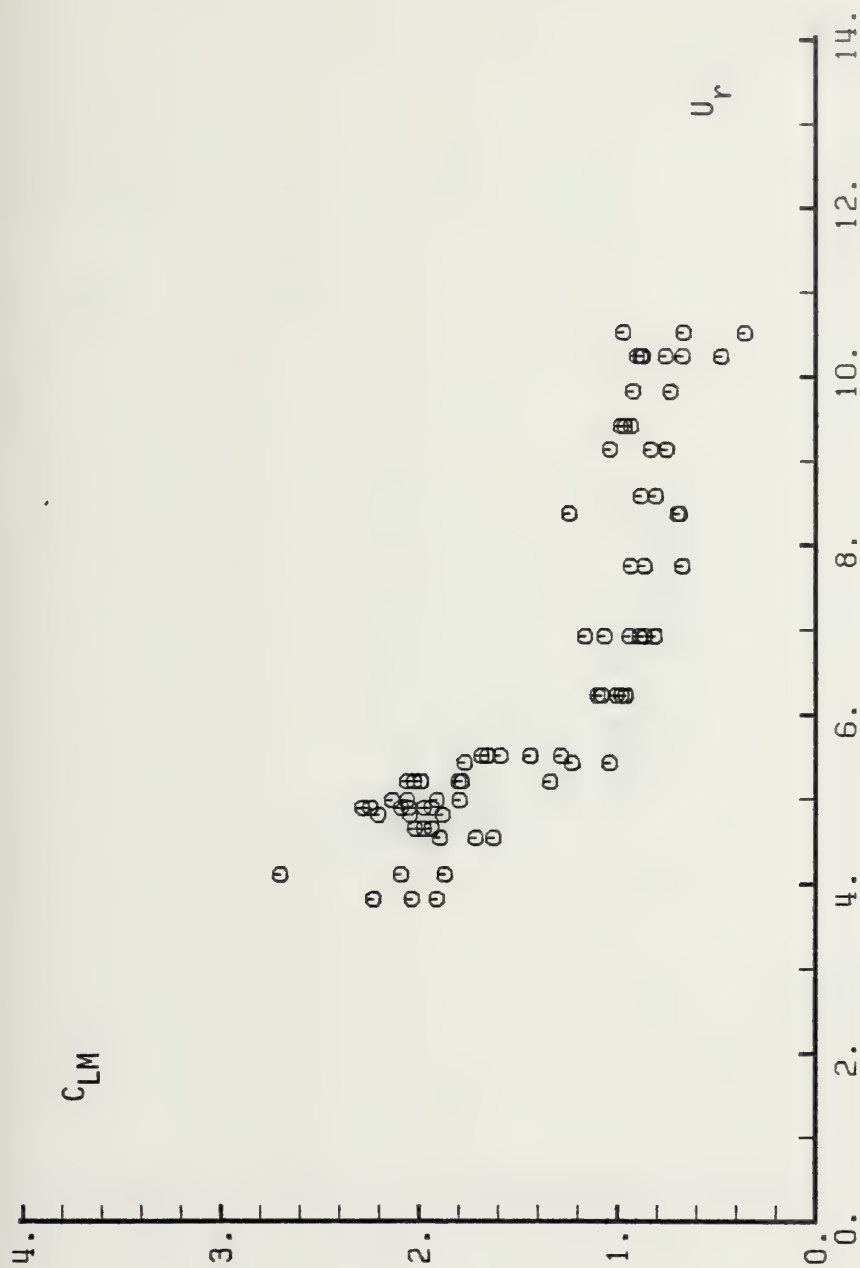


Fig. 79 C_{LM} versus U_r for 4 in. rough cylinder, $z = 0.060$.

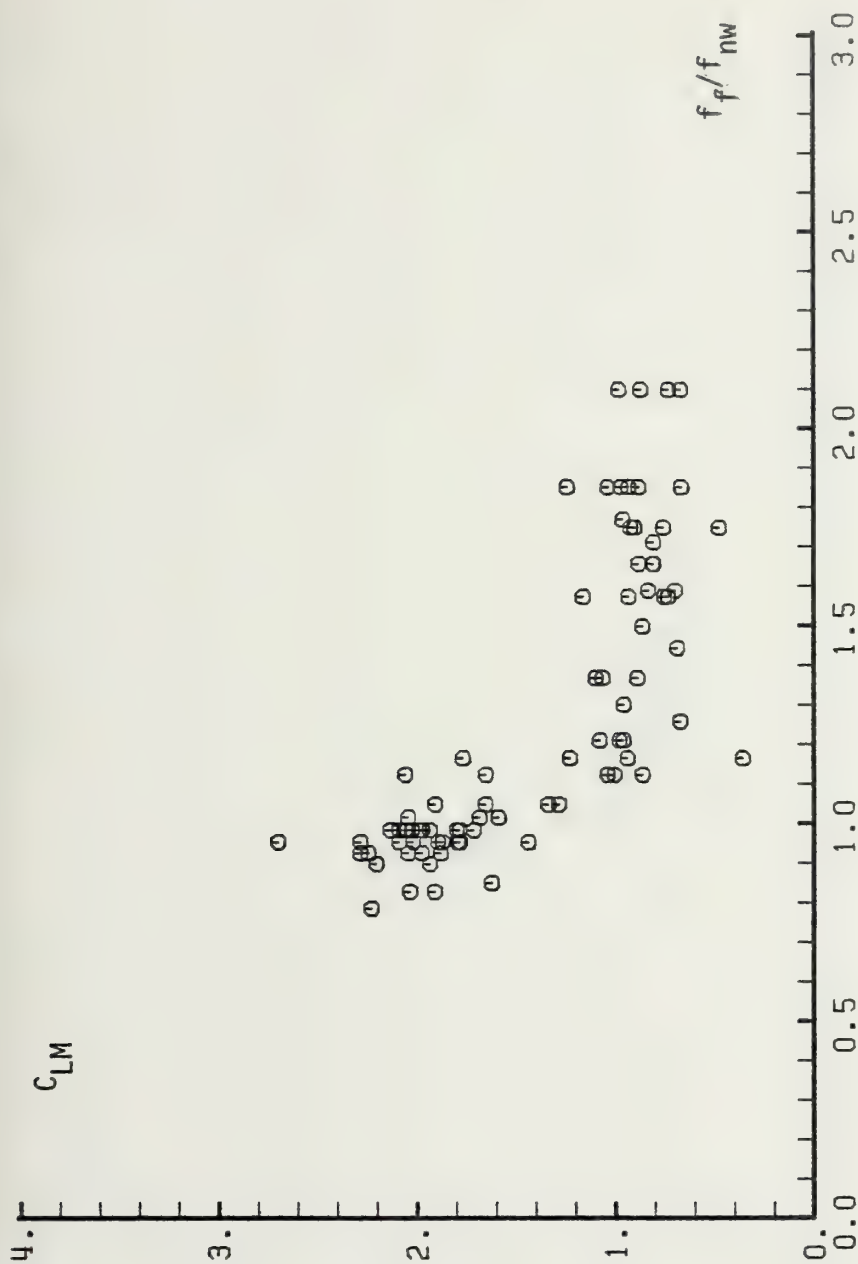


Fig. 80 C_{LM} versus f_f/f_{nw} for 4 in. rough cylinder, $z = 0.060$.

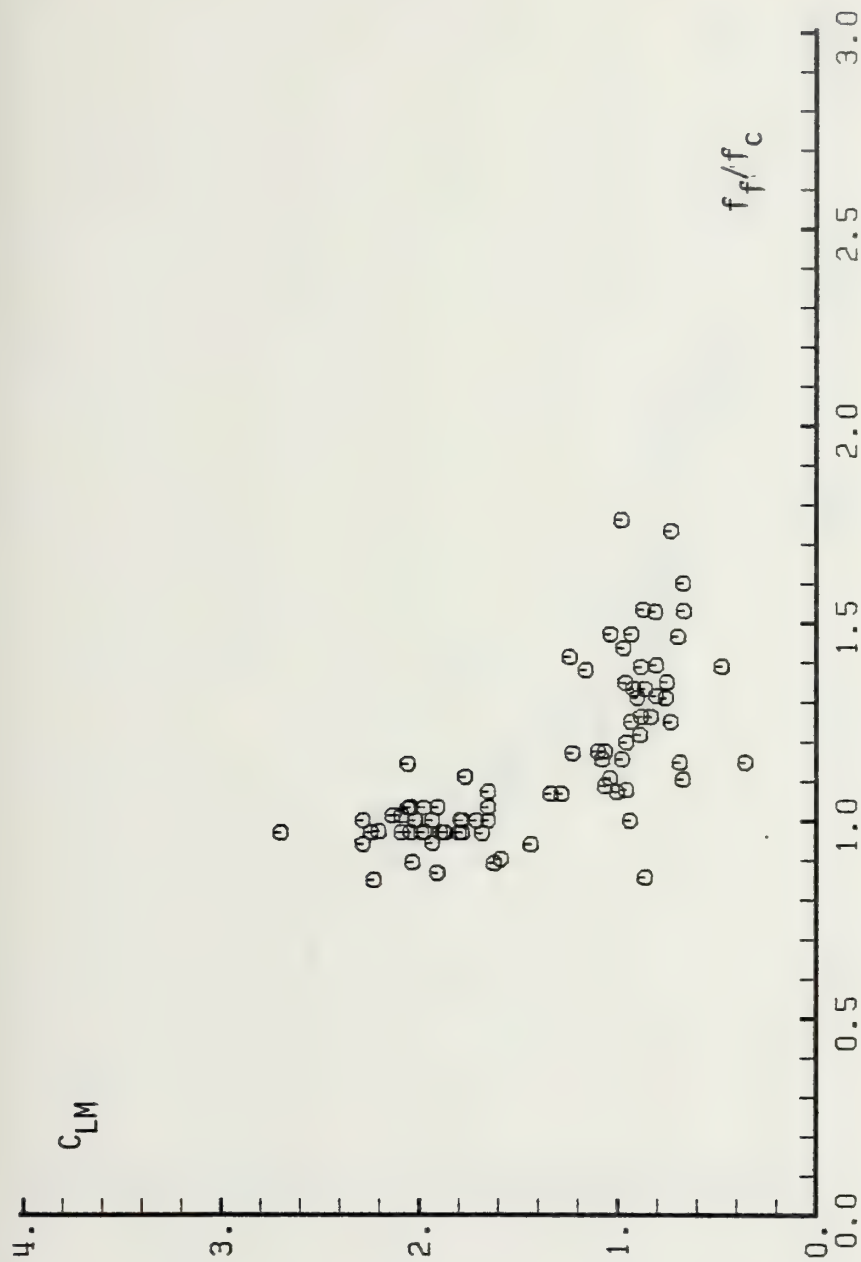


Fig. 81 C_{LM} versus f_f/f_c for 4 in. rough cylinder, $z = 0.060$.

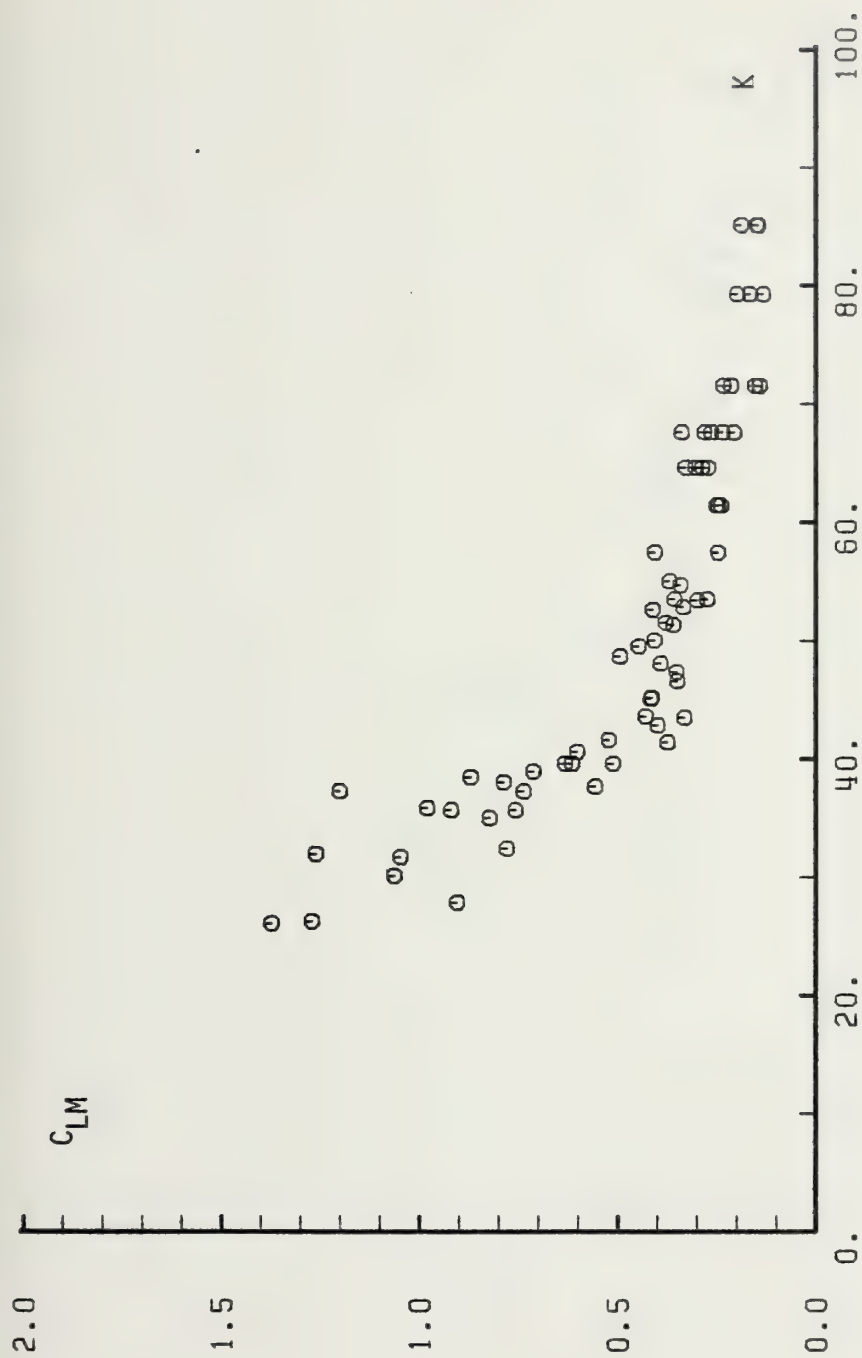


Fig. 82 C_{LM} versus K for 5 in. smooth cylinder, $z = 0.055$.

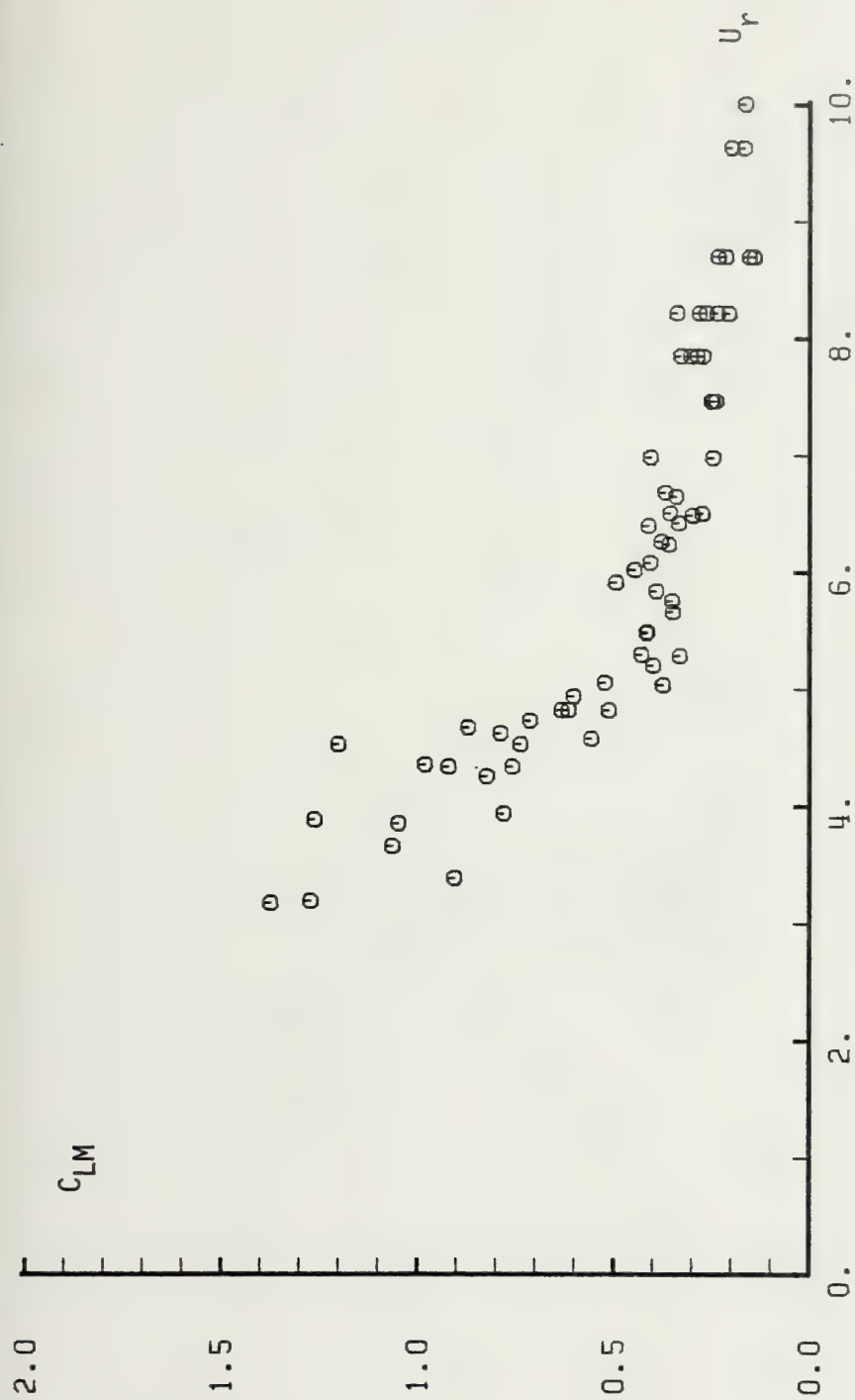


Fig. 83 C_{LM} versus U_r for 5 in. smooth cylinder, $z = 0.055$.

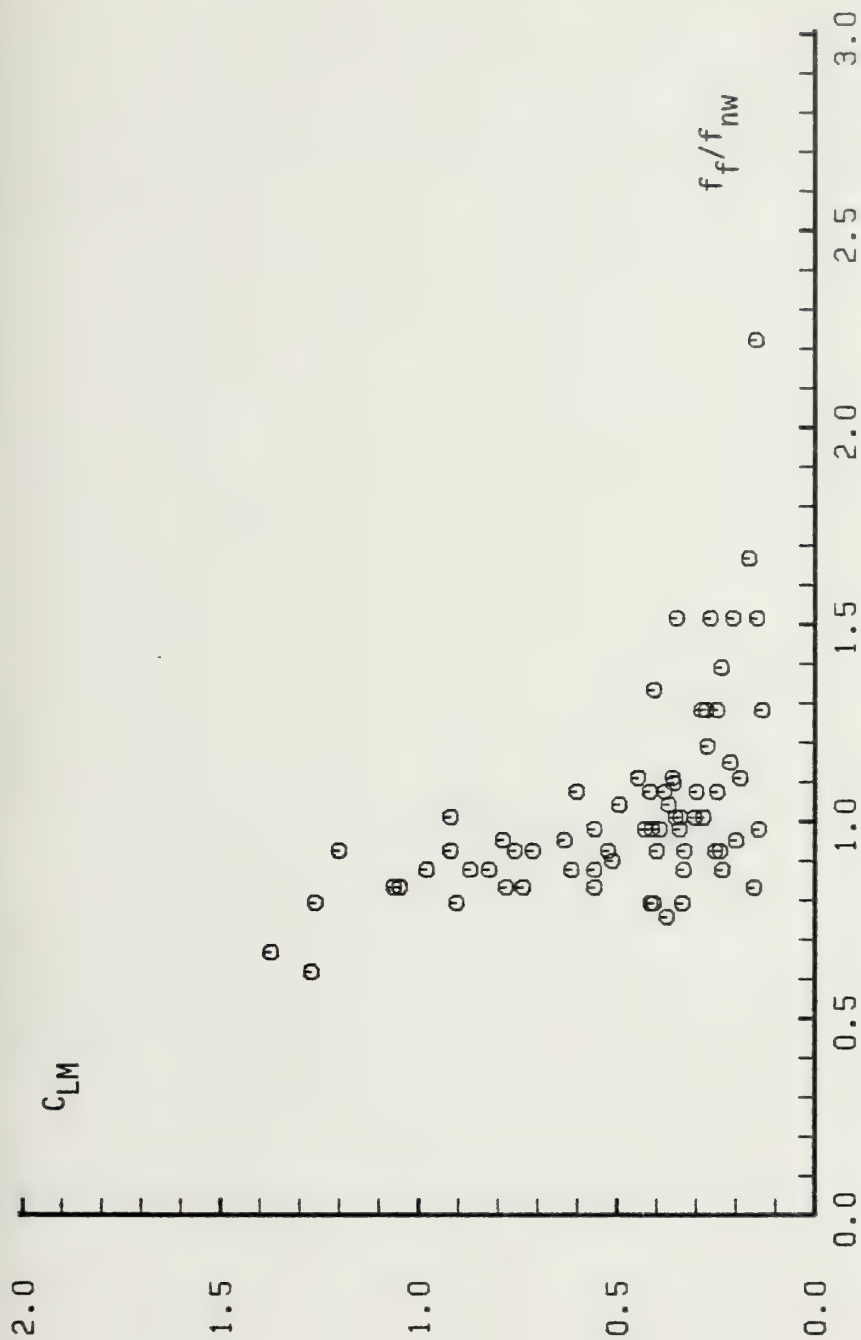


Fig. 84 C_{LM} versus f_f/f_{nw} for 5 in. smooth cylinder, $z = 0.055$.

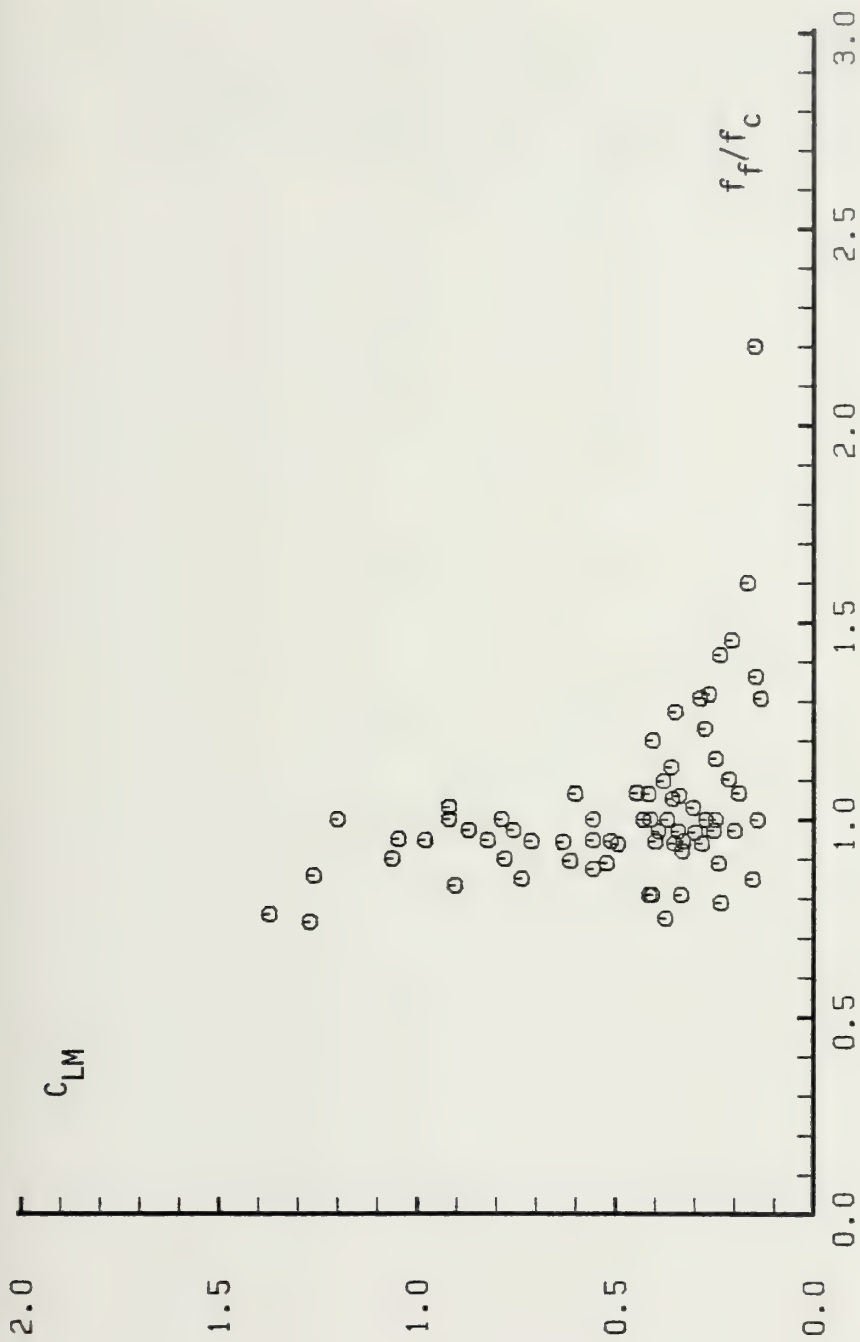


Fig. 85 C_{LM} versus f_f/f_c for 5 in. smooth cylinder, $z = 0.055$.

APPENDIX D

ROOT-MEAN-SQUARE VALUES OF THE LIFT COEFFICIENT
AS A FUNCTION OF K , U_r , f_f/f_{nw} , and f_f/f_c

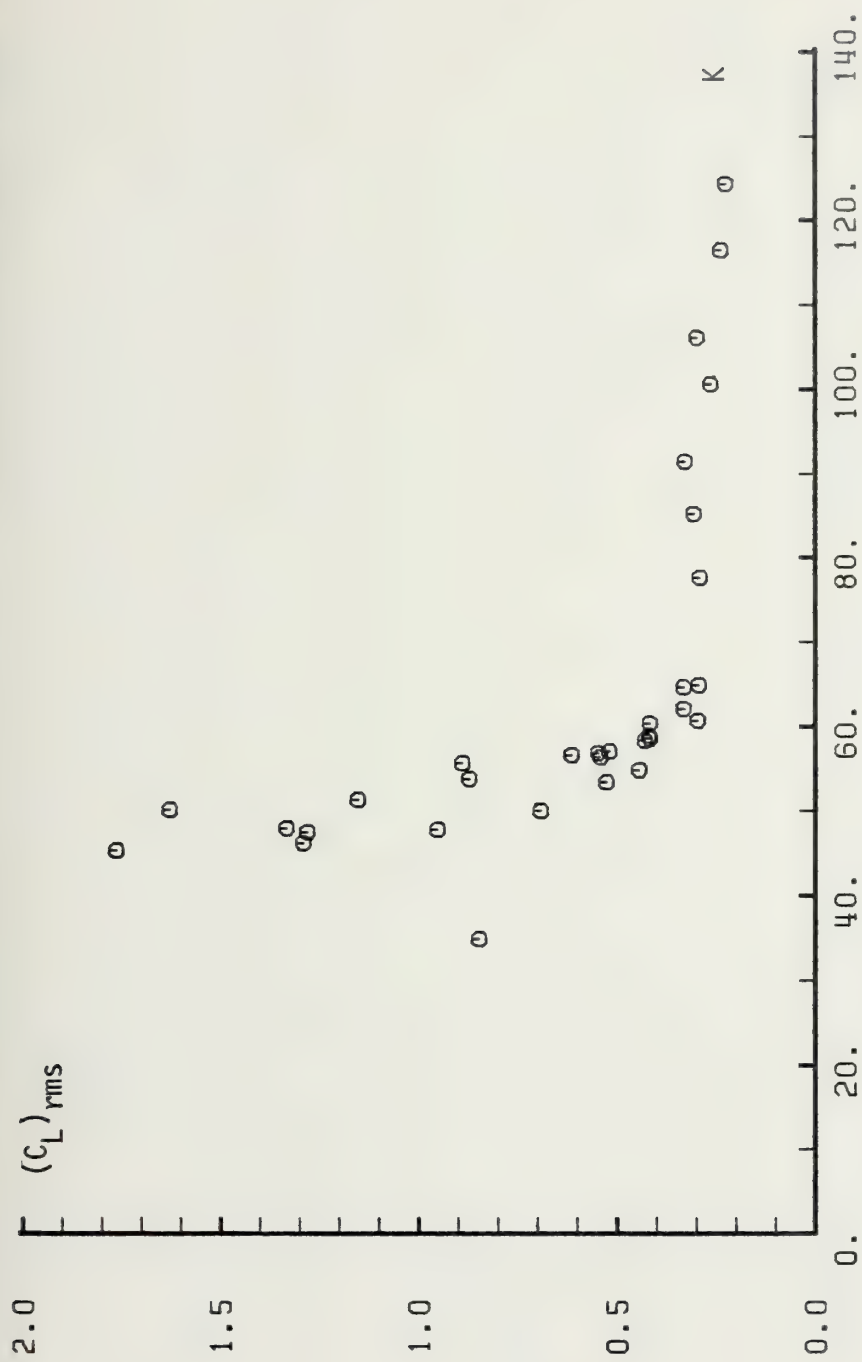


Fig. 90 $(C_L)_{rms}$ versus K for 3 in. rough cylinder, $\zeta = 0.067$.

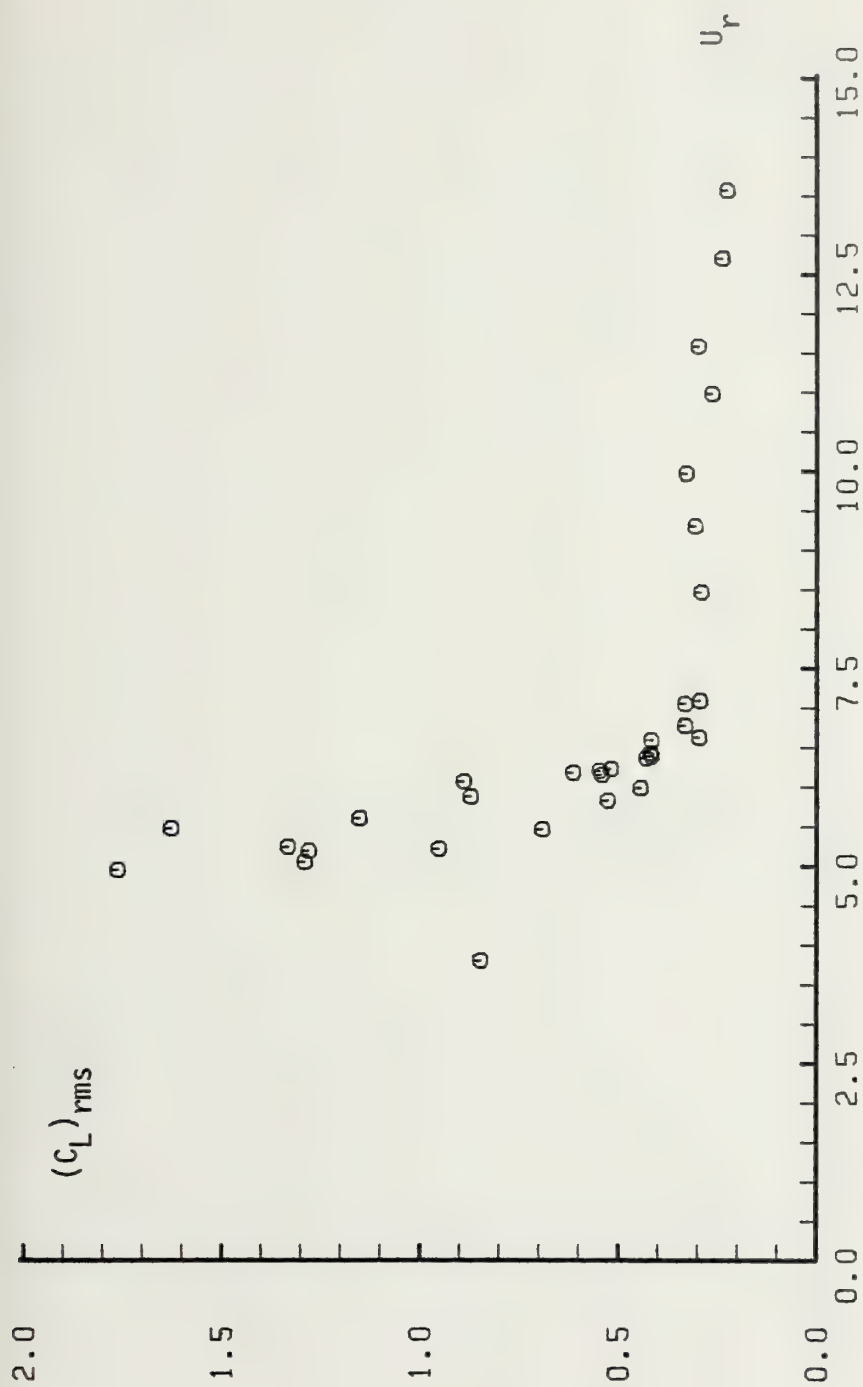


Fig. 91 $(C_L)_{rms}$ versus U_r for 3 in. rough cylinder, $z = 0.067$.

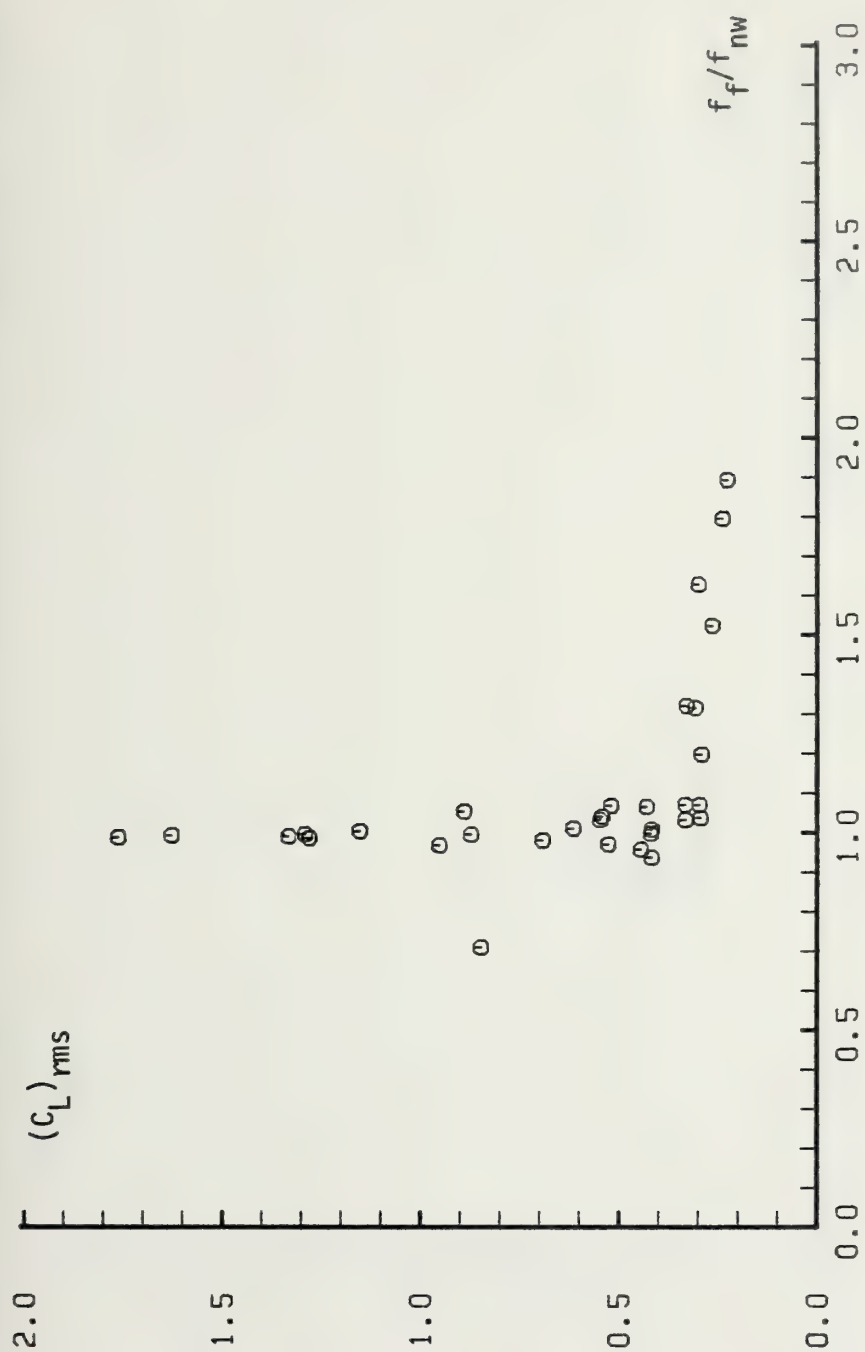


Fig. 92 $(C_L)_{rms}$ versus f_f/f_{nw} for 3 in. rough cylinder, $\zeta = 0.067$

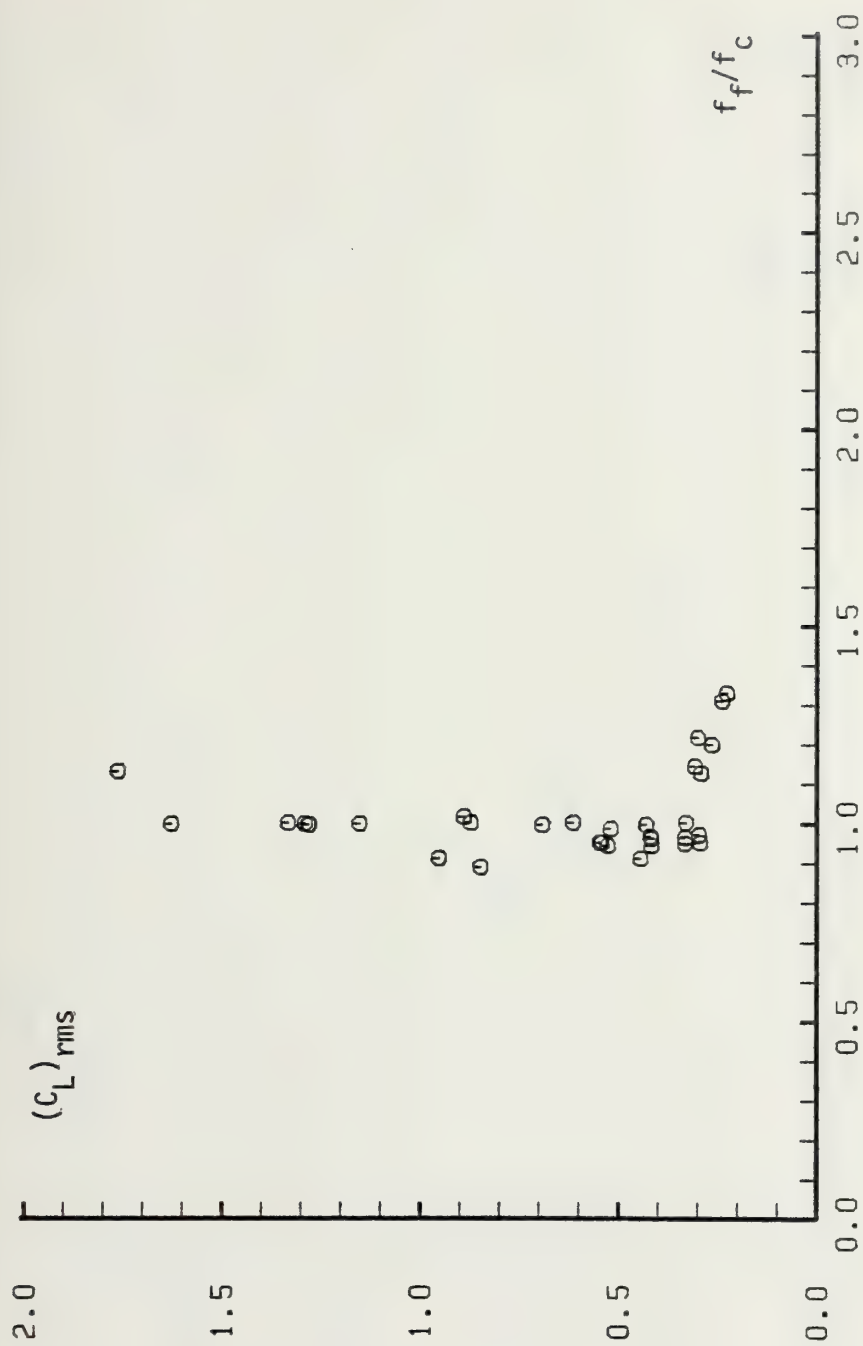


Fig. 93 $(C_L)_{rms}$ versus f_f/f_c for 3 in. rough cylinder, $z = 0.067$.

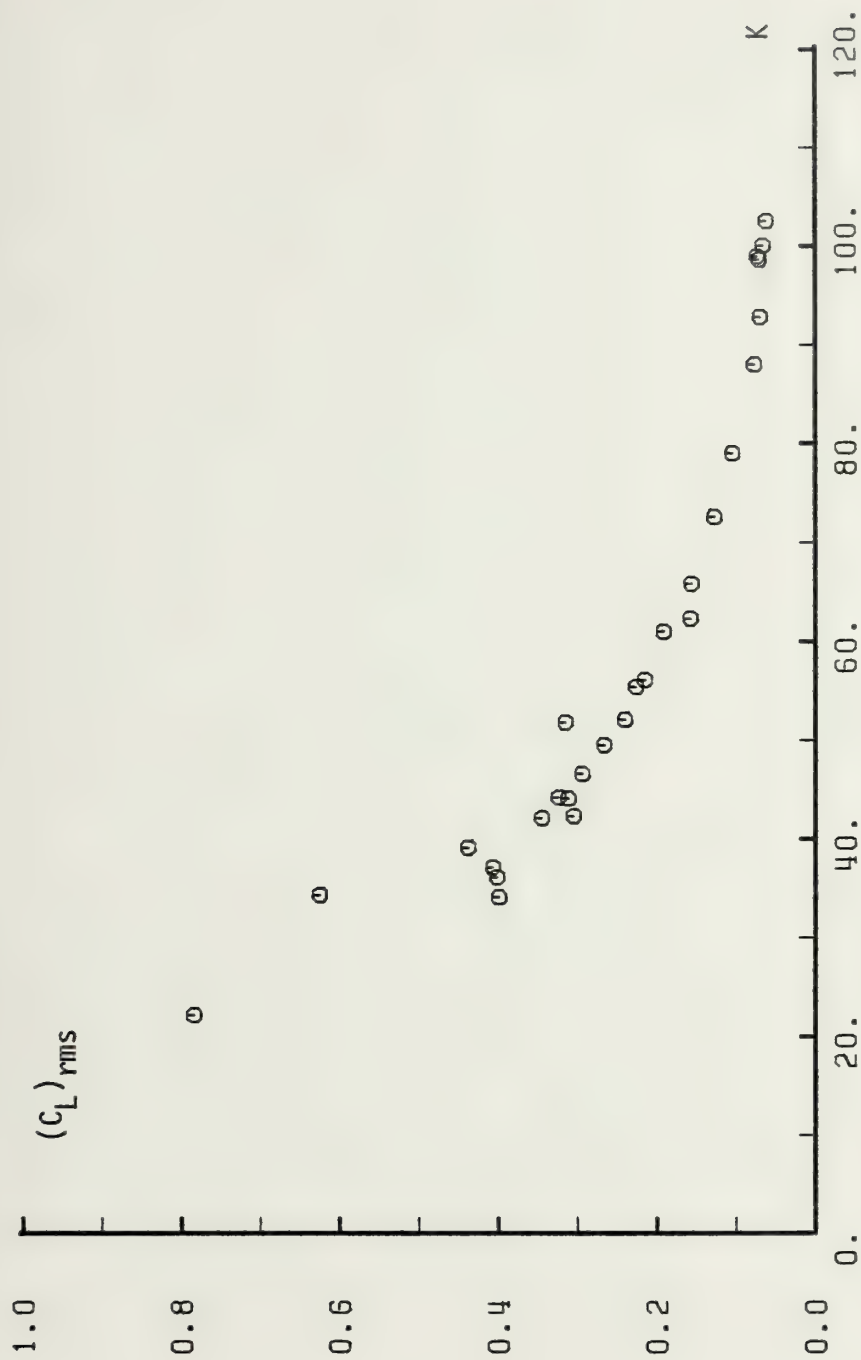


Fig. 94 $(C_L)_{rms}$ versus K for 4 in. smooth cylinder, $\zeta = 0.046$.

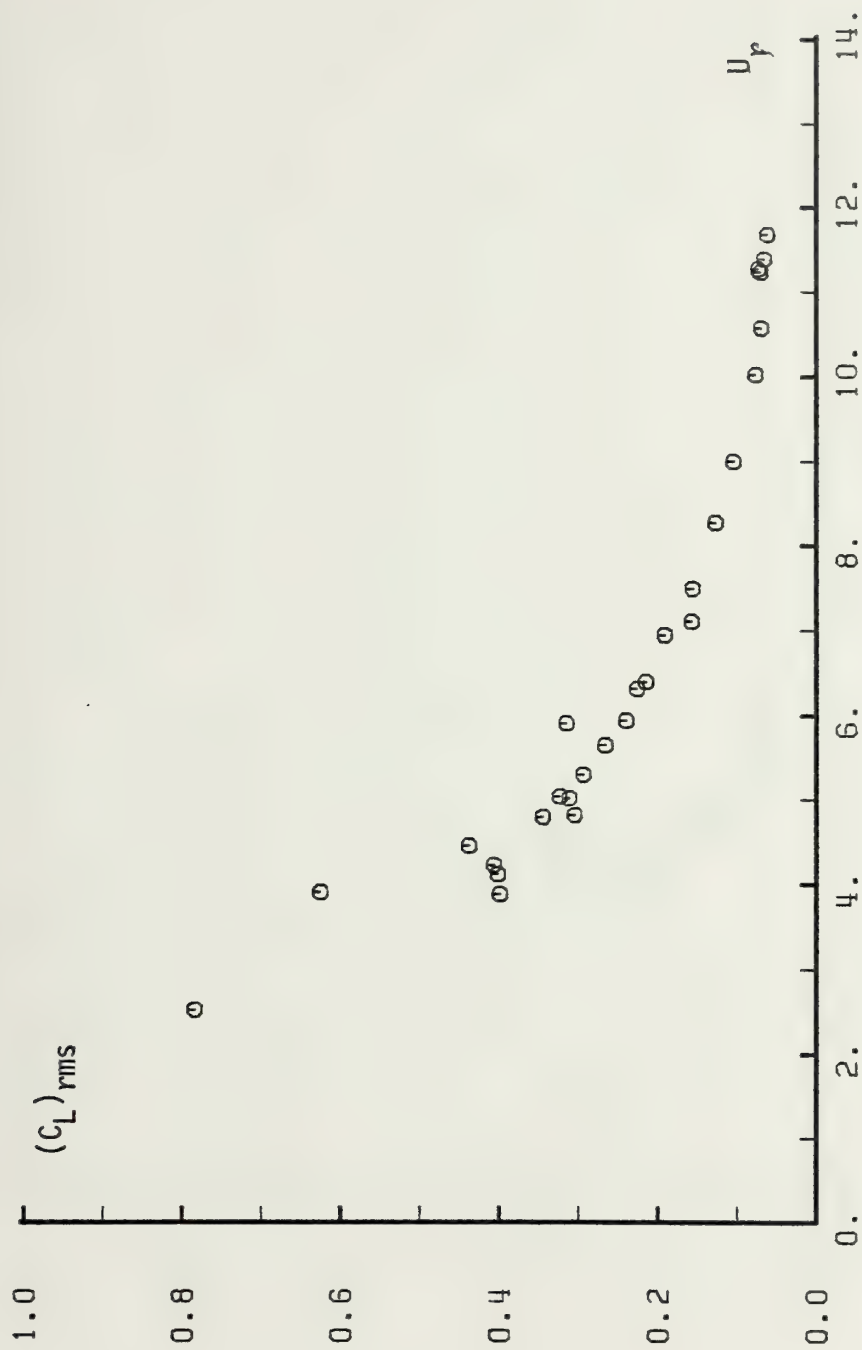


Fig. 95 $(C_L)_{rms}$ versus U_r for 4 in. smooth cylinder, $z = 0.046$.

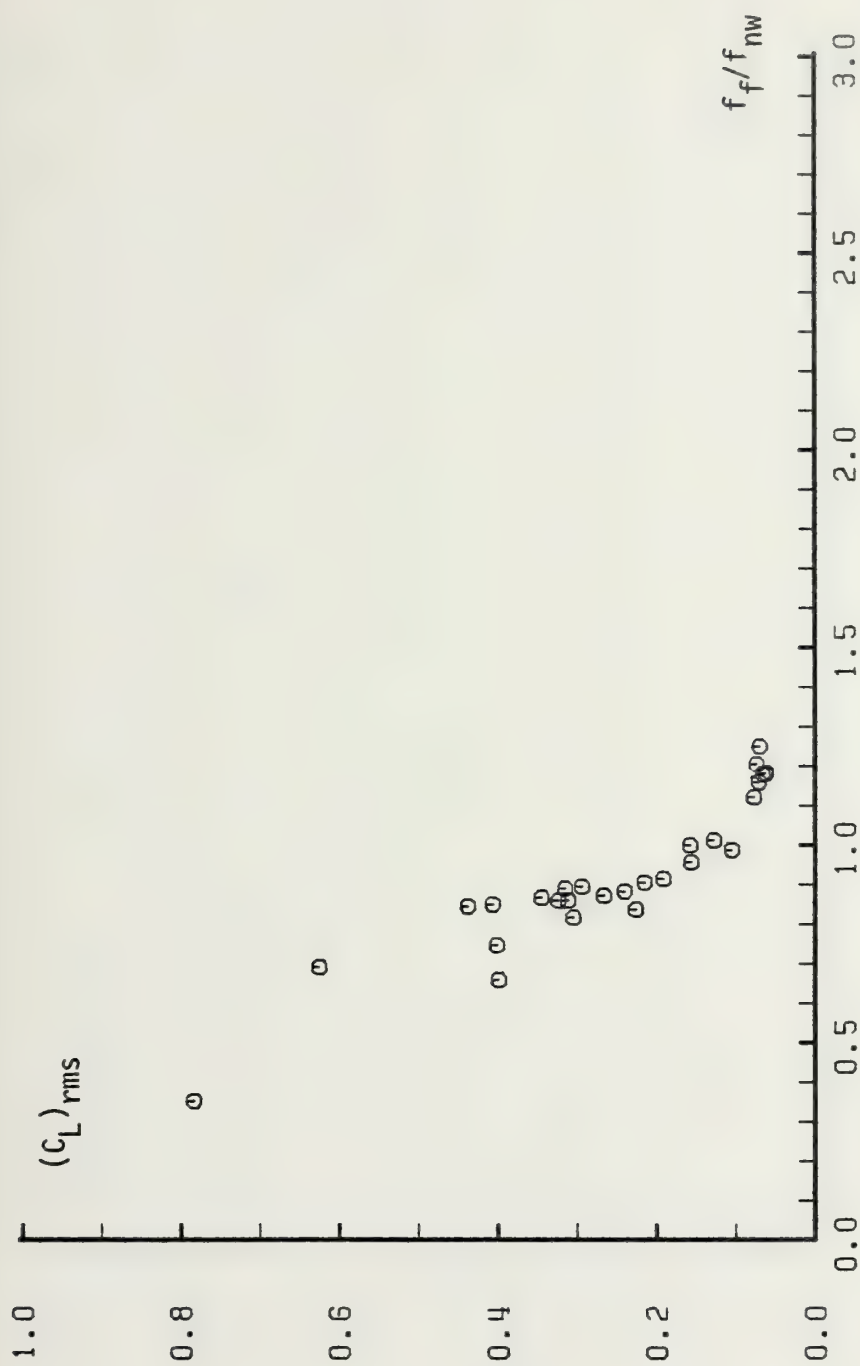


Fig. 96 $(C_L)_{rms}$ versus f_f/f_{nw} for 4 in. smooth cylinder, $z = 0.046$.

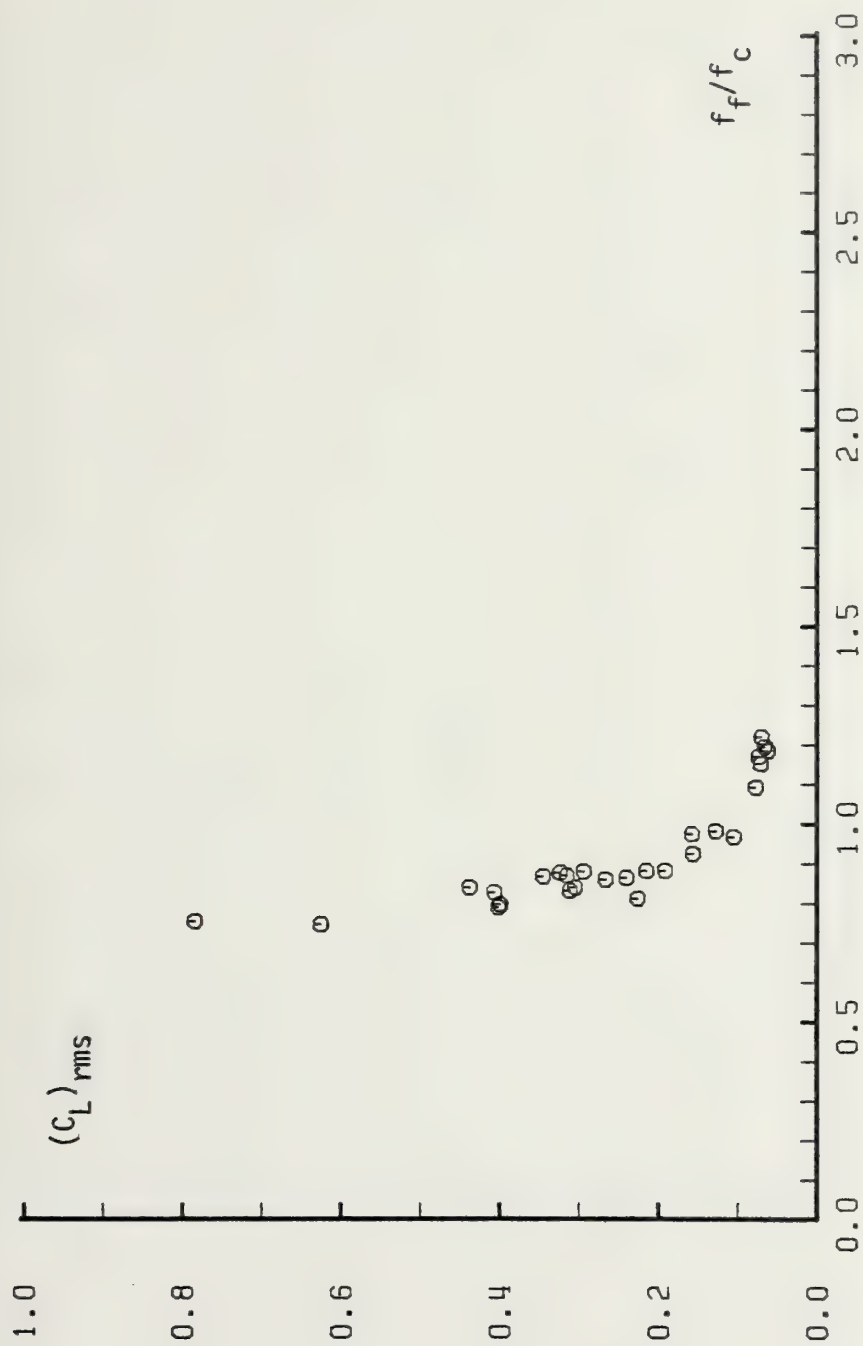


Fig. 97 $(C_L)_{rms}$ versus f_f/f_c for 4 in. smooth cylinder, $z = 0.046$.

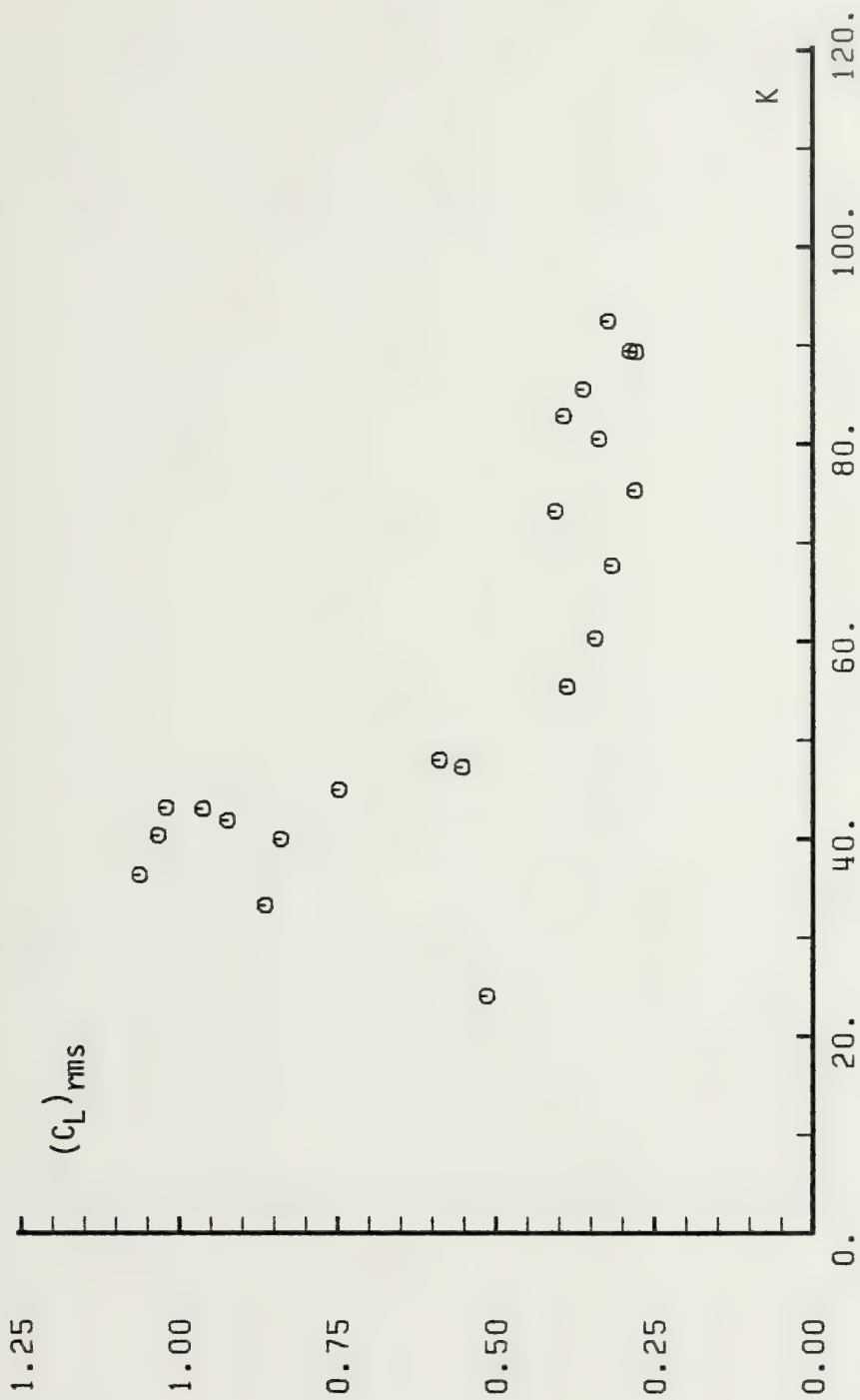


Fig. 98 $(C_L)_{rms}$ versus K for 4 in. rough cylinder, $\zeta = 0.060$.

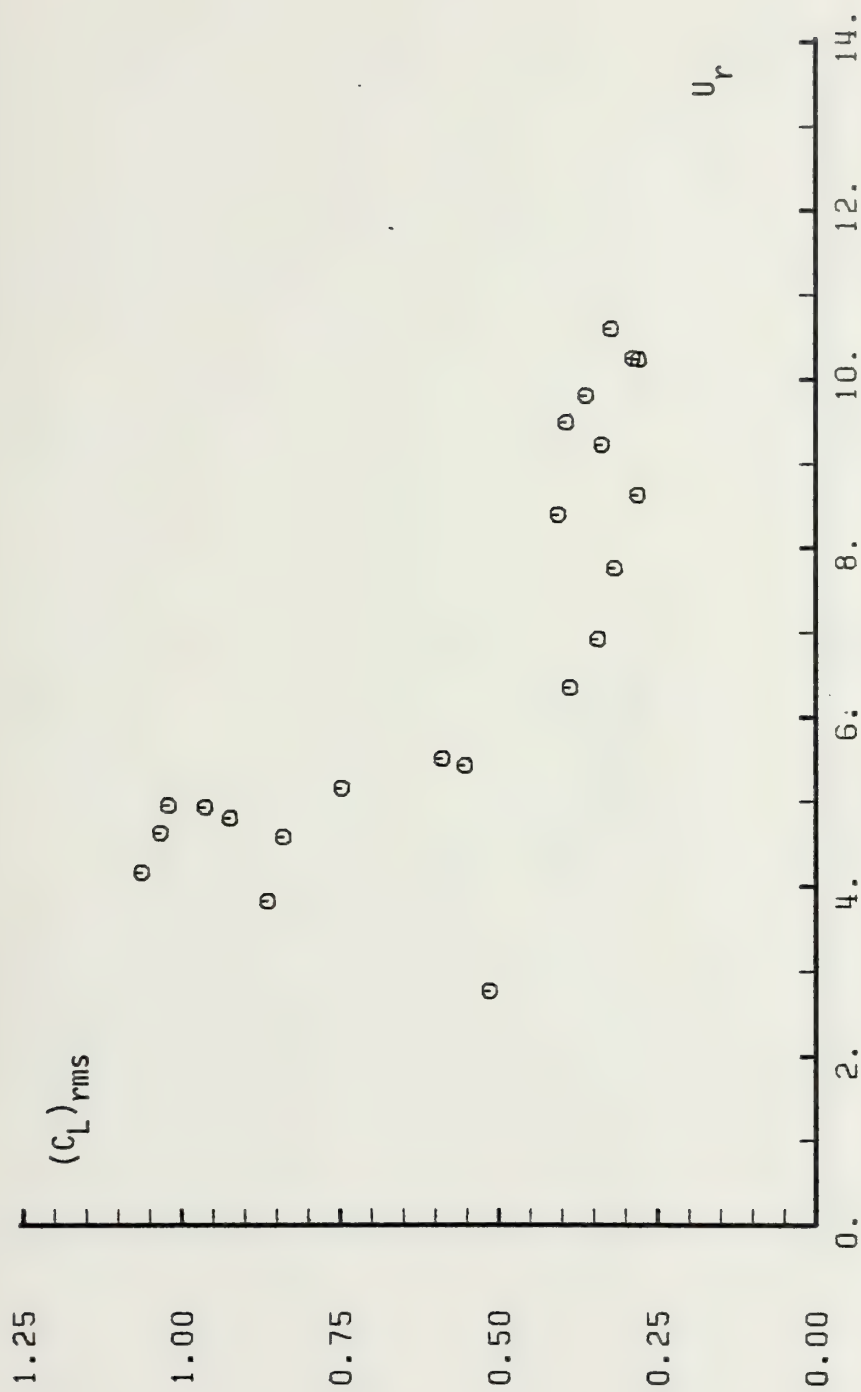


Fig. 99 $(C_L)_{rms}$ versus U_r for 4 in. rough cylinder, $z = 0.060$.

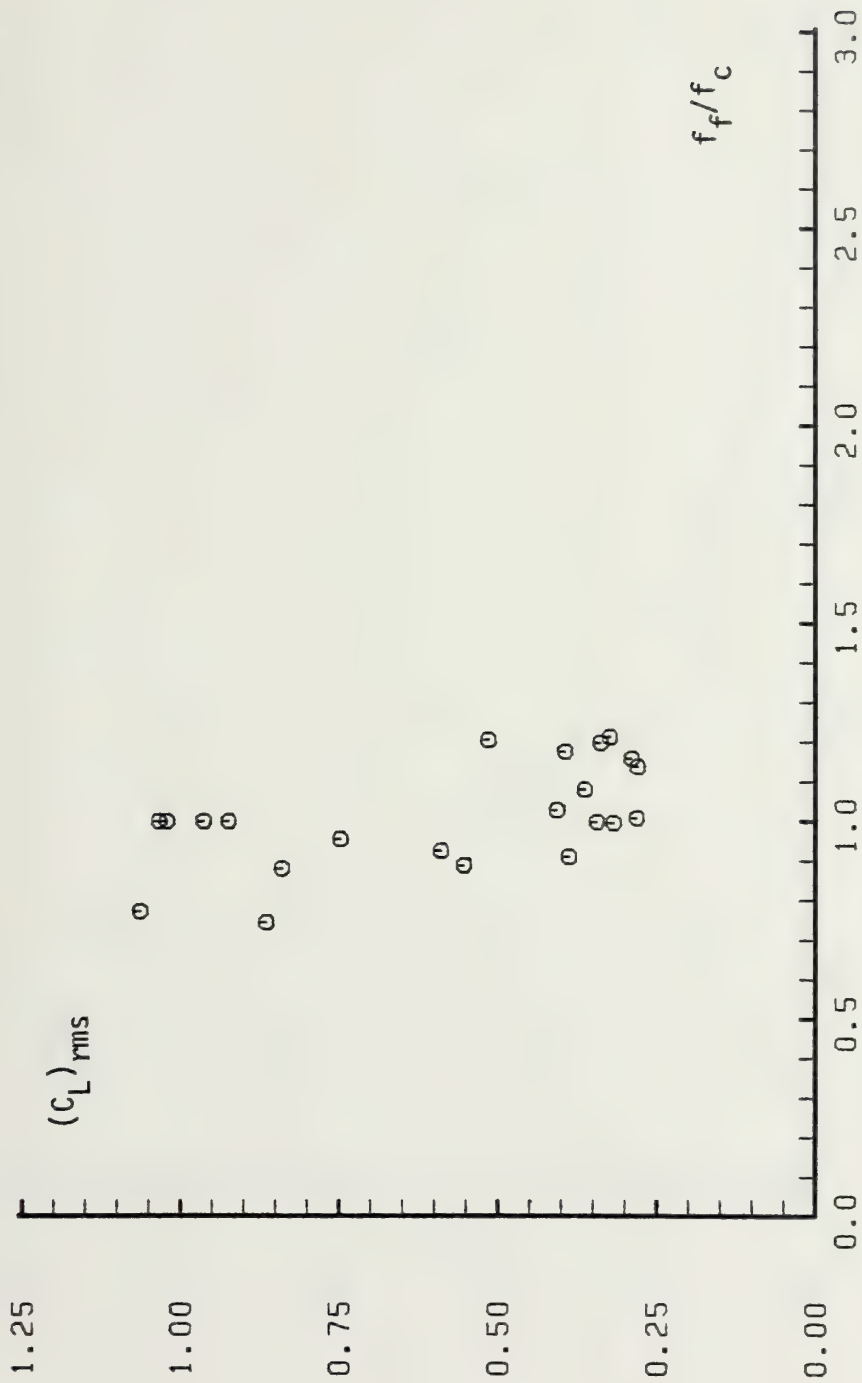


Fig. 101 $(C_L)_{rms}$ versus f_f/f_c for 4 in. rough cylinder, $\zeta = 0.060$.

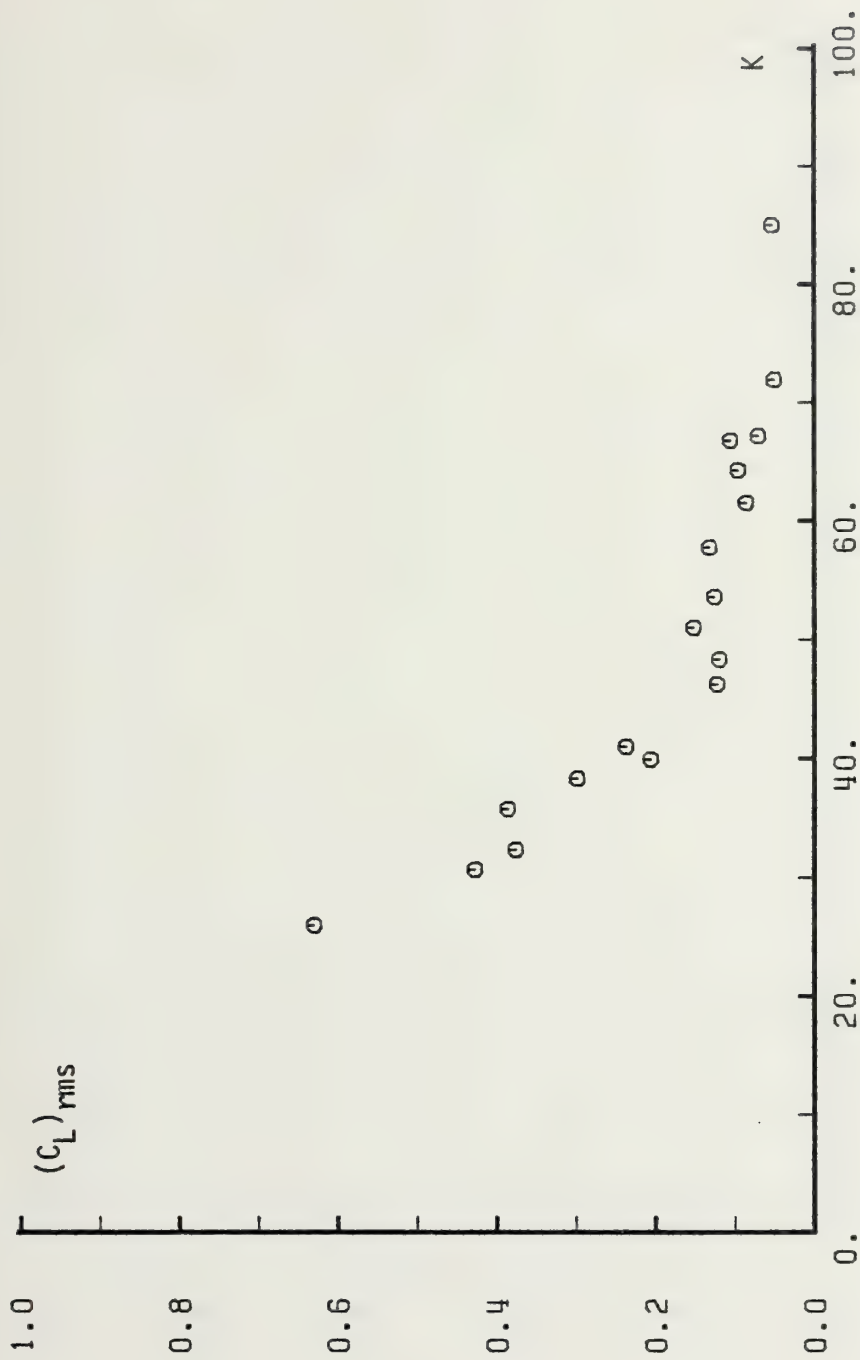


Fig. 102 $(C_L)_{rms}$ versus K for 5 in. smooth cylinder, $\zeta = 0.055$.

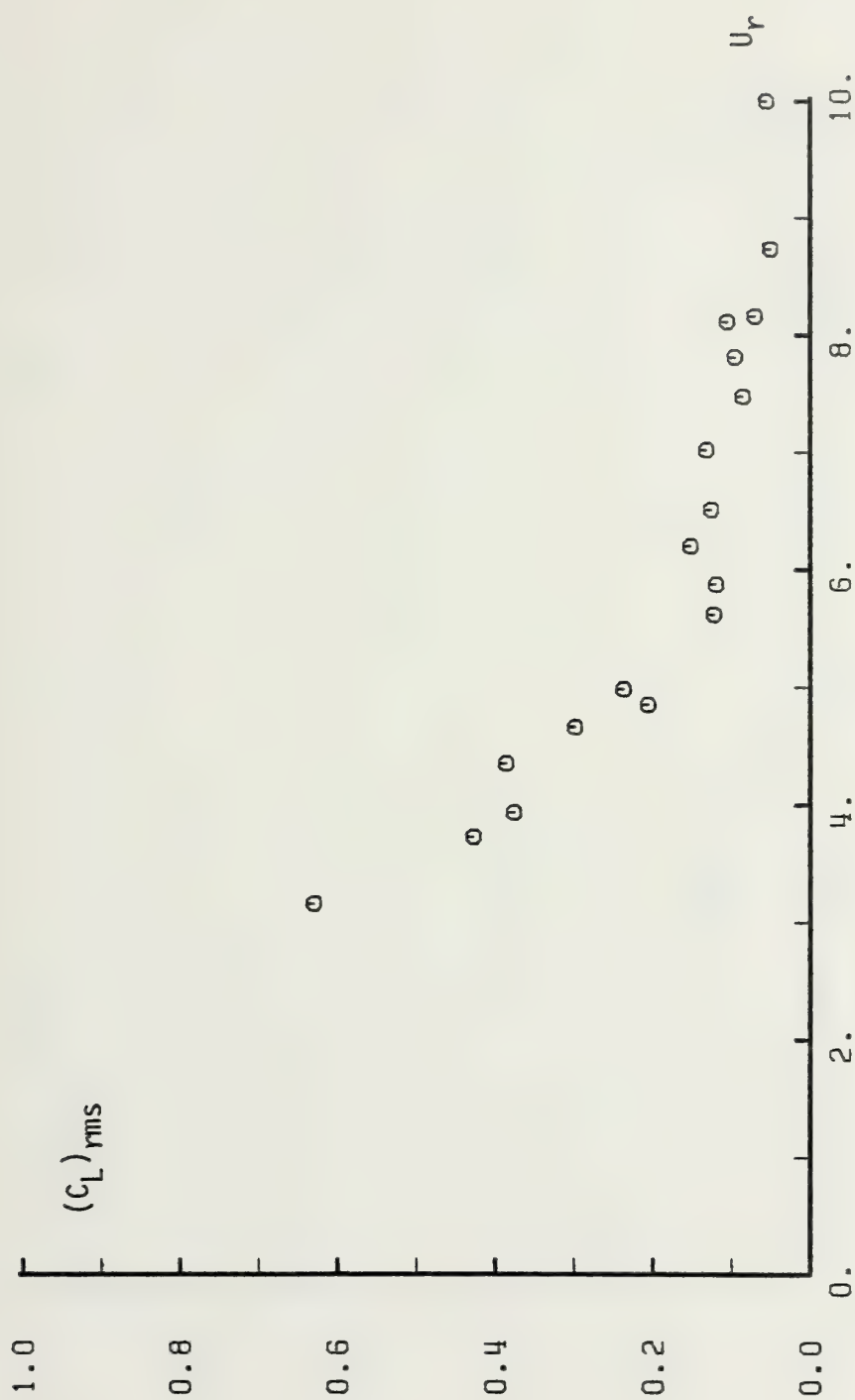


Fig. 103 $(C_L)_{rms}$ versus U_r for 5 in. smooth cylinder, $z = 0.055$.

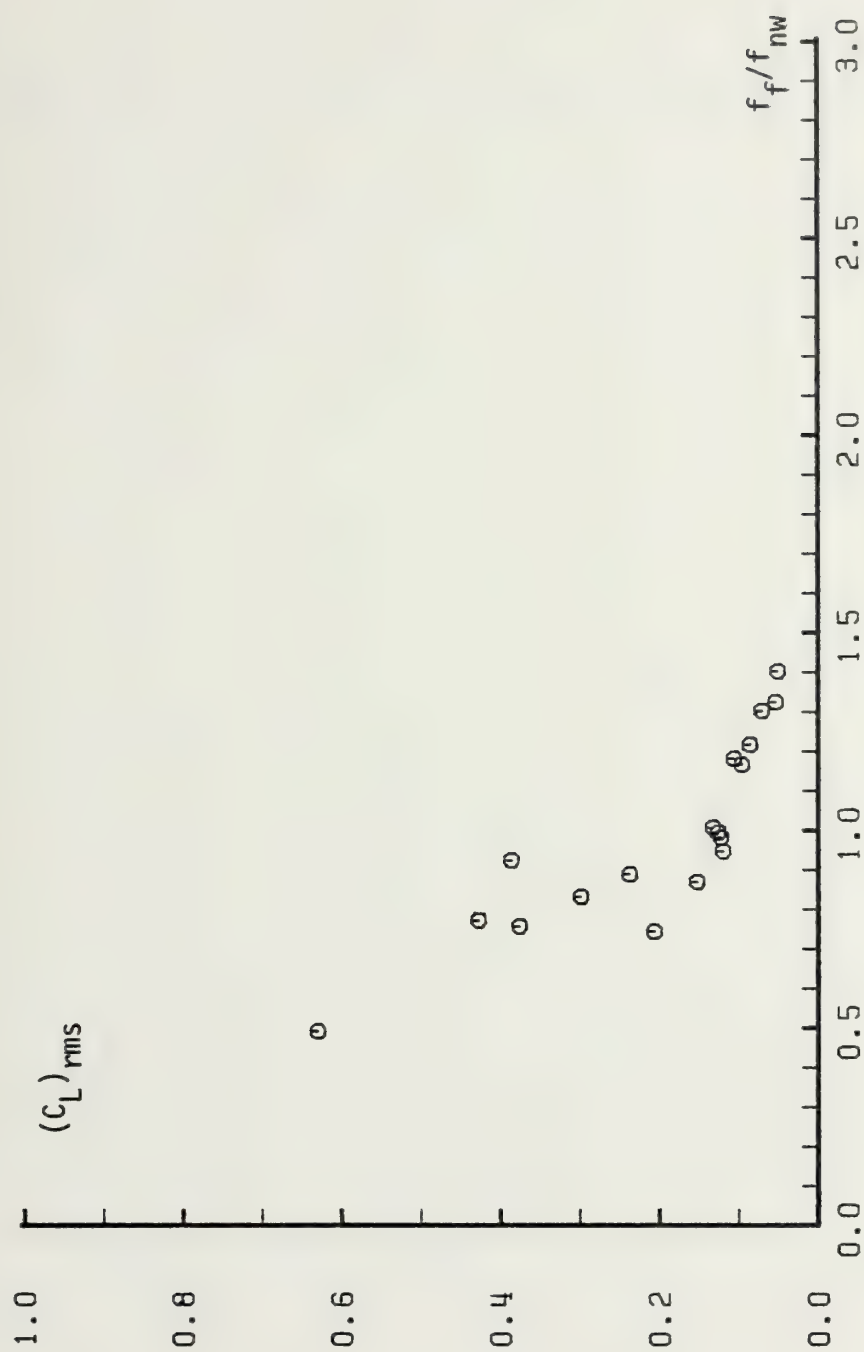


Fig. 104 $(C_L)_{rms}$ versus f_f/f_{nw} for 5 in. smooth cylinder, $z = 0.055$.

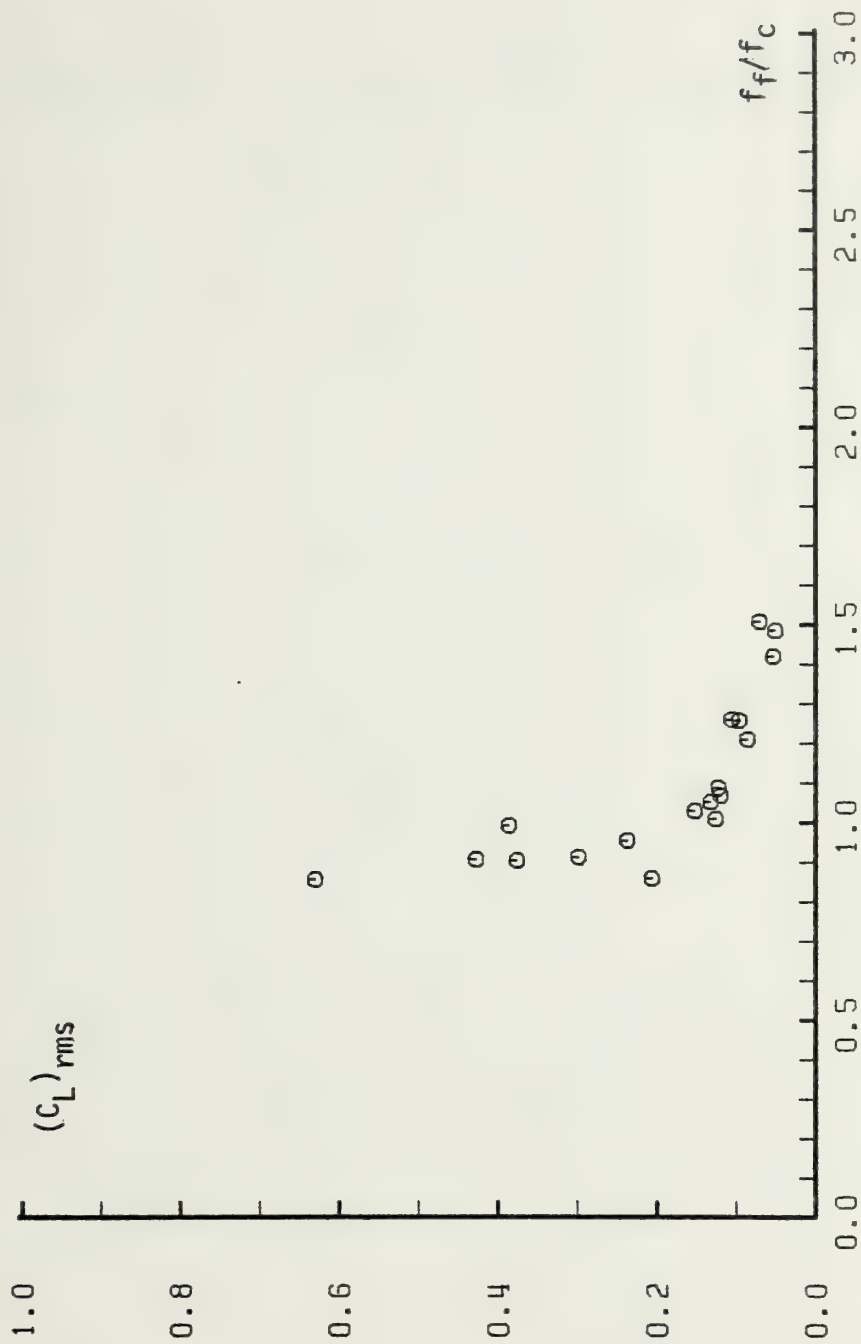


Fig. 105 $(C_L)_{rms}$ versus f_f/f_c for 5 in. smooth cylinder, $\zeta = 0.055$.

APPENDIX E

SPECTRAL ANALYSIS FOR A 3 in. SMOOTH CYLINDER FOR VARIOUS VALUES OF K

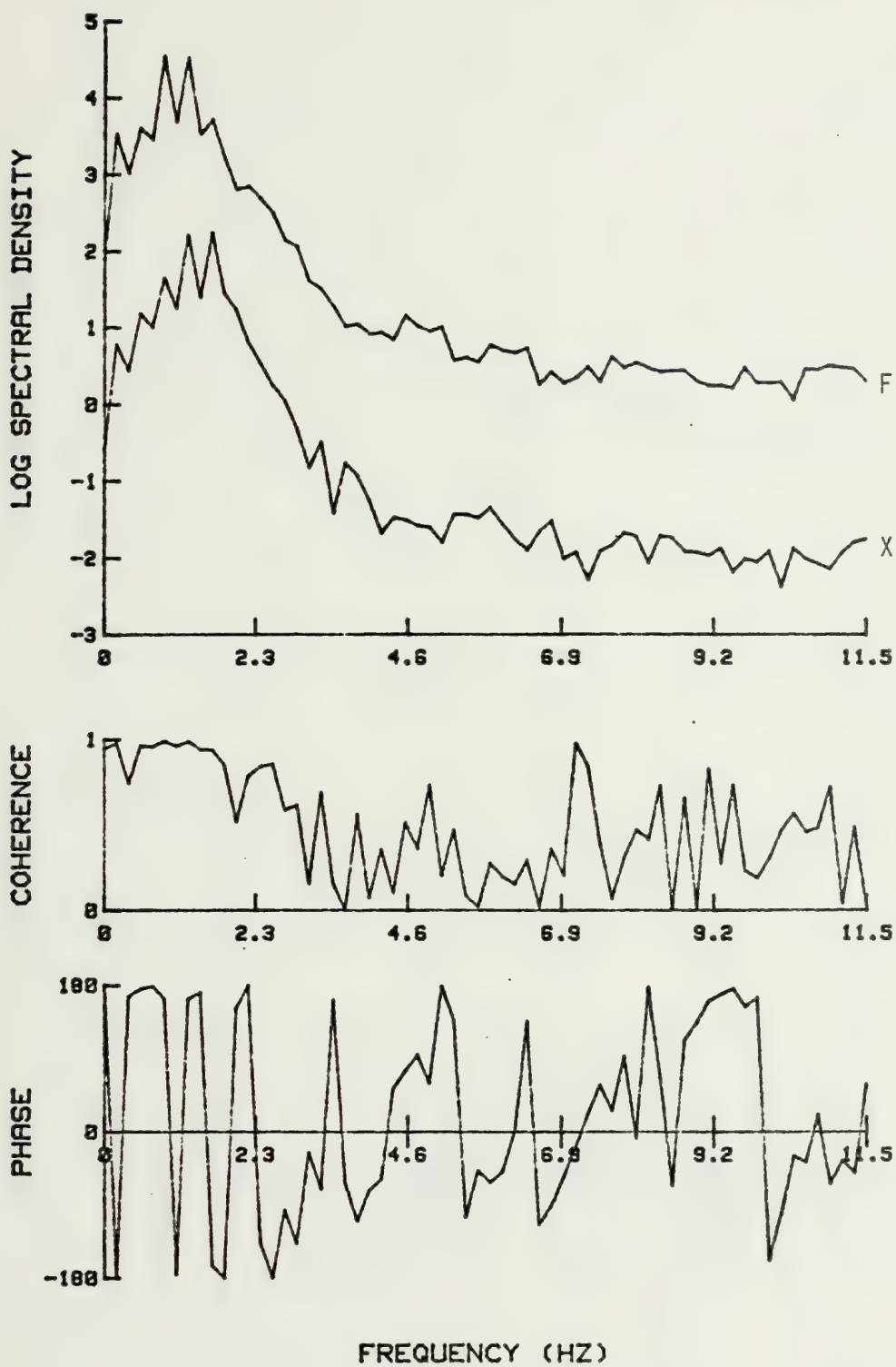


Fig. 128 Spectral analysis for a 3 in. smooth cylinder, $\zeta = 0.052$, $K = 36$

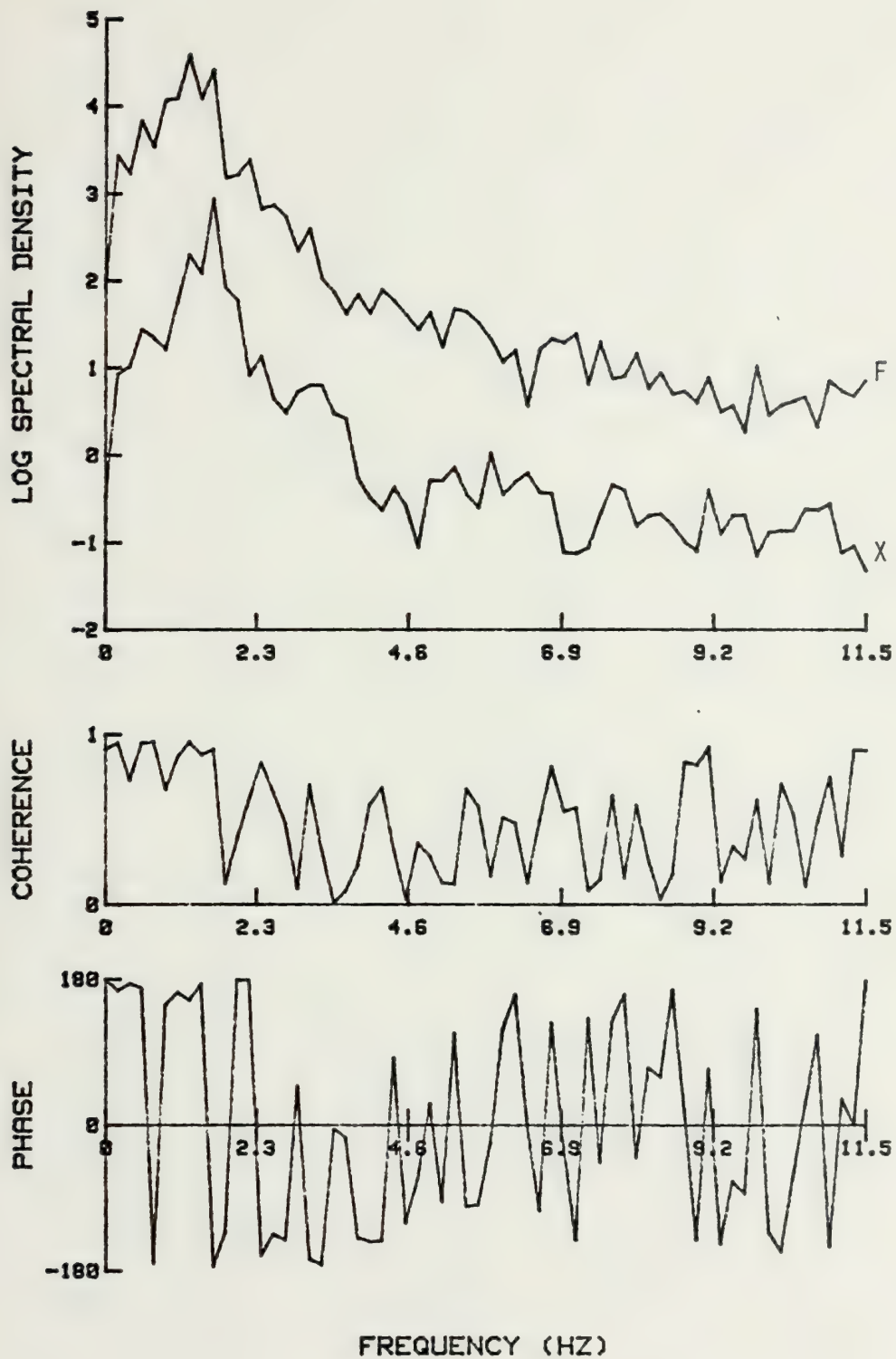


Fig. 129 Spectral analysis for a 3 in. smooth cylinder, $\zeta = 0.052$, $K = 39$

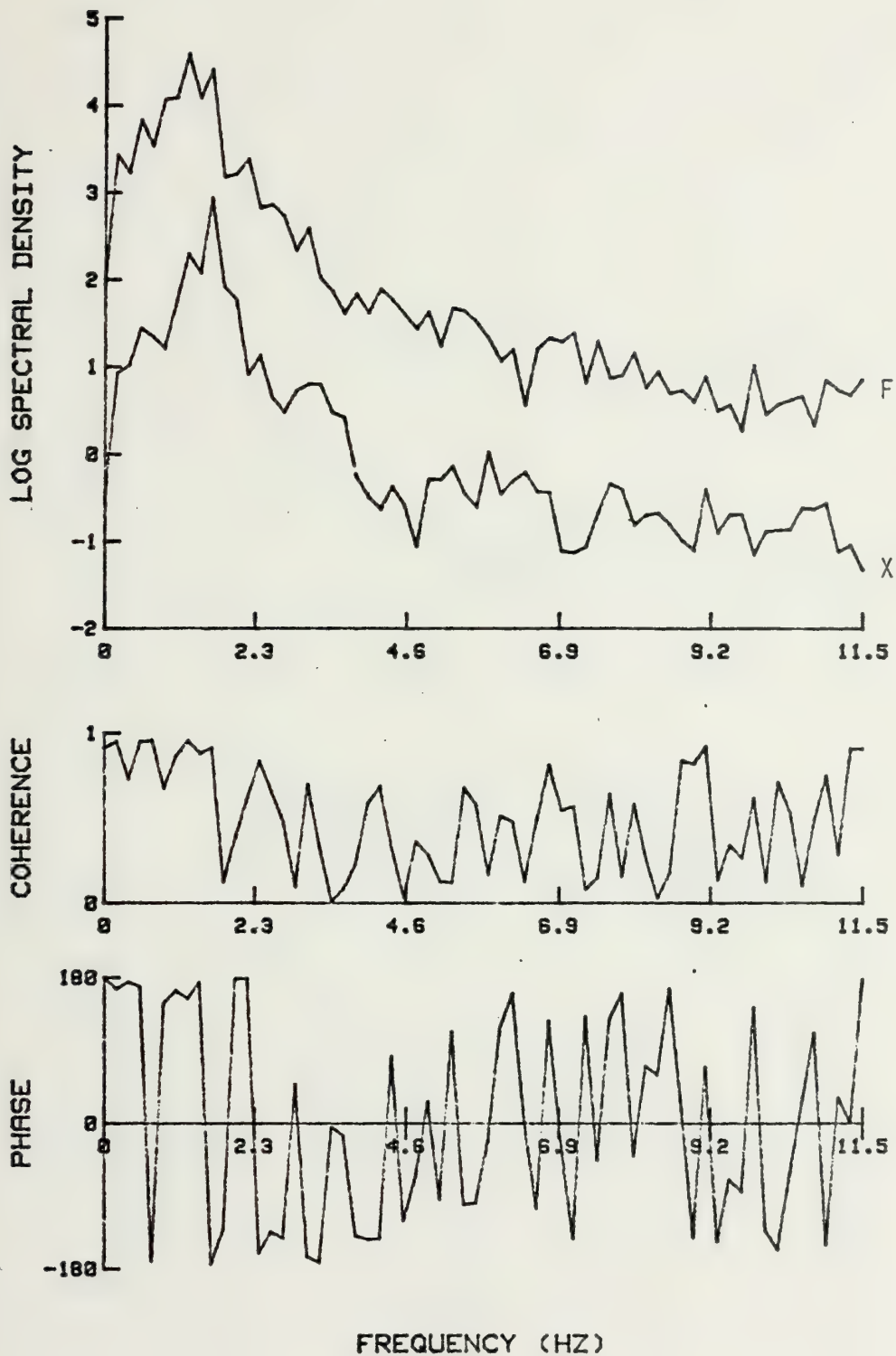


Fig. 130 Spectral analysis for a 3 in. smooth cylinder, $\zeta = 0.052$, $K = 43$

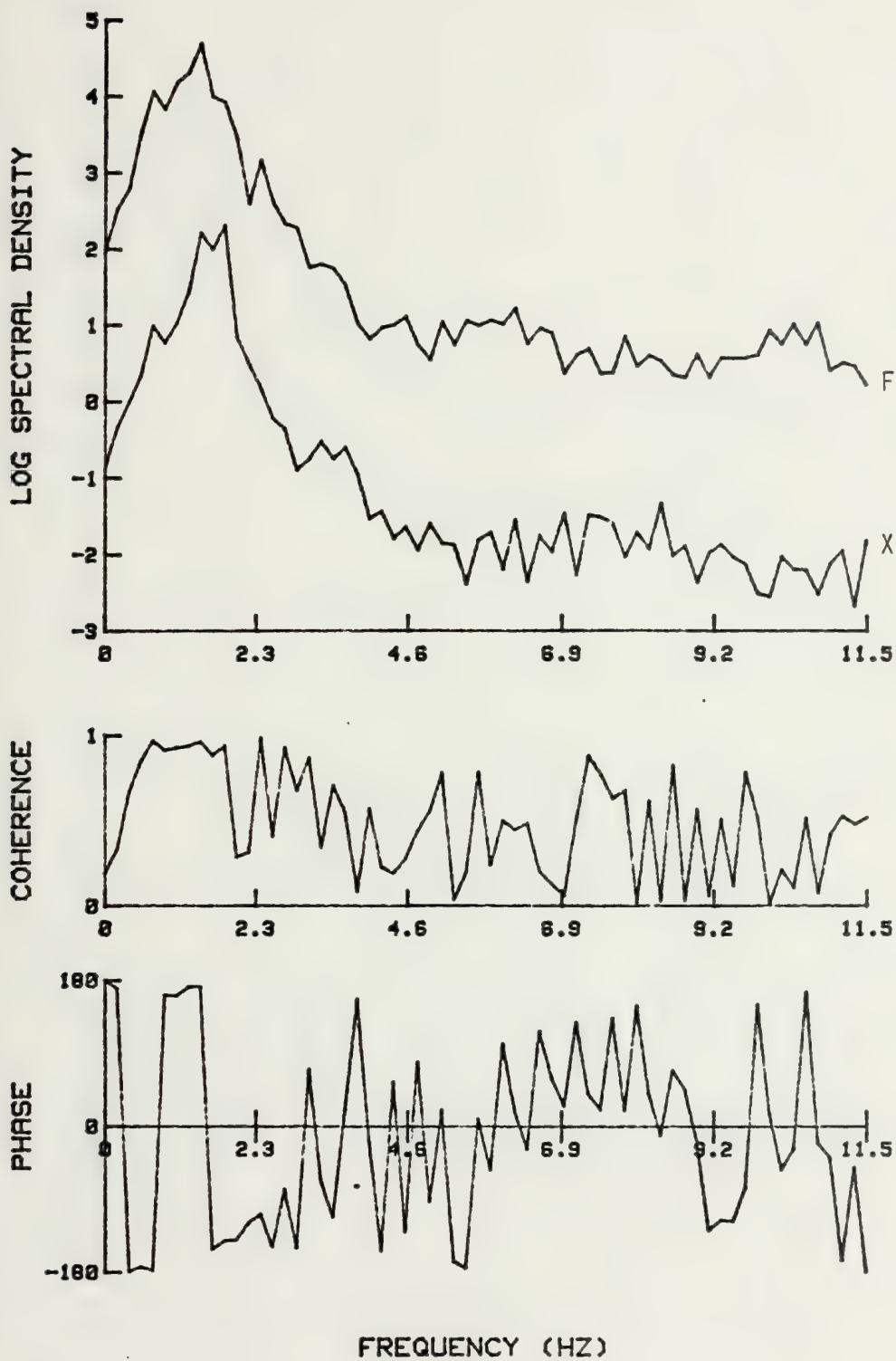


Fig. 131 Spectral analysis for a 3 in. smooth cylinder, $\zeta = 0.052$, $K = 46$

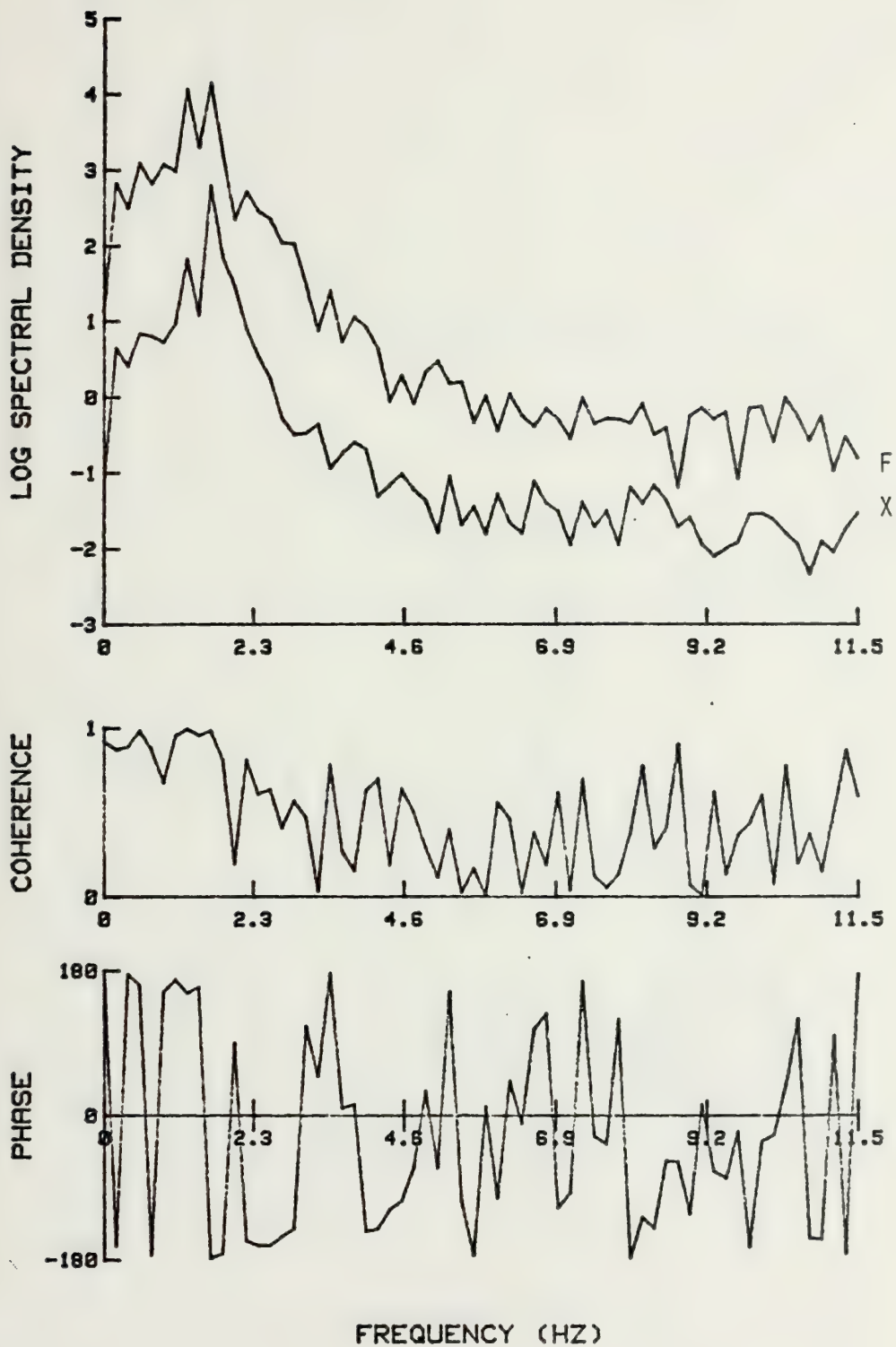


Fig. 132 Spectral analysis for a 3 in. smooth cylinder, $\zeta = 0.052$, $K = 48$

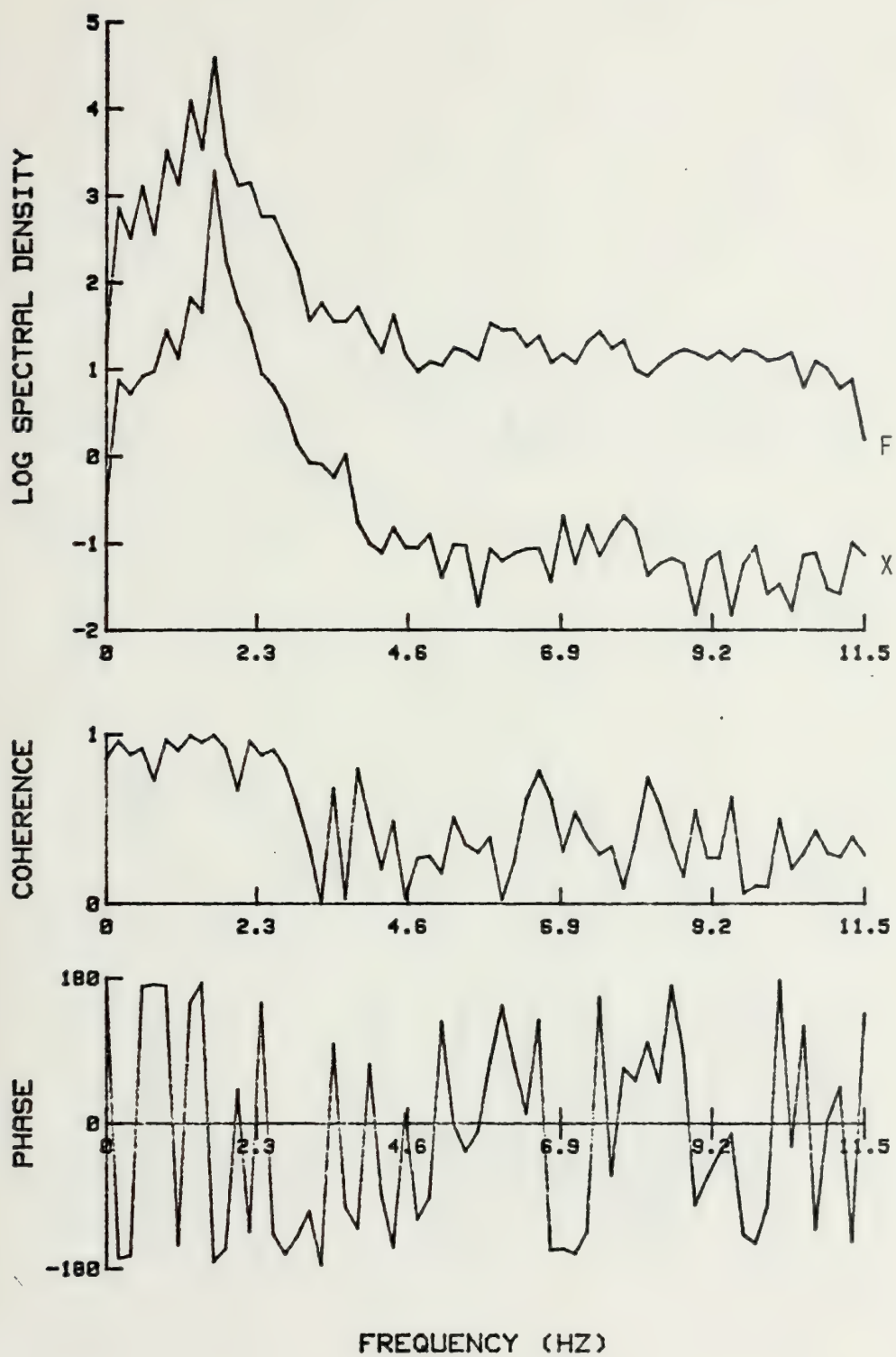


Fig. 133 Spectral analysis for a 3 in. smooth cylinder, $\zeta = 0.052$,
 $K = 56$

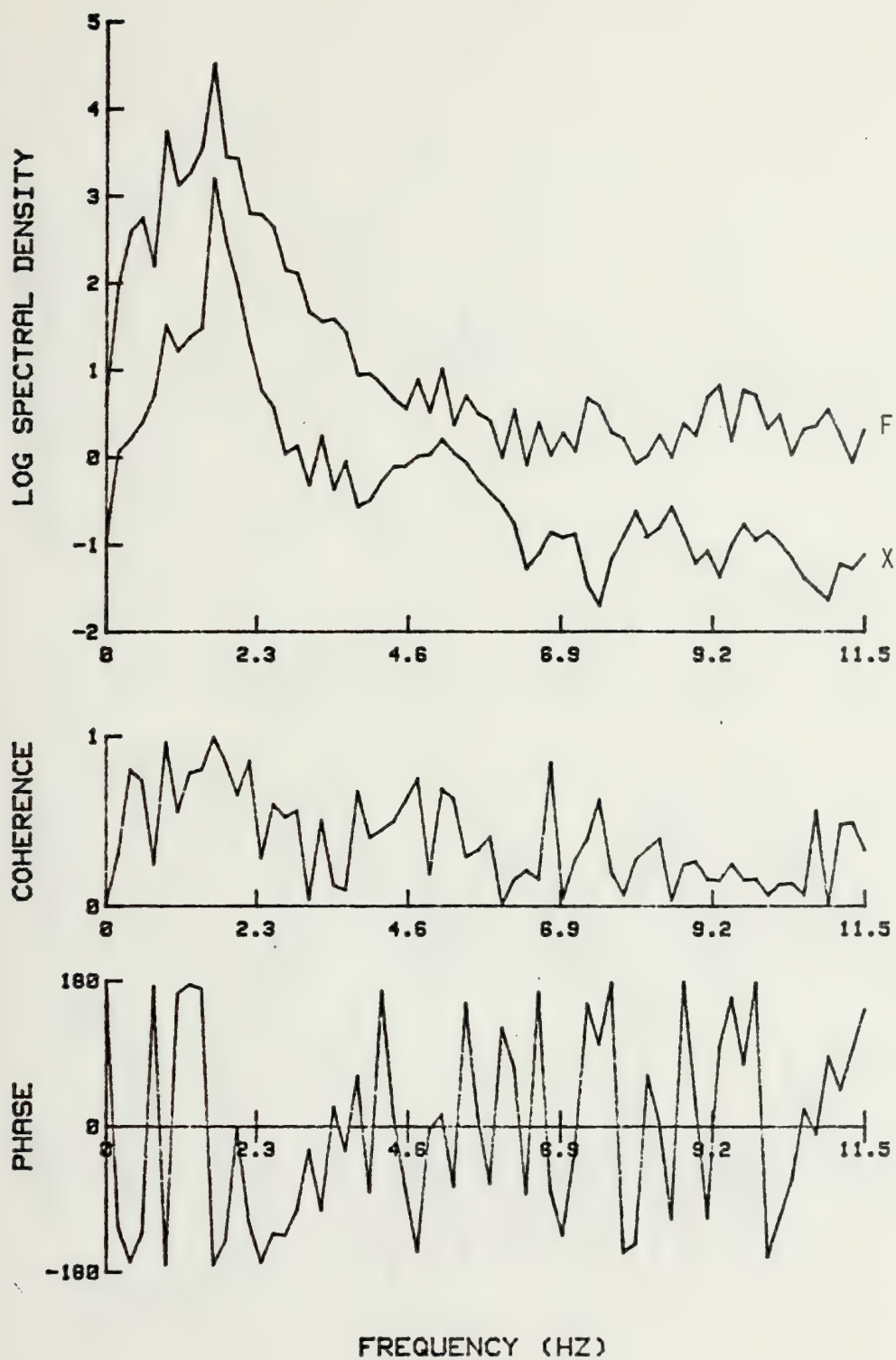


Fig. 134 Spectral analysis for a 3 in. smooth cylinder, $\zeta = 0.052$,
 $K = 57$

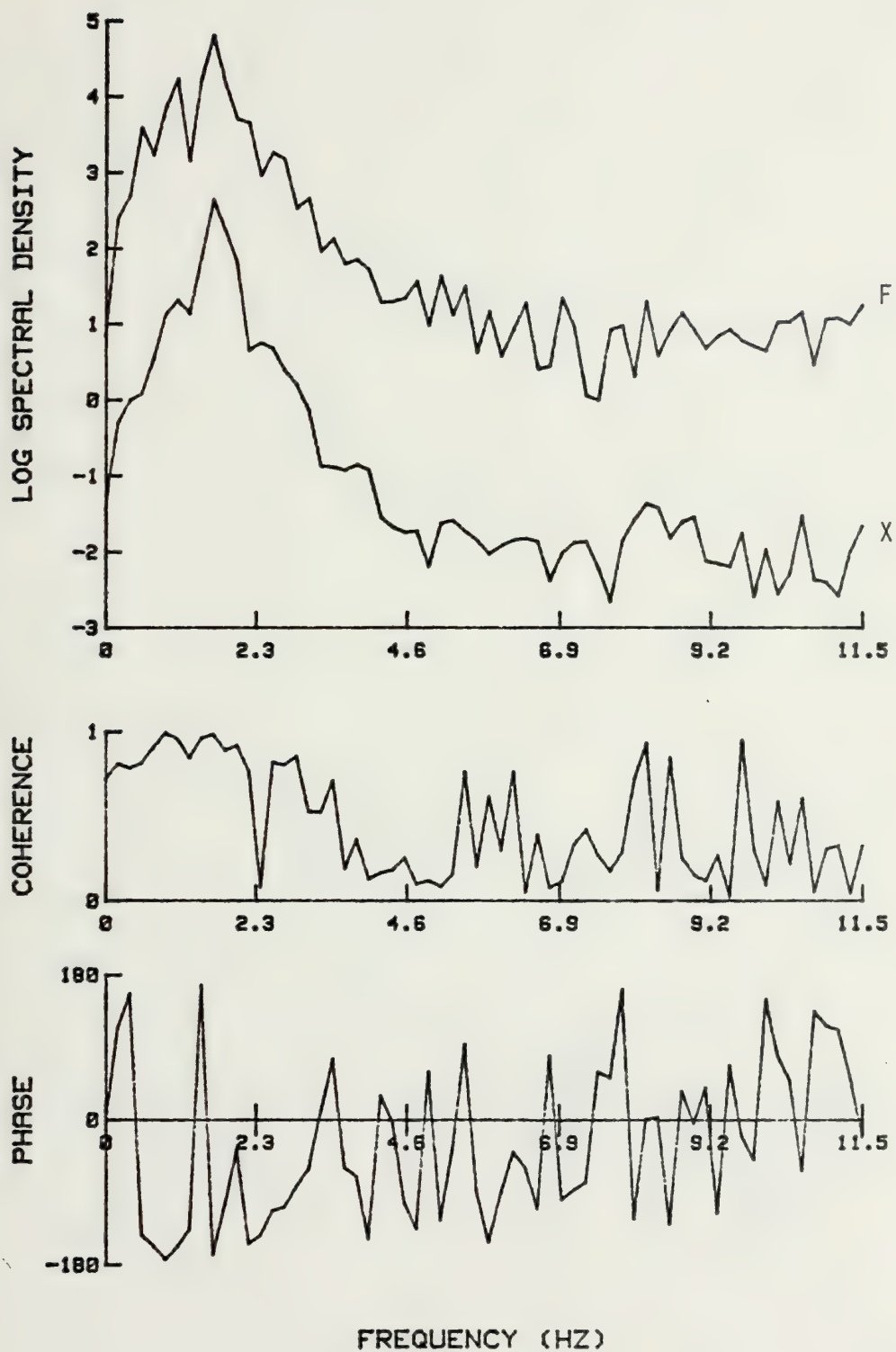


Fig. 135 Spectral analysis for a 3 in. smooth cylinder, $\zeta = 0.052$, $K = 60$

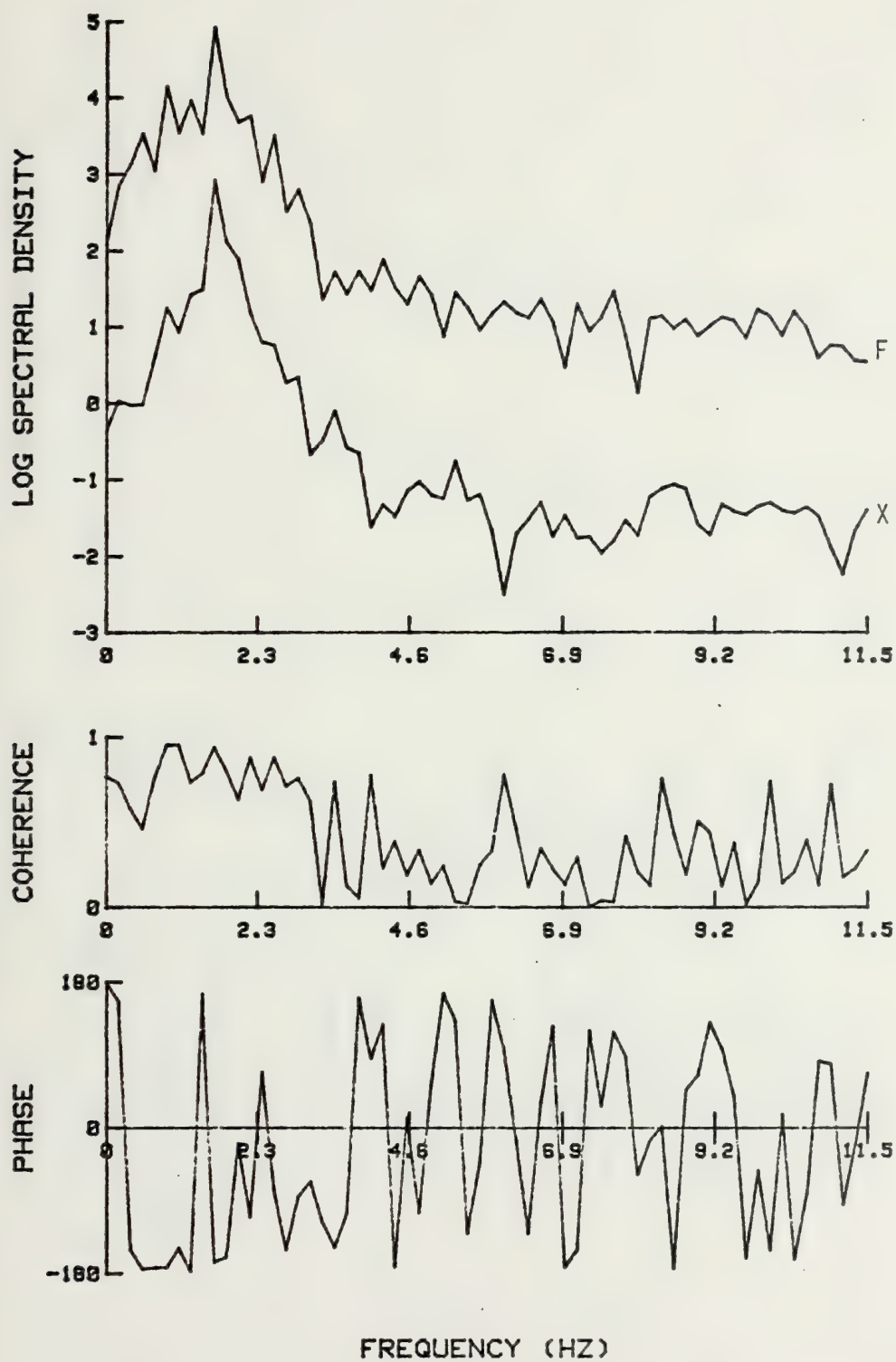


Fig. 136 Spectral analysis for a 3 in. smooth cylinder, $\zeta = 0.052$, $K = 64$

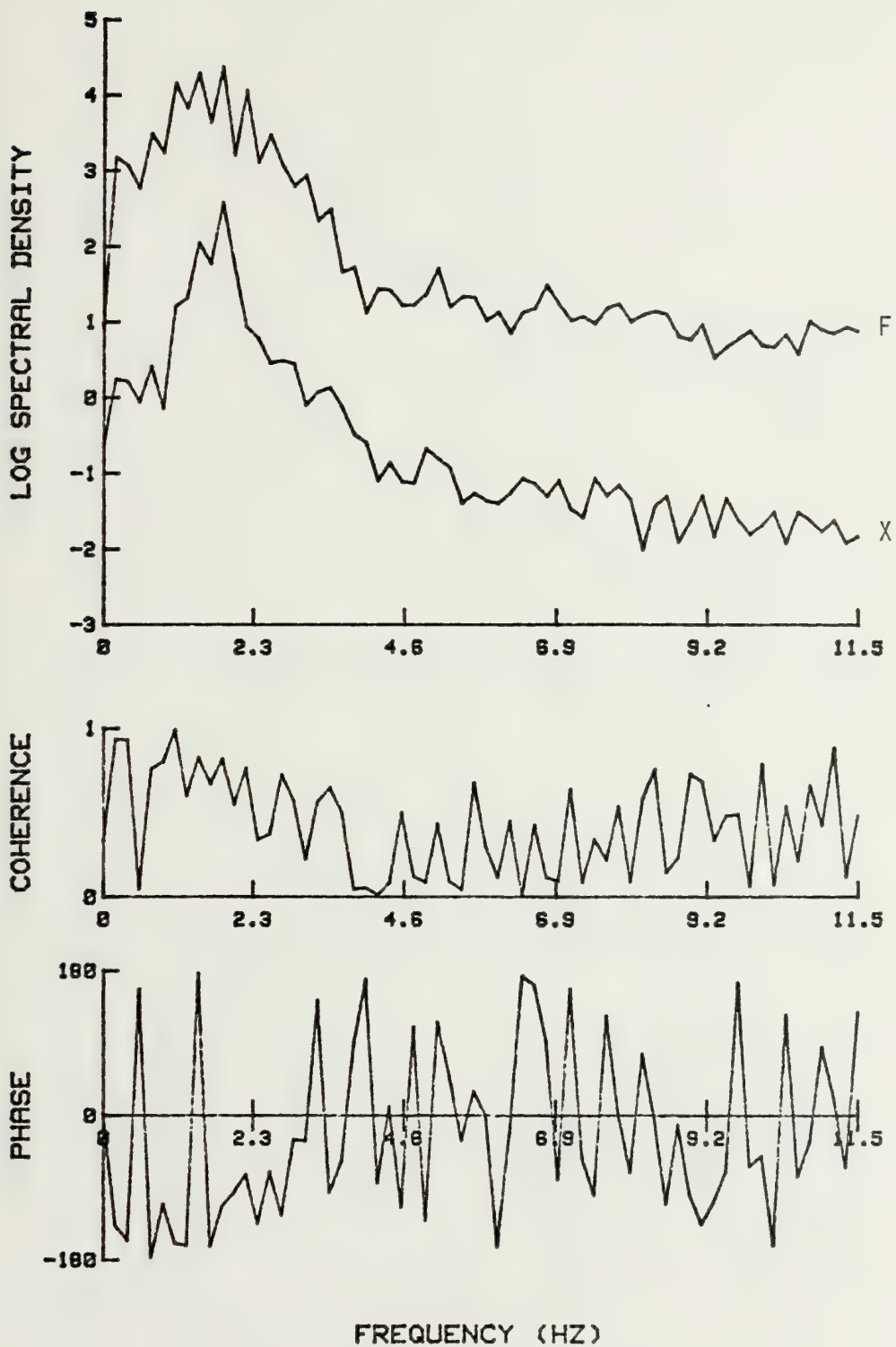


Fig. 137 Spectral analysis for a 3 in. smooth cylinder, $\zeta = 0.052$, $K = 69$

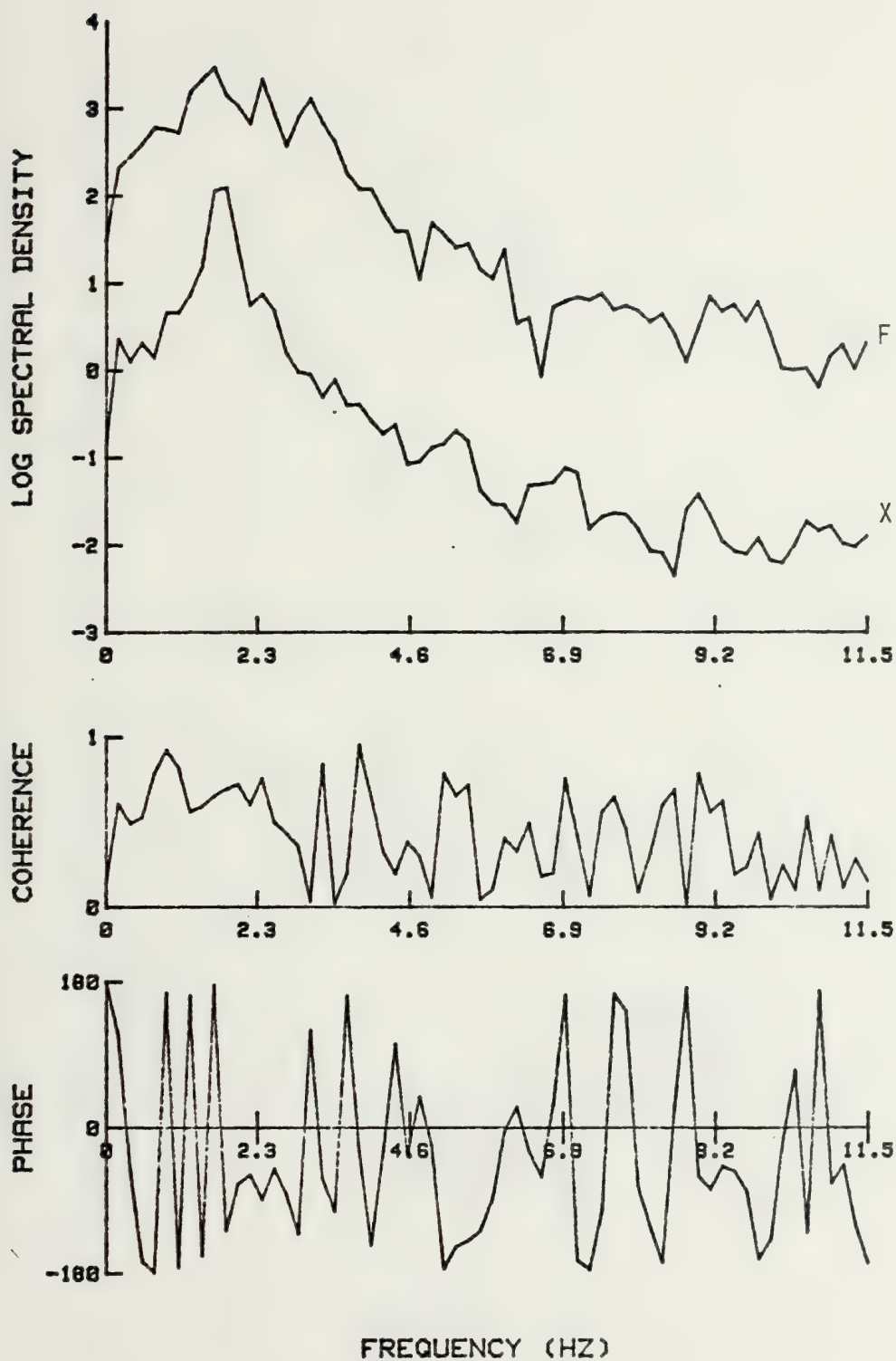


Fig. 138 Spectral analysis for a 3 in. smooth cylinder, $\zeta = 0.052$,
 $K = 88$

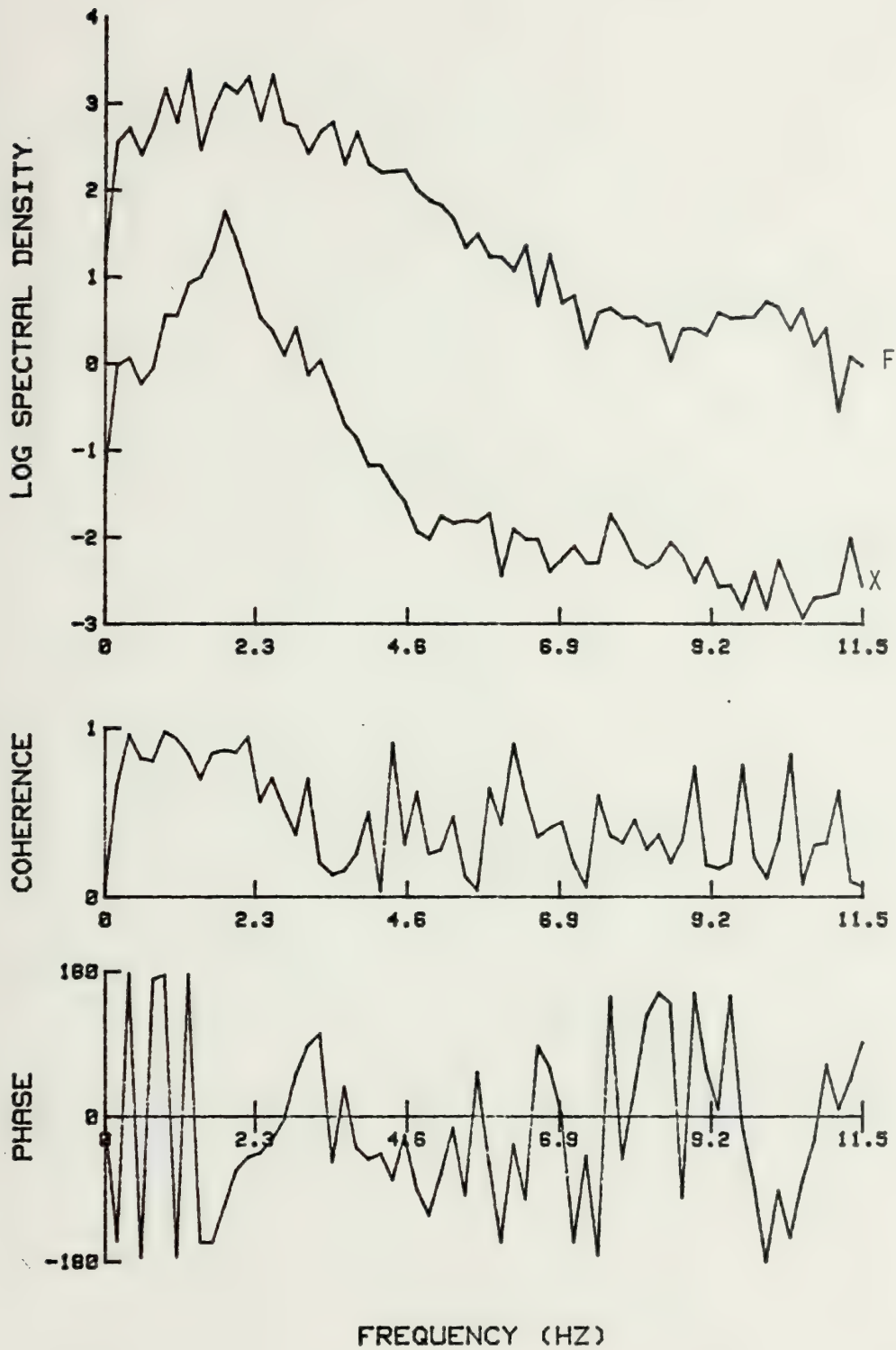


Fig. 139 Spectral analysis for a 3 in. smooth cylinder, $\zeta = 0.052$, $K = 99$

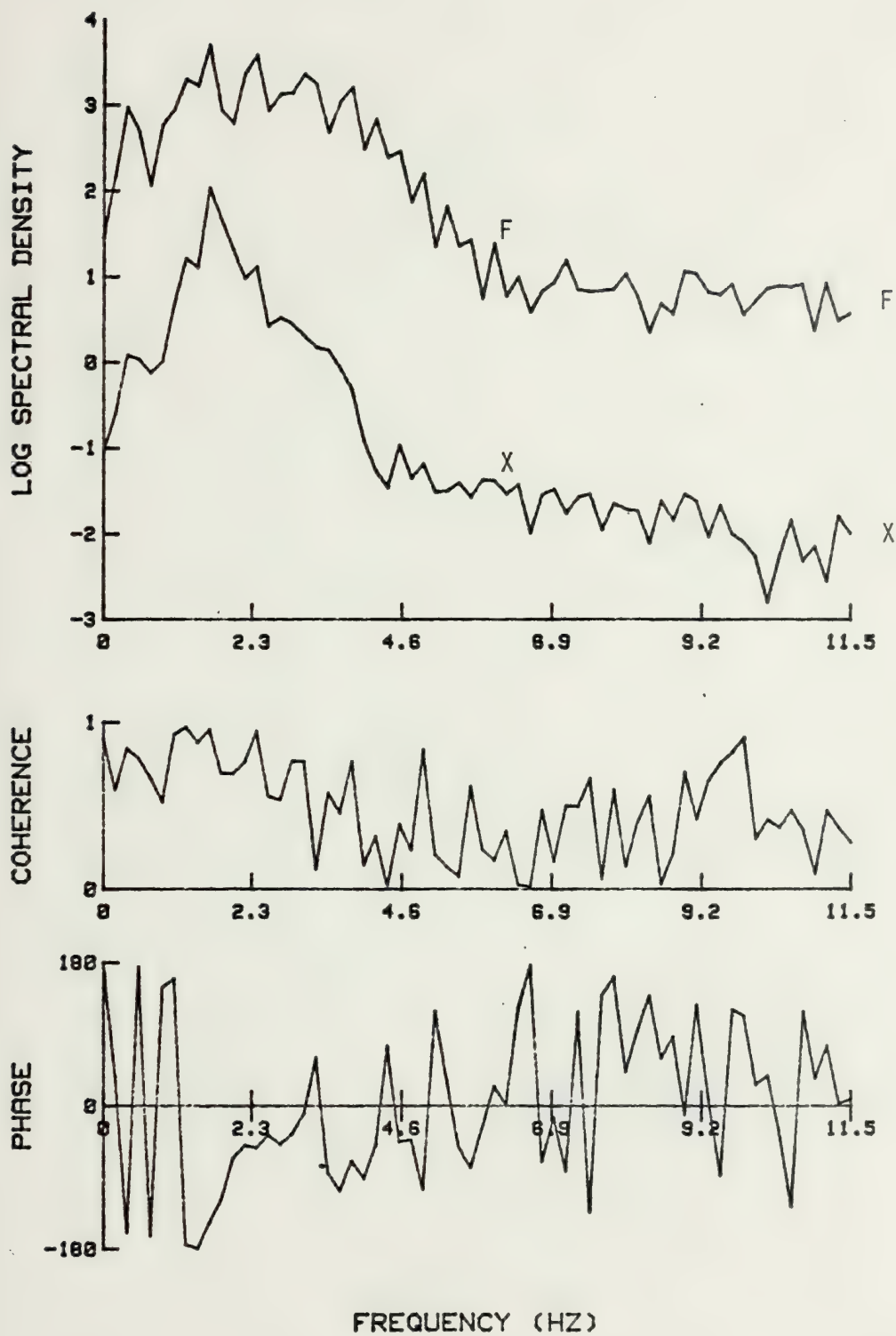


Fig. 140 Spectral analysis for a 3 in. smooth cylinder, $\zeta = 0.052$, $K = 112$

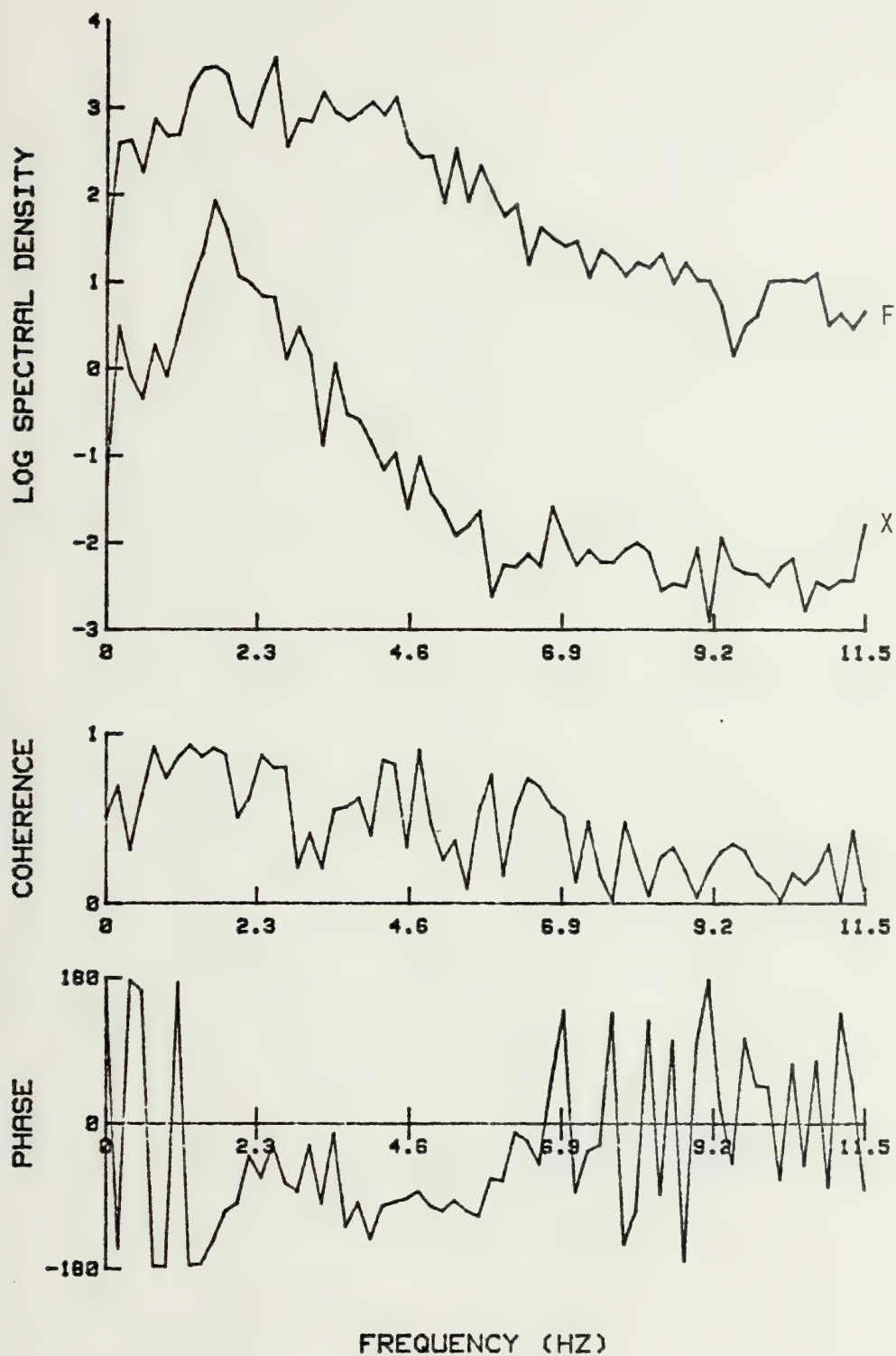


Fig. 141 Spectral analysis for a 3 in. smooth cylinder, $\zeta = 0.052$, $K = 123$

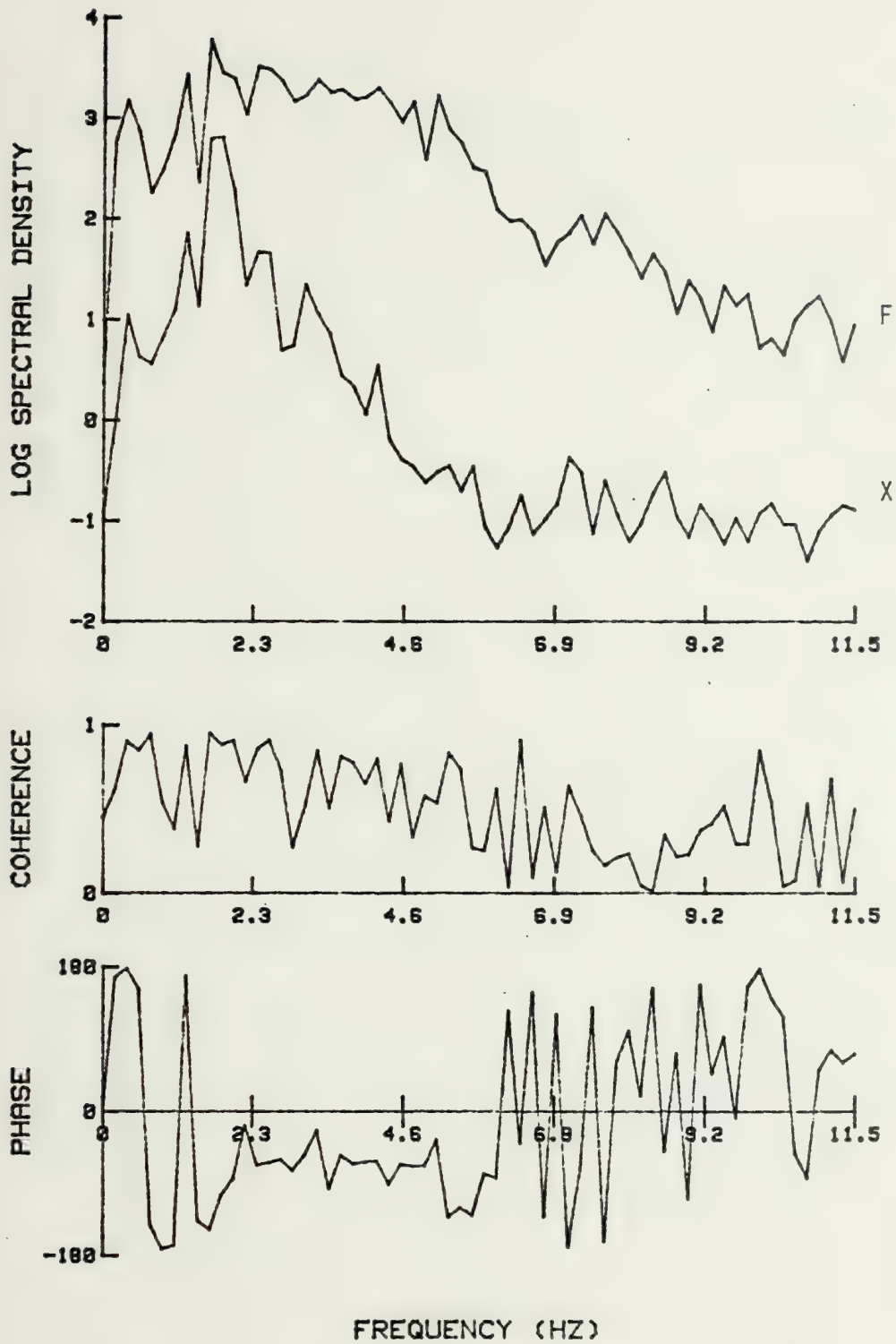


Fig. 142 Spectral analysis for a 3 in. smooth cylinder, $\zeta = 0.052$, $K = 134$

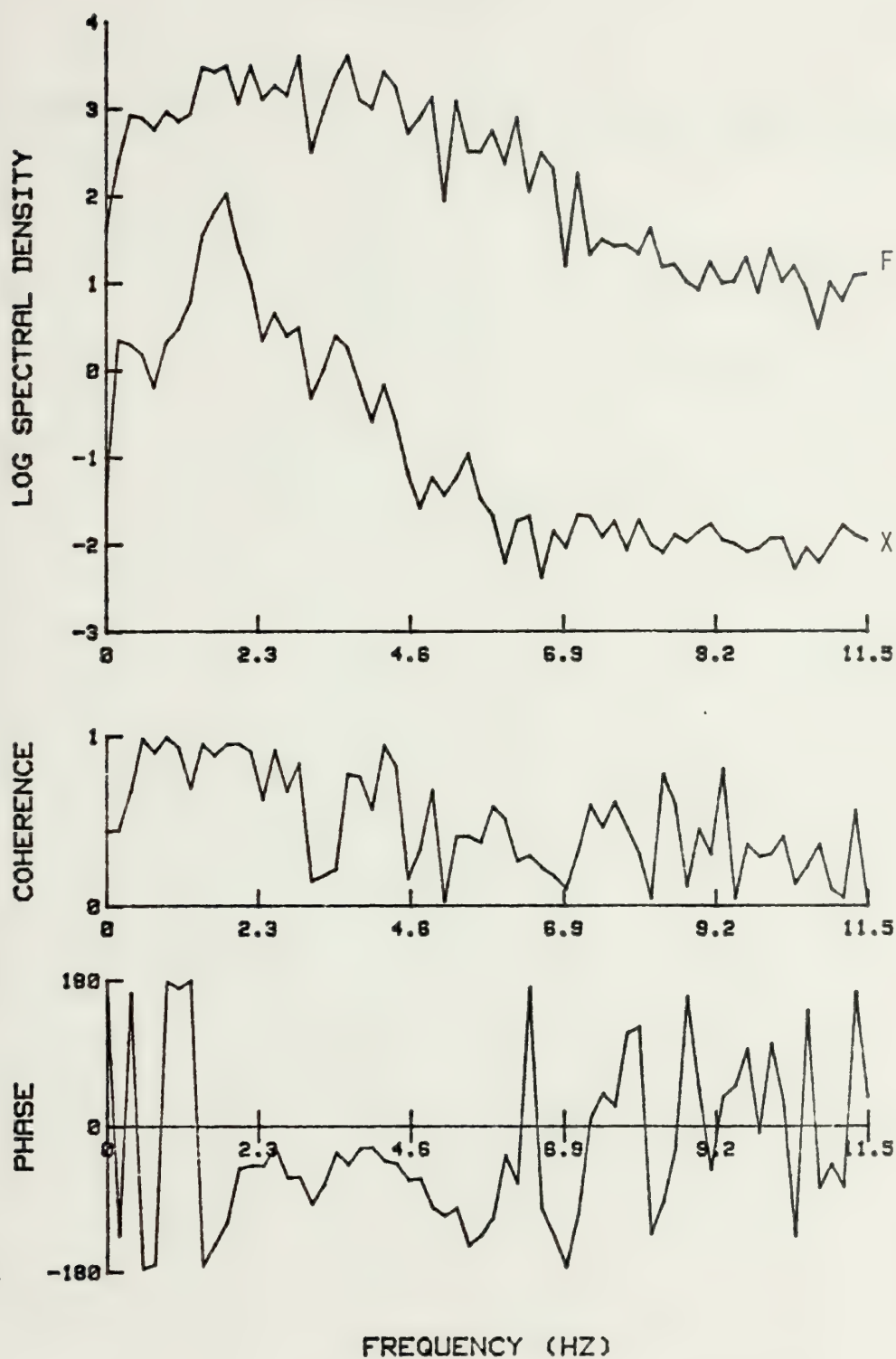


Fig. 143 Spectral analysis for a 3 in. smooth cylinder, $\zeta = 0.052$, $K = 141$

APPENDIX F

SPECTRAL ANALYSIS FOR A 4 in. ROUGH CYLINDER FOR VARIOUS VALUES OF K

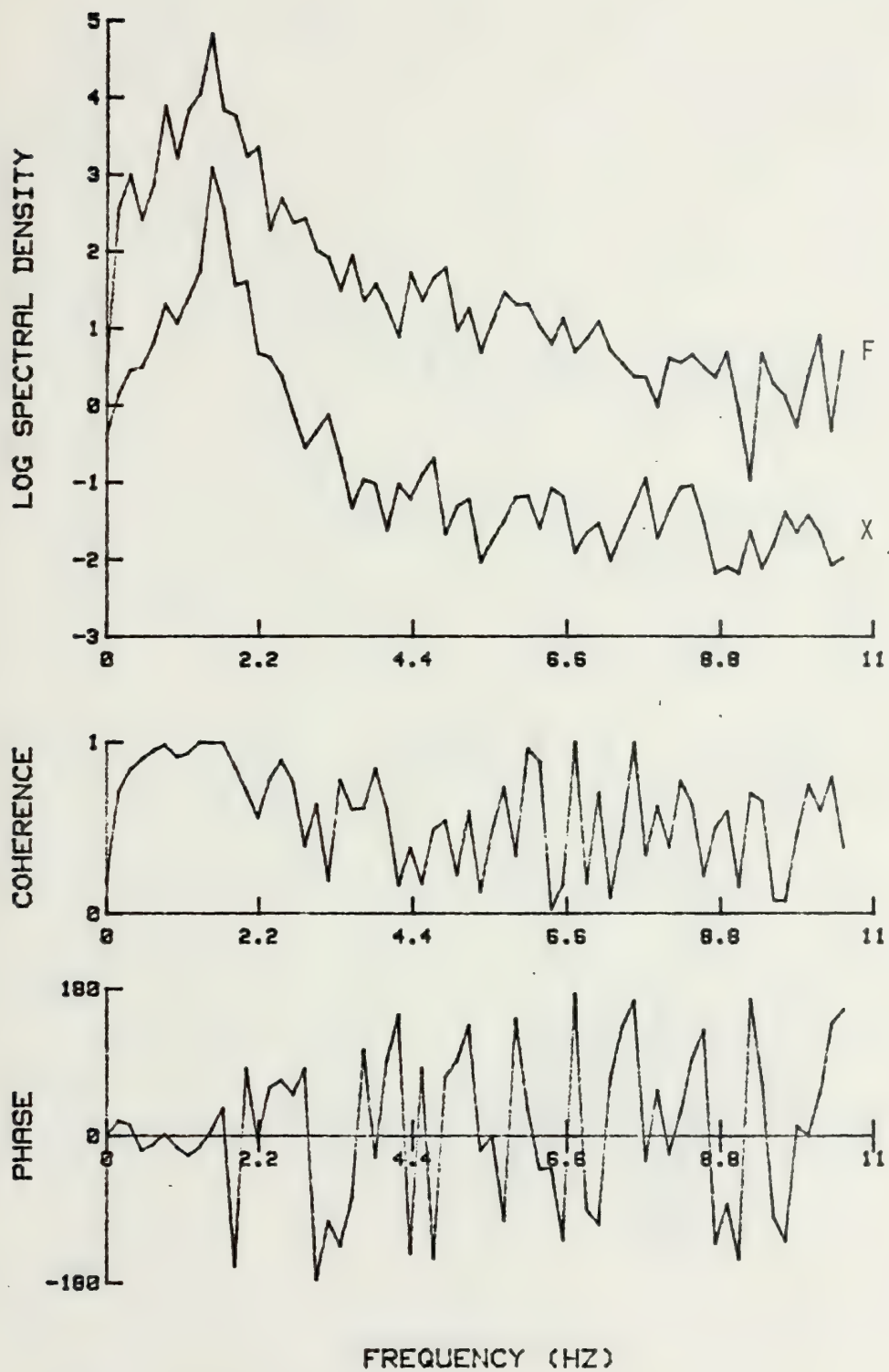


Fig. 144 Spectral analysis for a 4 in. rough cylinder, $\zeta = 0.030$, $K = 29$

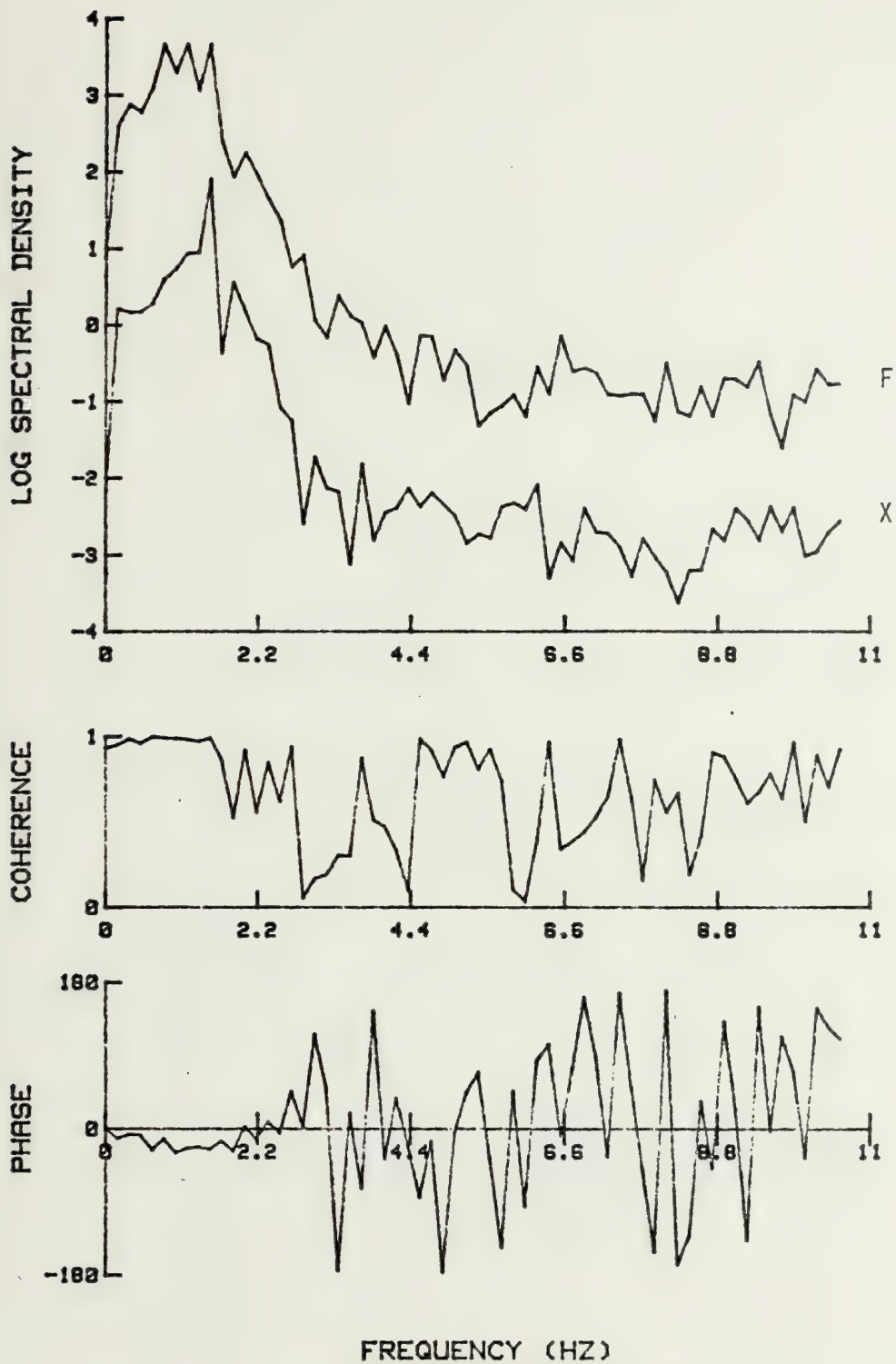


Fig. 145 Spectral analysis for a 4 in. rough cylinder, $\zeta = 0.030$, $K = 32$

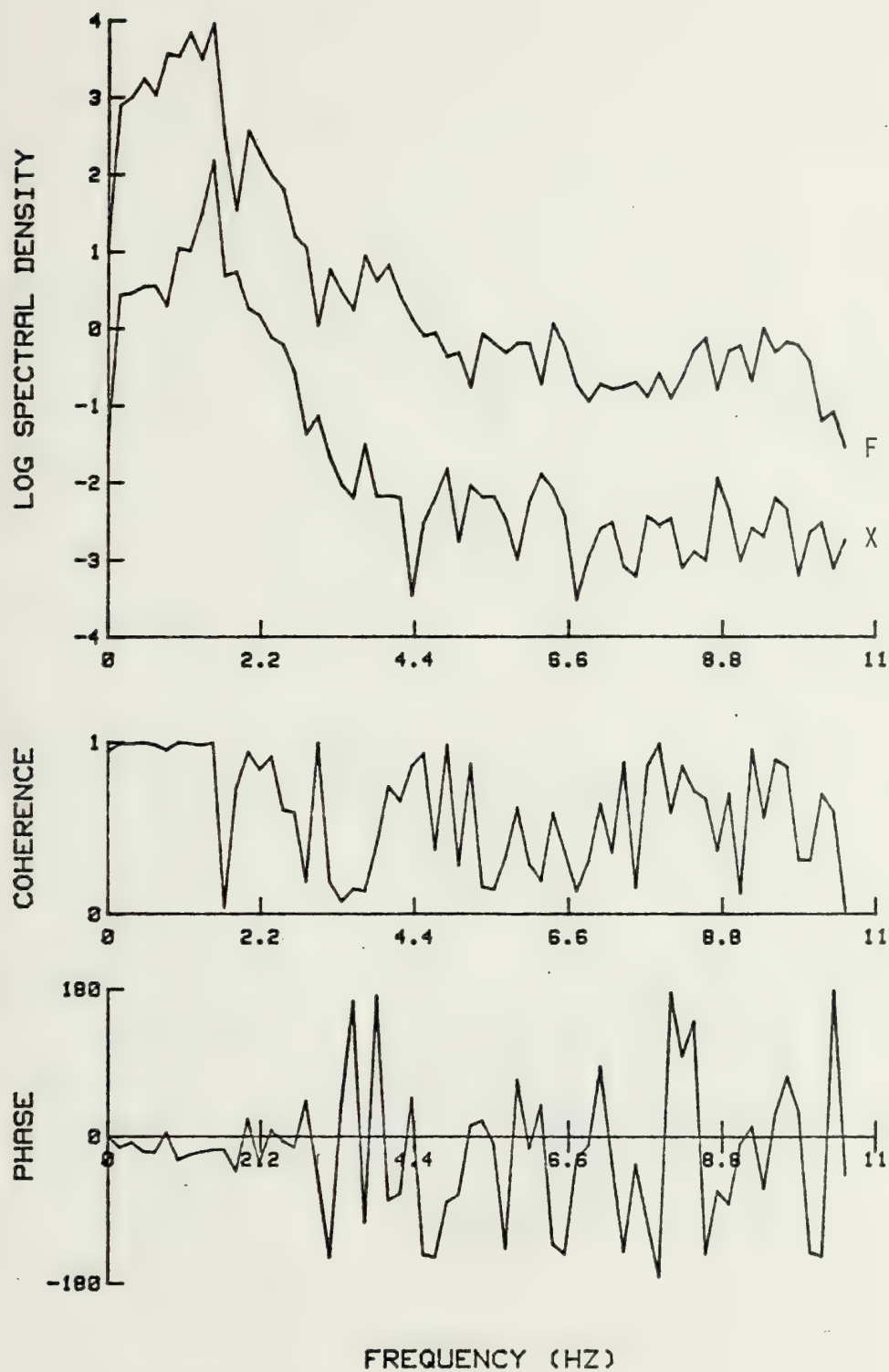


Fig. 146 Spectral analysis for a 4 in. rough cylinder, $\zeta = 0.030$, $K = 35$

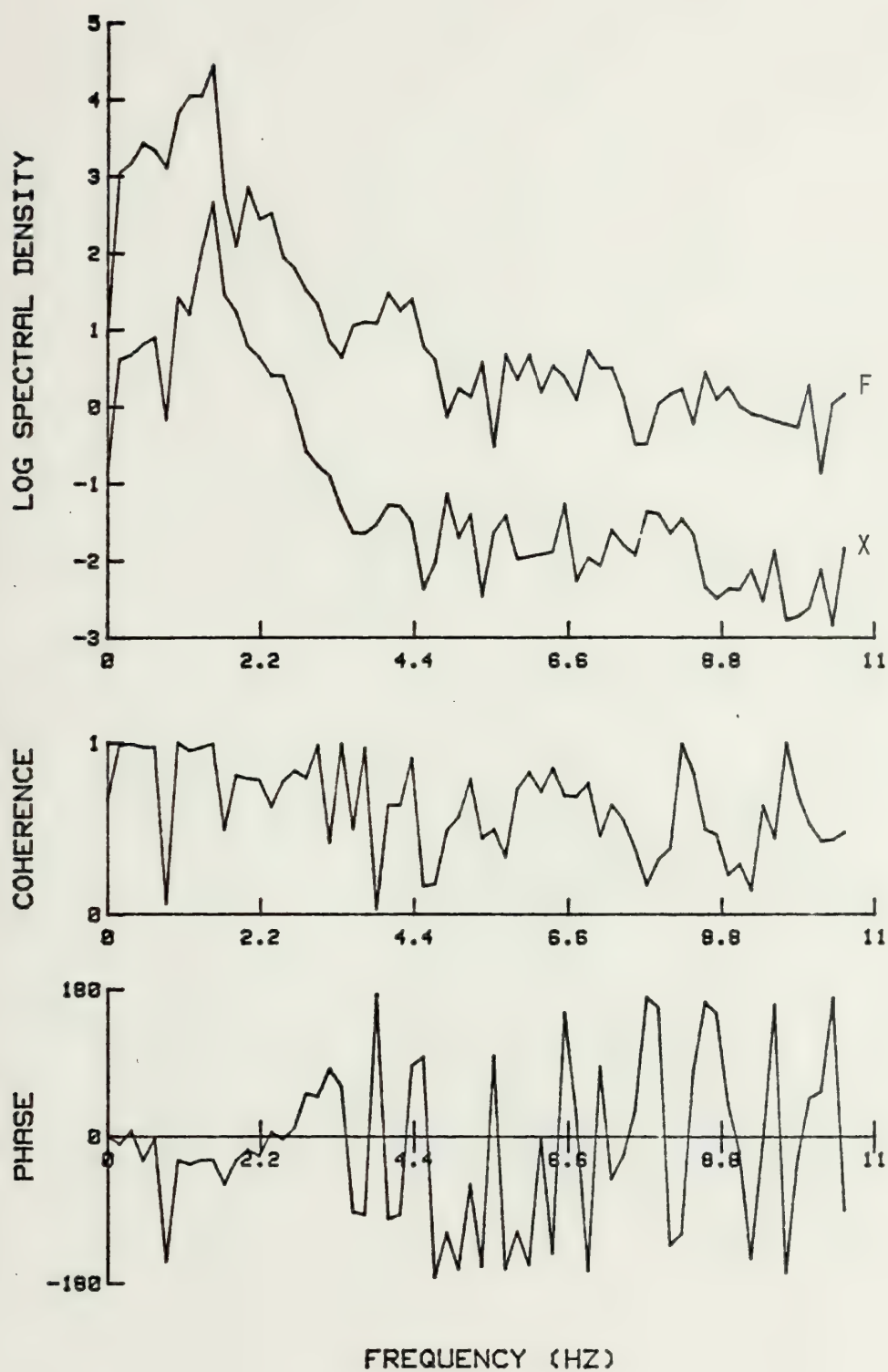


Fig. 147 Spectral analysis for a 4 in. rough cylinder, $\zeta = 0.030$, $K = 36$

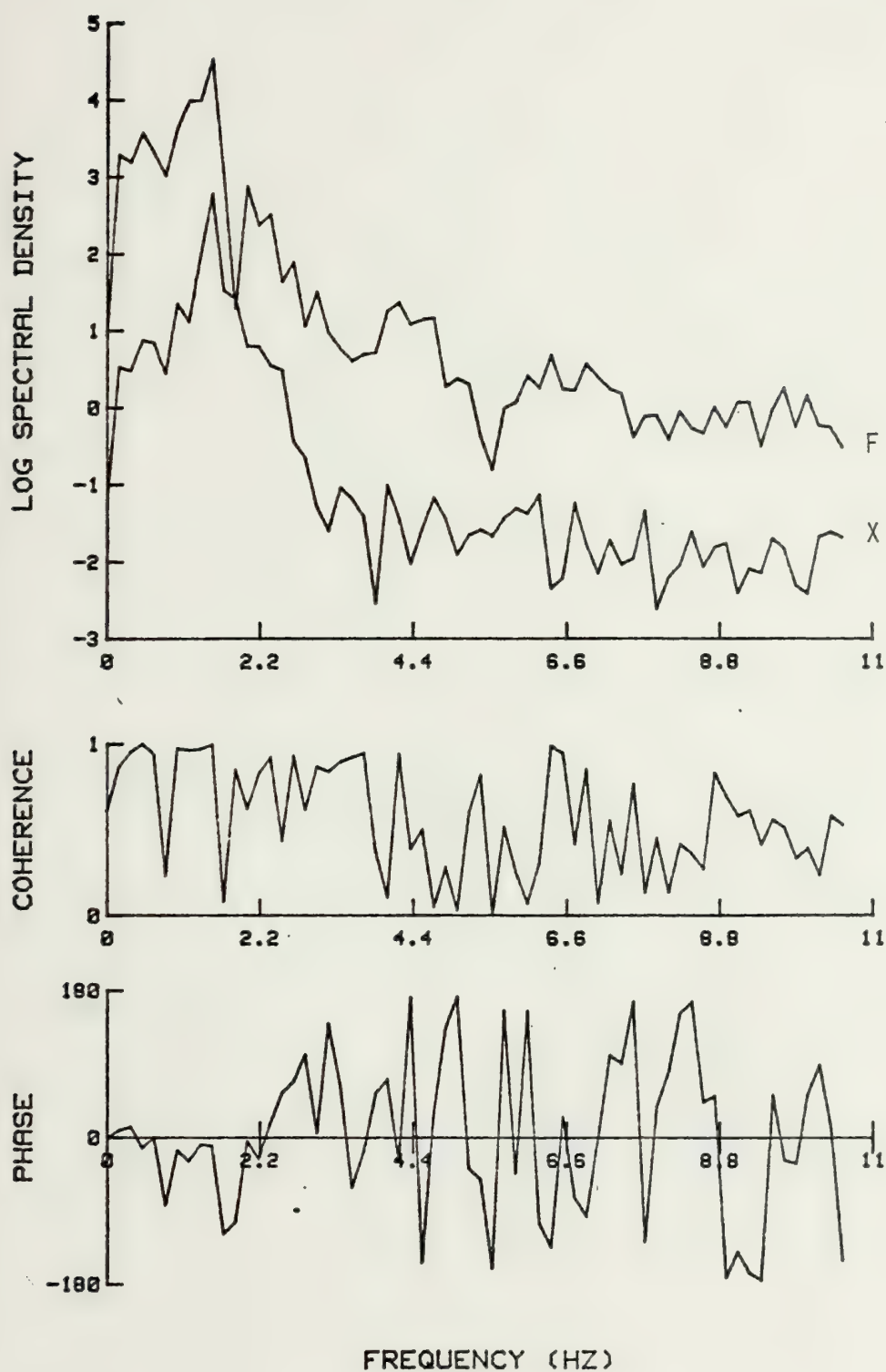


Fig. 148 Spectral analysis for a 4 in. rough cylinder, $\zeta = 0.030$,
 $K = 38$

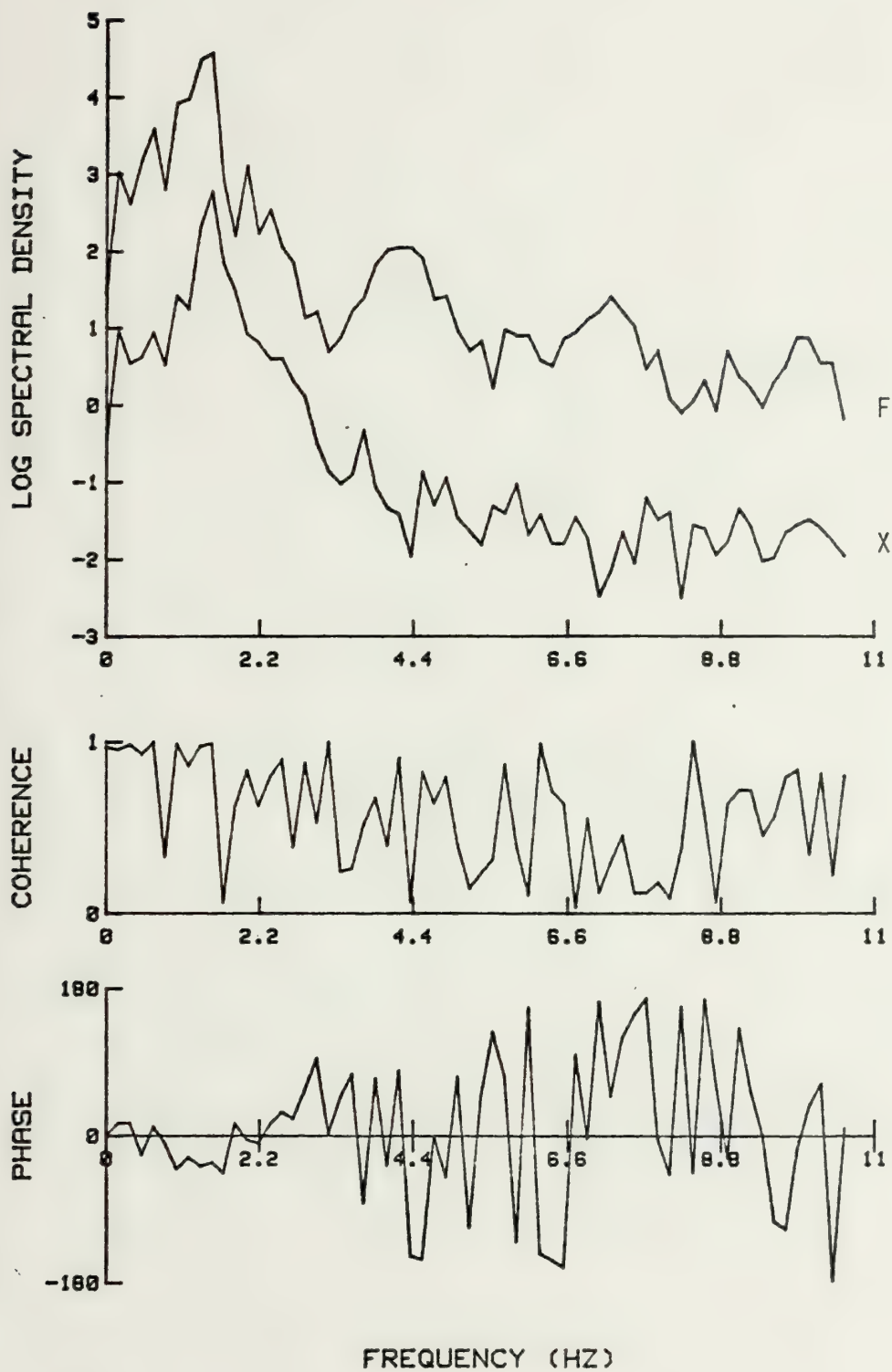


Fig. 149 Spectral analysis for a 4 in. rough cylinder, $\zeta = 0.030$, $K = 40$

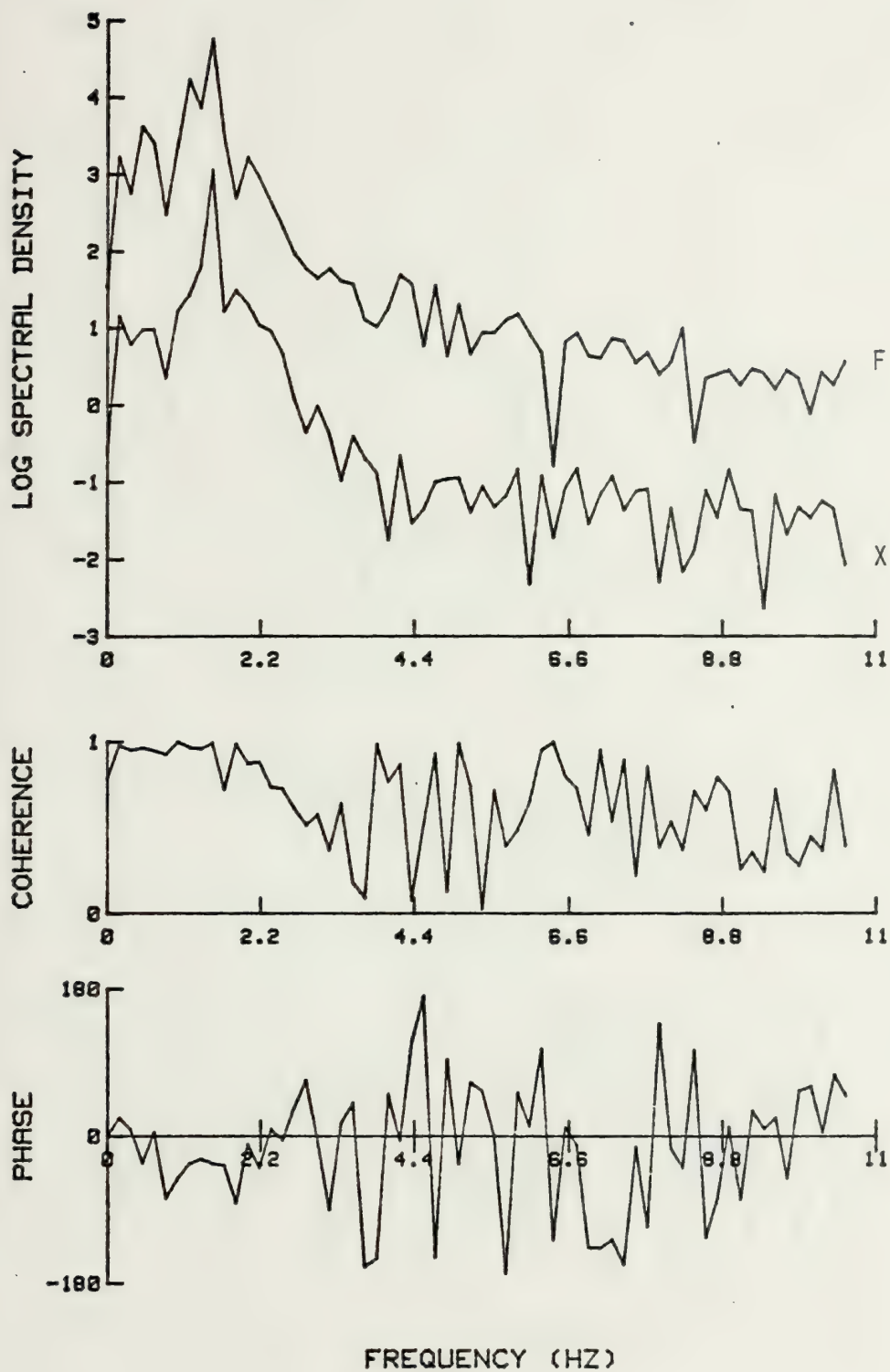


Fig. 150 Spectral analysis for a 4 in. rough cylinder, $\zeta = 0.030$, $K = 43$

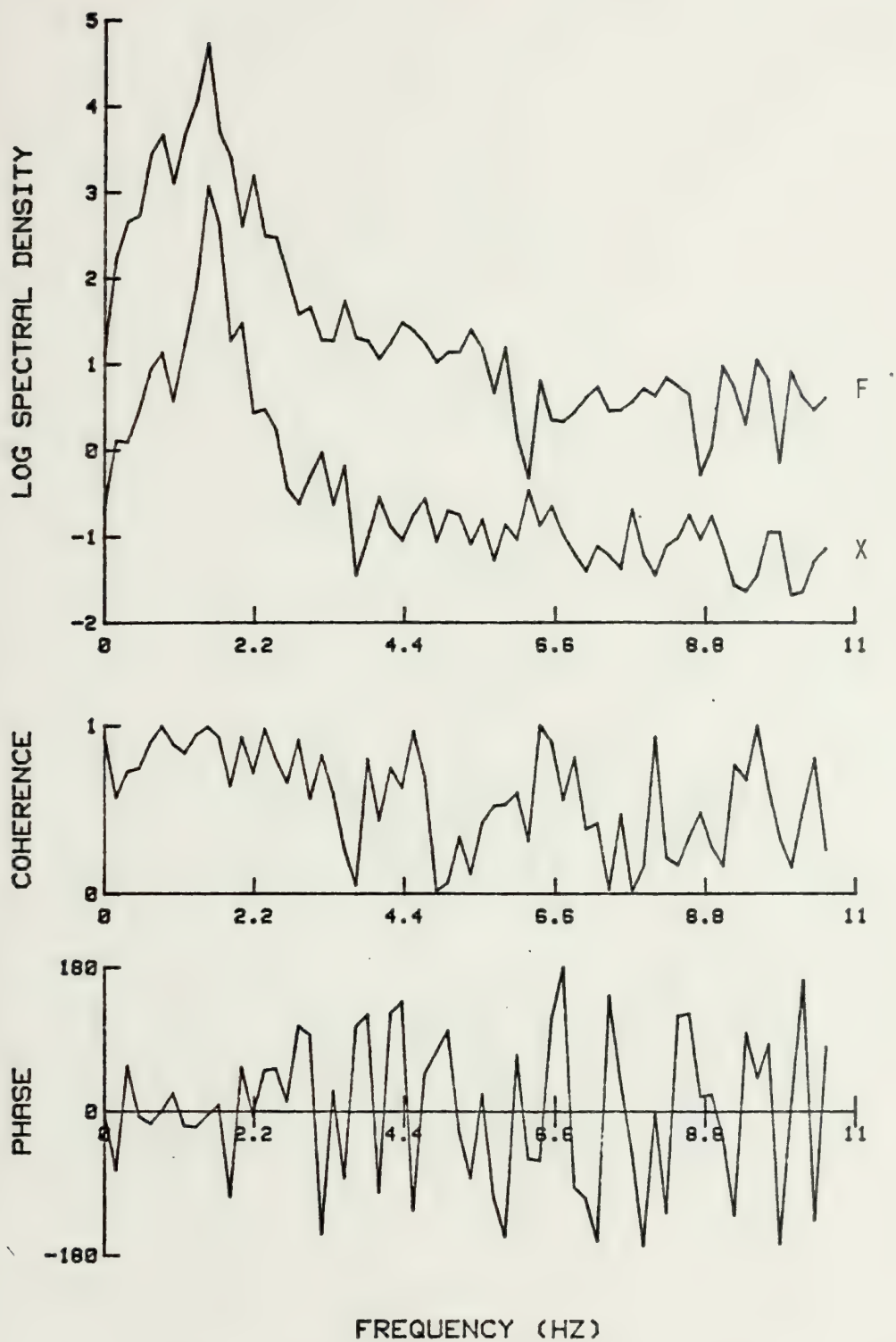


Fig. 151 Spectral analysis for a 4 in. rough cylinder, $\zeta = 0.030$, $K = 45$

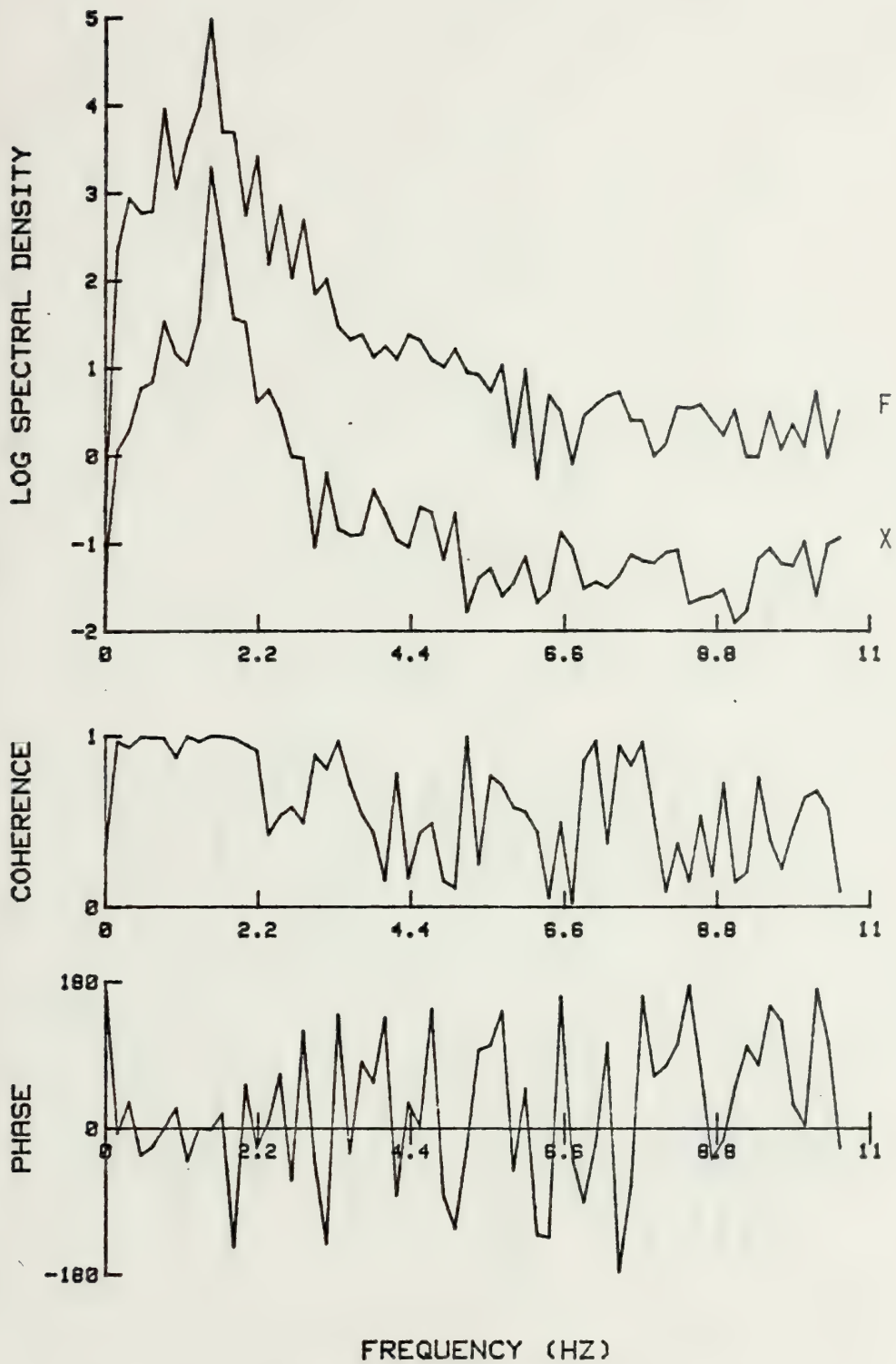


Fig. 152 Spectral analysis for a 4 in. rough cylinder, $\zeta = 0.030$, $K = 46$

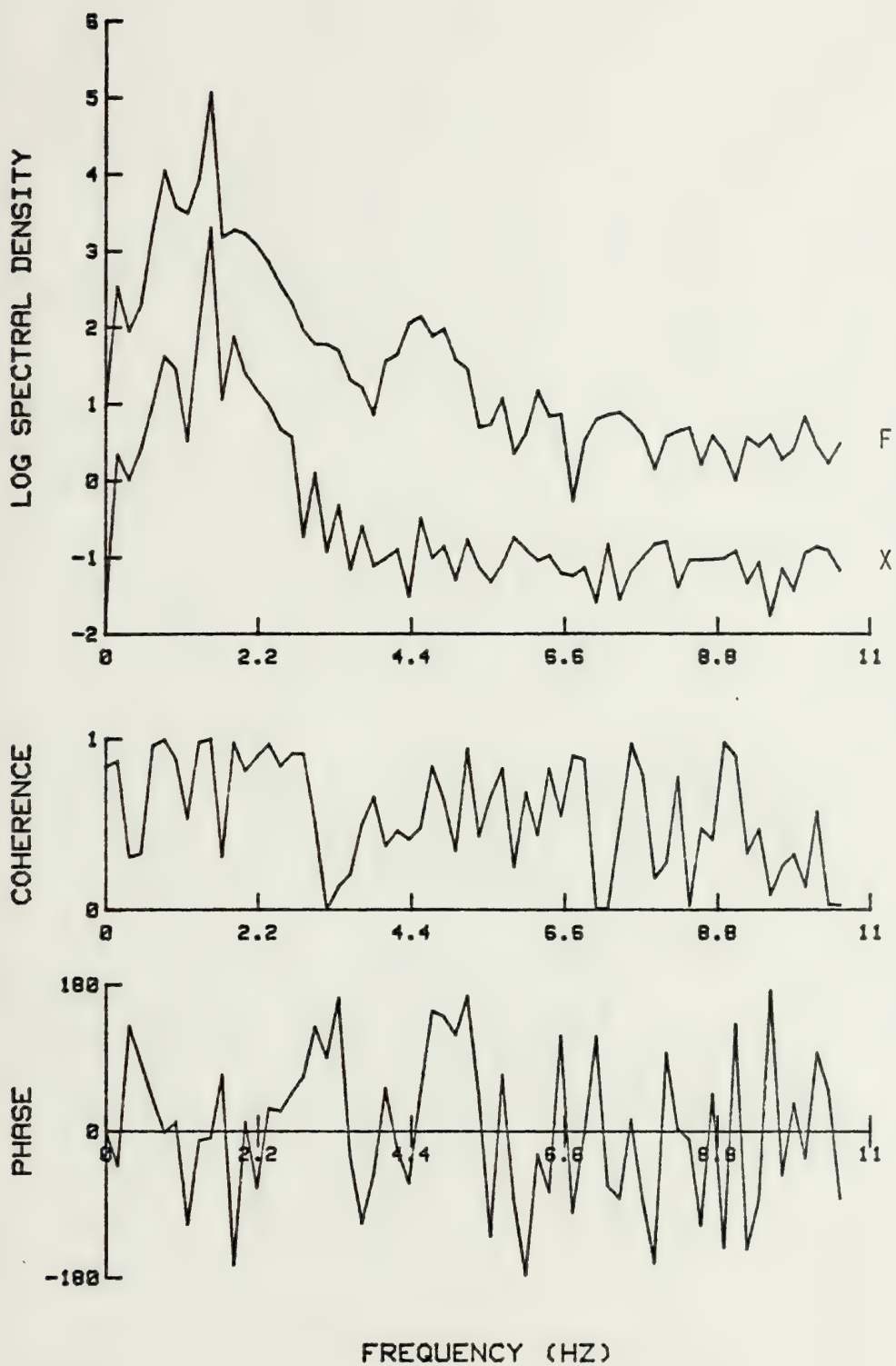


Fig. 153 Spectral analysis for a 4 in. rough cylinder, $\zeta = 0.030$,
 $K = 51$

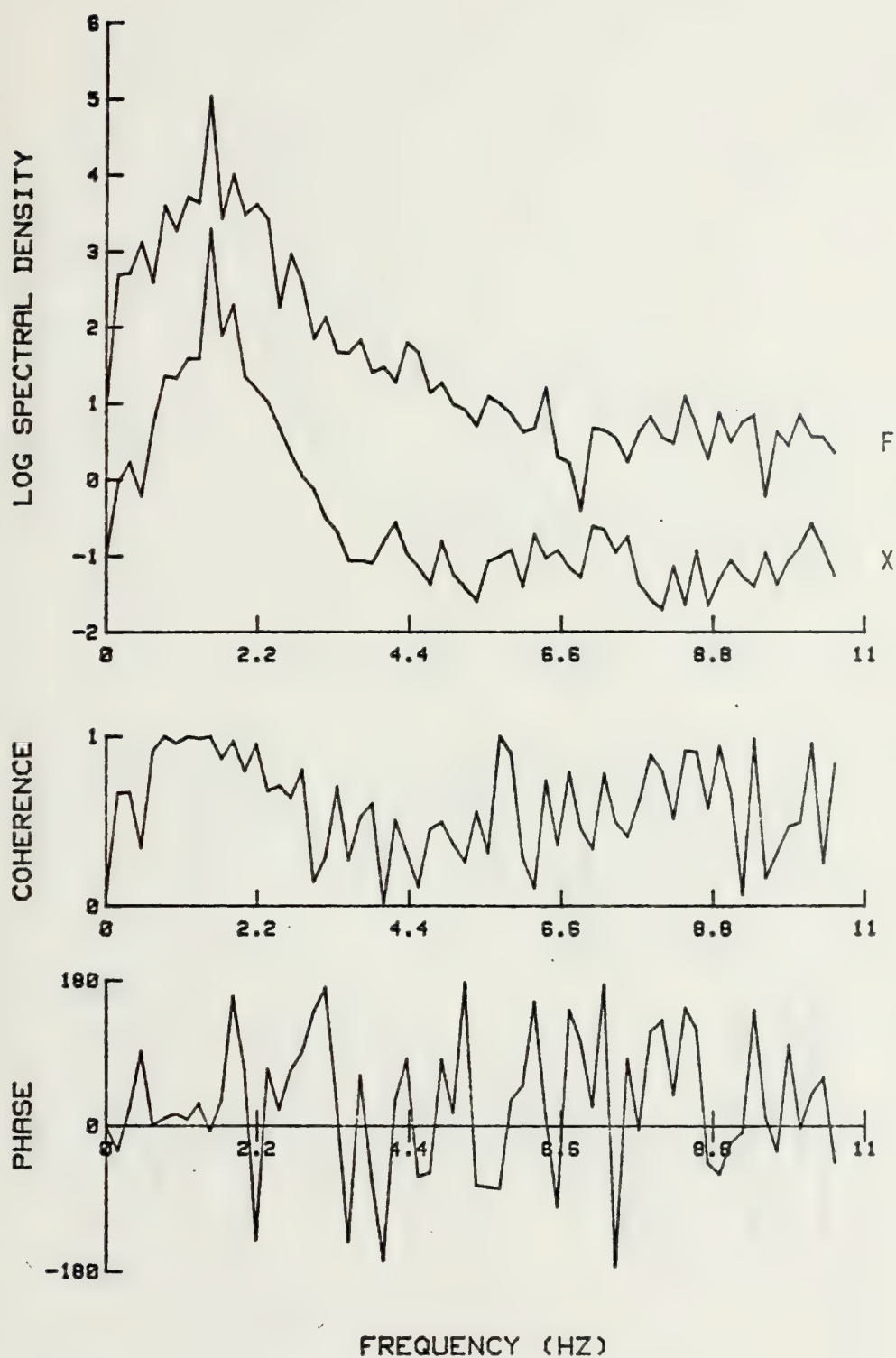


Fig. 154 Spectral analysis for a 4 in. rough cylinder, $\zeta = 0.030$, $K = 55$

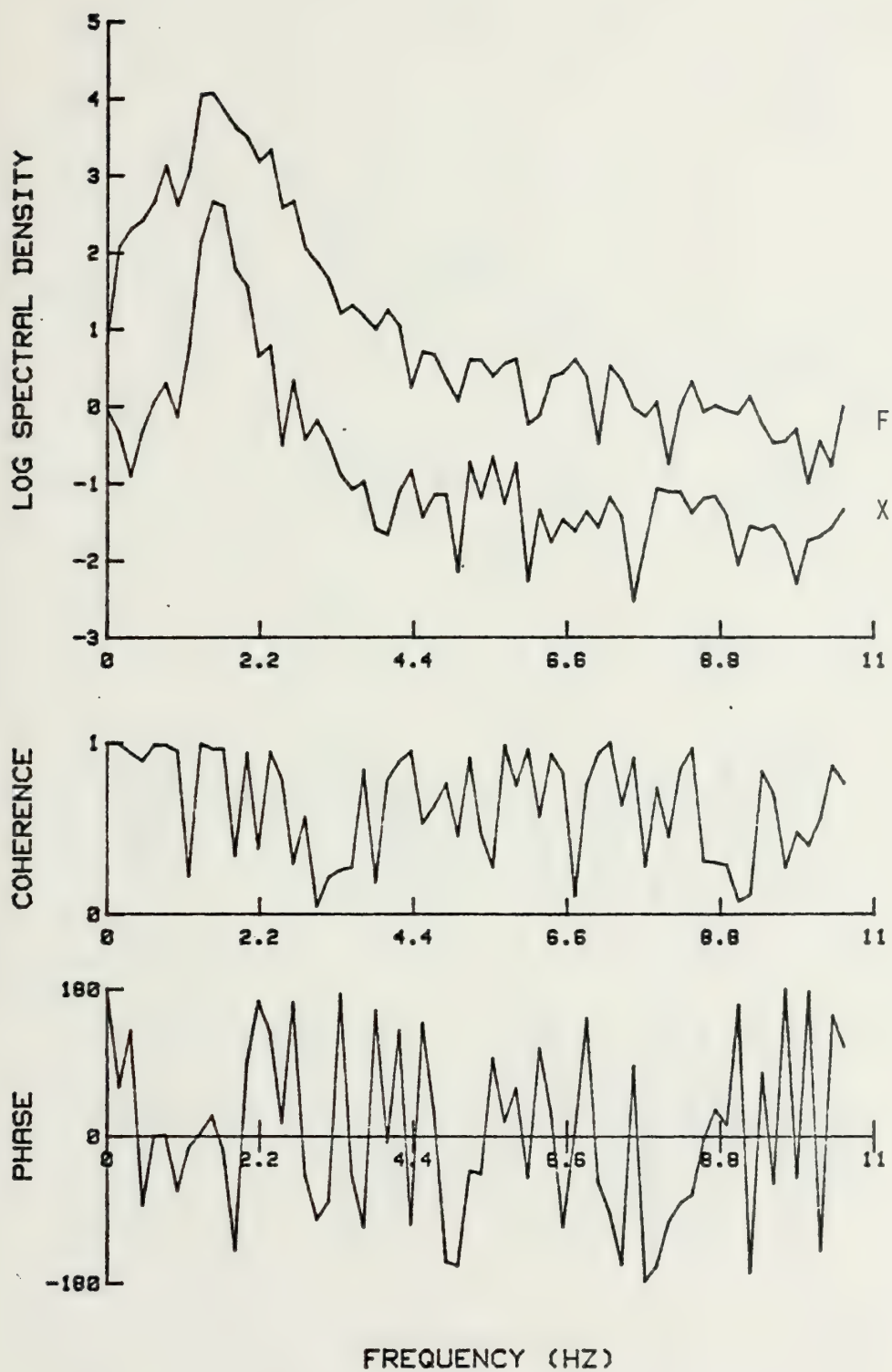


Fig. 155 Spectral analysis for a 4 in. rough cylinder, $\zeta = 0.030$, $K = 57$

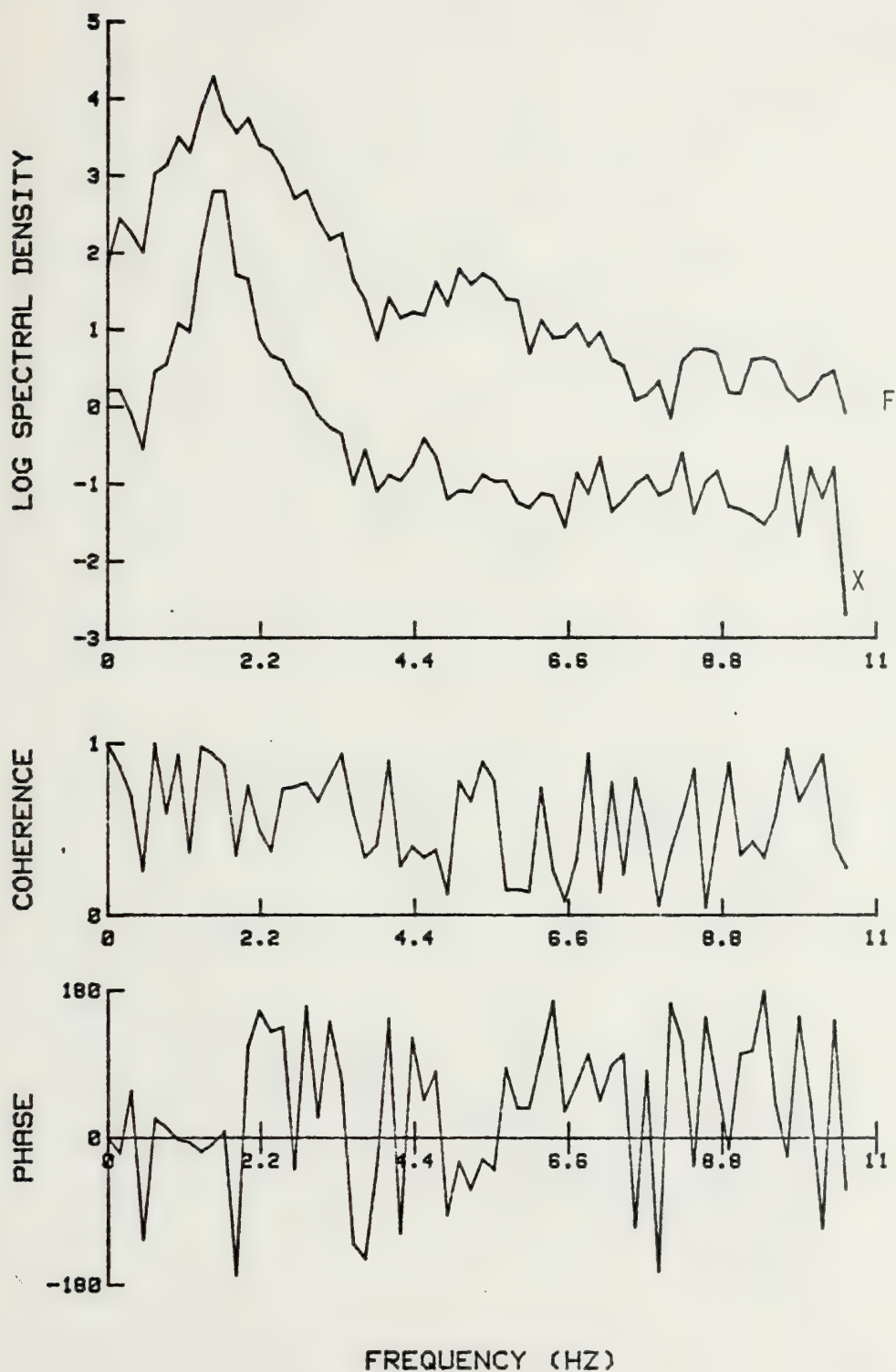


Fig. 156 Spectral analysis for a 4 in. rough cylinder, $\zeta = 0.030$, $K = 64$

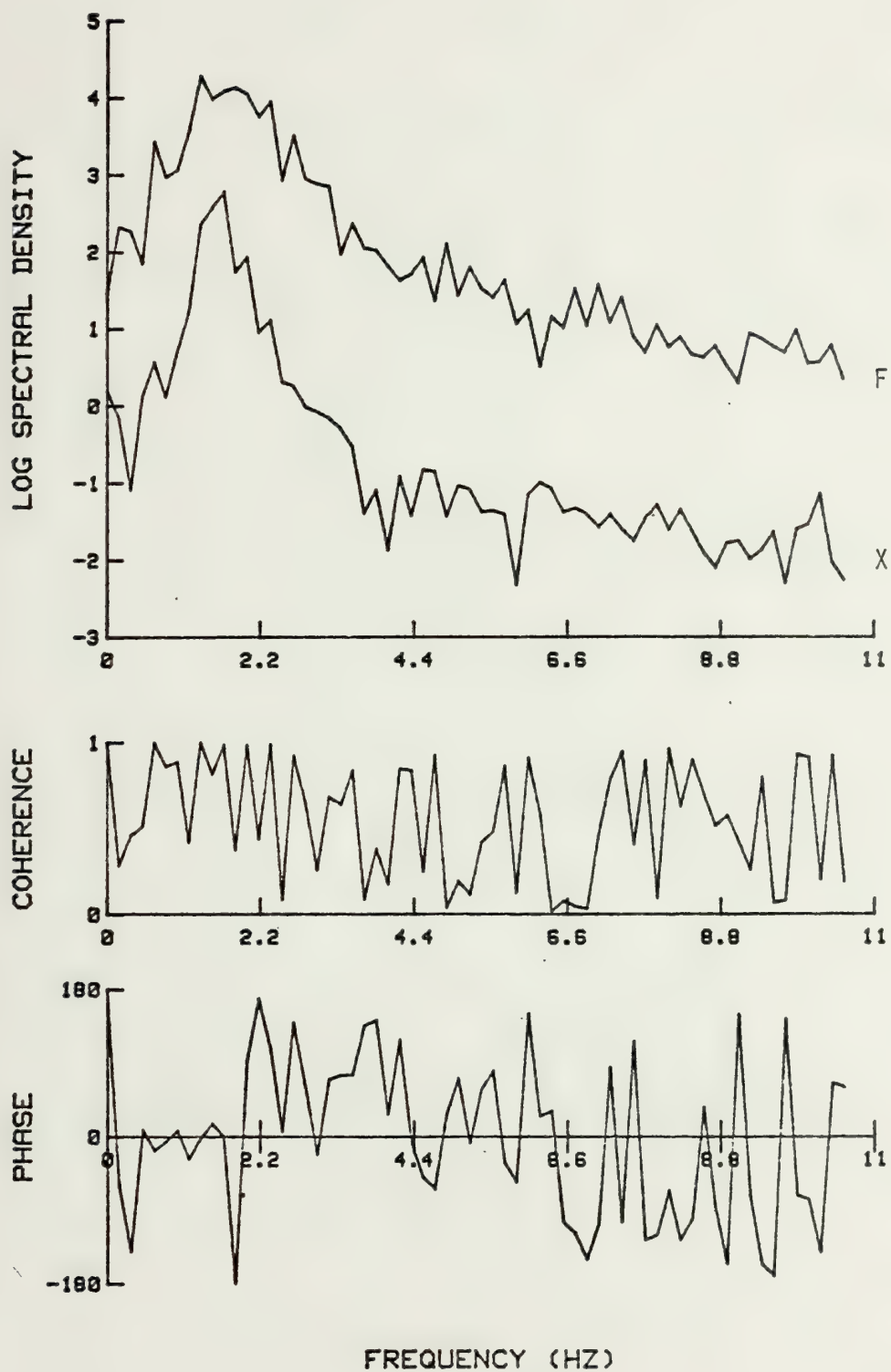


Fig. 157 Spectral analysis for a 4 in. rough cylinder, $\zeta = 0.030$, $K = 70$

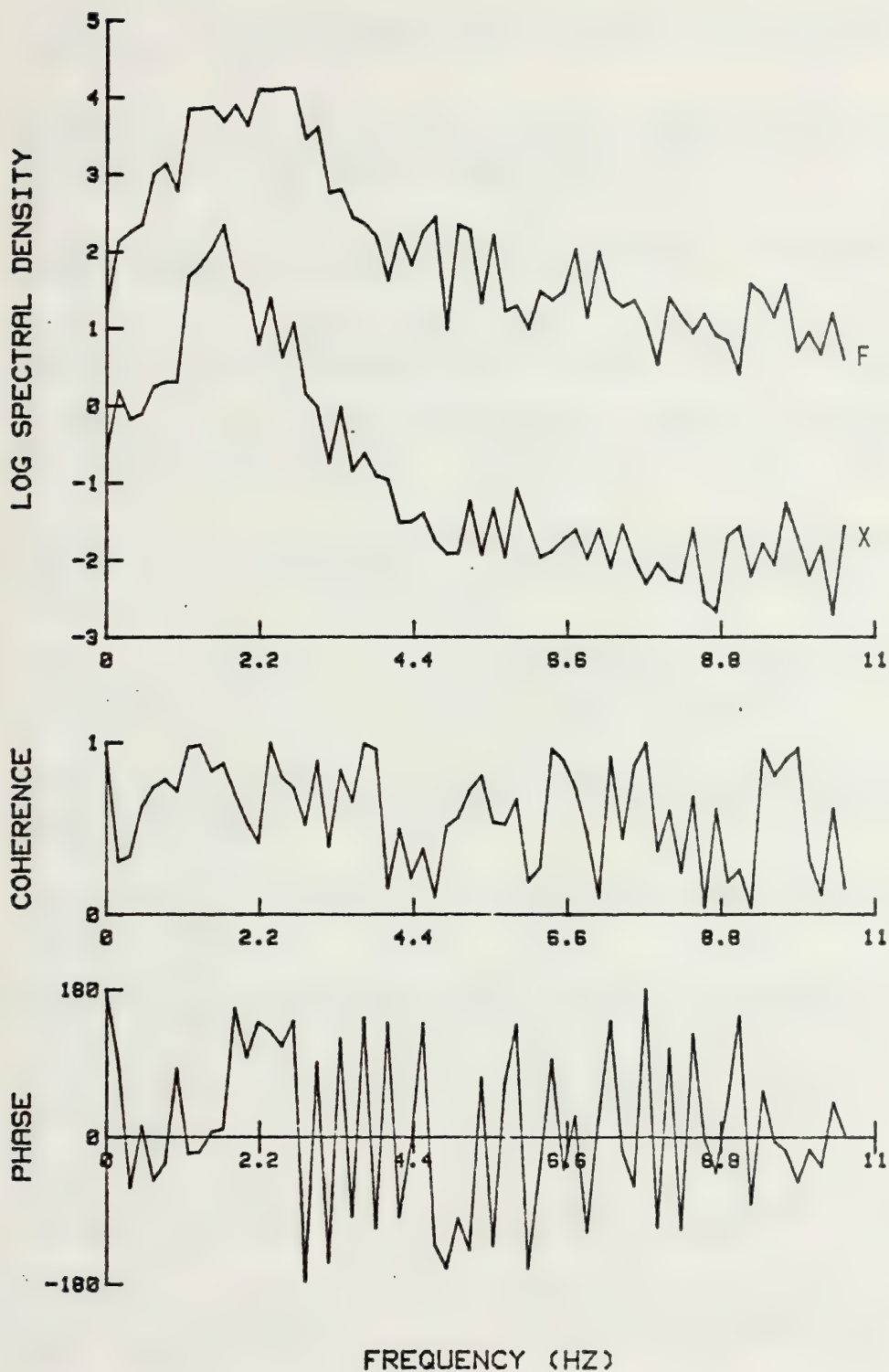


Fig. 158 Spectral analysis for a 4 in. rough cylinder, $\zeta = 0.030$, $K = 84$

LIST OF REFERENCES

1. Blevins, R. D., Flow-Induced Vibration, Van Nostrand Reinhold Company New York, 1977.
2. Parkinson, G. V., "Mathematical Models of Flow-Induced Vibrations of Bluff Bodies," in Flow-Induced Structural Vibrations, ed., Naudascher, E., Springer-Verlag, Berlin, 1974, pp. 81-127.
3. King, R., "A Review of Vortex Shedding Research and its Application," Ocean Engineering, Vol. 4, 1977, pp. 141-172.
4. McCroskey, W. J., "Some Current Research in Unsteady Fluid Dynamics," Journal of Fluids Engineering, Trans. ASME, Vol. 99, 1977, pp. 8-39.
5. Morkovin, M. V., "Flow Around Circular Cylinders. A Kaleidoscope of Challenging Fluid Phenomena," ASME Symposium on Fully Separated Flows, Philadelphia, PA., 1964, pp. 102-118.
6. Marris, A. W., "A Review on Vortex Streets, Periodic Wakes, and Induced Vibration Phenomena," Journal of Basic Engineering, Trans. ASME, Vol. 86, 1964, pp. 185-196.
7. Mair, W. A., and Maull, D. J., "Bluff Bodies and Vortex Shedding -- A Report on Euromech 17," Journal of Fluid Mechanics, Vol. 45, 1971, pp. 209-224.
8. Berger, E., and Wille, R., "Periodic Flow Phenomena," Annual Reviews of Fluid Mechanics, Annual Reviews Inc., Palo Alto, Calif., Vol. 4, 1972, pp. 313-340.
9. Schlichting, H., Boundary-Layer Theory, 6-th edition, McGraw-Hill, New York, 1968.
10. Sarpkaya, T., "Vortex-Induced Oscillations - A Selective Review," Journal of Applied Mechanics, Vol. 46, No. 2, June 1979, pp. 241-258.
11. Gerrard, J. H., "The Mechanics of the Formation Region of Vortices Behind Bluff Bodies," Journal of Fluid Mechanics, Vol. 25, 1966, pp. 401-413.
12. Strouhal, V., "Über eine besondere Art der Tonerregung," Ann. Phys. und Chemie. New Series Vol. 5, 1878, pp. 216-251.
13. Rayleigh, L., "Acoustical Observations II," Philosophical Magazine, Vol. VII, 1879, pp. 149-162 (also The Theory of Sound, Dover Publications, New York, 1945).
14. Goldstein, S., Modern Developments in Fluid Dynamics, Clarendon Press, Oxford, 1938.

15. Roshko, A., "On the Development of Turbulent Wakes from Vortex Streets," NACA Technical Note 2913, March 1953.
16. van Nunen, J. W. G., "Pressures and Forces on a Circular Cylinder in a Cross Flow at High Reynolds Numbers," in Flow-Induced Structural Vibrations, ed., Naudascher, E., Springer-Verlag, Berlin, 1974, pp. 748-754.
17. Jones, G. W., Cincotta, J. J., and Walker, R. W., "Aerodynamic Forces on a Stationary and Oscillating Circular Cylinder at High Reynolds Numbers," NASA TR-R-300, 1969.
18. National Physical Laboratory, "Strouhal Number of Model Stacks Free to Oscillate," National Physical Laboratory Aero Report No. 1257, 1968.
19. Roshko, A., "On the Wake and Drag of Bluff Bodies," Journal of Aerospace Sciences, Vol. 22, 1955, pp. 124-132.
20. Bearman, P. W., "On Vortex-Street Wakes," Journal of Fluid Mechanics, Vol. 28, 1967, pp. 625-641.
21. Calbert, J. R., "Experiments on the Low-Speed Flow Past Cones," Journal of Fluid Mechanics, Vol. 27, 1967, pp. 273-289.
22. Simmons, J. E. L., "Similarities Between Two-Dimensional and Axisymmetric Vortex Wakes," The Aeronautical Quarterly, Vol. 28, 1977, pp. 15-20.
23. Birkhoff, G., "Formation of Vortex Streets," Journal of Applied Physics, Vol. 24, 1953, pp. 98-103 (see also: Birkhoff, G., and Zarantonello, E. H., Jets, Wakes, and Cavities, Academic Press, New York, 1957, Chp. XIII).
24. Davies, M. E., "A Comparison of the Wake Structure of a Stationary and Oscillating Bluff Body, Using a Conditional Averaging Technique," Journal of Fluid Mechanics, Vol. 75, 1976, pp. 209-231.
25. Zdravkovich, M. M., "Smoke Observations of the Formation of a Karman Vortex Street," Journal of Fluid Mechanics, Vol. 37, 1969, pp. 491-499.
26. Clements, R. R., "Flow Representation, Including Separated Regions, Using Discrete Vortices," AGARD Lecture series No. 86, 1977.
27. Sarpkaya, T., "An Inviscid Model of Two-Dimensional Vortex Shedding for Transient and Asymptotically-Steady Separated Flow over an Inclined Plate," Journal of Fluid Mechanics, Vol. 68, 1975, pp. 109-128.
28. Sacksteder, R., "On Oscillatory Flows," The Mathematical Intelligencer, Vol. 1, 1978, pp. 45-51.
29. Humphreys, J. S., "On a Circular Cylinder in a Steady Wind at Transition Reynolds Numbers," Journal of Fluid Mechanics, Vol. 9, 1960, pp. 603-612.

30. Phillips, O. M., "The Intensity of Aeolian Tones," Journal of Fluid Mechanics, Vol. 1, 1956, pp. 607-624.
31. Prendergast, V., "Measurement of Two-Point Correlations of the Surface Pressure on a Circular Cylinder," University of Toronto, UTIA Technical Note 23, 1958.
32. El Baroudi, M. Y., "Measurement of Two-Point Correlations of Velocity Near a Circular Cylinder Shedding a Karman Vortex Street," University of Toronto, UTIAS, TN-31, 1960.
33. Etkin, B., Korbacher, G. K., and Keefe, R. T., "Acoustic Radiation from a Stationary Cylinder in a Fluid Stream (Aeolian Tones)," University of Toronto, UTIA, Rev. No. 13, 1958.
34. Gerlach, C. R., and Dodge, F. T., "An Engineering Approach to Tube Flow-Induced Vibrations," Proceedings of the Conference on Flow-Induced Vibrations in Reactor System Components, Argonne National Laboratory, 1970, pp. 205-225.
35. Chaplin, J. R., and Shaw, T. L., "On the Mechanics of Flow-Induced Periodic Forces on Structures," in Dynamic Waves in Civil Engineering, eds., Howells, D. A., Haigh, I. P., and Taylor, C., Wiley-Interscience, London, 1971, pp. 73-94.
36. Vickery, B. J., "Fluctuating Lift and Drag on a Long Cylinder of Square Cross-Section in a Smooth and in a Turbulent Stream," Journal of Fluid Mechanics, Vol. 25, 1966, pp. 481-494.
37. Gerrard, J. H., "A Disturbance Sensitive Reynolds Number Range of the Flow Past a Circular Cylinder," Journal of Fluid Mechanics, Vol. 22, 1965, pp. 187-196.
38. Wilkinson, R. H., Chaplin, J. R., and Shaw, T. L., "On the Correlation of Dynamic Pressures on the Surface of a Prismatic Bluff Body," in Flow-Induced Structural Vibrations, ed., Naudascher, E., Springer-Verlag, Berlin, 1974, pp. 471-487.
39. Gowda, B. H. L., "Some Measurements on the Phenomenon of Vortex Shedding and Induced Vibrations of Circular Cylinders," Deutsche Luft-und Raumfahrt Forschungsbericht No. 75-01, 1975.
40. Stansby, P. K., "The Effects of End Plates on the Base Pressure Coefficient of a Circular Cylinder," Aeronautical Journal, Vol. 87, 1974, pp. 36-37.
41. Etzold, F., and Fiedler, H., "The Near-Wake Structures of a Cantilevered Cylinder in a Cross Flow," Zeitschrift für Flugwissenschaften, Vol. 24, 1976, pp. 77-82.
42. Surry, D., "The Effect of High Intensity Turbulence on the Aerodynamics of a Rigid Circular Cylinder at Subcritical Reynolds Numbers," University of Toronto, UTIAS Report No. 142, 1969.

43. McGregor, D. M., "An Experimental Investigation of the Oscillating Pressures on a Circular Cylinder in a Fluid Stream," University of Toronto, UTIA, Technical Note No. 14, 1957.
44. Berger, E., "Unterdrueckung der Laminaren Wirbelstroemung und des Turbulenzeinsatzes der Karmanschen Wirbelstrasse im Nachlauf eines Schwingenden Zylinders bei kleinen Reynolds-Zahlen," Jahrbuch der WGLR, 1964, pp. 164-7172.
45. Tournier, C., and Pyb, B., "The Behaviour of Naturally Oscillating Three-Dimensional Flow Around a Cylinder," Journal of Fluid Mechanics, Vol. 85, pp. 161-186.
46. Roshko, A., "On the Aerodynamic Drag of Cylinders at High Reynolds Numbers," Paper presented at U.S.-Japan Research Seminar on Wind Loads on Structures, University of Hawaii, October, 1970.
47. Fage, A., and Johansen, F. C., "The Structure of the Vortex Sheet," Philosophical Magazine, Vol. 7, 1928, pp. 417-436.
48. Bloor, M. S., and Gerrard, J. H., "Measurement on Turbulent Vortices in a Cylinder Wake," Proceedings of the Royal Society, London, series A, Vol. 294, 1966, pp. 319-342.
49. Abernathy, F. H., and Kronauer, R. E., "The Formation of Vortex Streets," Journal of Fluid Mechanics, Vol. 13, 1962, pp. 1-20.
50. Schmidt, D. W., and Tilmann, P. M., "Über die Zirkulationsentwicklung in Nachläufen von Rundstäben," Acustica, Vol. 27, 1972, pp. 14-22.
51. Williams, J. C., "Incompressible Boundary-Layer Separation," Annual Reviews of Fluid Mechanics, Annual Reviews Inc., Palo Alto, Calif., Vol. 9, 1977, pp. 113-144.
52. Bloor, M. S., "The Transition to Turbulence in the Wake of a Circular Cylinder," Journal of Fluid Mechanics, Vol. 19, 1964, pp. 290-304.
53. Fink, P. T., and Soh, W. K., "Calculation of Vortex Sheets in Unsteady Flow and Applications in Ship Hydrodynamics," 10-th Symposium of Naval Hydrodynamics, Cambridge, Mass., 1974.
54. Feng, C. C., "The Measurement of Vortex Induced Effects in Flow Past Stationary and Oscillating Circular and D-Section Cylinders," M.A.Sc. thesis, University of British Columbia, 1968.
55. Naudascher, E., (Editor), Flow-Induced Structural Vibrations, Springer-Verlag, Berlin, 1974.
56. Bishop, R. E. D., and Hassan, A. Y., "The Lift and Drag Forces on a Circular Cylinder in a Flowing Fluid," Proceedings of Royal Society, London, series A, Vol. 277, 1963, pp. 32-50.

57. Toebe, G. H., "The Unsteady Flow and Wake near an Oscillating Cylinder," Journal of Basic Engineering, Trans. ASME, Vol. 91, 1969, pp. 493-502.
58. Vickery, B. J., and Watkins, R. D., "Flow-Induced Vibration of Cylindrical Structures," Proceedings of the First Australian Conference, held at the University of Western Australia, 1962, pp. 213-239.
59. King, R., "Hydroelastic Model Tests of Marine Piles - A Comparison of Model and Full-Scale Results," British Hydromechanics Research Association (BHRA) Report RR-1254, 1974.
60. Sarpkaya, T., "Dynamic Response of Piles to Vortex Shedding in Oscillating Flows," Proceedings of the Offshore Technology Conference, Paper No. 3647, Houston, TX, 1979.
61. Griffin, O. M., Skop, R. A., and Ramberg, S. E., "The Resonant Vortex Excited Vibrations of Structures and Cable Systems," Proceedings of the Offshore Technology Conference, Paper No. 2319, Houston, TX., 1975.
62. Koopman, G. H., "The Vortex Wakes of Vibrating Cylinders at Low Reynolds Numbers," Journal of Fluid Mechanics, Vol. 28, 1967, pp. 501-512.
63. Ferguson, N., and Parkinson, G. V., "Surface and Wake Flow Phenomena of Vortex-Excited Oscillation of a Circular Cylinder," Journal of Engineering for Industry, Trans. ASME, Vol. 89, 1967, pp. 831-838.
64. Ramberg, S. E., and Griffin, O. M., "Vortex Formation in the Wake of a Vibrating, Flexible Cable," Journal of Fluids Engineering, Trans. ASME, Vol. 96, 1974, pp. 317-322.
65. Ramberg, S. E., and Griffin, O. M., "Velocity Correlation and Vortex Spacing in the Wake of a Vibrating Cable," Journal of Fluids Engineering, Trans. ASME, Vol. 98, 1976, pp. 10-18.
66. Novak, M., and Tanaka, H., "Pressure Correlations on a Vibrating Cylinder," Proceedings of the 4-th International Conference on Wind Effects on Buildings and Structures, ed., Eaton, K. J., Cambridge University Press, Cambridge, 1975, pp. 227-232, and 273.
67. Griffin, O. M., "Effects of Synchronized Cylinder Vibrations on Vortex Formation and Mean Flow," in Flow-Induced Structural Vibrations, ed., Naudascher, E., Springer-Verlag, Berlin, 1974, pp. 454-470.
68. Oey, H. L., Currie, I. G., and Leutheusser, H. J., "On the Double-Amplitude Response of Circular Cylinders Excited by Vortex Shedding," Proceedings of the 4-th International Conference on Wind Effects on Buildings and Structures, ed., Eaton, K. J., Cambridge University Press, Cambridge, 1975, pp. 233-240 and 271.

69. Wood, K. N., and Parkinson, G. V., "A Hysteresis Problem in Vortex-Induced Oscillation," Proceedings of the 6-th Canadian Congress of Applied Mechanics (CANCAM), Vancouver, 1977, pp. 697-698.
70. Wood, K. N., "Coupled-Oscillator Models for Vortex-Induced Oscillation of a Circular Cylinder," M.A.Sc. Thesis, The University of British Columbia, Vancouver, August, 1976.
71. Currie, I. G., Hartlen, R. T., and Martin, W. W., "The Response of Circular Cylinders to Vortex Shedding," in Flow-Induced Structural Vibrations, ed., Naudascher, E., Springer-Verlag, Berlin, 1974, pp. 128-142.
72. Stansby, P. K., "Base Pressure of Oscillating Circular Cylinders," Journal of Engineering Mechanics Division of ASCE, Vol. 102, No. EM4, 1976, pp. 591-600.
73. Sarpkaya, T., "Fluid Forces on Oscillating Cylinders," Journal of Waterway, Port, Coastal and Ocean Division of ASCE, Vol. 104, No. WW4, 1978, pp. 275-290.
74. Mei, V. C., and Currie, I. G., "Flow Separation on a Vibrating Circular Cylinder," The Physics of Fluids, Vol. 12, No. 11, 1969, pp. 2248-2254.
75. Raudkivi, A. J., and Small, A. F., "Hydroelastic Excitation of Cylinders," Journal of Hydraulic Research, Vol. 12, No. 1, 1974, pp. 99-131.
76. Griffin, O. M., and Ramberg, S. E., "The Vortex-Street Wakes of Vibrating Cylinders," Journal of Fluid Mechanics, Vol. 66, 1974, pp. 553-576.
77. Taneda, S., "Experimental Investigation of Vortex Streets," Journal of the Physical Society of Japan, Vol. 20, 1965, pp. 1714-1721.
78. van der Pol, B., "Frequency Demultiplication," Nature, Vol. 120, 1927, p. 363.
79. Sainsbury, R. N., and King, D., "The Flow-Induced Oscillations of Marine Structures," Proceedings of the Institution of Civil Engineers, Vol. 49, 1971, pp. 269-302.
80. King, R., Prosser, M. J., and Johns, D. J., "On Vortex Excitation of Model Piles in Water," Journal of Sound and Vibration, Vol. 29, 1973, pp. 169-188.
81. Wootton, L. R., "Oscillations of Piles in Marine Structures," CIRIA Underwater Engineering Group Report No. 40, 1972.
82. Tatsuno, M., "Vortex Wakes Behind a Circular Cylinder Oscillating in the Flow Direction," Bulletin of the Research Institute of Applied Mechanics, Kyushu University, No. 36, 1972.

83. Tanida, Y., Okajima, A., and Watanabe, Y., "Stability of a Circular Cylinder Oscillating in Uniform Flow or in a Wake," Journal of Fluid Mechanics, Vol. 61, 1973, pp. 769-784.
84. Crandall, S. H., Vigander, S., and March, P. A., "Destructive Vibration of Trashracks due to Fluid-Structure Interaction," ASME Paper No. 75-DET-63, 1963.
85. Sarpkaya, T., and Isaacson, M., Waves and Wave Forces - In Theory and Application (to be published in 1980).
86. Griffin, O. M., and Ramberg, S. E., "Vortex Shedding from a Cylinder Vibrating in Line with an Incident Uniform Flow," Journal of Fluid Mechanics, Vol. 75, 1976, pp. 257-271.
87. Hartlen, R. T., and Currie, I. G., "Lift-Oscillator Model of Vortex-Induced Vibration," Journal of the Engineering Mechanics Division of ASCE, Vol. 96, EM5, 1970, pp. 577-591.
88. Skop, R. A., and Griffin, O. M., "A Model for the Vortex-Excited Resonant Response of Bluff Cylinders," Journal of Sound and Vibration, Vol. 27, 1973, pp. 225-233.
89. Iwan, W. D., and Blevins, R. D., "A Model for Vortex-Induced Oscillation of Structures," Journal of Applied Mechanics, Vol. 41, 1974, pp. 581-586.
90. Iwan, W. D., "The Vortex Induced Oscillation of Elastic Structural Elements," Journal of Engineering for Industry, Vol. 97, pp. 1378-1382.
91. Blevins, R. D., and Burton, T. E., "Fluid Forces Induced by Vortex Shedding," Journal of Fluid Engineering, Vol. 95, 1976, pp. 19-24.
92. Eaton, K. J., (editor), Proceedings of the Fourth International Conference of Wind Effects on Buildings and Structures, Cambridge University Press, Cambridge, 1975.
93. Laird, A. D. K., "Water Forces on Flexible Oscillating Cylinders," Journal of the Waterways, Harbors, and Coastal Engineering Division, ASCE, Vol. 88, No. WW3, pp. 125-137, August 1962.
94. Vaicaitis, R., "Cross-Flow Response of Piles due to Ocean Waves," Journal of the Engineering Mechanics Division of ASCE, Vol. 102, No. EM1, pp. 121-134, 1976.
95. Selna, L. and Cho, D., "Resonant Response of Offshore Structures," Journal of the Waterways, Harbors and Coastal Engineering Division, ASCE, Vol. 98, No. WW1, pp. 15-24, 1972.
96. Morison, J. R., O'Brien, M. P., Johnson, J. W., and Schaaf, S. A., "The Forces Exerted by Surface Waves on Piles," Petroleum Transactions, AIME, Vol. 189, 1950.

97. Verley, R. L. P. and Every, M. J., "Wave Induced Vibrations of Flexible Cylinders," Proceeding of the Offshore Technology Conference, Paper No. 2899, May 1977.
98. McConnell, K. G. and Wilson, T. J., "Modeling Self-Excited Vibrations of Offshore Structures due to Wave Motion," Engineering Research Institute Report No. 77337, Iowa State University, May 1977.
99. Sawaragi, T., Takayuki, N. and Hideki, M., "Dynamic Behavior of Circular Pile due to Eddy Shedding in Waves," Coastal Engineering in Japan, Japan Society of Civil Engineers Vol. 20, 1977.
100. Sarpkaya, T. and Tuter, O., "Periodic Flow about Bluff Bodies, Part-1: Forces on Cylinders and Spheres in a Sinusoidally Oscillating Fluid," NPS Technical Report No. NPS-59SL74091, September 1974.
101. Sarpkaya, T., "Vortex Shedding and Resistance in Harmonic Flow about Smooth and Rough Cylinders at High Reynolds Numbers," Technical Report No. NPS-59SL76021, Naval Postgraduate School, Monterey, California, 1976.
102. Klinkhamer, D. J., "Self-Excited Oscillations of the Smooth Circular Cylinder in Harmonic Flow," M. S. Thesis, Naval Postgraduate School, Monterey, California, 1978.
103. Bendat, J. S., and Allan, G. P., Random Data: Analysis and Measurement Procedures, Wiley-Interscience, New York, 1971.
104. Churchill, R.V., Fourier Series and Boundary Value Problems, McGraw-Hill, New York, 1978.
105. Davenport, W. B. Jr. and Root, W. L., An Introduction to the Theory of Random Signals and Noise, McGraw-Hill, New York, 1958.
106. Newland, D. E., An Introduction to Random Vibrations and Spectral Analysis, Longman, London, New York, 1975.
107. Cooley, J. W., and Tukey, J. W., "An Algorithm for the Machine Calculation of Complex Fourier Series," Mathematics of Computation, Vol. 19, No. 90, pp. 297-301, 1965.
108. Runge, C., Zeit für Math. and Physik, Vol. 48, pp. 433, 1903.
109. Runge, C., Zeit für Math. and Physik, Vol. 53, pp. 117, 1905.
110. Keulegan, G. H. and Carpenter, L. H., "Forces on Cylinders and Plates in an Oscillating Fluid," Journal of Research of the National Bureau of Standards, Research Paper No. 2857, Vol. 60, No. 5, May 1958.

111. Thomson, W. T., Theory of Vibration with Applications, Prentice Hall, Inc., Englewood, New Jersey, 1972.
112. King, R., "The 'Added Mass' of Cylinders," The British Hydromechanics Research Association (BHRA) Report TN-1100, 1971.
113. Sarpkaya, T., "Transverse Oscillations of a Circular Cylinder in Uniform Flow, Part-I," Technical Report No. NPS-69SL77071-R, 1977, Naval Postgraduate School, Monterey, Calif.

INITIAL DISTRIBUTION LIST

	No. Copies
1. Defense Documentation Center Cameron Station Alexandria, Virginia 22314	2
2. Library, Code 0142 Naval Postgraduate School Monterey, California 93940	2
3. Professor T. Sarpkaya, Code 69SL Mechanical Engineering Naval Postgraduate School Monterey, California 93940	5
4. Department of Mechanical Engineering, Code 69 Naval Postgraduate School Monterey, California 93940	2
5. Farhad Rajabi Mechanical Engineering, Code 69 Naval Postgraduate School Monterey, California 93940	4

Thesis

186376

R148 Rajabi

c.1

Hydroelastic oscillations of smooth and rough cylinders in harmonic flow.

thesR148

Hydroelastic oscillations of smooth and



3 2768 002 05265 6

DUDLEY KNOX LIBRARY